Reorganization of carbonaceous materials during geological burial and deformation: Experiments and natural examples

Benjamin Moris-Muttoni

UNIVERSITÉ D'ORLÉANS

ÉCOLE DOCTORALE ENERGIE, MATERIAUX, SCIENCES DE LA TERRE ET DE L'UNIVERS

Institut des Sciences de la Terre d'Orléans

THÈSE présentée par :

Benjamin MORIS-MUTTONI

soutenue le : **7 décembre 2021**

pour obtenir le grade de : **Docteur de l'Université d'Orléans**

Discipline/ Spécialité : **Sciences de la Terre**

Doctoral thesis in Geosciences

Reorganization of carbonaceous materials during geological burial and deformation: Experiments and natural examples

THÈSE dirigée par :

CHEN Yan	Professeur, ISTO, Orléans *(Directeur de thèse)*
AUGIER Romain	Maitre de conférences, ISTO, Orléans *(Co-encadrant de thèse)*
RAIMBOURG Hugues	Professeur, ISTO, Orléans *(Co-encadrant de thèse)*

RAPPORTEURS :

BEHR Whitney	Professeur, ETH Zürich
IKARI Matt	Research associate, University of Bremen

JURY :

BEHR Whitney	Professeur, ETH Zürich
IKARI Matt	Research associate, University of Bremen
LELOUP Philippe Hervé	Directeur de recherche, Université de Lyon
VITALE BROVARONE Alberto	Professeur, University of Bologna
AUGIER Romain	Maitre de conférences, ISTO, Orléans
RAIMBOURG Hugues	Professeur, ISTO, Orléans
LAHFID Abdeltif	Ingénieur-chercheur, BRGM, Orléans
SCAILLET Bruno	Professeur, ISTO, Orléans Président du jury

INVITÉS :

CHEN Yan	Professeur, ISTO, Orléans
HERWEGH Marco	Professeur, University of Bern

Remerciements

9772, c'est le nombre d'analyses Raman qui ont permis à ce travail de voir le jour. Mais 9772 c'est aussi le nombres de merci que je tiens à dire à toutes les personnes qui m'ont aidé, encadré, guidé, surprise, intrigué, relaxé, apaisé, enthousiasmé. Et puis qui m'ont fait rire, sourire, pleurer, danser, douter, rêver et surtout aimé. Un doctorat, c'est 3 ans de vie dans un laboratoire et une immensité de sentiments et d'émotions qui nous traversent. Alors pour toutes ces personnes qui m'ont fait vivre ce moment de hauts et de bas, je vous remercie profondément.

Romain et Hugues, merci pour cet encadrement au cours de ces trois années. Merci pour votre temps et pour la confiance que vous m'avez accordée pour mener à bien ce projet. Merci pour ces souvenirs, notamment sur le terrain, j'ai quelques pépites en photo que je garderais pour moi évidemment. Et surtout merci pour votre façon d'être, votre humanité et votre gentillesse.

Comment vous oublier, les collègues, ceux qui partagent les galères et les joies du quotidien mais surtout les grandes pintes et verres de Chartreuse après une bonne raclette. Merci à vous tous pour ces moments d'évasions et de folies qui nous ont permis de relativiser et d'extérioriser face à de mauvaises passes qui peuvent se présenter à nous. A ceux également qui sont partis au cours de cette thèse, à mes chercheurs de champignons préférés. Et puis, à vous trois, oui vous là, je terminerais facilement en vous disant que « C'EST VOTRE TOUR MAINTENANT ! ». / Pièce.

Une pensée pour toutes les personnes travaillant à l'ISTO et qui m'ont aidé dans ce projet en m'apportant leurs expertises, leurs connaissances, leur temps et leur bonne humeur.

Un merci à ma famille, à ceux qui pensent encore que je suis étudiant, pour leur soutien, leur amour et ces moments qui m'ont permis de sortir du train-train quotidien en rentrant le temps d'un week-end à la maison. Merci pour ces colis gourmands, quand ce n'est pas la joie, il y a toujours un morceau de Comté ou un kit pour faire ses macarons au fond d'un carton pour vous réconforter. Et donc, oui on peut être docteur en « cailloux » mais non on ne fait pas que lécher.

Un petit point pour vous les copains de longues dates, ceux qui sont restés et aussi à ceux qui sont partis pour quelconque raisons. Merci beaucoup pour ces moments de joies, d'amitié et de partage. Et à vous « les Canards » en ce 18 octobre 2021. Merci pour vos conseils pas toujours super appropriés mais qui ont eu le mérite d'être drôles. A ces après-midi perdus à rire et débattre de sujet dont tout le monde s'en fou, surtout moi. Alors on résume : le nucléaire bien ou pas bien ? JLM c'est vraiment le goat ? D'ailleurs vous avez vu sa dernière vidéo, elle dure que 4 heures 37 ? Memphis c'est le nouveau Messi ou le nouveau Drake ? Est-ce que l'OL a le meilleur milieu de terrain du monde ? Vous avez vu le double contact de Cherki contre Vaulx-en-Velin en D8 ce week-end ? Je vais épargner les lecteurs de vos discussions scabreuses et légèrement déplacées. Vous me soulez mais qu'est-ce que je vous aime.

Abstract

Carbonaceous material (CM) is a common component of metasediments in collision and accretion belts, mainly deriving from the diagenetic and then the metamorphic evolution of the organic matter initially present within the sediment. When exposed to temperature increase, its progressive transformation through carbonization and graphitization corresponds at microscopic scale to the irreversible organization of the carbonaceous materials toward to well-crystallized graphite, and represents the last step in the evolution. In addition, in strongly sheared rocks, anomalously high CM crystallinity observed locally may reflect the effect of the deformation. The connection between CM crystallinity and strain is nevertheless relatively unclear, firstly because of lack of natural and experimental data, secondly due to a large range of deformation processes, from viscous slip at slow strain rate to fast seismic slip, with potentially different effects on CM crystalline organization.

Here we propose to explore the strain effects on the CM crystallinity with natural examples, from accretionary complexes (Shimanto belt, Kodiak Accretionary Complex, Alps), and experiments encompassing both seismic and non-seismic deformation. We focused on the low temperature range, from 200 to 360°C, spanning the carbonization and the early graphitization stages. The combination between the RSCM using high-resolution profile approach and the microstructures observations enabled us to document the strain effect on the CM crystallinity. Intensity ratio (IR), as a RSCM parameter, appears to be the most relevant variable to record deformation. Its increase reflects the degree of CM crystallinity in domains of high strain, irrespective of deformation regime. This CM crystallinity increase is explained by the effect of shear that results in a better organization of the aromatic carbon layers and of the crystallite growth. Irrespective of the deformation mechanism (i.e. in low and high strain-rate examples), IR is increased where strain is localized. There seems to be a positive correlation between strain intensity and IR increase. Indeed, the highest IR values are observed in the core of Black Fault Rock, where microstructures such as ultra-comminution point to very large strain intensity. In opposition, for moderate IR increase in low strain rate domains, strain localization and weakening

processes are induced recrystallization (i.e. white mica and chlorite) and destabilization of phases (i.e. quartz and albite).

In addition, the effects of short-life contact metamorphism have been explored through the study of immature sediments and mature sediments in contact with basalt bodies. The spatially limited “flash-heating”, detected thanks to the $D_3/G_{sl.}$ Ratio considered as a new RSCM parameter, is spotted on CM grains in both immature and mature sediments up to 300°C where the signal is overprinted by regional metamorphism. This new parameter allows us to detect the frictional “flash-heating” in BFR observed in accretionary complexes and discriminate its genesis.

These results bear major consequences on the strain influence on the carbonaceous material crystallinity and on the interpretation of the Raman Spectroscopy of Carbonaceous Material temperature, obtained through extensive measurements in high strained terranes for seismic and non-seismic regimes. In addition, the correlation between the CM crystallinity and the strain quantity reveals the potential of the Raman spectroscopy as a future tool to evaluate the strain quantity. Finally, the new $D_3/G_{sl.}$ ratio is a efficient RSCM parameter to decipher if the CM crystallinity increase is induced by a flash heating or a mechanical process.

Résumé

La matière carbonée (CM) est un composant commun des méta-sédiments, observée dans les zones de collisions et les prismes d'accrétions, et dérivée de la matière organique initiale contenue dans les sédiments, via les processus de diagenèse et de métamorphismes. L'évolution progressive lors d'une exposition à un chauffage, à travers les processus de carbonisation et de graphitisation, correspond à l'échelle nanoscopique à la réorganisation irréversible de la matière carbonée jusqu'au stade ultime du graphite, où la CM est parfaitement ordonnée. Les études précédentes attribuaient des anomalies localisées de cristallinité de la CM à l'effet de la déformation. Cependant, malgré la diversité des microstructures et des mécanismes de déformation à faible température, de 200 à 360°C, l'effet de la déformation sur la cristallinité de la CM faiblement organisée reste peu étudié à l'exception de déformation rapide provoquant un échauffement par friction.

Dans cette étude, nous proposons d'explorer les effets de la déformation sur la cristallinité de la CM à travers l'étude d'objets naturels et expérimentaux. Les objets naturels consistent des échantillons prélevés le long de gradients de déformation à plusieurs échelles et imbriqués dans d'anciens prismes d'accrétions exhumés (Shimanto Belt, Kodiak Accretionary Complex, Alpes). Ils nous ont permis d'observer à la fois des régimes de déformations liés à des phénomènes sismiques ou non-sismiques. La combinaison des microstructures avec l'approche du RSCM, grâce à coupes perpendiculaires aux structures de haute résolution, a permis de documenter ces effets sur la cristallinité. Le ratio d'intensité (IR), sensible à la déformation et évoluant de façon monotone sur la gamme de température étudiée ici, a montré une croissance significative de la cristallinité de la CM dans les deux régimes de déformations et à toutes les échelles. Cette augmentation de la cristallinité dans les zones déformées s'explique à l'échelle nanoscopique par la réorganisation des feuillets aromatiques du carbone et par l'agrandissement des cristallites. Une corrélation positive semble se dégager entre la quantité de déformation et l'augmentation de l'IR. En effet, les plus grandes valeurs de l'IR ont été mesurées dans le cœur des Black Fault Rocks (BFR) où les microstructures telles que de l'ultra-comminution indiquent une grande quantité de déformation. A l'opposé, pour des augmentations de l'IR plus modérées dans les

domaines déformés à faible vitesse, la localisation de la déformation ainsi que les processus d'affaiblissement rhéologique sont induits par la recristallisation de phyllosilicates ainsi que la déstabilisation des phases dites dures.

De plus, les effets d'un métamorphisme de contact de courte durée ont été explorés à travers l'étude de sédiments immatures et matures en contact avec de corps de basaltes. Le « flash-heating », spatialement limité et détecté à l'aide du ratio $D_3/G_{sl,}$, un nouveau RSCM paramètre, est remarqué sur les grains de CM pour tous les sédiments jusqu'à 300°C où le métamorphisme régional efface les vestiges de ce chauffage court et intense. L'utilisation de ce paramètre a également permis la détection de chauffages courts générés par friction lors de la rupture sismique formant les BFR et en définir leur processus de formation.

Ces résultats renforcent l'idée que la déformation, qu'elle soit sismique ou non, est un facteur contrôlant la cristallinité de la CM et que l'interprétation des températures issues des thermomètres RSCM devrait être faite avec prudence dans le cas d'une utilisation pour des terrains déformés. De plus, la corrélation entre la quantité de déformation et l'augmentation de l'IR montre l'importance de la RSCM afin d'évaluer la quantité finie de déformation. Enfin, l'utilisation de la RSCM et du ratio $D_3/G_{sl.}$ ont démontré leurs utilités quant à la dissociation entre les effets du 'flash heating' et mécanique sur la cristallinité de la CM.

Contents

Table of abbreviations

BFR: Black Fault Rock

CL: Cathodoluminescence

CM: Carbonaceous Material

EBSD: Electron Back Scattered Diffraction

EPMA: Electron Probe Micro-Analysis

HRTEM: High-Resolution Transmission Electron Microscopy

HVR: High Velocity Friction Experiment

IR: Intensity Ratio

LM: Light Microscopy

OM: Organic Matter

RSCM: Raman Spectroscopy of Carbonaceous Material

SEM: Scanning Electron Microscopy

TOC: Total Organic Content

%VR: Vitrinite reflectance

XRD: X-ray diffraction

XRF: X-ray Fluorescence

Résumé étendu

1. Introduction

La compréhension des processus géodynamiques représente un enjeu majeur dans le monde des géosciences. L'étude de zones actives fossiles, aujourd'hui exhumées, est nécessaire à la compréhension de ces processus actuellement actifs, notamment dans les zones de convergences telles que les prismes d'accrétions ou les chaines de montagnes. Le chemin P-T-t obtenu à l'aide des méthodes de pétrologies conventionnelles couplé à l'étude de l'évolution structurale sont utilisés en géosciences afin d'augmenter notre savoir vis-à-vis de ces processus géodynamiques. Cependant, la mise en place de ces outils nécessite l'occurrence d'assemblages minéralogiques, qui ne sont pas toujours visibles, notamment pour le métamorphisme de bas grade dans les sédiments impliqués dans les zones de convergences.

La matière carbonée (CM), qui correspond à la partie résiduelle de la matière organique, après les processus de diagénèse et de métamorphisme, est un composant ubiquiste des méta-sédiments impliqués dans les zones de convergences. La CM, quand elle est chauffée, réorganise sa structure cristalline jusqu'à atteindre le stade final de graphite où elle est parfaitement cristallisée et ce à travers les processus maturation appelés la carbonisation et la graphitisation. L'étude de la structure cristalline de la CM utilisant la diffractométrie de rayons X (DRX), la microscopie électronique à transmission ainsi que la réflectance de la vitrinite (%VR) (Beny-Bassez and Rouzaud, 1985; Oberlin, 1989; Wada et al., 1994) a permis de définir l'évolution de la cristallinité de la CM comme un indicateur des conditions du pic du métamorphisme (Pasteris and Wopenka, 1991; Wada et al., 1994; Wopenka and Pasteris, 1993). De plus, la spectroscopie Raman de la matière carbonée (RSCM) est utilisée afin de refléter l'organisation cristalline de la CM basée sur l'évolution du spectre Raman et de ses paramètres respectifs (Beny-Bassez and Rouzaud, 1985; Pasteris and Wopenka, 1991). Cette méthode regroupe les avantages d'être rapide, facile à mettre en place et est non-destructive pour une multitude de matériaux contenant de la CM. Dans les deux dernières décennies, l'augmentation de la précision de la méthode RSCM, plusieurs calibrations ont vu le jour liant la cristallinité de la CM et la température maximale atteinte lors du métamorphisme qu'il soit régional ou de contact (Aoya et al., 2010; Beyssac et al., 2002; Kouketsu et al., 2014; Lahfid et al., 2010; Rahl et al., 2005). Ces thermomètres RSCM sont aujourd'hui largement

acceptés par la communauté de pétrologistes et utilisés dans des terrains métamorphiques (Beaudoin et al., 2015; Clerc et al., 2015; Lanari et al., 2012).

Cependant, des facteurs externes, comme le type de CM, l'interaction fluide-roche, le type de matrice ou la déformation, peuvent influer la cristallinité de la CM notamment dans le cas d'une faible organisation cristalline (Lahfid et al., 2010). Le dernier facteur cité a montré différentes conclusions et interprétations allant de la graphitisation (Bustin et al., 1995) à l'amorphisation (Kirilova et al., 2018) de la CM. Ces conclusions semblent cependant liées aux mécanismes de déformation (Nakamura et al., 2015) et au degré de cristallinité de la CM initialement contenue dans le sédiment (Kaneki and Hirono, 2019). La littérature étudiant ce phénomène reste cependant très limitée. En effet, la majorité des études portant sur l'effet de la déformation sur la cristallinité de la CM sont concentrées sur l'analyse d'objets naturels et expérimentaux pour des degrés de cristallinité très élevés et attachés à la graphitisation (Bonijoly et al., 1982a; Bustin, 1983a; Bustin et al., 1995; Kedar et al., 2020; Kouketsu et al., 2017; Kuo et al., 2018; Nakamura et al., 2015; Ross et al., 1991a; Ross and Bustin, 1990; Suchy et al., 1997; Wilks et al., 1993). Les études concernant de plus faibles degrés de cristallinité de la CM, typiquement lors de la carbonisation et les premières étapes de la graphitisation (i.e. 200 à 360°C), restent à ce jour très restreintes à l'exception de déformation très rapide et liée à des phénomènes sismiques où la distinction entre l'effet de la déformation et la température générée par friction sont indissociables (Ito et al., 2017; Ujiie et al., 2021). De ce fait, l'effet de la déformation sur la cristallinité de la CM peu organisée reste peu documenté malgré l'occurrence d'une multitude de microstructures couvrant des déformations de faible (non-sismique) ou très rapide vitesses (sismique) ou au caractère cassant ou visqueux.

Le but de ce travail est d'explorer les effets de la déformation sur la cristallinité de la CM principalement lorsque la CM est faiblement organisée, lors de la carbonisation et des premières étapes de la graphitisation, à travers des gradients de déformation naturels issus de zones de déformation lente (Partie I) ou rapide (Partie II). Ces gradients de déformation ont été prélevés dans des prismes d'accrétions (Shimanto Belt, Kodiak Accretionary Complex, Complexe Infrahelvetic) offrant des structures de déformation à diverses échelles et une multitude de quantité de déformation finie. Cependant, les échantillons naturellement déformés présentent le désavantage de ne pas pouvoir quantifier les

paramètres de déformation et de superposer plusieurs événements de déformations. De ce fait, des expériences de déformation ont été réalisées afin de contrôler ces paramètres. Pour les deux jeux d'échantillons la cristallinité de la CM a été évaluée via la méthode RSCM, proposant une approche de haute résolution, et liée aux microstructures obtenues à l'aide des méthodes conventionnelles pétrologiques (microscopie optique, cathodoluminescence optique, microscopie électronique et microsonde). Une dernière partie (Partie III) se consacre à l'effet du métamorphisme de contact court sur la cristallinité de la CM sur des échantillons immatures et maturés jusqu'à 330°C (i.e. température RSCM) en contact avec des corps de basaltes.

2. La méthode RSCM et l'évolution du ratio d'intensité

La méthode RSCM, qui nous a permis d'évaluer la cristallinité de la CM, est basée sur la vibration des liaisons entre les différents atomes de la CM. Ceci permet via le décalage (Raman shift), entre la longueur d'onde émise et celle analysée par le spectromètre, d'obtenir un spectre dont la forme évoluera en fonction de l'organisation cristalline de la CM (Figure 1a et 1b). Ce spectre se compose de deux bandes appelées D-band et G*sl.* band, respectivement centrées à 1350 et 1600cm^{-1}. A travers la méthode de déconvolution décrite par (Lahfid et al., 2010), adaptée à une cristallinité faible de la CM (i.e. ce thermomètre couvre des températures allant de 200 à 330°C), la bande D se compose des bandes D4, D1 et D3 et la bande G*sl.* des bandes G et D2 (Figure 1a). A partir de cette déconvolution, de multiples paramètres peuvent être obtenus comme l'aire des bandes, leurs intensités ou leurs largeurs à mi-hauteur. Le ratio entre l'intensité de la bande D et de la bande G*sl.*, appelé ratio d'intensité (IR), est considéré comme un paramètre majeur de la RSCM qui reflète la cristallinité de la CM (Pasteris and Wopenka, 1991; Tuinstra and Koenig, 1970; Wopenka and Pasteris, 1993). Ce paramètre évolue en deux phases avec d'abord une augmentation lors de la phase carbonisation et les premières étapes de la graphitisation (i.e. l'intervalle étudié ici) allant de 0.5 à 1.6 puis s'en suit une diminution de 1.6 à 0 lorsque la CM atteint le stade de graphite (Figure 1b et 1c). Cependant, basé sur notre expérience et sur la littérature (Bustin et al., 1995; Kedar et al., 2020; Kuo et al., 2018), l'IR est sensible à la déformation au même titre que la largeur à mi-hauteur de la bande G ou l'intervalle séparant les bandes D et G. Cependant ces deux derniers paramètres présentent des évolutions ambiguës et ont préféré être évités. Basé sur la

sensitivité de l'IR à la déformation, nous avons produit notre propre calibration de l'IR en fonction de la température RSCM grâce à l'analyse d'échantillons faiblement ou pas déformés (Figure 1c).

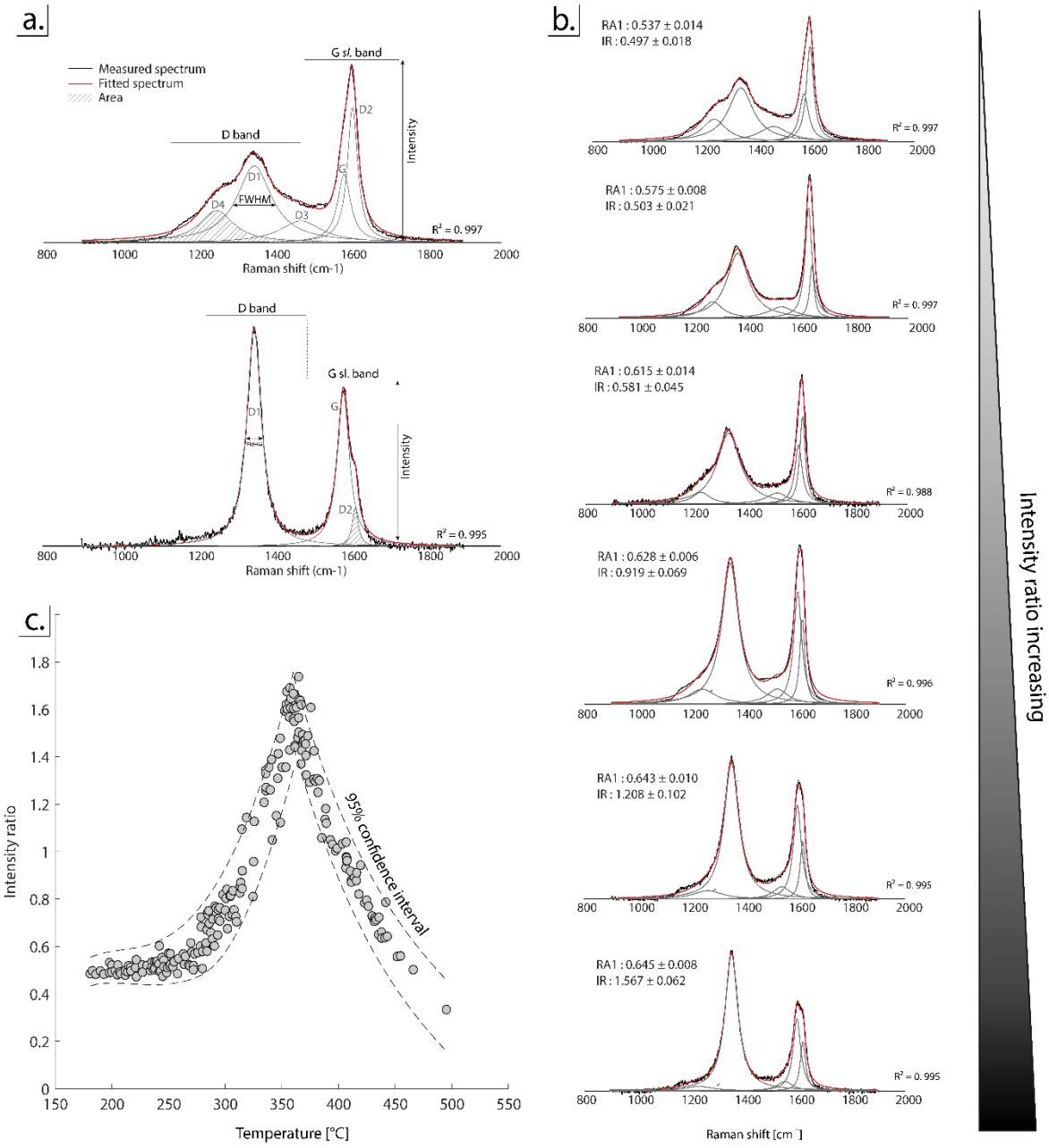

Figure 1 : Spectre Raman de la matière carbonée. a. Spectres typiques de la CM et les paramètres Raman respectifs pour des grains de CM peu organisé et organisé utilisant les méthodes de déconvolution proposées par (Beyssac et al., 2002; Lahfid et al., 2010). b. Evolution de la forme du spectre Raman et de laugmentation de l'IR lors de la carbonisation et des premiers stades de la graphitisation. c. Calibration obtenue de l'IR avec la température RSCM pour des échantillons peu ou pas déformés montrant un intervalle de confiance de 95%.

3. L'influence de la déformation lente non-sismique sur la cristallinité de la CM (Chapitres IV et V)

Des gradients de déformation ont été analysés grâce à la méthode RSCM afin d'en comprendre l'effet de la déformation lente et non-sismique sur la cristallinité de la CM. Différentes tailles de gradients de déformation ont été prélevées allant de l'échelle millimétrique (Figure 2) jusqu'à des gradients métriques (Figure 3) avec des quantités de déformation différentes. De plus, les échantillons ont été sélectionnés dans des zones couvrant la totalité du degré de cristallinité de la CM recherché, soit des températures allant de 200 à 360°C. Ceci se traduit par des microstructures dans les zones où la déformation est localisée montrant d'abord un caractère fragile via l'observation de cataclasite puis le développement de bandes de cisaillements (i.e. shear-zones) visqueuses (Figure 2) allant jusqu'à la mylonitisation (Figure 3).

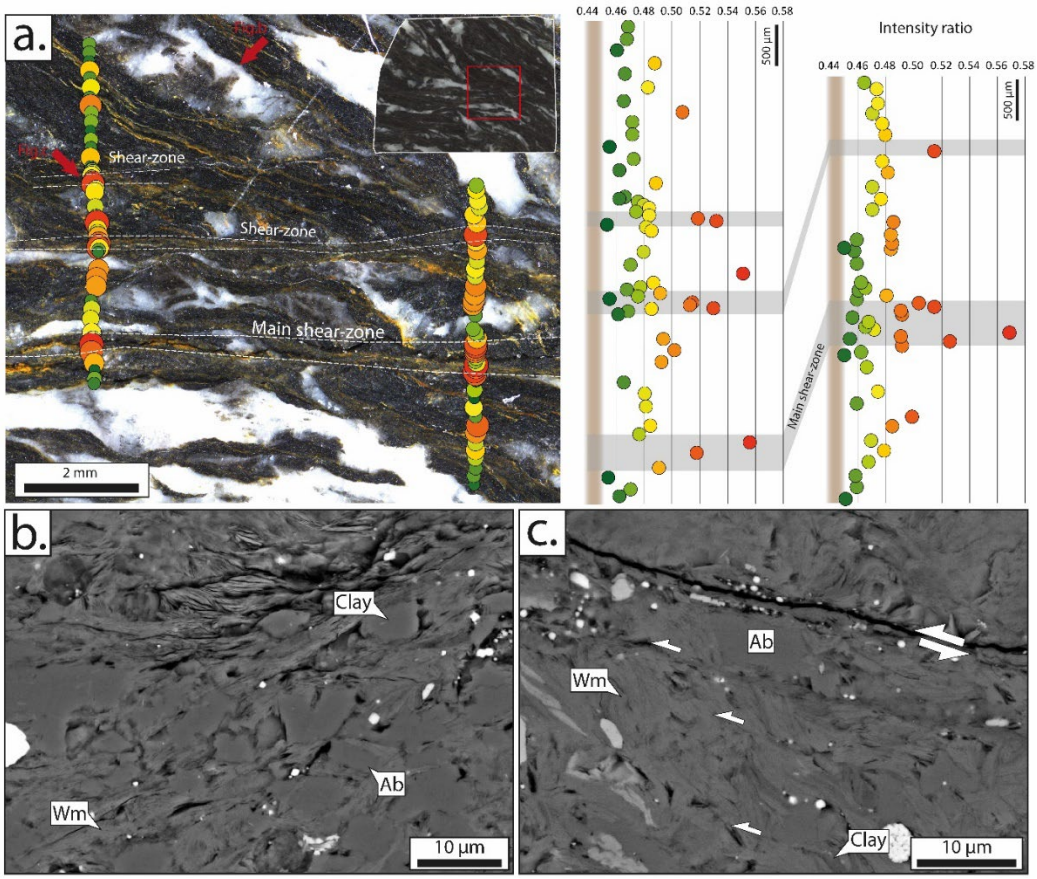

Figure 2 : Profile Raman recoupant des shear-zones dans l'échantillon HN64 provenant du Shimanto Belt et microstructures. a. Profile montrant l'IR à travers les shear-zones et les diagrammes respectives montrant les évolutions de l'IR b. Argile et micas blancs marquant la foliation principale dans l'encaissant c. Majorité de micas blancs recristallisés avec des argiles intercalées montrant une multitude de shear-bands dans la zone déformée.

En réponse à ces déformations l'IR mesuré montre toujours une augmentation qui correspond à une meilleure cristallinité de la CM. Les profils de l'IR réalisés à travers les structures de déformation montrent des évolutions très continues avec une dispersion des données allant de valeurs supérieures à celles observées dans l'encaissant. Cependant des nuances sont à distinguer en fonction du type de déformation observé. En effet, dans les zones où la déformation est cassante et limitée, l'augmentation de la cristallinité reste cependant très faible voir insignifiante (i.e. < 5%) alors que dans les zones de cisaillements visqueuses, cette augmentation est modérée mais significative (i.e. 10 – 20%). Dans le cas d'une grande quantité de déformation, comme celle observée sous le Glarus thrust, dans la mylonite au contact, une augmentation très importante est constatée (i.e. ± 50%). Il semblerait donc que la déformation non-sismique montre une corrélation positive avec la quantité de déformation.

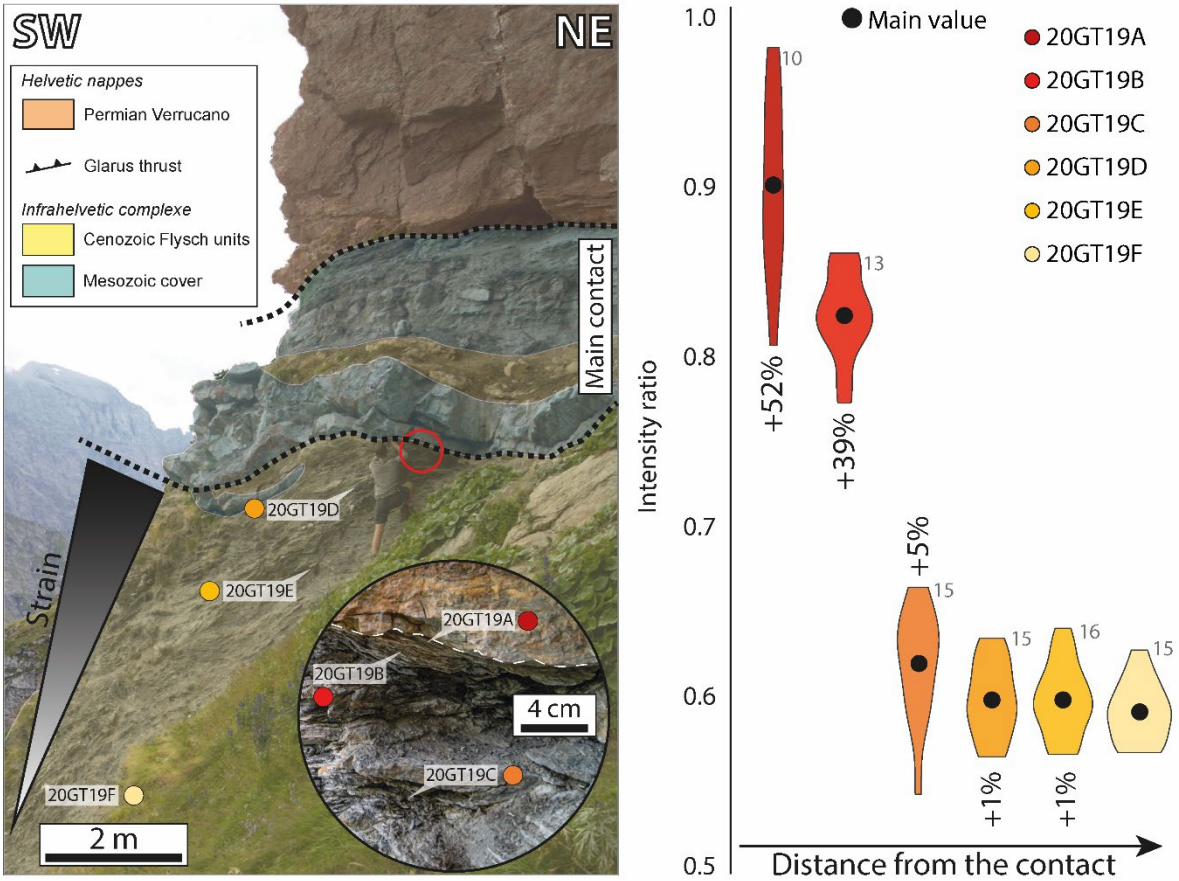

Figure 3 : 20GT19 gradient de déformation sous le Glarus Thrust dans la région du Foostock. Structure et gradient d'échantillonnage dans les flysch du Cénozoïque avec la localisation des échantillons analysées ainsi qu'un zoom sur la zone de contact où des mylonites sont observées. Evolution de l'IR à travers le gradient de déformation montrant une augmentation en se rapprochant du contact

Couplés aux données sur des échantillons naturels, des objets déformés expérimentalement ont été analysés. Les microstructures, identiques à celles observées dans les zones déformées naturelles, indiquent le développement de bandes de cisaillement visqueuses généré par la recristallisation de phyllosilicates et la déstabilisation de phases dites 'dures' (i.e. quartz et albite) (Figure 4b et 4d). Le développement de ces zones de déformation plastiques est directement lié avec les données mécaniques (Figure 4a). En parallèle, à l'instar des zones de cisaillement naturelles, l'IR montre une augmentation modérée et une évolution identique (Figure 4c).

De ce fait, les données microstructurales et sur la CM, entre les zones de déformations entre les échantillons naturels et expérimentaux, sont semblables et indiquent toutes deux une augmentation de la cristallinité de la CM et une corrélation avec la quantité de déformation.

4. L'influence de la déformation rapide (sismique) sur la cristallinité de la CM (Chapitres VI et VII)

Dans une seconde partie, l'effet de la déformation rapide, générée lors de déplacement sismique, sur la cristallinité du CM, a été étudié. Pour cela, trois Black Fault Rocks (BFR), décrites dans la littérature comme des pseudotachylytes issues d'une fusion par friction, ont été analysées. Cependant les microstructures, certes proches de celles observées dans le cas d'objets fondus, ne montrent pas les caractéristiques irréfutables de ce mode de genèse pour ces BFR (Figure 5a à 5c). L'analyse RSCM montre un IR augmentant de façon considérable (i.e. 40 à 60%) dans les zones déformées, dont les profils, une fois synthétisés, montrent une évolution abrupte aux bordures du cœur de la faille ainsi qu'une valeur relativement constante au sein des BFR (Figure 5d et 5e). L'application d'un modèle numérique mimant la diffusion de la chaleur couplée à la réponse cinétique sur la cristallinité de la CM, calculée en amont via des expériences de maturation à température et pression constantes, ne correspond pas à la forme du profil mesuré dans le cas des 3 BFR. L'association des microstructures ambigües et de la différence entre les mesures de l'IR et celles modélisées ne permettent pas de confirmer l'hypothèse de genèse de ces BFR par fusion. De ce fait, le travail mécanique est considéré comme étant le facteur principal contrôlant l'évolution de la cristallinité de la CM pour ces trois objets.

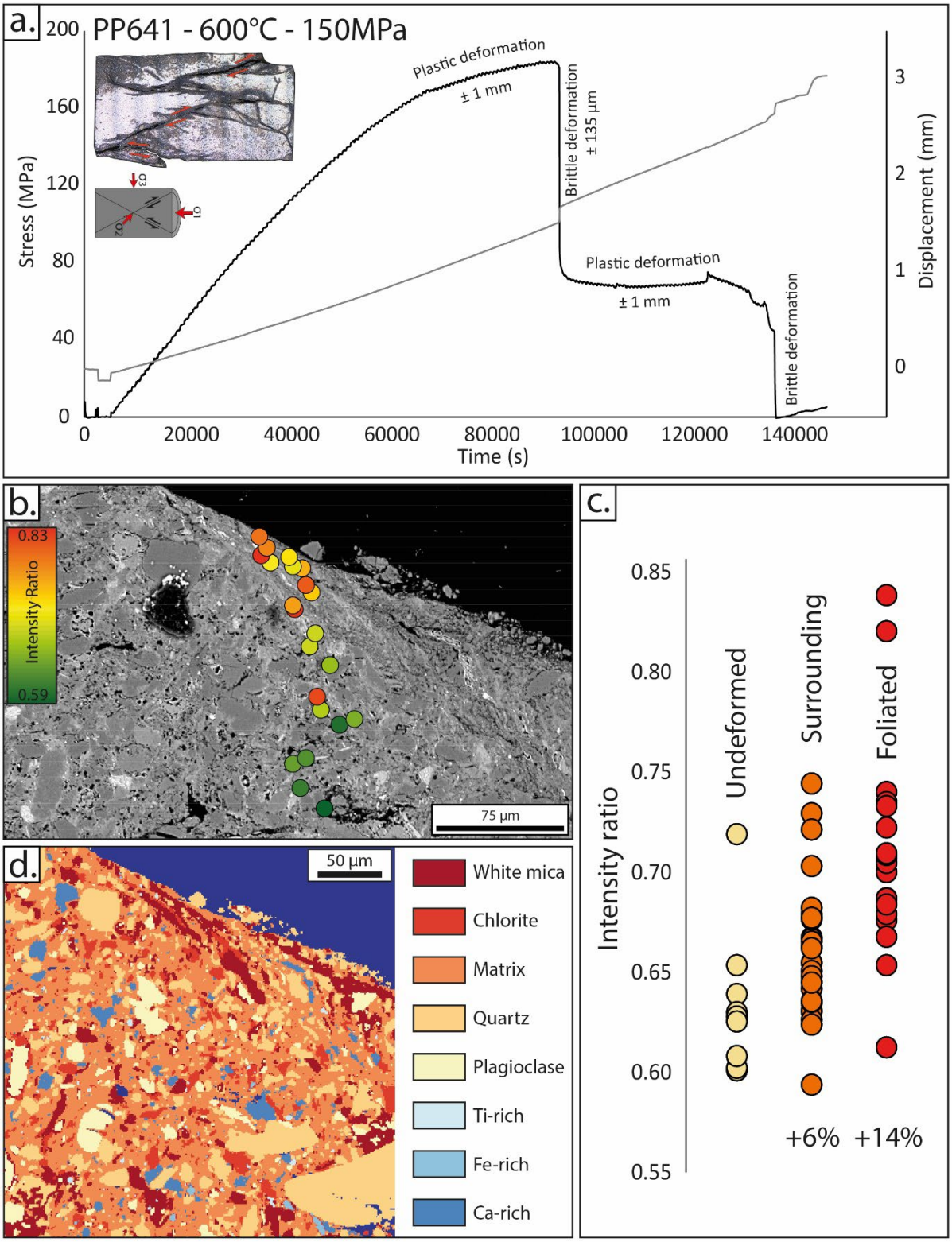

Figure 4 : Données mécaniques, Raman et microstructurales issues de l'expérience en presse Paterson PP641. a. Données mécaniques montrant l'évolution de la contrainte et le déplacement en fonction du temps ainsi que l'interprétation des régimes de déformation b. Evolution de l'IR le long d'une shear-zone formée lors de l'expérience c. Diagramme de l'évolution de l'IR en fonction des différentes zones analysées et les augmentations de l'IR respectives d. Carte des phases obtenue à l'aide d'une imagerie microsondes et du logiciel XMapTools montrant la recristallisation de phyllosilicates dans les shear-zones.

En supplément, des données microstructurales et sur la cristallinité de la CM pour deux autres BFR, prélevées dans un environnement cette fois-ci majoritairement gréseux, ont été obtenues. Pour celles-ci les microstructures liées à une origine issue d'une fusion sont présentes et montrent peu de doute vis-à-vis de ce processus de formation. De plus, l'empreinte de ce chauffage rapide et intense (i.e. flash heating) est visible sur la forme des spectres de la CM via une augmentation significative de la bande D3 et du nouveau ratio D3/Gsl ainsi que d'une augmentation de l'IR significative. Ce même genre de forme de spectres a été observé dans la littérature à travers des exemples expérimentaux générant des chaleurs excessives sur de très courtes périodes comme des expériences de stick-slips (Aubry et al., 2018), de pyrolyses (Aubry et al., 2018; Muirhead, 2012) ou de fusion par friction rotationnelle (Ito et al., 2017).

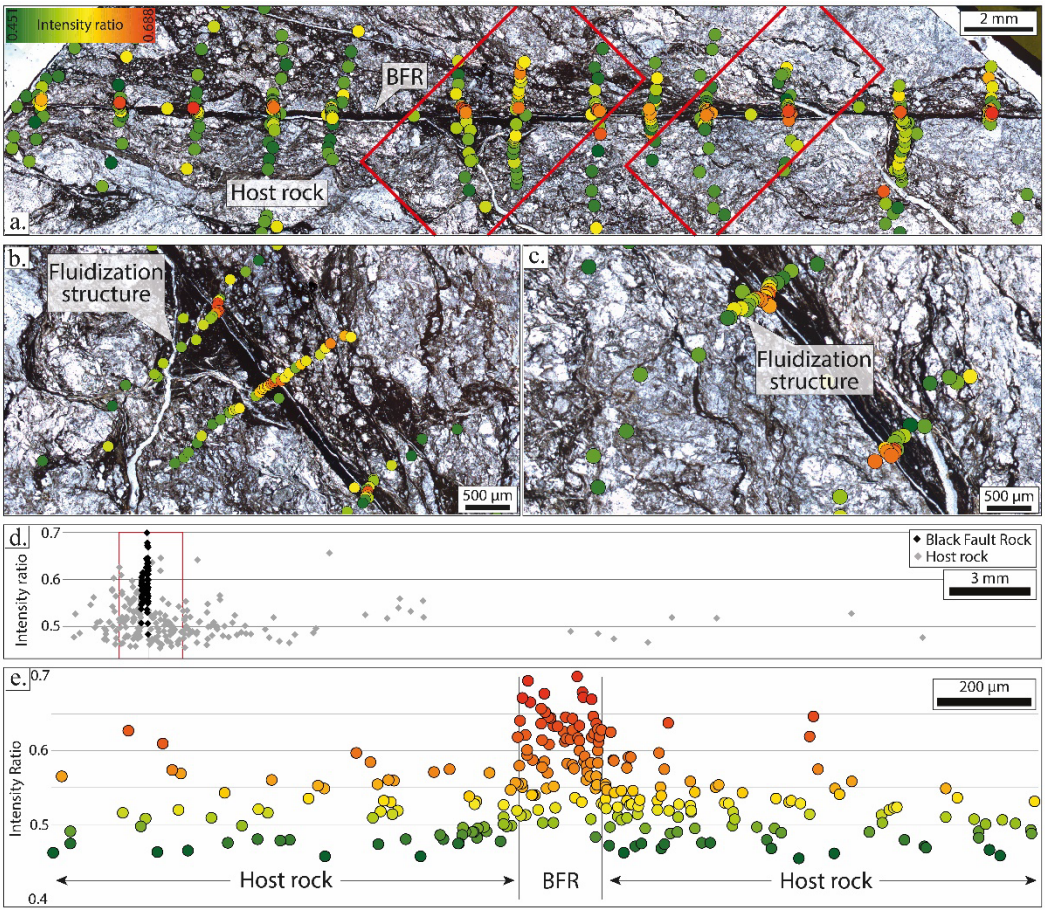

Figure 5 : Résultats du RSCM obtenus pour la Black Fault Rock d'Okitsu (Shimanto Belt) et de son encaissant. a. Evolution de l'IR à travers des coupes sériées recoupant la BFR et son encaissant b.et c. Zoom sur les structures de fluidisation et le cœur de la faille d. Profil composite montrant l'évolution de l'IR e. Zoom sur le profil composite (rectangle rouge en d.) montrant une évolution abrupte aux limites de la BFR.

Afin de confirmer l'hypothèse d'une détection du flash-heating, grâce au nouveau ratio D3/Gsl., des expériences de flash-heating ont été réalisées exposant des éclats de pélite mature (i.e. 200°C) du Shimanto Belt à deux lasers générant une température de 1400°C pour temps allant de 0.5 à 60 secondes. Ces résultats montrent une évolution similaire de la cristallinité de la CM à celles observées pour les expériences de flash-heating et pour les deux BFR étudiées (Figure 6). De ce fait, le RSCM semble être un outil adapté à la détection de chaleur intense et de très courte durée. Ceci a également permis de confirmer d'une part que les deux BFR étaient bien issues d'une fusion de l'encaissant et de pouvoir caractériser, à l'avenir, le mécanisme de genèse des BFR dans les prismes d'accrétion.

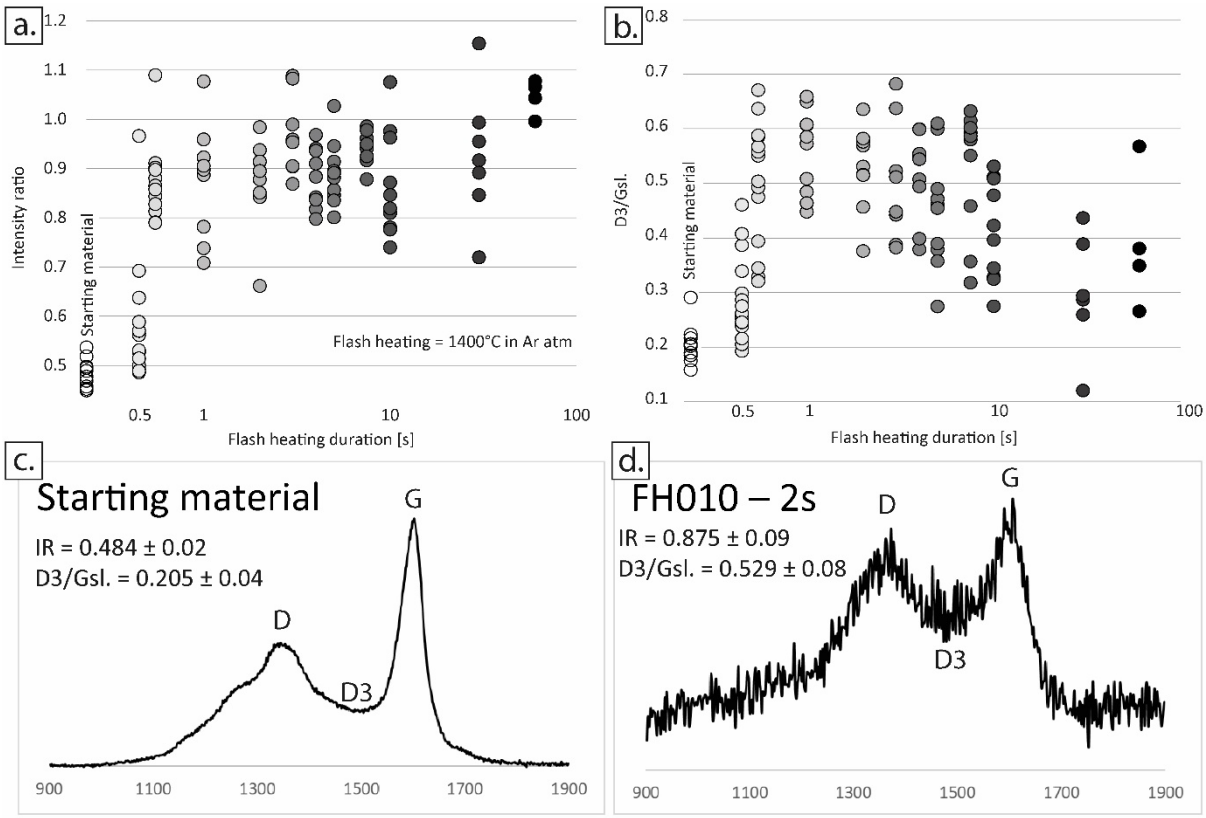

Figure 6 : Evolution de l'IR et du D3/Gsl. ratio mesurés sur les échantillons expérimentaux obtenus lors des expériences de flash-heating. a. et b. Evolution de l'IR et du D3/Gsl. ratio obtenus depuis le matériau de départ jusqu'à un chauffage de 60 secondes à environ 1400°C c. et d. Spectres obtenus pour le matériau de départ et après un chauffage de 2 secondes à 1400°c environ.

L'utilisation de ce paramètre RSCM, le ratio D3/Gsl., a également permis de détecter les cas de flash-heating provoqué par des coulées ou des intrusions de basaltes sur des sédiments immatures dans les prismes d'accrétions et conservé après la maturation par le métamorphisme régional (Chapitre VIII). Les résultats suggèrent que le flash-heating est détectable sur une faible distance (i.e. du millimètre à quelques centimètres) en fonction de la taille du corps basaltique jusqu'à des températures de 300°C où le métamorphisme régional sur-imprime le métamorphisme de contact. Ces résultats permettront par la suite de débattre de l'occurrence des lentilles de basaltes observées dans les prismes d'accrétions et de la possibilité de coulées de basaltes de la ride directement dans la fosse.

5. Discussion et conclusion

Dans cette étude, l'effet de la déformation sur la cristallinité de la CM a donc été exploré à travers des exemples naturels et expérimentaux pour des déformations allant à des vitesses lentes à des vitesses très rapides. Pour les deux régimes de déformation, la cristallinité de la CM lors des phases de carbonisation et de graphitisation précoce, reflétée par l'IR, montre une augmentation dont l'intensité est en lien avec les microstructures. Ces augmentations ont été commentées dans la littérature pour de degrés de cristallinité de la CM plus important lors de la phase de graphitisation (Bonijoly et al., 1982a; Bustin et al., 1995; Kedar et al., 2020; Kuo et al., 2018; Nakamura et al., 2015; Suchy et al., 1997). Ces transformations s'expliquent par l'action du cisaillement provoquant une coalescence des pores et un alignement des unités structurales de bases du carbone ce qui va impliquer une réorganisation cristalline des feuillets aromatiques du carbone et une croissance des cristalline (Bonijoly et al., 1982a; Bustin et al., 1995).

Les objets naturels et expérimentaux étudiés ont montré de nombreuses similitudes tant dans l'observation des microstructures que dans l'effet de la déformation sur la cristallinité de la CM pour des températures allant de 260 à 300°C. En effet, la reproduction des structures de déformations a été choisie dans cette gamme de température pour deux raisons : c'est dans cette gamme que l'IR évolue de façon significative passant de 0.5 à environ 1.0 et les meilleurs résultats naturels ont été obtenus pour ce degré de cristallinité. Sur cet intervalle de cristallinité de la CM, les microstructures ont montrés un affaiblissement rhéologique et une localisation de la déformation guidés par les mêmes mécanismes. De

plus la cristallinité de la CM indique le maximum de cristallinité atteint sans être affecté par les réactions rétrogrades. De ce fait, la multiplication des phases de déformation dans les cas naturels ou une unique phase de déformation ne montrera toujours que le maximum de cristallinité atteinte, à l'exception de l'occurrence d'une déformation tardive cassante provoquant une amorphisation (Kirilova et al., 2018). Ceci permet donc d'expliquer que les évolutions de la cristallinité de la CM sont identiques pour les échantillons naturels et expérimentaux, tant dans leur intensité que dans leur évolution le long des gradients de déformation.

Les déformations rapides (i.e. sismique) et lentes (i.e. non-sismique) ont montré une augmentation de la cristallinité de la CM. Cependant, certaines caractéristiques peuvent les séparer (Figure 7). En effet, l'intensité de la déformation rapide est plus importante que celle lente, à l'exception d'une grande quantité de déformation très localisée où les valeurs demeurent similaires. De plus, la forme des profils de l'IR à travers les zones déformées et leurs encaissants respectifs montrent une forme plus continue pour la déformation lente alors que dans les zones déformées rapidement la forme est abrupte formant une fonction porte. Pour finir, L'homogénéité des valeurs dans les zones déformées est différente avec un effet remarqué sur la quasi-totalité des grains de CM dans les Black Fault Rocks (i.e. déformation sismique). Ces augmentations et leurs intensités sont intimement liées aux microstructures et à la quantité de déformation finie. En effet dans les Black Fault Rocks, une ultra-comminution est observée et indique une quantité de déformation très importante, c'est aussi l'objet pour lequel les plus grandes valeurs d'IR sont mesurées. De plus, pour ces deux régimes de déformation, des facteurs externes peuvent s'additionner à l'effet de la déformation comme la circulation de fluides ou la production de chaleur par friction. Cependant, le premier cité a été testé à travers des expériences de maturation à pression et température constantes et des augmentations insignifiantes ont été révélées (i.e. < 1%). En ce qui concerne le deuxième facteur, le Chapitre VI de cette étude a montré que dans le cas des objets sismiques l'augmentation de la cristallinité était uniquement due à un effet mécanique et que la température dégagée lors de la friction n'affectait pas la cristallinité de la CM. De ce fait, les augmentations de la cristallinité de la CM discutées dans cette étude sont majoritairement causées par

la déformation et doivent être prises en compte dans l'analyse de la cristallinité de la CM lors de l'utilisation de la méthode RSCM.

Pour terminer, l'effet de la déformation lente et rapide montre une augmentation de la cristallinité de la CM. Cependant les thermomètres calibrés dans la littérature sont liés à cette cristallinité et leur utilisation dans les zones déformées nécessite d'être discutée. Dans le cas de quantité de déformation limitée à modérée, c'est-à-dire quand une augmentation jusqu'à 20% de l'IR est mesurée, l'effet de la déformation peut être contenu et lissé grâce aux erreurs liées à la technique elle-même qui est de l'ordre de ± 50°C (Beyssac et al., 2002; Lahfid et al., 2010). Cependant, pour des augmentations d'environ 20% de l'IR une augmentation de la température sera de l'ordre de 50°C ce qui pourrait provoquer des problèmes dans l'interprétation des résultats avec de telles anomalies. De plus, l'effet de la déformation génère une dispersion des résultats ce qui rendra l'erreur liée à la mesure plus importante et par conséquent les résultats moins précis. En revanche, l'utilisation des thermomètres RSCM et l'interprétation des résultats, pour des terrains fortement déformés dans des régimes sismiques ou non-sismiques, devrait être faite avec la plus grande prudence. En effet, ces déformations ont indiqué des augmentations de l'IR très importantes qui correspondent à des augmentations de la température calculée supérieur à 50°C et pouvant atteindre quasiment 100°C localement. Dans ce cas de telles surestimations ne peuvent plus être absorbées par les erreurs liées à la méthode et l'estimation des températures doit être complétée par une méthode qui n'est pas affectée par la déformation.

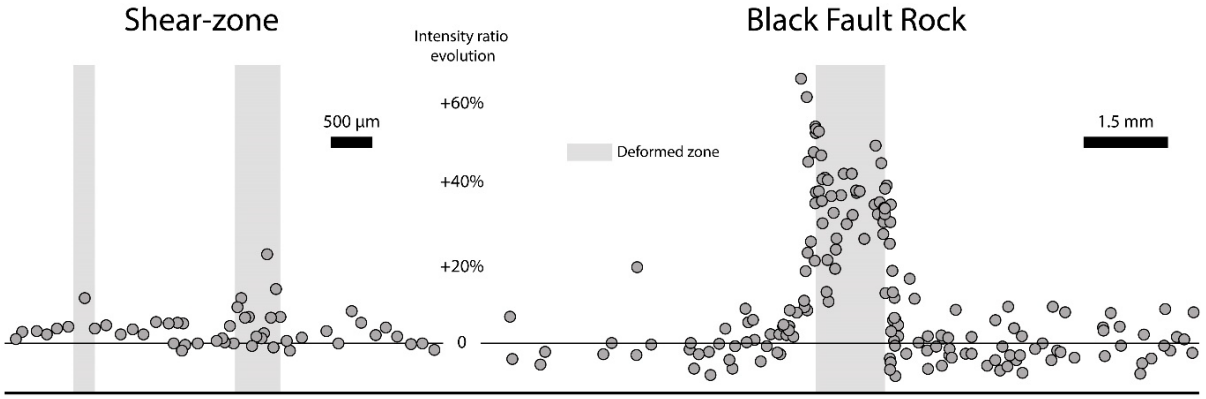

Figure 7 : Evolution de l'intensité de l'augmentation de l'IR et de la forme des profils de l'IR en fonction du régime de déformation (i.e. Non-sismique vs. Sismique)

Chapter I – Introduction

I.1 Scientific context and motivations

The understanding of the geodynamics processes has always been a major challenge in geosciences. Indirect studies of fossil zones are necessary to understand the dynamics processes in active zones such as the subduction and collision zones. The P,T,t paths obtained using conventional petrological tools and the structural evolution are widely used in geosciences in order to reconstruct the time evolution of convergent margins. These tools need the presence of mineralogical assemblages, not always detectable, especially at low metamorphic grade in turbidite meta-sediments.

However, carbonaceous material (CM), corresponding to residual organic matter derived from diagenesis and metamorphic evolution, is a common component of meta-sediments involved in these dynamic zones. CM subjected to temperature stress irreversibly reorganize its crystalline lattice toward the perfectly-organized graphite through the carbonization and the graphitization maturation stages. The study of the crystalline organization of the CM, using X-ray Diffraction (XRD), vitrinite reflectance (%VR) and High Resolution Transmission Electron Microscopy (HRTEM) (Beny-Bassez and Rouzaud, 1985; Oberlin, 1989; Wada et al., 1994), leads to consider the degree of crystalline organization of the CM as a reliable indicator of the metamorphic conditions at peak-conditions (Pasteris and Wopenka, 1991; Wada et al., 1994; Wopenka and Pasteris, 1993). In addition, Raman Spectroscopy of Carbonaceous Material (RSCM) has been used in order to reflect the crystalline organization of the CM through the evolution of the Raman spectra and several associated parameters (Beny-Bassez and Rouzaud, 1985; Pasteris and Wopenka, 1991). This method gathers the advantage of a quick, no destructive and easy application on several type of material containing CM. More recently, thanks to the higher resolution and precision of the RSCM, the CM crystallinity and the maximum peak temperature have been correlated to regional (Beyssac et al., 2002; Kouketsu et al., 2014; Lahfid et al., 2010; Rahl et al., 2005) or contact metamorphism (Aoya et al., 2010). These new thermometers cover a wide range of temperature, from 200 to 650°C and are now widely accepted and used by petrologists (Beaudoin et al., 2015; Clerc et al., 2015; Lanari et al., 2012) in metamorphic terranes.

However, external factors such as CM type, matrix, fluids interaction, pressure or strain could influence the CM crystallinity especially for poorly organized CM, as revealed by (Lahfid et al., 2010). The effect of strain is complex, as different patterns of evolution have been described, i.e. towards higher crystallinity (Bustin, 1995) or on the contrary towards amorphization (Kirilova et al., 2018), depending on the type of deformation (Nakamura et al., 2015) and on the degree of crystallinity of the starting CM in the strained zone (Kaneki and Hirono, 2019). Moreover, the majority of literatures, which deals with the effect of strain on the CM crystallinity, are focused on well-organized CM (*i.e.* during late graphitization stage) and for high finite strain (Bonijoly et al., 1982a; Bustin, 1983a, 1995; Kedar et al., 2020; Kouketsu et al., 2014; Kuo et al., 2018; Nakamura et al., 2015; Ross et al., 1991b; Ross and Bustin, 1990; Suchy et al., 1997; Wilks et al., 1993). However, for poorly organized CM, during the carbonization stage and the early graphitization stage (*i.e.* 200 to 360°C), the effect of the strain on the CM crystallinity remains poorly studied except for seismic deformation where the heating and strain effects are not distinguishable (Ito et al., 2017; Ujiie et al., 2021). This lack of existing studies contrasts with the large range of possible deformation types, from viscous deformation at plate tectonic rates to fast seismic deformation. The study of the influence of strain on the CM crystallinity presents an importance in low grade material, and the RSCM is one of few efficient tools that provide constraints on the conditions of metamorphism and deformation.

I.2 Thesis outline

This study aims to explore the effect of deformation on the CM crystallinity focusing on poorly organized CM during the carbonization and early graphitization stages, at different scales, finite strain and deformation mechanisms (*i.e.* non-seismic vs. seismic deformation). In addition, auxiliary questions have been explored such as the scale effect and the discrimination of the basalt blocks origins in the wedge sediments.

Strain gradients from natural well-known fossil accretionary wedges (Shimanto Belt, Kodiak Accretionary Complex and Infrahelvetic Complex) including seismic and non-seismic deformations at different scales and finite strains have been targeted and sampled. However, natural deformed rocks present only the final stage of the deformation and could superpose different mechanisms or types of

deformation even if the RSCM records only the metamorphic peak temperature. In addition, deformation parameters (quantity of strain, strain rates) or the deformation conditions (pressure, fluids, temperature) are often unknown. In order to control the deformation parameters and conditions, deformation experiments have been carried out to explore the effect of the different variables (Pressure, Temperature, strain rate and finite strain) and to compare the CM crystallinity evolution with natural strained zones.

For both natural and experimental samples, CM crystallinity and degree of maturation of the CM have been evaluated using mainly Raman Spectroscopy of Carbonaceous Material and complementary methods (RockEval pyrolysis, vitrinite reflectance) and linked with microstructures of deformation.

The other chapters of this manuscript are composed as follow:

- Chapter II consists in the scientific knowledge about the CM, its chemical and morphological evolutions through maturation stages. In addition, the evolution in the knowledge on the CM crystallinity using different methods and the RSCM one are described. Finally, an extended synthesis of the deformation effects, through the review of existing literature, including all types of deformation types from seismic to non-seismic is provided at the end of this chapter.

- Chapter III describes material and all the analytical methods, regarding to the CM crystallinity estimation and the microstructural observations that have been used in this study. Experimental apparatus descriptions and procedures are also presented in this section.

Part I (Non-seismic deformation) and Part II (Seismic deformation) containing, respectively Chapters IV, V and Chapters VI, VII have been written in the style of scientific publications. They have been modified, adapted and extended in order to avoid repetition between chapters.

- In Chapter IV microstructures and associated CM crystallinity evolutions from natural non-seismic shear-zones are presented using the intensity ratio parameters (i.e. R1 defined in (Beyssac et al., 2002). Results from strain gradients or sampling profiles, from the sample to the outcrops and at temperature ranging from 200 to 360°C, from the Shimanto Belt, the Kodiak

Accretionary Complex and the Infrahelvetic Complex (Glarus Thrust) are described. This chapter refers to a publication proposed in the journal Tectonophysics called: “The role of viscous shear on the carbonaceous material crystallinity enhance: Raman Spectroscopy and microstructural analyzes of strain gradients from ancient accretionary complexes” and will be submitted in few weeks.

- Chapter V explores the effect of the non-seismic deformation through experimental samples obtained using Paterson Rig and solid-medium Griggs apparatuses at constant pressure and temperature through co-axial and shear assemblies. Mechanical curves, microstructures and RSCM responses are exhibited in order to interpret the CM crystallinity evolution.

- Chapter VI investigates the seismic deformation in natural fault zones called Black Fault Rocks. This chapter discriminates the mechanical wear from the frictional heating effects on the faulted veins observed in accretionary complexes and discusses the Black Fault Rocks genesis in rich-shale sediments. High-resolution RSCM cross-section, microstructures observations and numerical modellings of the heat diffusion and associated CM kinetics have been used to explore this question. This chapter refers to a scientific publication in the journal Scientific Reports called: “Pseudotachylyte veins in accretionary complexes: melt or mechanical wear?”, under consideration by the editor board.

- Chapter VII aims to discriminate, using the RSCM method, the molten occurrence resulting from the intense and short-life heating of samples during frictional events such as earthquake. RSCM results from flash heating experiments using CO_2 laser and natural Black Fault Rocks, interpreted as pseudotachylytes, along with other examples of flash heating, are compared. In this chapter the RSCM and a new parameter $D3/G_{intensity}$ ratio are presented as a discriminative tool for intense short-life heating detection.

Part III contains the Chapter VIII, which somehow deviates from main scientific questions tackled in the manuscript. Indeed, this part contributes to understand how tectonic mélange forms.

- Chapter VIII contains the results of the RSCM approach using the D3/G and intensity ratio evolution in order to detect the short-life heating evidences of basalt flows on pelitic sediments. Sediments in contact with basalts from the Shimanto Belt (Japan) and immature sediments from IODP drillings have been studied.

These chapters providing the principal results are followed by a general discussion concerning:

- The comparison between seismic and non-seismic deformation effects on the poorly organized CM crystallinity.
- The comparison between the natural and experimental non-seismic shear-zones in terms of CM crystallinity and mineralogical evolutions.
- The application of the geothermometer calibrations proposed in strained terranes.
- The comparison between the Paterson Rig and Griggs apparatus experiments and the control of the pressure on the CM kinetics.

The manuscript ends on a general conclusion recalling the main results of this study and suggestions for the perspectives of this work in the future.

Chapter II – Carbonaceous material and Raman Spectroscopy: state of the art

II.1 Carbonaceous material maturation and crystallinity enhance

Carbonaceous material (CM) is mainly composed of carbon chains linked by C-C and C-H covalent bonds. Living beings, as bacteria, alga or plants, are recycled or trapped in oceanic sediments after dying. Organic matter irreversibly evolves in CM through different complex processes during the geological burial under the influence of the temperature and pressure, leading to a chemical and structural evolution (Figure II.1). However, maturation kinetics also depend on external factors such the initial type of organic matter (Guedes et al., 2010, 2005) , the depositional environment and the burial conditions or the rock types (Pasteris and Wopenka, 1991; Wada et al., 1994). The first process, the carbonization, occurs during two first thermal maturation stages, the diagenesis and catagenesis (Tissot and Welte, 1984). During these stages, the vitrinite reflectance (%VR) is estimated to evolve from 0-0.5 to 2.0%VR, so, up to 200°C (Barker, 1988; Sweeney and Burnham, 1990). During the diagenesis stage, the CM is mainly composed of kerogen and during the catagenesis oil and wet gas are produced. During the carbonization, structural and chemical evolution occur by a rearrangement of the aromatic layers by the crystal defects elimination. These defects are heteroatoms (H, S, N, O), isolated Basic Structural Unit (BSU) or tetrahedral carbons. Under increasing temperature and pressure, these heteroatoms are expulsed out of the carbonaceous material lattice as water (H_2O), oil (hydrocarbon) or gases (CO_2, CH_4, H_2S). Thanks to this evolution, nanometric polyaromatic ring structures (diameter < 10 Å) are created. Two or 3 planar polyaromatic structures will be associated and form the Basic Structural Unit (Beny-Bassez and Rouzaud, 1985). Then, during the carbonization, these BSU are rearranged and shaped in polyaromatic sheets. By the end of the carbonization stage, the CM is weakly organized, polyaromatic structures are stacked by 2 or 3 and zig-zag structure begins to occur. At higher depth, with increasing temperature, the transitional stage between the carbonization and the graphitization is led by the chemical and structural modifications of the polyaromatic sheets. This step occurs during the end of the metagenesis (*ie.* 2.0 to 4.0%VR), i.e. 200°C to 300°C, where dry gas from the kerogen are released, mainly CH_4 and H_2. At the end of this process, most of heteroatoms and hydrogen have been expulsed out of the system. The residual carbon is now considered as disordered graphite presenting a zig-zag structure, only composed of methane and residual carbon (Bonijoly et al., 1982a). This material will

progressively evolve to well-organized graphite during the graphitization stage, from the beginning of the greenschist metamorphic zone (Tissot and Welte, 1984), i.e. after 4.0%VR, so 300°C, up to amphibolite-facies metamorphism. The CM structural evolution from the diagenesis until the end of the graphitization can be recognized by several tools such High-resolution transmission electron microscopy (HRTEM), X-Ray Diffraction (XRD) vitrinite reflectance (VR) or RockEval pyrolysis. In addition, the Raman Spectroscopy of Carbonaceous Material is a powerful tool to decipher the structural evolution of the CM.

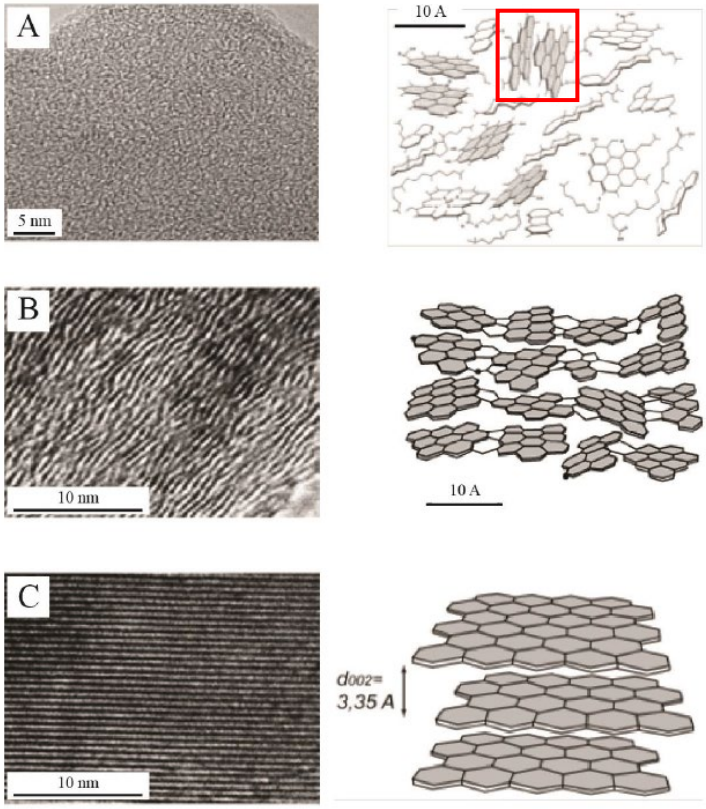

*Figure II.1 – HRTEM images and structural drawings of the carbonaceous material during the maturation (from Oberlin (1989) and Delchini (2018). **A** immature kerogen, red square shows BSU; **B** Mature kerogen; **C** well-organized graphite*

II.2 Raman Spectroscopy of Carbonaceous Material and crystallinity evolution

II.2.1 RSCM spectrum description

Tuinstra and Koenig (1970) were the first to demonstrate the utility of the Raman Spectroscopy in order to trace the maturity of carbonaceous material looking at the c-axis, normal to the carbon sheets, of CM crystallinity evolution. The frequency shift between the laser emission and the back scattered signal is measured by a spectrometer and indicates the Raman shift. Based on this method, the presence of two

bands, i.e. the Disoredered (D) and the Graphite (G) Bands, has been described. These bands are observed at 1355cm^{-1} and 1575cm^{-1}, respectively (Tuinstra and Koenig, 1970) and are associated to the vibrational mode A_{1g} and E_{2g} (Beny-Bassez and Rouzaud, 1985; Tuinstra and Koenig, 1970) (Figure II.2a). In addition, the deconvolution permits to characterize more precisely this spectrum. In fact, the Raman spectrum is composed of a first-order region (1000-1800cm^{-1}) and a second-order region (2400-3500cm^{-1}). The first-order region contains two bands, the D-band (around 1355cm^{-1}) and the G*sl.* band (around 1575cm^{-1}) (i.e. on the raw spectra). During this work, we only focused on the first-order region of the Raman signal and more precisely during the end of the carbonization process and the graphitization. Thereby, in the following only the evolution of this region will be described in the temperature range higher than 200°C. During the deconvolution process, additional bands are observed and necessary to fit with the Raman spectrum. At low temperature (*i.e.* 200°C), a 5-bands deconvolution is possible according to Lahfid et al. (2010). Under the D band, D4 and D1 are described respectively at 1200 cm^{-1} and 1350 cm^{-1} when the G*sl*. band is composed of the G and D2 bands respectively at 1580cm^{-1} and 1620cm^{-1} (Figure II.2a). The D2 band corresponds to the vibrational mode of the E_{2g2} symmetry and at low temperature is merged with the G band. A transitional band, called D3, is located between the D and G*sl.* bands at 1500cm^{-1} and corresponds to the out-of-plane vibration due to the defects and heteroatoms. Two additional bands, i.e. D5 and D6, have been described in the literature (Ferralis et al., 2016; Romero-Sarmiento et al., 2014), however, they are not considered in calibrations that we will discuss later based on the additional complexity generated by these two bands. Parameters derived from each deconvoluted band, such as area, amplitude, Full Width Half Maximum (FWHM) or center position, evolve during the maturation of the CM (Figure II.2a and II.2b). All the defect bands tend to decrease and disappear with the increasing temperature except the G band that reflects the perfect-ordered graphite lattice.

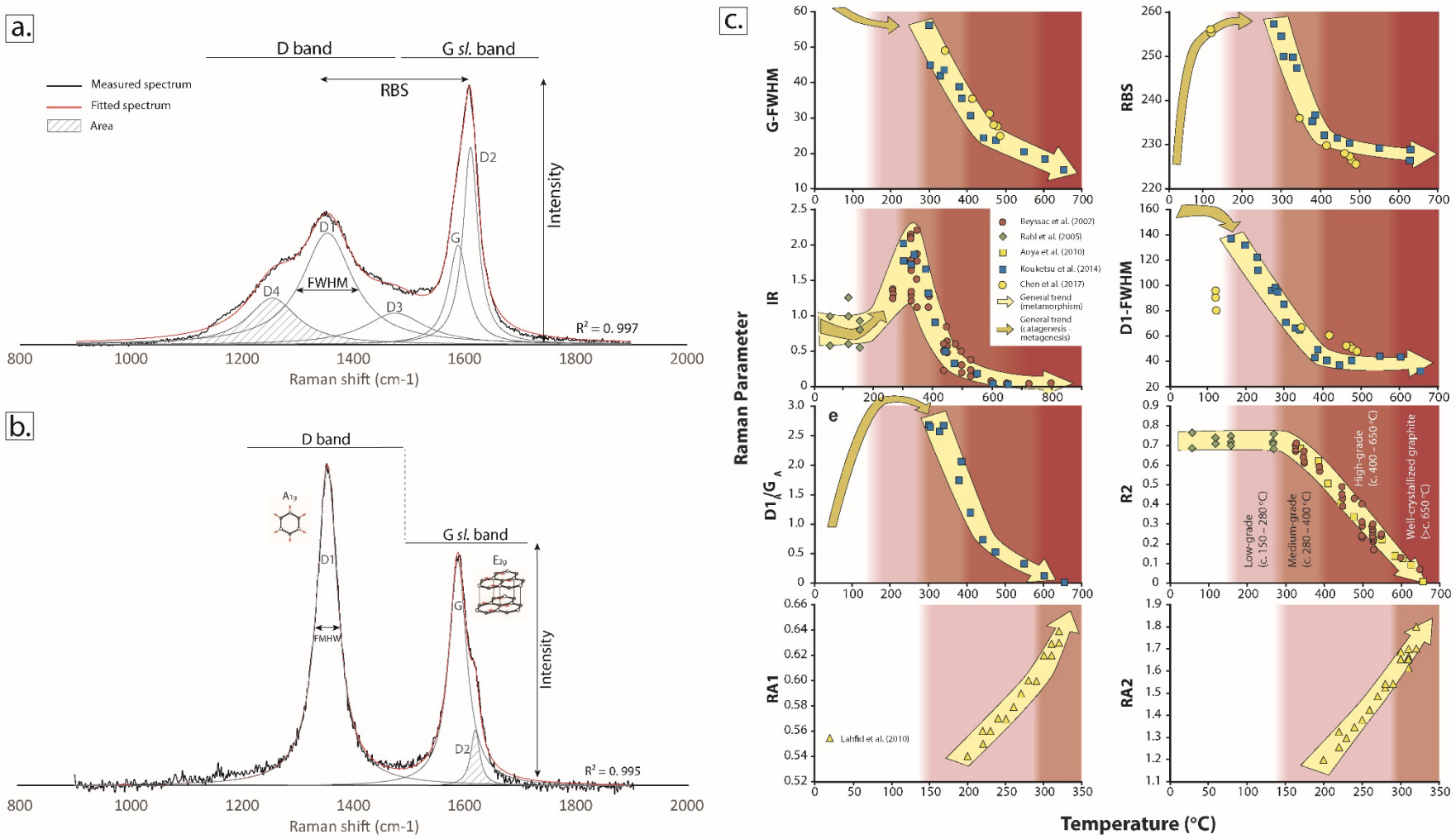

Figure II.2 – Raman spectra and associated parameters evolution through the metamorphism grades. a. and b. Typical CM spectra from the end of the carbonization and from the graphitization stage and respective Raman parameters obtained from deconvolution methods described in (Beyssac et al., 2002; Lahfid et al., 2010). c. Raman parameters evolution as a function of increasing temperature (Modified from (Henry et al., 2019))

The evolution of Raman spectra and associated parameters has been described from the diagenesis to the high temperature metamorphism (Henry et al., 2019). Intensity ratio (IR) (i.e. R1 in (Beyssac et al., 2002), measured on raw spectrum, is the first Raman parameter used in order to follow the crystallinity evolution of the CM (Pasteris and Wopenka, 1991). During the diagenesis, catagenesis and metagenesis, the IR slightly increases from 0 to 300°C. During the metamorphism, this parameter increases sharply until 360°C and then decreases quickly until the CM reaches the well-organized graphite state. In the following, the CM crystallinity evolution will be based on the IR evolution. Additional parameters, based on raw spectrum (RBS) and deconvoluted (G-FWHM), also show a monotonic evolution through the maturation of the CM. The distance between the D and G*sl.* bands (RBS) and the G-FWHM are the most used parameters to describe the process of the maturation from the diagenesis to the metagenesis (Guedes et al., 2010; Kelemen and Fang, 2001; Romero-Sarmiento et al., 2014; Wopenka and Pasteris, 1993) . G- and D-Raman shift, G-FWHM or D-FWHM have been proposed, in addition to the IR, to evaluate the crystallinity enhance during the further maturation stages. Moreover, peak areas and area ratio can also be used to follow the maturation. In particular, the area ratio evolution with increasing metamorphic temperature was quantitatively assessed and served as a geothermometer (Figure II.2c).

III.2.2 The geothermometric approach of the RSCM

Based on this parameter evolution, several studies have shown the link between the structural evolution of the CM during the maturation and the metamorphic range.

Beny-Bassez and Rouzaud (1985) highlighted the fact that the Raman Spectroscopy could be used to characterize the maturation stages of the CM. Through experimentally heated organic matter, micro-structural and Raman spectra evolution have been correlated thanks to HRTEM and Raman Spectroscopy observation from the carbonization to the graphitization stage. Based on the height of these two main bands of the Raman spectra, the intensity ratio can be calculated. Pasteris and Wopenka (1991) show the correlation between the intensity ratio (IR) and the metamorphism peak temperature from the chlorite to the sillimanite zones (*i.e.* 400 to 600°C). Nowadays IR parameter is still largely used to reveal the crystallinity enhance (Ito et al., 2017) during the carbonization (*i.e.* after the oil and gaz maturity range) and graphitization stage. In addition, Wopenka and Pasteris (1993) described the

correlation different Raman parameters, such as the area of the D or G bands and the D and G FWHM, with the CM crystallite diameter (L_a) from the kerogen to the sillimanite metamorphic zone (Figure II.3). Since these new results, the Raman spectroscopy became more important in geosciences and in physics due to it easy, quick and non-destructive characteristics. The relationship between these Raman parameters and the metamorphism has been made on the raw spectrum of the CM.

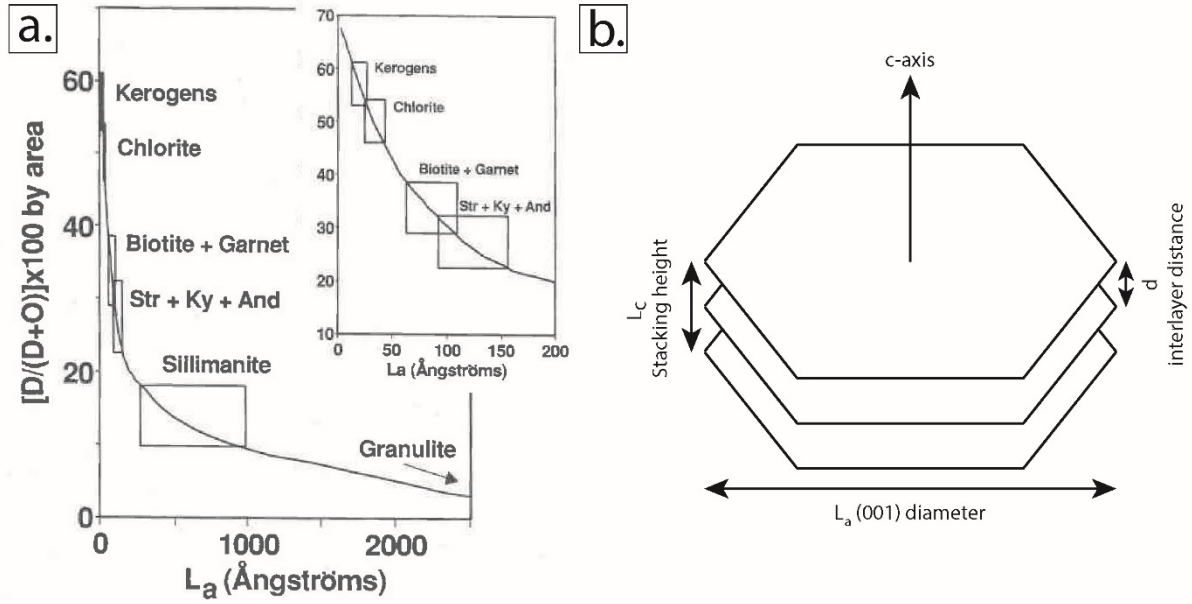

Figure II.3 – a. Correlation diagram between the area ratio D/D+Gsl. and the diameter of coherent polyaromatic sheets (La) (Modified from (Wopenka and Pasteris, 1993)) b. Drawing illustrating the parameters of the coherent graphene

More recently, Beyssac et al. (2002) were the first to calibrate an empirical equation between the metamorphic peak temperatures and R2 area ratio (*i.e.* R2 = D1 / D1 + D2 + G) for the temperature range between 330 to 600°C (Figure II.4a). Moreover, an additional calibration based on area ratios (RA1 = (D1 + D4) / (D1 + D2 + D3 + D4 + G) and RA2 = (D1 + D4) / (D2 + D3 + G) area ratios) has been also developed by Lahfid et al. (2010) for temperatures from 200 to 330°C (Figure II.4b). Complementary thermometer calibration on different Raman parameters also exist. In fact, Rahl et al. (2005) presented a new calibration based on the combination of the IR and R2 area ratio when Kouketsu et al. (2014) used the FWHM of the D1 and D2 bands in order to calibrate their own thermometer. These thermometers are applicable to regional temperature information at the metamorphic peak temperature that corresponds to a metamorphic heating. However, Aoya et al. (2010) extends the application of the RSCM thermometer to intrusive bodies such as granite or dykes intrusion with a short-lived heating.

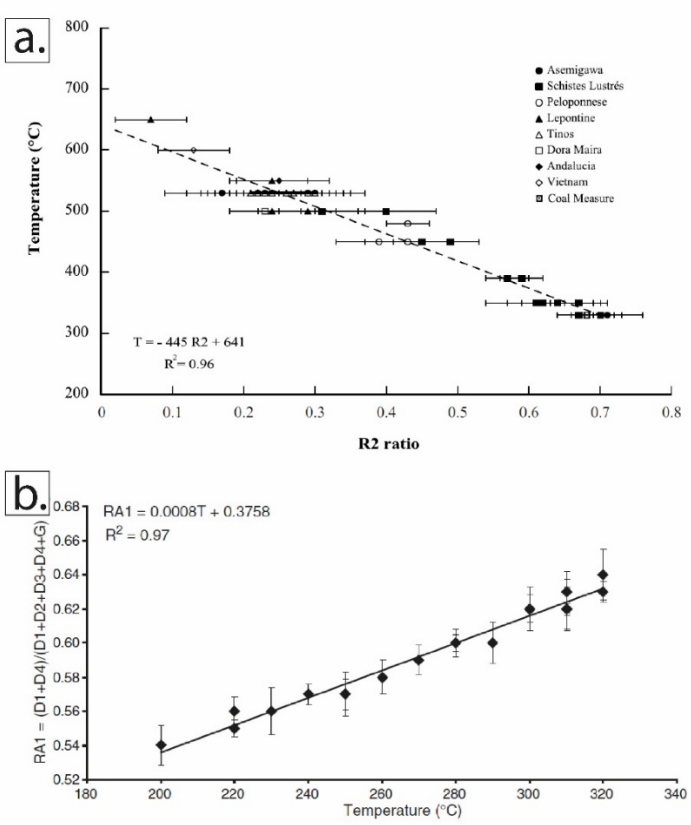

Figure II.4 – Correlation between area ratios and metamorphic temperatures from 200 to 650°C (Modified from (Beyssac et al., 2002; Lahfid et al., 2010). ***a.*** *R2 area ratio calibration used by (Beyssac et al., 2002) for the thermometer calibration in high grade metamorphism* ***b.*** *RA1 area ratio calibration used by (Lahfid et al., 2010) for the thermometer calibration in low grade metamorphism*

Nowadays, these geothermometers are now well accepted by the geosciences community and the RSCM thermometers are powerful tools used in metamorphic petrology (Beaudoin et al., 2015; Clerc et al., 2015; Lanari et al., 2012) (Figure II.5).

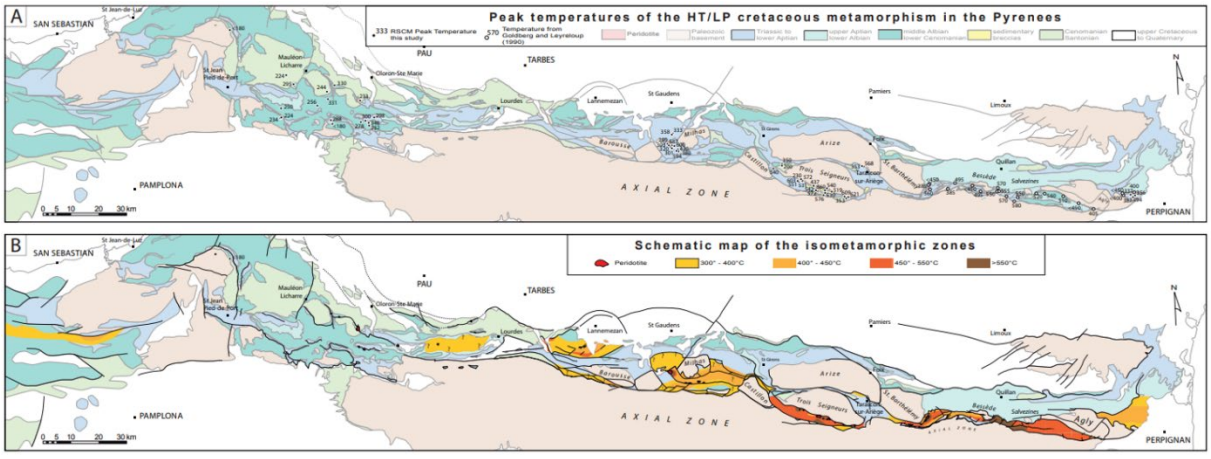

Figure II.5 – Example of the RSCM thermometry application to the Pyrenees mountains (France) (From (Clerc et al., 2015))

II.3 Factors controlling Raman spectra

While in all the description above, the temperature is considered as the only factor influencing RSCM, in fact other factors may also play a role on Raman spectra.

Sample preparation could influence the spectra. During the preparation of the sample, polishing generates defects visible on the D bands that show a higher intensity (Katagiri et al., 1988; Pasteris, 1989; Wang et al., 1989). However, in low temperature range, the mechanical abrasion that conducts to an amorphization is less visible (Ammar and Rouzaud, 2012). Furthermore, the mounting media used in the sample preparation could contain C-C or C-H bonds that generate fluorescence (Pasteris, 1989). It seems, based on our experience, that the epoxy used during this work does not show this problem.

CM grain orientation might also influence the spectra (Katagiri et al., 1988; Wang et al., 1989). Additionally, Delchini (2018) shows that an additional D band intensity is attributed to the 'edge effect' when the laser is focused on the rim of grain.

Intrinsic problems linked with the method itself could also influence the RSCM spectrum shape. The type of machine used during the acquisition, the laser wavelength, the operational procedures or the operator himself could generate deviation of the data (Henry et al., 2018; Lünsdorf et al., 2014). To prevent this deviation, the same operator, operational procedures and machine have been used for all the RSCM analyzes in this work.

The type of organic matter has shown that the response to increasing temperature on the Raman spectrum (Guedes et al., 2010, 2005), especially on the intensity ratio, is different depending on the type of organic matter of starting material. Indeed, not all the organic matter has the same graphitization power, hard-CM rich in oxygen, as high volatile bituminous coal, is non-graphitizable. In opposition soft-CM rich in hydrogen, such as anthracite, it can attain the perfect-organized graphite state (Bonijoly et al., 1982a; Bustin, 1995). Moreover, the shape of pores, micro- or macro-porous more or less flattened, is important in the graphitization process because not all the pore shapes could coalesce (Bonijoly et al., 1982a).

The rock type is also important in the kinetics of maturation of the CM. Pasteris and Wopenka (1991) and Wada et al. (1994) have shown that the crystallinity is higher in carbonates than that in shale at the

same metamorphic peak temperature. This is interpreted as a matrix effect because of the grain size of matrix and due to the free fluids available during the metamorphism that could influence the metamorphic reactions (Pasteris and Wopenka, 1991).

The pressure has to be considered as a major controlling factor during the maturation. Different experiments have shown that an important pressure will reduce the activation energy and catalyze the reaction during the graphitization stage (Bonijoly et al., 1982a; Nakamura et al., 2017, 2020; Ross and Bustin, 1990). In opposition, Beyssac et al. (2002) proposed another conclusion showing no correlation between the pressure and R2 area ratio parameter during the same maturation stage. However, in this article all temperatures ranging from 330 to 600°C with wide R2 values are mixed and do not permit to properly compare the effect of pressure for the same calculated temperature.

The last important external factor that could conduct to enhance the CM crystallinity in addition to the temperature is the deformation. Indeed, several authors have revealed the power of deformation on the CM crystallinity natural and experimental high strained rocks (Barzoi, 2015; Barzoi and Guy, 2002; Bonijoly et al., 1982a; Bustin, 1995; Ross et al., 1991a; Ross and Bustin, 1990; Suchy et al., 1997) using RSCM, VR, DRX and HRTEM. Additionally, the influence of strain has been discussed through the RSCM analysis of samples deformed during an intense shear associated to a seismic deformation (Furuichi et al., 2015; Ito et al., 2017; Kouketsu et al., 2017; Kuo et al., 2018).

II.4 The influence of strain on CM crystallinity

II.4.1 The effect of the seismic deformation

The first aim of the using of RSCM on seismic deformed rocks was to explore the possible detection of frictional heating during fast slip along fault zones. Furuichi et al. (2015) and Ujiie and Kimura (2014) were ones of the first to use the vitrinite reflectance in fault zone in order to detect a higher CM crystallinity interpreted as the frictional heating records in the CM. Moreover, RSCM analyzes proceeded on natural pseudotachylytes have shown an increase of the intensity ratio (Figure II.6a) in the deformed zone (Ito et al., 2017; Ujiie et al., 2021). Experimental approach, using High Velocity Friction Experiments (HVR) in order to reproduce frictional melting, has provided the same results (Ito et al.,

2017). However, fault gouges RSCM analyzed by Kouketsu et al. (2017) and Kuo et al. (2018) show a decrease of the CM crystallinity (Figure II.6b). The same conclusions is proposed by Nakamura et al. (2015), illustrating that micro-structural evidence of amorphization of the CM is observed along fault zones caused by micro to nano-delamination in high metamorphic grade rocks. It seems that the seismic deformation provides very ambiguous results on the CM crystallinity evolution. However, these samples do not present the same degree of crystallinity before the deformation. Ujiie et al. (2021) and Ito et al. (2017) discussed about the results of strain on poorly organized CM when Kouketsu et al. (2017), Kuo et al. (2017) and Nakamura et al. (2015) discussed the seismic deformation effect of organized CM. Therefore, the degree of crystallinity of the undeformed CM is very important and influences the crystallinity evolution. This conclusion is highlighted by the work of Kaneki and Hirono (2019) by which an enhance of the crystallinity of CM at low temperature grade is observed, while, for higher temperature and higher crystallinity, for the same seismic objects, a decreased CM crystallinity is measured. However, as suggested by Kaneki et al. (2016), Kaneki and Hirono (2018), Kuo et al. (2018) and Nakamura et al. (2015), the effects of frictional heating and deformation are simultaneously recorded by the RSCM. However, this heating is indivisible from the deformation effect and the estimation of the calculated temperature is difficult with calculation ranging from 300 to 1000°C for the same experimental conditions (Ito et al., 2017; Kuo et al., 2017). Finally, the question of the seismic deformation is difficult to answer because of the diversity of the objects produced during the seismic slip and the large variation in kinematic parameters during slip. In Chapter VI, the main controlling factor that influences the CM crystallinity, poorly organized, will be discussed on Black Fault Rocks samples described in the literature as pseudotachylytes bearing fault in accretionary complexes.

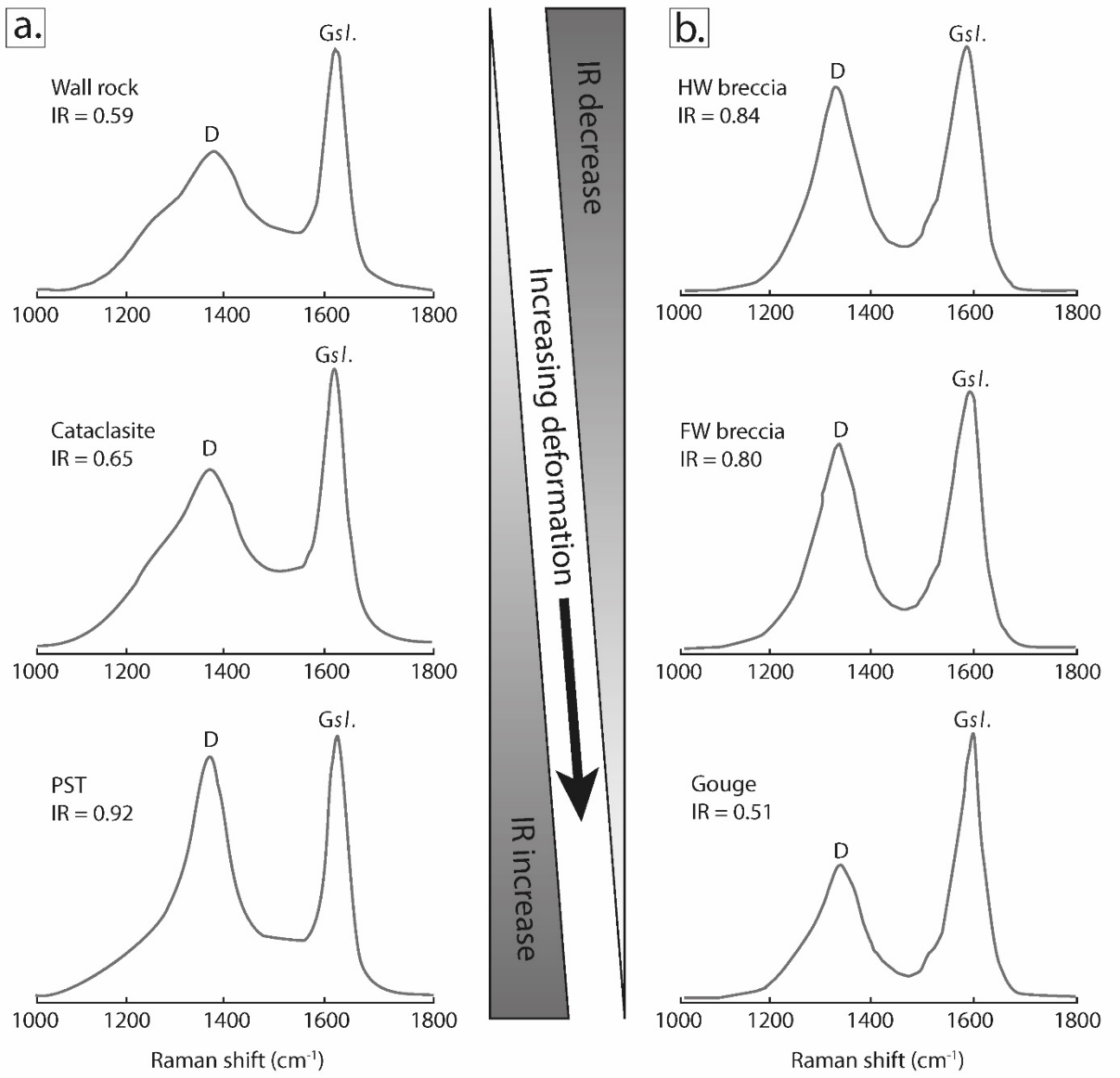

Figure II.6 – The seismic deformation effect on the Raman spectrum and intensity ratio. ***a.*** *Evolution of the intensity ratio from the wall rock to the pseudotachylyte (PST) (Modified from (Ujiie et al., 2021).* ***b.*** *Evolution of the intensity ratio in the fault zone of Longmenshen from the fault core and surroundings (Modified from (Kuo et al., 2018)) HW = Hangingwall ; FW: Footwall.*

II.4.2 The effect of the non-seismic deformation

The effect of shear during the graphitization has been discussed on natural and experimental high strain rocks. In addition, majority of the works done on the viscous deformation have been made on high grade rocks, therefore, they correspond mostly to the late graphitization stage. In natural rocks, Tagiri and Tsuboi (1979) explored the CM crystallinity using the crystallite thickness and spacing. Their results suggested that in deformed zone, the shearing increases the crystallite thickness and decreases the interlayer space generating higher crystallinity of the CM. Using the vitrinite reflectance, Bustin (1983)

and Suchy et al. (1997) have shown an increasing reflectance in the shear-zones. The latter work described a correlation between the increasing reflectance, the microstructures and the quantity of strain. Shear zones are associated to thrust and the crystallinity enhance is interpreted as a short-life shear heating. However, for the microstructures described in this article, no evidence of frictional heating is visible and conceivable for its deformation rate. Nakamura et al. (2015) have shown similar results with increasing crystallinity in viscous mylonite from the high metamorphic grade rocks of Hidaka Belt in Japan. Moreover, experimentally deformed rocks show the same evolution. In fact, Ross and Bustin (1990) and Wilks et al. (1993) observed on experimentally sheared samples an increase of the vitrinite reflectance and a smaller activation energy needed for the CM crystallinity evolution. In addition to this increase of the reflectance, a better structural organization is observed (Ross et al., 1991a). This CM crystallinity enhance is interpreted as the effect of the deformation that nano-structurally reorganize the BSU and generate the pores coalescence (Bonijoly et al., 1982a; Ross et al., 1991a). In addition, a bi-reflectance is measured in the deformed carbon flakes. The same observation has been made in naturally deformed samples (Suchy et al., 1997). Bustin (1995) payed attention to the effect of different deformation mechanisms comparing of hydrostatic, co-axial and shear experimentally deformed samples with RSCM, XRD and HRTEM. The results suggest that both types of deformation generate higher crystallinity of CM even if no well-organized graphite is observed after the co-axial deformation. Thereby, more effective effect of deformation (i.e. higher crystallinity) is observed by the shear deformation with respect to the co-axial deformation. Moreover, as previously reported for the vitrinite reflectance evolution, a higher dispersion of the RSCM results is reported in the deformed zones.

Kedar et al. (2021) measured the intensity ratio in thrust-stack carbonates that shows a ductile and brittle deformation. The CM crystallinity obtained in these deformed zones shows a decreased crystallinity based on the decrease in the intensity ratio. However, this work does not show any microstructure, it is therefore difficult to associate this crystallinity evolution to the brittle or the plastic deformation and to compare our conclusions with this one. In addition, slow creep experiments at low strain rate on graphite powder have shown a decrease of the crystallinity based on the R2 area ratio increase. Micro- to nano-structural observations reveal that brittle deformation confirm that the shear deformation generate

amorphization (Kirilova et al., 2018). We can discuss, however, the absence of heat and pressure during the deformation experiments. Finally, in these two studies, ambiguities are shown on the CM crystallinity evolution. However, it seems that the brittle deformation that occurs lately (Kedar et al., 2021) or on perfectly-organized graphite (Kirilova et al., 2018) induces amorphization on CM.

II.4.3 Summary of the strain effects

To summary, the crystallinity of CM is sensitive, measured through the intensity ratio, to strain intensity. This effect has been documented during both seismic and non-seismic deformation (Bustin, 1995; Ito et al., 2017; Kedar et al., 2021, 2020; Kouketsu et al., 2017; Kuo et al., 2018, 2017; Nakamura et al., 2015; Ujiie et al., 2021) principally during graphitization processes. Before comparing CM crystallinity, especially based on the IR, it is important to take into consideration (1) the degree of crystallinity of the CM and (2) the type of deformation regime that occurred. The degree of crystallinity of the CM is important because the evolution of the IR is not monotonous (see Figure III.13c) and changes at the beginning of the graphitization stage (i.e. 360°C). In addition, as shown by Kaneki and Hirono (2019) the degree of crystallinity of the starting material is important and could generate either enhance or decrease of crystallinity for the same type of deformation. Saying that, the effect of strain during non-seismic deformation shows a CM crystallinity that increases for all degree of crystallinity of the CM (i.e. from poorly organized to organized). This increase is explained by a chemicophysical reorganization of CM lattice induced by the deformation. In seismically deformed samples, results are more ambiguous due to the variety of microstructures that could be produced. However, for poorly organized CM it seems that the CM crystallinity in the deformed zone increases whereas for high degree of crystallinity this deformation suggests a decrease of the CM crystallinity. Finally, for both seismic and non-seismic deformation in high degree of CM crystallinity, brittle deformation show an amorphization (Kirilova et al., 2018; Kouketsu et al., 2017; Kuo et al., 2017; Nakamura et al., 2015).

Indeed, it seems very important to understand well what happens during the deformation processes at different scales (micro- to metric scale), temperatures (brittle to viscous domain) and deformation mechanisms (non-seismic to seismic deformation) using the same range of maturity for the starting material. Such understanding is necessary in order to assess (1) the possible effect of strain on the

existent thermal calibration and (2) the possibility to use the CM crystallinity evolution as a strain gauge. In addition, no work has been made on the lastest stage of the carbonization and the transition between the carbonization and the graphitization (*i.e.* from 200 to 360°C) except for seismic objects where it is impossible to disentangle the deformation from the heating effects (Ito et al., 2017; Ujiie et al., 2021). It seems crucial to explore the effect of deformation at this temperature range because few other thermometers else than RSCM are available at these temperatures especially for pelitic rocks. Moreover, this temperature range offers the opportunity to explore the effect of the strain over a large range of strain rates and deformation styles, covering brittle and viscous mechanisms.

Chapter III – Sample preparation, experiments and analytical methods

Introduction

Identification and then understanding of the potential effect of the deformation on the crystallinity of the carbonaceous material (CM) requires the use of a combination of several experimental techniques as well as analytical methods (Figure III.1). On one hand, a set of methods has been used in order to characterize the CM crystallinity of natural samples with different strain gradients or experimental samples at different maturity or deformation stages. On the other hand, classic petrological tools have been used to link the CM crystallinity with the microstructure at different scales. All these methods are presented below.

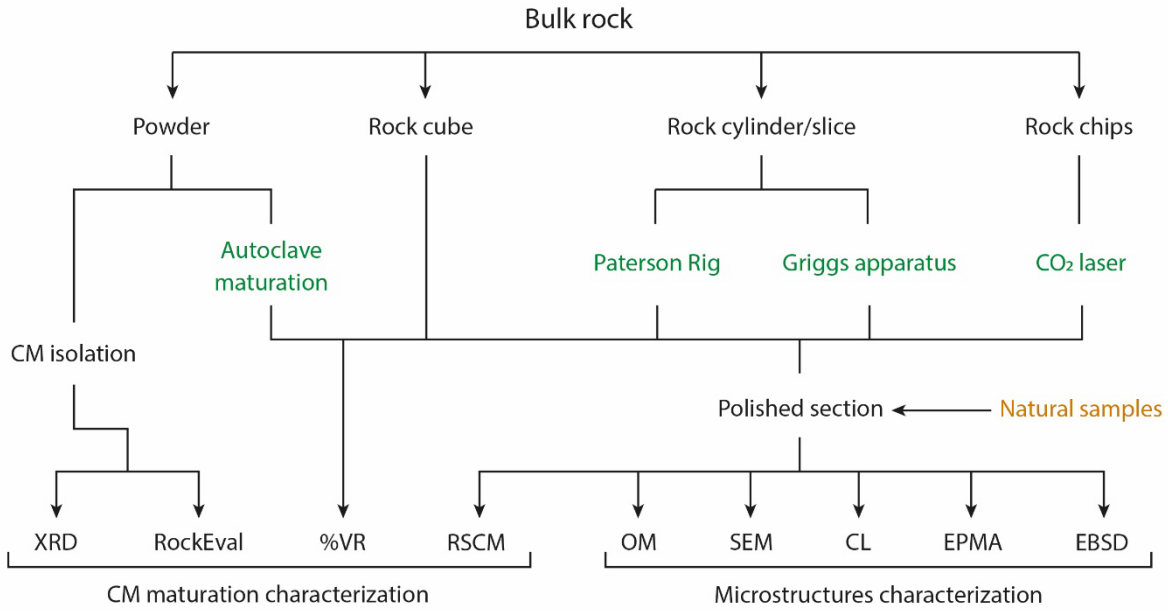

Figure III.1 – Tree diagram summing the scientific analytical procedure from sample preparation to the analytical methods used during this work from natural samples with different strain gradients and starting materials used during experiments. In green: Experimental methods using starting materials and simulating maturation under stress or not. CM: Carbonaceous material. %VR: Vitrinite Reflectance. RSCM: Raman Spectroscopy of Carbonaceous Material. OM: Optical microscopy. SEM: Scanning electron microscopy. CL: Cathodoluminescence. EPMA: Electron probe micro-analysis. EBSD: Electron back scattered diffraction.

III.1 Description of samples

At a first glance, two approaches, conducted in parallel, have been used to identify the potential effects of deformation on the crystallinity of carbonaceous material. A “natural” approach using field investigation on strain gradient and samples in ancient/exhumed accretionary complexes, and an

experimental approach aiming to reproduce natural deformation using experimental conditions in the lab.

III.1.1 Natural samples

The study of natural samples consisted in selecting natural strain gradients in accretionary complexes (Shimanto Belt, Kodiak Accretionary Complex and Glarus Thrust area). Sampling was performed from the millimetric to the metric scales on samples with different finite strain from low to large amount strain. Two types of samples have been selected for this work. The first one consists in rocks that experienced a non-seismic deformation at the outcrop scale and localized along a network of shear-zones. In this case, finite deformation was acquired at low strain rates. These samples have been selected from the brittle to viscous behaviors of deformation in the temperature range of 200°C to 360°C of "regional" burial temperature. This type of samples is ideal to follow the effect of deformation along continuous strain gradients with several mechanisms of deformation and at different finite strain. An extended description of these strain gradients is made in Chapter IV referring to the description of natural shear-zones. The second type of natural samples consists in those experienced localized and fast deformation generated during a seismic event. These samples have been selected in deformed veins of fault zones, called Black Fault Rocks in this manuscript, with also the term of "genuine" pseudotachylyte veins. An extended description of these samples is made in Chapters VI and VIII of Part II referring with the study of BFR.

III.1.2 Experimental samples

Experimental samples correspond to immature (i.e. 80°C) and poorly mature (i.e. 200°C) shale selected respectively in the Myazaki Group and the Hyuga coherent unit of the Shimanto Belt and they may be regarded as internal standards. Microstructures and CM maturity have been characterized thanks to the methods presented below. The description of the starting materials is presented in the Chapter V. Experiments have been carried on these shales to understand the effects of hydrostatic maturation (Autoclaves), intense short-life thermal events (Laser CO_2) and deformations in co-axial and shear configurations (Paterson Rig and Griggs apparatus).

III.1.3 Preparation of the samples

Both naturally and experimentally deformed samples and reference samples have been all cut in the XZ plane. For natural samples, X is the direction of the main elongation and Z is the direction orthogonal to the main foliation plane. For experimental samples, the XZ plane corresponds to the same stress conceptions, X is the direction orthogonal of the main extension and Z the direction of the maximum shortening. Thick and thin sections of about 200 µm and 30 µm respectively have been polished for standard petrography observations and imagery of Raman Spectroscopy of Carbonaceous Material.

III.2 Experimental maturations at hydrostatic conditions and controlled stress

III.2.1 Hydrostatic maturation apparatus

The fine understanding of the carbonaceous material maturation from the carbonization zone and the beginning of the graphitization zone is poorly studied (*i.e.* in the temperature range of 200 to 360°C). Hydrostatic maturation has been carried out for this work on immature and poorly mature shale in external and internal heating system autoclaves. These experiments aimed at (1) following the evolution of RSCM parameters along maturation processes and calibrating a kinetics modelling and (2) comparing the RSCM values obtained, from the same material, on the experimental products during deformation experiments, and eventually the construction of a strain gauge modelling. Hence, the hydrostatic conditions have been carefully defined based on the literature similar experiments and on the limitation and consistency of the hydrostatic heating and deformation apparatus. These conditions are described in the following section.

III.2.1.1 Fixing the experimental maturation conditions

Confining pressure

A temperature-time pairs mainly control the maturation of CM (Nakamura et al., 2017). However, additional controlling factor may exist. Indeed, the confining pressure seems to play a major role on the kinetics of maturation of the CM as shown by Nakamura et al. (2020). In addition, in the different deformation experiments realized during the graphitization stage (Bustin et al., 1995; Ross et al., 1991a; Ross and Bustin, 1990) the activation energy of the CM maturation is highly reduced when the pressure increases. The choice of pressure is therefore major and has to be taken carefully. Based on this point, two factors have been considered for the pressure of maturation, the “natural” burial pressure estimated from the natural samples selected in the field and the experimental window of the autoclaves. Natural samples selected for this work are from the Shimanto Belt, the Kodiak Accretionary Complex and the Infrahelvetic complex in the Alps with an estimated temperature range from 200 to 360°C. Though temperatures are well constrained by RSCM geothermometer and others as well (Hara and Kimura, 2008; Kondo et al., 2005; Mukoyoshi et al., 2009, 2007; Raimbourg et al., 2019; Sakaguchi, 1999), pressures are less precisely known. However, as measured in fluid inclusions in Kodiak (Vrolijk et al.,

1988), estimated by the chlorite barometer (Bourdelle et al., 2013; Bourdelle and Cathelineau, 2015; Vidal et al., 2006) and using by Kristijan Rajic (personal communication), pressures assumed to be reached at peak-temperature conditions fall at ca. 3 kbars. Autoclave using external heating system is limited to a pressure of 2 kbar at its maximum capacity. Considering the low pressure measured in the natural samples and the limitation of the machine, a confining pressure of 1.5 kbar has been selected for these experiments.

Temperature-duration pairs

The temperature-duration pairs have been adapted from a pre-existing maturation in the graphitization stage (Nakamura et al., 2017). In order to reach the maturation stage required, starting materials have been matured with different durations from 3 hours to 45 days at temperatures ranging from 500 to 800°C with a slow heating rate limited and fixed at 4.5°C/min. Experiments at 500 and 600°C have been carried out in the external heating system autoclaves and those at 700 to 800°C in internal heating system autoclaves. These two apparatuses are described in detail below.

Sample medium conditions

The oxidation of CM could be problematic during maturation experiments. Hence, a confining system was created using welded gold capsules containing the sample packed with a neutral argon atmosphere.

Water is a common component of poorly mature shales in nature. However, Landais et al. (1994) have shown that no excess of water is necessary to drive the CM maturation during the experiments in confined system. No additional water was therefore added in the sample medium. However, in 13 experiments, 10 %wt of distilled water was added on the gold capsules in order to discuss the effect of excess of free water during the CM maturation and the implication of fluids in a deformed zone.

In addition to the sample powder, standard vitrinite with similar features as the immature starting material (CM type, degree of maturity) was add in capsules to follow the maturation of CM thanks to existing kinetics model (Burnham and Sweeney, 1989).

Table III.1 : Experiments summary of the conditions

Experiments	Name	Number of exp.	Type of exp.	Time	Temperature	Pressure	Comments
Autoclave maturation	Cps1 to Cps59	41	Hydrostratic maturation	3 hours to 45 days	500 to 800°C	150 MPa	13 exp. in hydrous conditions
Flash-heating	FH06 to FH025	10	Maturation	0.5 to 60 seconds	1400°C	Ambient	-
Paterson Rig	PP6xx to PP6xx	8	Deformation	4 to 72 hours	600 to 700°C	150MPa	Coaxial and shear assemblies
solid-medium Griggs	TxxxBM and ORxxBM	4	Deformation	20 to 175 hours	400 to 600°C	1000MPa	Shear assemblies

III.2.1.2 Sample preparation

41 hydrostatic maturation experiments were conducted using approximately 1g of sample powder, dried at air, and 100 mg of "purified" vitrinite from Candiota (Silva and Kalkreuth, 2005) separated by a gold foil placed in a gold capsule (5 cm x Ø 5.0/5.4 mm) and welded under argon atmosphere (less than 0.2% oxygen). In the 13 hydrous maturation experiments 10 %wt of distilled water was added. Before loading the gold capsules were washed in hydrochloric acid and distilled water, and heated for removing all external contaminants. After the welding, capsules were placed in autoclaves for the thermal maturation experiments.

III.2.1.3 External heating apparatus

This type of autoclave has been used for low temperature experiments at 500 and 600°C. This apparatus is composed of a "high-pressure" (limited to 2 kbars) stainless-steel autoclave in which 4 samples are loaded. The confining pressure is applied thanks to a water flow and controlled by an external pump. External heating system encircled the autoclave and the temperature is controlled by a K-type thermocouple inserted into the autoclave (Figure III.2). Temperature was increased by a 4.5°C/min rate ramp until reaching the final temperature. When the temperature required was reached, the experiments began for the time set at fixed temperature (Table III.1). At the end of the experiment, the oven was turned off in order to quench CM maturation. Autoclave was depressurized slowly to prevent rupture of the gold capsules.

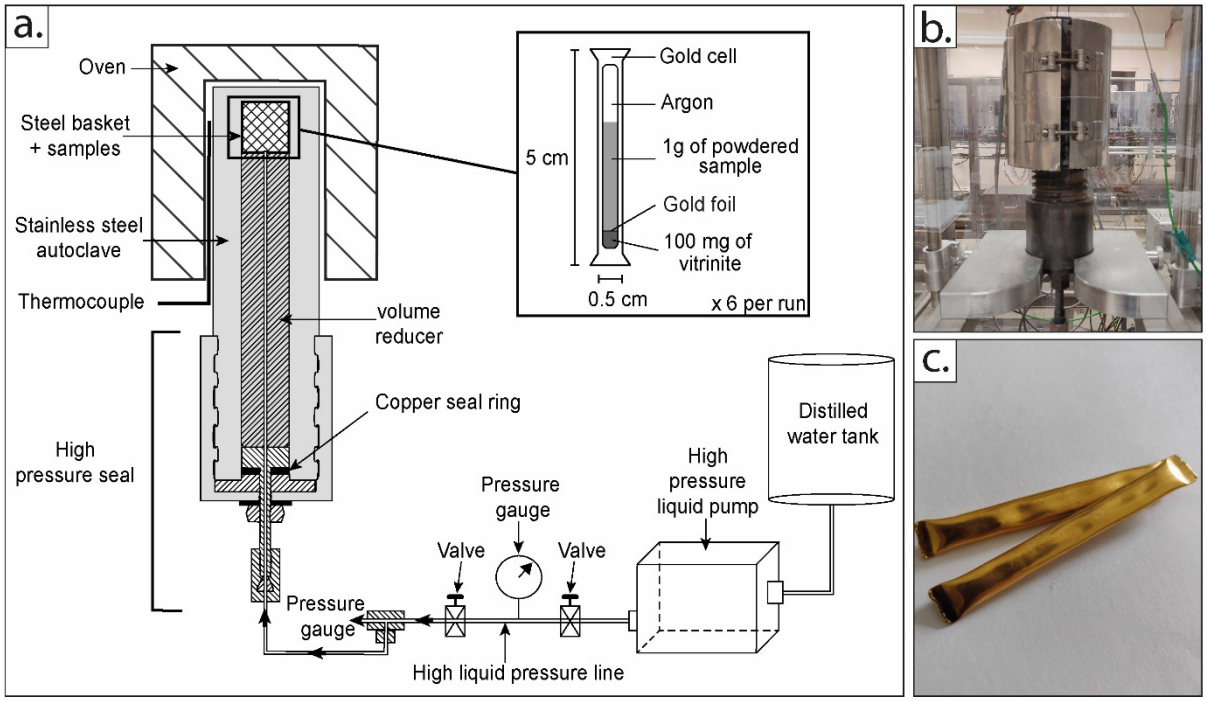

Figure III.2 : Thermal maturation apparatus with internal heating system used for hydrostatic maturation. ***a.*** *Schematic drawing of the maturation system and of the gold capsules.* ***b.*** *Photography of the maturation system.* ***c.*** *Gold capsules used during the maturation experiments. (Modified from (Cavelan, 2019)).*

III.2.1.4 Internal heating apparatus

This type of autoclave has been used for higher temperature experiments at 700 and 800°C. In opposition with the previous type of autoclave, the heating system is intern to the autoclave ensured by Kanthal oven managed by an Eurotherm electronic regulator. This oven is composed of two spires of Kanthal, each supply independently placed at the top and at the bottom of the samples. Each heating element is controlled by K-type thermocouple, with a 5°C resolution and this set-up allows obtaining a ca. 5 centimeters isothermal zone (Figure III.3). In addition, the pressure is applied by argon gas in the autoclave, first injected and then pressurized thanks to hydraulic pumps. 6 samples can be placed simultaneously in the oven during experiment. As for the lower temperature maturation experiments, the temperature was raised at 4.5°C/min until the required temperature for the desired time of the experiments (Tables III.1). At the end of the experiments, the oven is turned off and the temperature drops down quickly (ca. 80°C/min). Then, the autoclave is depressurized slowly.

The gold capsules, from this apparatus and from the low temperature apparatus, were opened and the experimental products are prepared for the CM characterization using the Raman Spectroscopy and the Vitrinite Reflectance analyses described below.

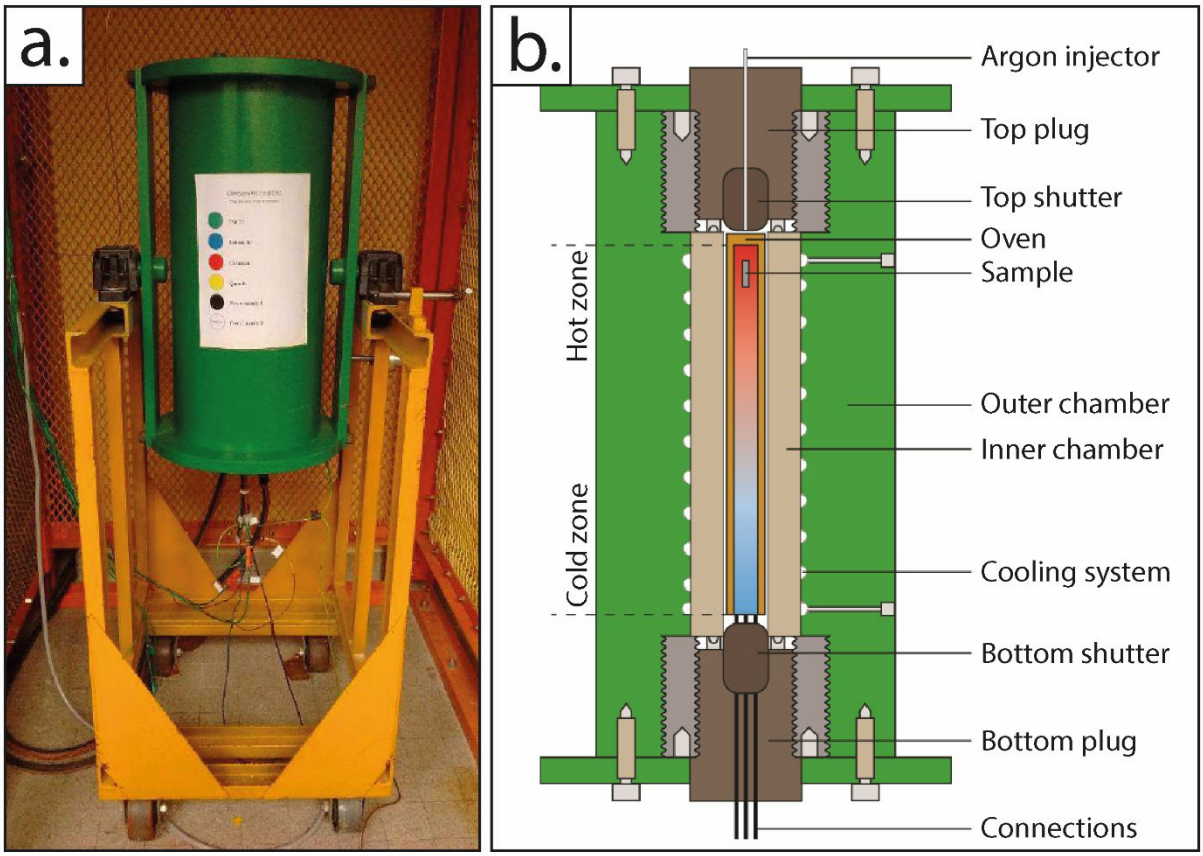

Figure III.3: Internal heating apparatus. ***a.*** *Photography of the internal heating autoclaves called "Gros Vert" at ISTO, Orléans.* ***b.*** *Schematic drawing of the internal heating autoclave and representation of the internal temperature gradient (red to blue). (Modified from (Ferraina, 2018)).*

III.2.2 Paterson Rig

III.2.2.1 Generalities

The first apparatus used for the deformation experiment concerns the Paterson Rig (Figure III.4). This machine is a typical autoclave with internal heating system equipped with an additional deformation system and measurement cells (Figure III.4b). The internal heating system is composed of a 3 spires of molybdenum each supply independently by a specific current. A maximum 1400°C ±40mm isothermal zone (± 2°C) is generated thanks to this set-up and is controlled by a K-type thermocouple inserted in the deformation column at 3mm from the sample. The confining pressure is applied thanks to argon influx injected in the autoclave and pressurized by hydraulic pump up to 500MPa. In addition, a pore

fluid can be placed at the top of the column in order to applicate fluid pressure in subtraction to the confining pressure.

At ISTO, the Paterson Rig is equipped with two deformation modules. The first one is an axial load cell that conducts to co-axial deformation on cylinder or shear-deformation on incline plane assembly. The second one is a torsion module attached at the superior half of the column whereas the bottom-half is fixed. The last one simulates intense shear (i.e. more efficient than the shear assembly in co-axial module) in cylinder sample. Only the first module of deformation presented here was used during the deformation experiments through co-axial and shear assembly.

The deformation system is placed outside of the autoclave, namely, at room pressure whereas the measurement cell is intern and pressurized (Figure III.6a). Two measurements cells are present in the apparatus and can support up to 30% deformation from the initial sample length. A classic, with a 1µm resolution for the displacement and a range from 10^2 to 10^5N for the force. The 'high sensibility' cell has a shorter range of force from 1 to 10^3N but the resolution is 0.1N versus 10N for the classic cell. The deformation rate is comprised between 10^{-2} and 10^{-7} s^{-1}. All mechanical parameters (internal and external displacement and force) and further parameters (time, upstream flow) are transformed into electric signal and are read and recorded by a computer each second. In-situ mechanical curves could be made and compared to the post-mortem finite microstructures development and RSCM signal evolution.

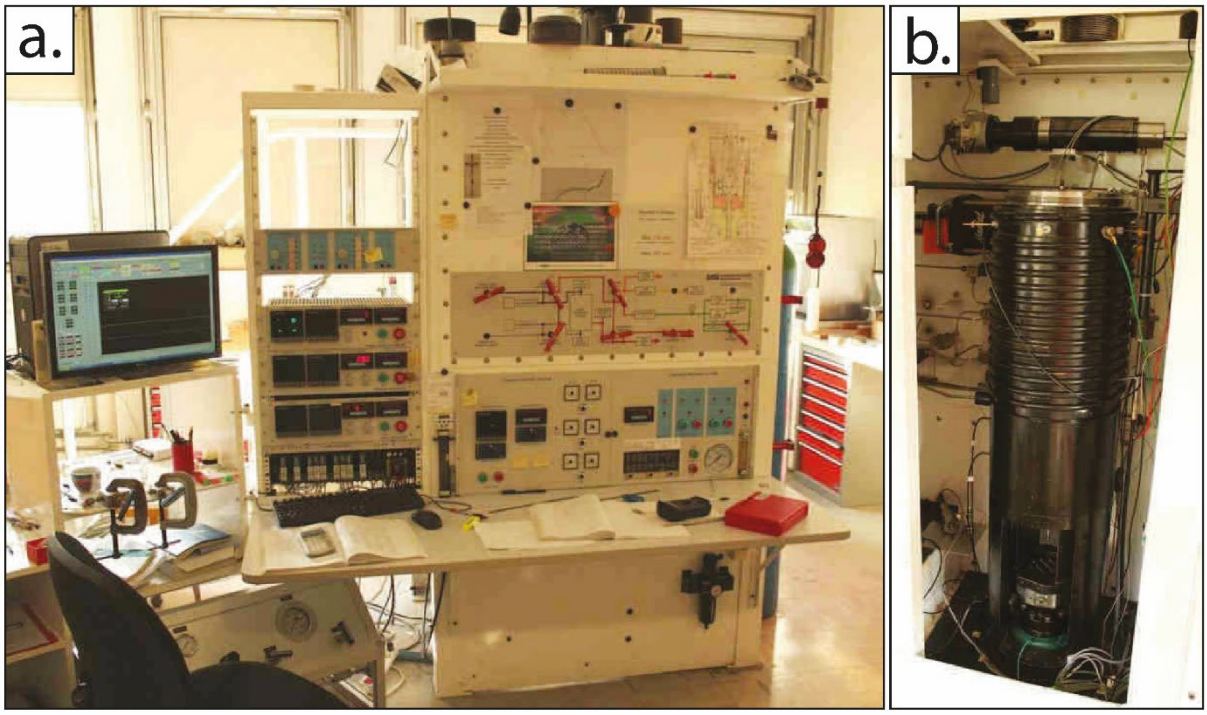

Figure III.4 : Paterson Rig apparatus operating at ISTO, Orléans. ***a.*** *Controller face of the Paterson Rig apparatus.* ***b.*** *Autoclave of the Paterson Rig.*

III.2.2.2 Sample and column geometry

The column, for co-axial or shear deformation, that contains the sample is composed of alumina (Al_2O_3) and partially stabilized zirconia (PSZ) Ø15mm cylinders and is enveloped by a metal (iron or copper) jacket. This assembly is approximately 200mm-long (Figure III.5). At each extremity of the column, pistons are found to set the column in the apparatus. The top piston used for deformation experiments is topped by a pore fluid connector. The jacket, that guarantees the confining pressure, could be made of iron or copper, however, iron has been chosen for the resistance and contribution to the stress during the experiment even if its thermal conductivity is lower than copper. Before each experiment, the jacket is scratched in order to follow the finite quantity and the possible localization of deformation. Pistons play the role to transfer the stress to the sample. A hole in the middle of the pistons from the top to the sample makes the passage for the thermocouple. An important point is the flat surfaces between each pair of pistons because these places are preferential sliding planes. To reduce the sliding hazard between the sample and pistons, each face has been rectified to decrease the irregularity size at less than 0.01mm. The length of pistons in the column were adjusted in order to place the sample in the isothermal zone.

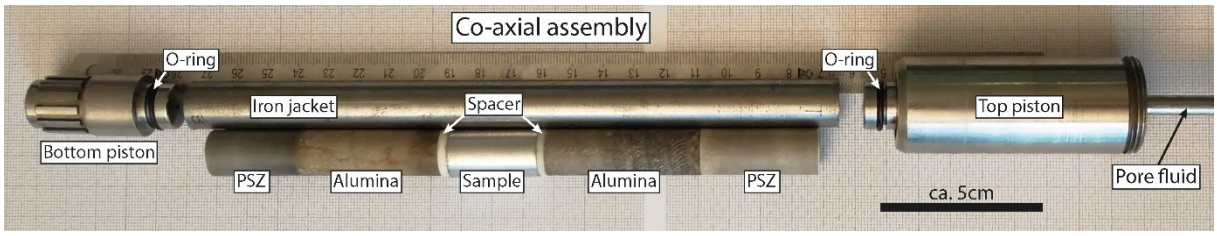

Figure III.5 : Typical column assembly containing partially stabilized zirconium (PSZ), alumina pistons, alumina spacers, sample in an iron jacket. O-ring on each extremity pistons insures airtightness.

During run of experiments, two geometries have been used with only a difference at the central part of the column. Both geometries are composed from the extremities to the center of PSZ and Alumina pistons. The sample used for Paterson Rig experiment was immature shale.

Shear geometry

The so-called "shear geometry" consists in a central part with alumina shear-pistons cutting at 45° containing the powdered sample (Figure III.6b). In order to preserve a zone within the sample without deformation, a hole was drilled in the center of the bottom shear-piston. About 1.2g of powdered samples was added and compressed in order to create a 4mm width disk of sample. Due to the geometry and the hardness of the sample that occurs during the heating, ruptures occurred at the sample/shear-piston interface, even after making the shear-piston plane irregular. Indeed, shear-planes with mirror and striations generated during slip-stick have been described. However, no localization of the continuous strain has been observed in the center of the sample and a co-axial geometry has been used.

Co-axial geometry consists in a central part composed of a cylinder of rock drilled (Ø15mm x 30mm) and separated with two alumina spacers of 3mm (Figure III.6c). As to the pistons, the cylinder has to be rectified avoiding sliding between the pistons and sample. In addition, the rock cylinder has to be perfectly drilled without discontinuous shape avoiding the overpressure on the jacket in one point and the risk of burst. However, the main problem with this geometry is the lack of localization of the deformation without pre-existing brittle fractures.

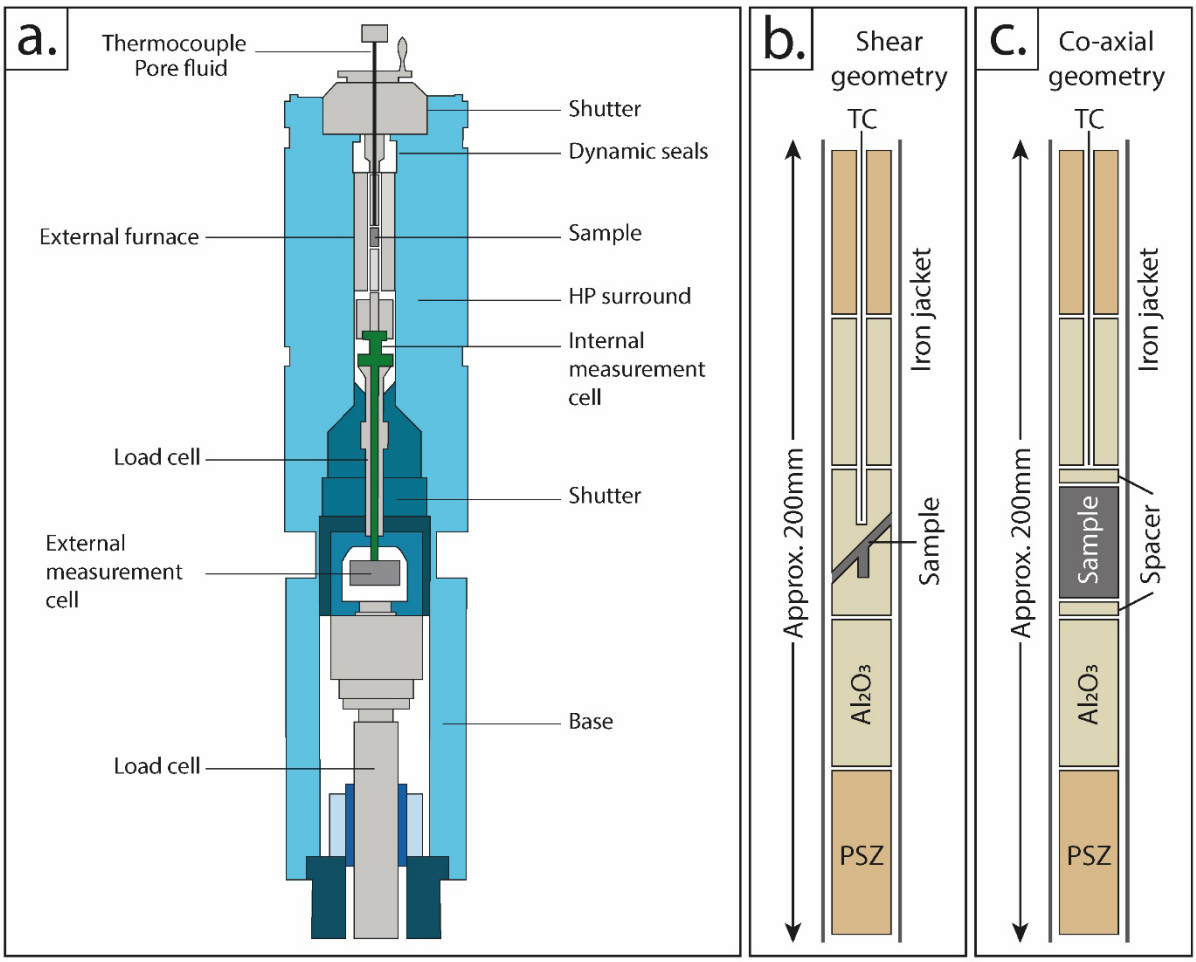

Figure III.6 : Paterson Rig apparatus and columns in shear and coaxial geometry configurations. ***a.*** *Paterson Rig apparatus schematic draw.* ***b.*** *Shear geometry column* ***c.*** *Co-axial geometry column. TC = K-type thermocouple*

III.2.2.3 Experimental conditions

Samples in the column were placed in the Paterson Rig apparatus and connected to the pore fluid. At the beginning of the experiment, the airtightness between the jacket and sample is not yet done perfectly. Hence, air was present in the column and had to be removed by a systematic process described in the following. 10MPa of argon was introduced in the autoclave and flush, in a second time, 2MPa of argon was introduced in the column thanks to the pore fluid connection. After 3 minutes, this argon was flushed by the pore fluid system. This operation was reproduced twice. For a second time, 10 MPa was injected in the autoclave and flush. Due to the absence of airtightness, the oxygen present in the air should be removed from the apparatus to avoid the oxidation of the CM contained in the sample. The confining pressure was then injected up to 100MPa thanks to the pump and the oven is then started. The temperature was raised up to the experiment final temperature following the 4.5°C/min heating rate.

When the temperature required was reached, the confining pressure was adjusted at 150 MPa, identical to the hydrostatic experiments. In addition, about 2MPa of argon are injected in the column to prevent the dehydration of the sample during the heating. When the temperature and the pressure were stabilized, the load-cell was run to begin the deformation. Deformation experiments were carried out at 150MPa, from 600 to 700°C (time function), for 3 to 42 hours with a constant displacement rate from 0.1 to 0.01 µm/s (Table III.2). One 72h experiment was conducted at constant load with an equivalent $10^{-7}s^{-1}$ strain rate. At the end of the experiment, the oven is turned off and the temperature dropped down very quickly under 100°C in few minutes. At this temperature, the autoclave is depressurized very slowly to prevent decompression cracks.

"Long" experiments, lasting more than 10 hours using the Paterson Rig, are difficult to run because this apparatus needs a quasi-continuous observation and control from an operator. In addition, after a long period of running, seals that ensure the airtightness became weary and the risk of jacket rupture increase and leaks were observed.

After experiments, the column was taken out from the autoclave and the sample was cut and prepared for analyses. All pistons, except shear-pistons or spacers, can be reused for further experiments.

Table III.2: Experimental conditions of the Paterson Rig and solid-medium Griggs apparatus experiments

Experiments	Name	Deformation mode	Time	Temperature	Pressure	Displacement	Strain rate	Gamma
Paterson Rig	PP629	Shear	5 hours	700°C	150MPa	1.4 mm	-	-
	PP630	Shear	6 hours	700°C	150MPa	3.5 mm	-	-
	PP632	Shear	7 hours	700°C	150MPa	3.5 mm	-	-
	PP633	Shear	4 hours	700°C	150MPa	1.0 mm	-	-
	PP636	Shear	6 hours	700°C	150MPa	1.6 mm	-	-
	PP638	Co-axial	7 hours	700°C	150MPa	2.6 mm	-	-
	PP641	Co-axial	42 hours	600°C	150MPa	3.0 mm	$5.7E10^{-7}$	-
	PP649	Co-axial	72 hours	600°C	150MPa	2.3 mm	$2.7E10^{-7}$	-
Medium solid Griggs	T609BM	Shear	34 hours	600°C	1000MPa	1.5 mm	$2.6E10^{-7}$	3.1
	T610BM	Shear	72 hours	400°C	1000MPa	2.3 mm	$2.2E10^{-7}$	3.0
	OR87BM	Shear	175 hours	600°C	1000MPa	3.1 mm	$9.9E10^{-6}$	5.3
	OR92BM	Shear	20 hours	600°C	1000MPa	8.1 mm	$5.0E10^{-4}$	-

III.2.3 Solid-medium Griggs apparatus

The second deformation apparatus used during this work, to reproduce natural viscous shear-zones, is the solid-medium Griggs-type apparatus. This type of press permits to reach higher confining pressure that avoids the rupture between the sample and piston in a shear sample assembly. In addition, pressure is one of the main factors that controls CM maturation kinetics and would be interesting to be

investigated. In the following, the description of the apparatus, the sample assembly preparation and the processes from the charging to the data processing are given.

III.2.3.1 Generalities

The Griggs-type apparatus is a solid confining medium piston-cylinder apparatus developed in the 60's by David T. Griggs and then improved through the years (Green and Borch, 1989; Tullis and Tullis, 1986). Today, the Griggs apparatus allows reproducing deformation observed in natural strained fields up to high pressure (< 4GPa) and temperature (< 1200°C) for various types of samples contained in a salted solid medium (here NaCl or KI). Simple or pure shear can be applicated to samples by creating a differential stress generated by a vertical stress. This tri-axial apparatus consists in a 3-horizontal-platens connected by four vertical columns (Figure III.7). The main hydraulic cylinder, which consists in the confining pressure ram, is held by the medium platen when the deformation ram is supported by the upper platen. These rams are both connected to respective pistons, i.e. σ_3-piston and σ_1-piston respectively, the confining pressure piston and the deformation piston made in tungsten carbide (WC) and activated by hydraulic ram. On the lower platen, the pressure vessel, containing the sample assembly and the base plate, is set down (Figure III.7 and III.8a). The sample assembly requires a specific manufactured preparation and will be detailed further. σ_3-piston and σ_1-piston are inserted in the end-load piston, set on the pressure vessel and serve to transfer the force between the confining and deformation rams and the WC pistons (Figure III.8b) (Précigout et al., 2018). While heating during experiments, the cooling of the apparatus is insured through a water flow in the base plate and the pressure vessel and a silicon oil flow in the confining pressure ram. In the new-Griggs apparatus (see below) at ISTO, all the monitoring is led computationally and controls the constant flows of the hydraulic system that conducts in a constant rate displacement or load in the deformation ram and a constant confining pressure in the confining pressure ram. During experiments, confining pressure, displacement and forces of both WC pistons, room temperature and temperature in the sample assembly are all automatically recorded with a pre-defined time-step. The last cited is controlled thanks to a couple of S-type thermocouples placed in the sample assembly (Figures III.8b and III.9c).

Figure III.7 : The new-Griggs apparatus installed at ISTO. From (Mansard, 2019).

Two Griggs apparatuses have been used during this work: a "Tullis-modified" press recently arrived at ISTO, Orléans (France) from the University of Tromsø (Norway) and a new generation "Sanchez" apparatus installed at ISTO, Orléans (France). Most of the experiments have been run using the new "Sanchez" Griggs apparatus, and for a sake of simplicity and clarity, the following description is mainly focused on this machine. Differences between these two types of apparatus correspond mainly to dimensions of the sample assembly and the recording of the data during the experiments. Detailed descriptions of the "Tullis modified" Griggs are available in Pec et al. (2012) and in the PhD theses of Richter (2017) and Marti (2017). Additional information on the new Griggs apparatus can be found on Jacques Précigout's webpage (https://www.jacques-precigout.fr/recherche/griggs-lab-en) and a video of the procedure to carry out experiments is available at https://www.jove.com/video/56841/.

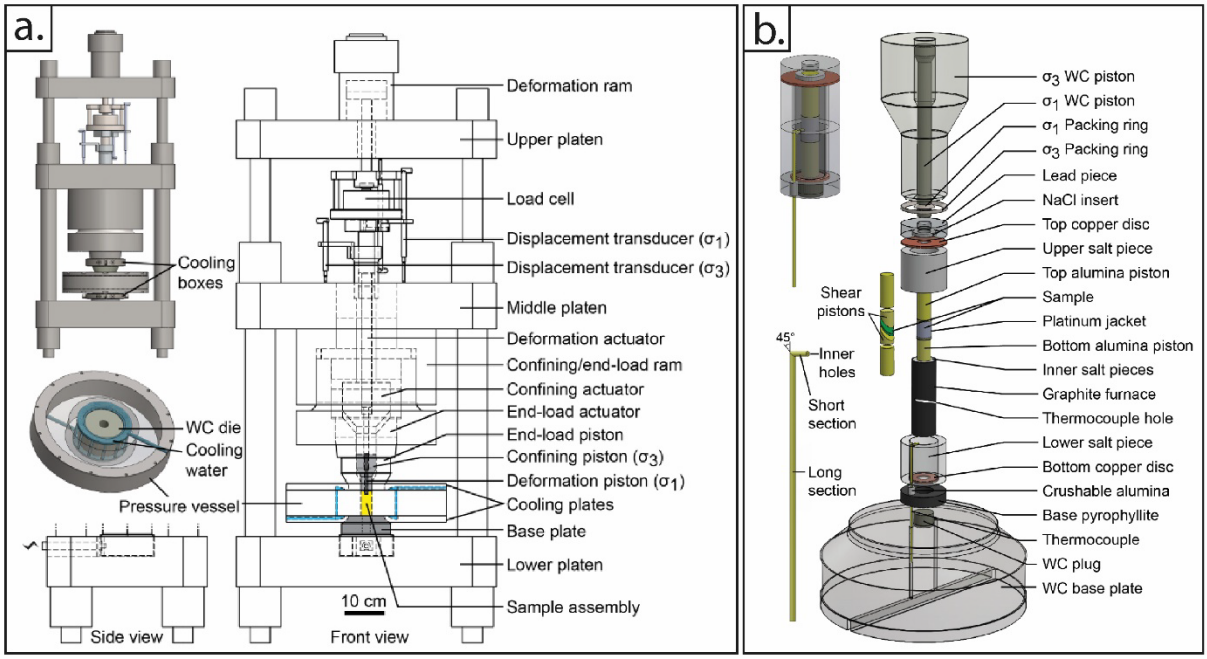

Figure III.8 : Schematic drawing of the ***a.*** *new-Griggs apparatus at ISTO and* ***b.*** *the respective sample assembly. (Modified from (Précigout et al., 2018)).*

III.2.3.2 Sample assembly

The sample assembly is composed of several pieces that needs a specific manufacturing before each experiment (Figure III.9a). The assembly core, placed in a welded Pt-jacket, is composed of two shear pistons including a 1 mm-width sample disc previously cut at 45° from a drilled sample wrapped in a Nickel foil (Figure III.9d). Before the seal of the shear sample in the Pt-Jacket, the last is annealed at 900°C during 2 hours in a high temperature atmospheric oven at ISTO. The assembly core is encircled in a solid-medium composed of two layers of very pure salt (NaCl or KI depending on the experimental temperature) specially created thanks the pressure-solution process of salt when a pressure is applied on weakly humidified salt. The first layer of salt, called “Inner salt pieces”, is directly placed on the contact of the assembly core and followed by the furnace composed of graphite and pyrophyllite. The furnace and inner salt piece are perforated in order to install the pair of S-type thermocouples, composed of Pt/Pt-Rh wires in a mullite sheath, on the contact of the Pt-jacket. A second layer of salt, “Outer salt piece”, finished the exterior of the sample assembly (Figure III.9a and c). Two copper discs are put in contact on each extremity of the furnace in order to transfer the electric current that allows the heating of the sample assembly. The bottom part of the sample assembly is composed of unfired pyrophyllite drilled and filled by crushable alumina to hold the two thermocouples. A tungsten carbide piece is

inserted in the unfired pyrophyllite to ensure the conduction of the current from the base plate to the furnace. On the top of the sample, a lead piece is placed to prevent the deformation the sample during the pressurization and heating phase (Pumping phase).

The sample assembly is similar in the Tromsø "Tullis-modified" Griggs apparatus except the diameter of the alumina pistons and the use of only one K-type thermocouple.

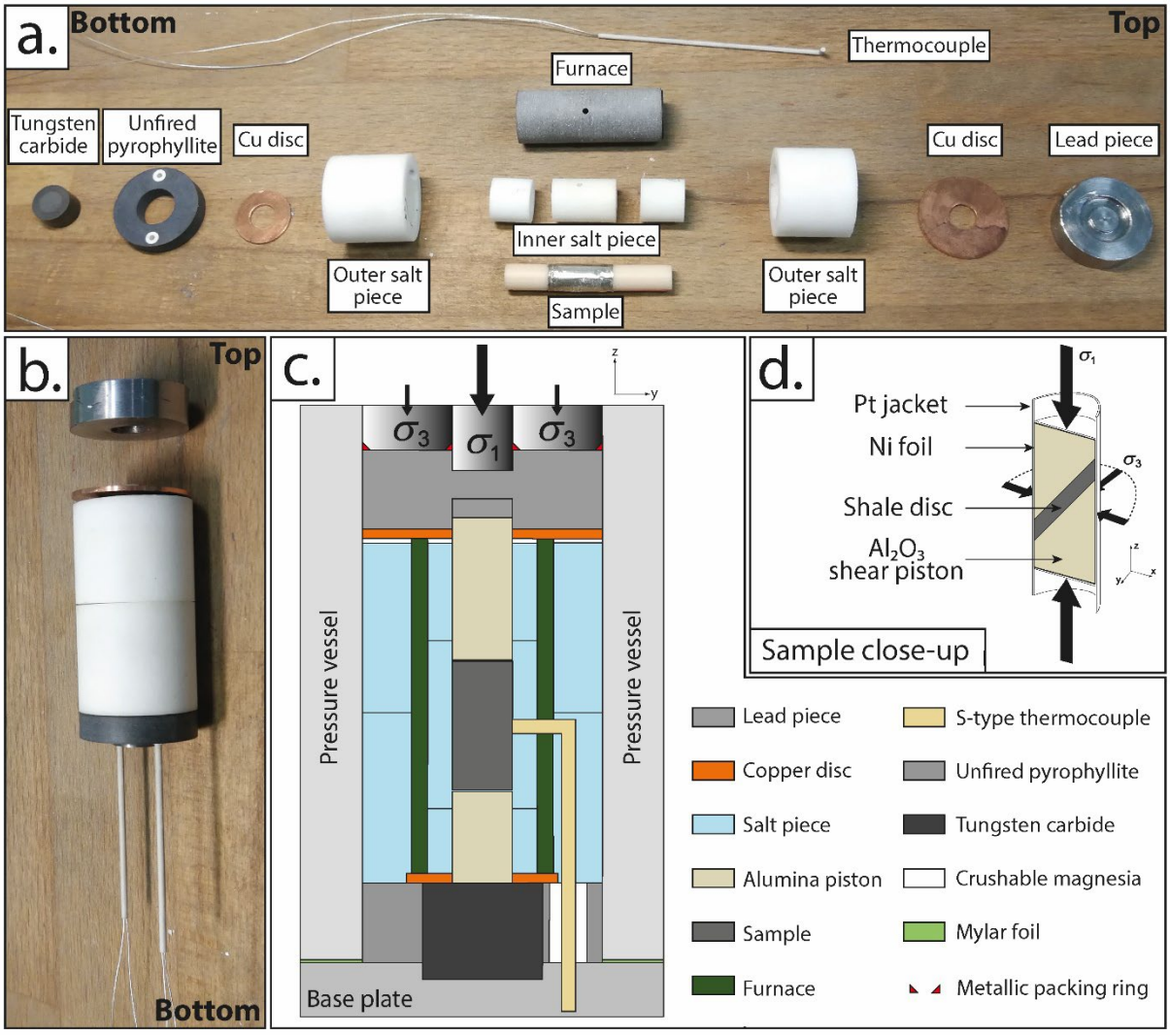

Figure III.9 : Sample assembly used in the new-Griggs apparatus at ISTO (Orléans, France). ***a.*** *Manufactured pieces of the sample assembly.* ***b.*** *Sample assembly.* ***c.*** *Schematic drawing of the sample assembly in the pressure vessel (Modified from (Mansard, 2019; Pec et al., 2012a)).* ***d.*** *Close-up view on the sample geometry (modified from (Pec et al., 2012a)).*

III.2.3.3 Assembly charging

The charging phase consists in installing the sample assembly fitted together (Figure III.9b) into the pressure vessel and the base plate. The alignment between the pressure vessel and the base plate is very

important before the insertion of the sample assembly. After the application of Teflon PTFE all around the sample assembly, thermocouples are threaded in the base plate when the pressure vessel is hanging by an arbor press. A Mylar foil is placed around the sample assembly, that isolates the pressure vessel from the supplied base plate (Figure III.9c), and the pressure vessel is come down carefully. On the top of the pressure vessel on the sample assembly, the top copper disc following by the lead piece are placed and sealed with the σ_3 packing ring avoiding lead leak during the experiment. After insulating the thermocouples, the end-load is placed on the pressure vessel with the two σ_3 and σ_1 pistons where the σ_1 packing ring is placed on the last cited. When all the assembly is complete, it is placed in the Griggs apparatus and WC-pistons well-aligned carefully with the hydraulic rams. The last step consists in plugging the thermocouples and connecting the cooling system. At that stage, the experiment is now ready to start.

III.2.3.4 Performing the experiment

An experiment is composed of different steps after the installation of the assembly in the apparatus. They consist in (1) the pumping phase, (2) the deformation phase, (3) the quenching phase and (4) the extraction of the assembly at the end of the experiment. Detailed features are given in the following about each of these phases.

Pumping phase

The first step corresponds to the pumping phase during which the sample is gradually heated and pressurized (Figure III.10). Heating is generated thanks to a constant current applied to the base plate and conducted through the assembly until reaching the graphite of the furnace. The confining pressure is applied by moving forward the confining pressure piston alternatively with the deformation piston respecting a maximum distance of 3 mm between these two pistons. The confining pressure and the temperature are slowly increased by steps alternatively, in such a way the pumping phase is lasted for half a day. When the required temperature and confining pressure are reached, the apparatus is kept for ca. 12 hours (generally during the night) in order to regulate these constants.

Deformation phase

During the deforming phase, a constant flow of oil is set in the confining pressure ram to keep the confining pressure constant and only the deformation ram is fed. Two possibilities can be used, a constant strain rate and a constant load applied to the sample. Both possibilities were used, the first cited using the "Tullis-modifed" Griggs apparatus and the second using the new-Griggs apparatus. Experiments conditions and information are found in Table III.2.

The deformation phase is itself split in two stages (Figure III.10): (A) the run-in stage where the friction of the packing rings is observed when the σ_1 piston is passing through the lead piece. The second stage (B) starts when the σ_1 piston crosses over all the lead piece and reaches the alumina piston of the sample assembly. This particular point between stage A and B is called the "hit-point" that corresponds to the point of intersection between the gentle and steep slopes on the Force vs. time diagram (Figure III.10). The sample deformation begins properly at the "hit-point" with first an elastic deformation followed by a plastic one. The record of this force/time or stress/time curve is important because it helps to interpret the microstructure observations made after the experiment. When the quantity of strain required is attained, the σ_1 piston is stopped and the quenching phase (3) can begin.

Quenching phase

This phase is the last one of the experiment but needs to be carefully done to avoid damages and artefacts within sample by opening unloading-cracks. After stopping the σ_1 piston, the stress drops down and the temperature is quickly reduced to 200°C (Figure III.10). The next step consists in pulling both σ_1 and σ_3 pistons out slightly from the sample assembly conserving a maximum differential stress between $\sigma_1 - \sigma_3$ of 100 MPa. It is necessary that the σ_3 never begins higher than σ_1, otherwise, the sample assembly could be in extension and damages could be produced. At 100 MPa of confining pressure, the temperature is set to 30°C and both pistons are pulled out reaching 0 MPa at the same time.

Extraction of the sample assembly

After the quenching phase and the removal of stress, the pressure vessel can be removed from the Griggs apparatus. Thanks to a hydraulic press, the sample assembly is removed from the pressure vessel and the pressure vessel is cleaned carefully for further experiments. Salt medium and external layers are

cautiously removed and the orientation of the sample and the tick of the thermocouples are marked on the Pt-jacket. This sample is then placed in epoxy resin in the X-Z plane and prepared for microstructure and RSCM analyzes.

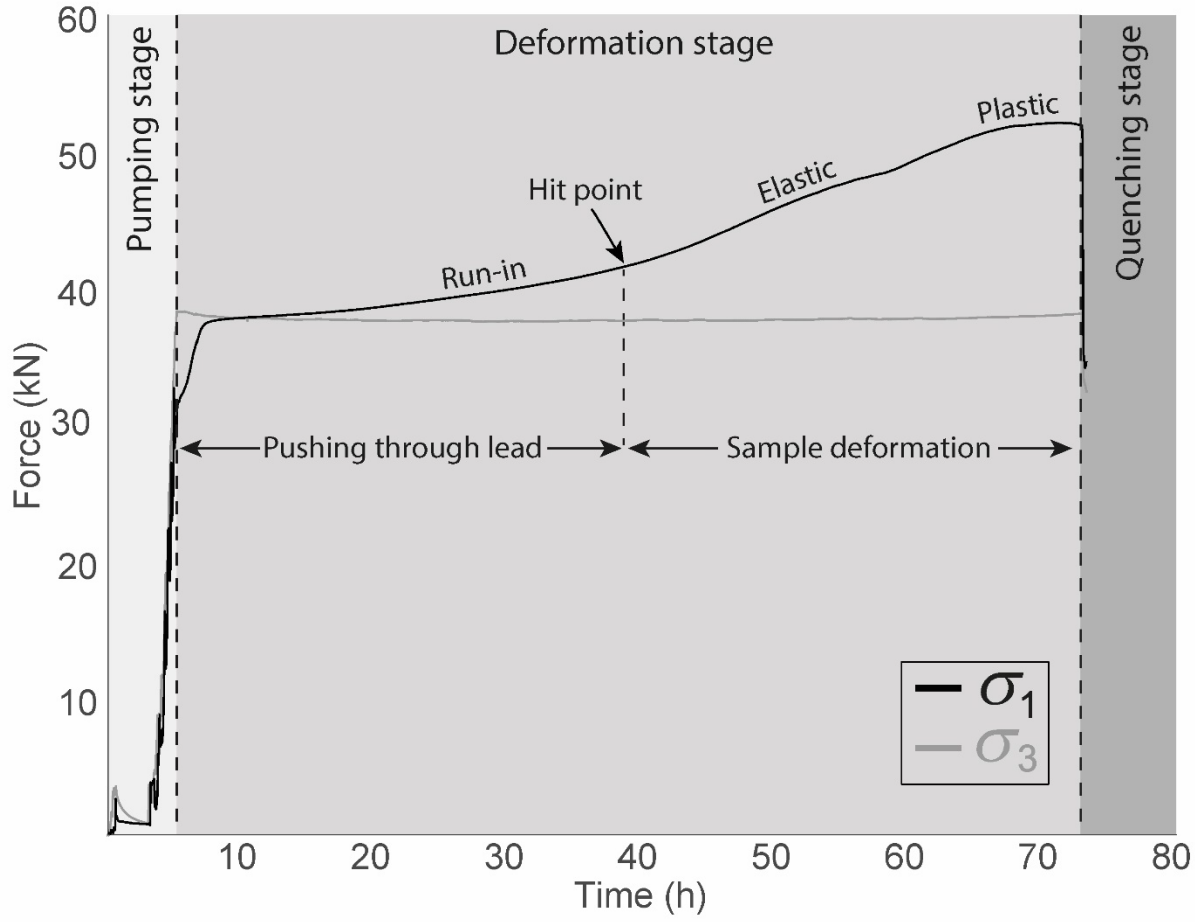

Figure III.10: Force-time curves from the T609BM experiments highlighting the pumping, deformation and quenching stages. During the deformation stage, two phases are observed (1) the run-in phase when the deformation piston pass through the lead piece followed by (2) the sample deformation. (Adapted from (Précigout et al., 2018)).

III.2.3.5 Data processing

During experiments, several routine data (displacement, force, time, temperature, confining pressure, etc.) have been recorded in order to be interpreted and compared with the finite deformation of the sample, trying to connect this continuous record and the microstructure development. However, before this step, raw data need to be corrected. These corrections are done using the Matlab script written by Jacques Précigout and available on his website (https://www.jacques-precigout.fr/ressources). After determining the hit-point, corrections are applied on the data (record by CatmanEasy AP). The displacement and the force are corrected as a function of the apparatus stiffness. The compaction is

changed and the area of the sample, that evolves, when sheared, is corrected using the following equation:

$$Shear\ surface = 2\ .R^2.\cos^{-1}\left(\frac{d}{2\ .R}\right) - d\ .\sqrt{R^2} - \left(\frac{d}{2}\right)^2$$

Where R and d are respectively, the radius and the displacement. Finally, the force tied to the assembly friction is removed following this equation:

$$Force\ (corrected) = Force\ (uncorrected) - displacement\ from\ the\ hit\ point\ .Friction$$

The friction value used is 1.3 based on the experiences of Matej Pec and Renée Heilbronner (Personal communication).

III.2.3.6 Experimental conditions

Immature shale from the Myazaki group in the Shimanto belt (Japan) has been used during experiments. Two types of deformation experiments have been done: (1) at constant deformation rate and (2) at constant load.

Experiments at constant strain rate have been achieved using the "Tullis-modified" Griggs apparatus at 10^{-5} s^{-1} at 400°C (T610BM) and 600°C (T609BM) and a confining pressure at 10 kbar respectively in a KI-medium and NaCl-medium (Table III.2). A total strain of $\gamma \approx 3$ have been reached, however, a lack of viscous deformation and localization of brittle deformation have been observed, consequently, it has been decided to carry out deformation experiments at constant load using the new-Griggs apparatus. For this second type of deformation experiments, an important issue was the balance between the time and the temperature of the experiments because of the CM kinetics in order to set a specific range of maturation. For this reason, experiments were carried out at 600°C from 200 to 500 MPa differential stress, equivalent to 10^{-4} to 10^{-6} s^{-1} (Table III.2). Important strains were reached ranging from $\gamma \approx 5$ to $\gamma \approx 34$ and the role of the dehydration of the sample appears to be an important factor on the material strength. All the results of these experiments are in detail presented in Chapter V.

III.2.4 Flash heating maturation experiment

Intense yet short-duration heating experiments have been carried out in addition to the "long-term" thermal maturation and the deformation experiments. These experiments aim to understand the effect of temperature alone during a short-event that could conduct to the melt of samples without strain-work.

III.2.4.1 Experimental settings

The melting temperature of the sample used in these experiments had been to be set. Powder sample of poorly mature has been placed in Pt-crucible and put in a classic atmospheric oven at ISTO, Orléans. The sample has been heated and let in the oven at least for 10 minutes in order to observe its behavior with increasing temperature. At atmospheric pressure, the first clue of melting has been observed at 1250°C and the total fusion of the sample has been observed at 1400°C.

III.2.4.2 Aerodynamic levitation and CO_2 laser

Aerodynamic levitation coupled with a CO2 laser has been used to generate the short and intense heating pulse using the system at CEMHTI, Orléans. This system is mainly used for vitrification and consists in 2 infrared CO_2 laser (λ = 10.6 μm) focalized thanks to mirrors coupled with levitation nozzle where continuous argon flux is blown (Figure III.11a and b). Levitation avoids contaminating the sample by touching the crucible, and oxidation of the CM present in the sample. During experiments, millimetric, more or less rounded chip of sample, was placed in the nozzle and the temperature was controlled using pyrometer (Figure III.11a). At the end of experiments, the laser is turned off and quenching of the sample is very fast.

Before the experiments, the lasers powering were set based on the fusion temperature observed with the atmospheric oven. Due to the large amount of water contained in the sample used (*i.e.* ca. 5%), an excessive heating from the room temperature to 1400°C can generate the explosion of the sample. The sample was pre-heated during 120 seconds from the room temperature to around 300°C. When the laser power reaches this equivalent temperature, lasers turn their powering to an equivalent of 1400°C in 0.1 second and stay at this powering for the time of Flash heating required. After this time, lasers were turned off. Pairs of experiments have been made for each duration time, from 0.5 to 60 seconds.

At the end of the experiments, the samples have been prepared for optical microscopy and RSCM analyses (Figure III.11c).

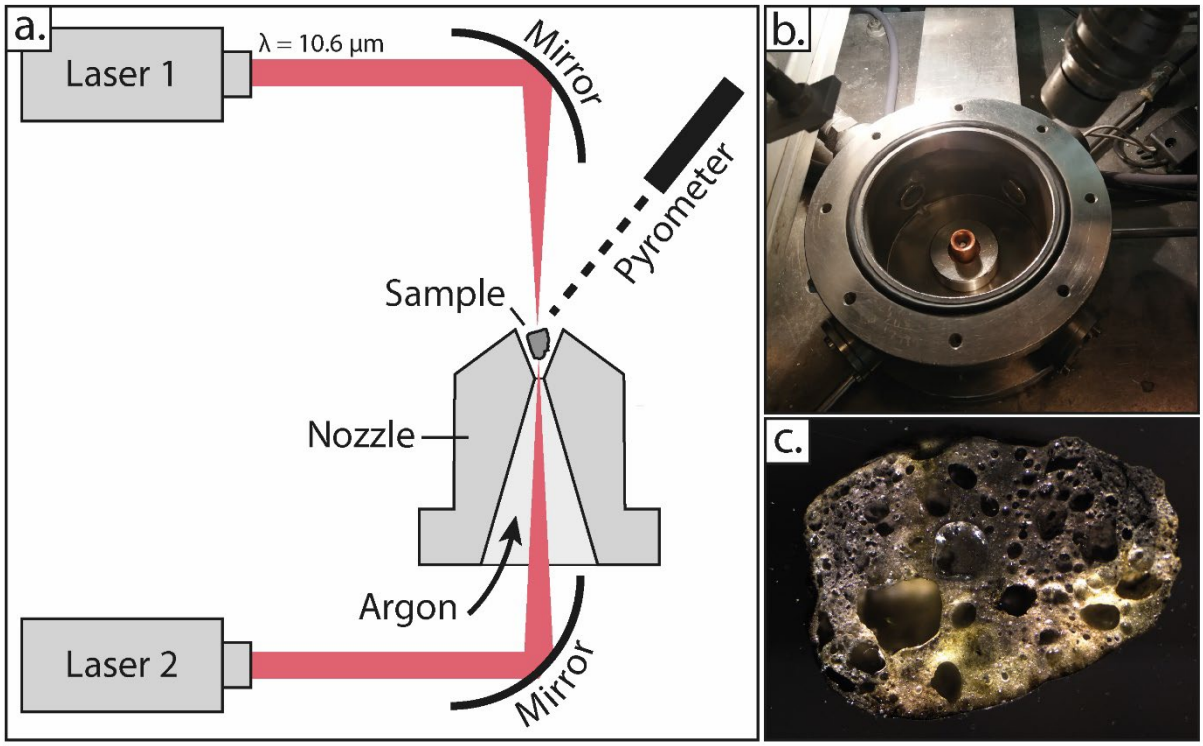

Figure III.11 : Flash heating experiment apparatus and samples resulted from intense and short-life heating. ***a.*** *Simplified drawing of the aerodynamic levitation apparatus (Adapted from (Boyer, 2016)).* ***b****. Aerodynamic levitation apparatus.* ***c.*** *Finite product after the flash-heating experiment using a fragment of poorly mature shale.*

III.3 Characterization of natural and experimental samples

III.3.1 Sample geochemistry and phase discrimination

III.3.1.1 Bulk geochemistry

Major elements of the two starting materials have been obtained by the X-ray Fluorescence (XRF) on the whole rock, operating by ALS Global company (https://www.alsglobal.com/). Samples were first crushed and dried and then analyzed thanks to the XRF. The homogenized powder, after melting, is exciting by X-ray emission, in response secondary X-ray are emitted by the material with characteristic features for each chemical composition of the sample. 14 major elements have been measured through this method (%wt, SiO, TiO_2, Al_2O_3, Fe_2O_3, MgO, MnO, BaO, CaO, Na_2O, K_2O, Cr_2O_3, P_2O_5, SO_3, SrO) and the LOI (%wt) have also been obtained.

III.3.1.2 Phase definition: X-ray diffraction (XRD)

Inorganic phase identification and semi-quantitative estimation of the starting materials were obtained using the X-ray diffraction (XRD). After crushing the whole samples, the fine powder was placed in capillary and analyzed using an INEL diffractometer equipped with a CPS120 curve detector at ISTO, Orléans. The qualitative compositions of the samples were obtained. Moreover, thanks to the Rietveld method and the area under the XRD curve, a semi-quantitative mineralogical composition has been obtained.

III.3.2 Characterization of the maturation state of the carbonaceous material

III.3.2.1 Rock Eval pyrolysis

The amount (wt% TOC), type (I, II, II, IV) and thermal maturity (T_{max}) of the CM contained in the starting materials have been obtained using the Rock Eval pyrolysis. This classic method developed for petroleum exploration aims to reproduce in lab the cracking process by measuring several petroleum parameters such as the quantity and quality of hydrocarbons and an estimate of natural/geological cracking temperature for example. All explanations about this method and the corresponding parameters are described by Espitalié et al. (1985a, 1985b). About 50 mg of dried crushed samples were pyrolysed using the Vinci Technologies Rock-Eval 6 Turbo at ISTO, Orléans. Thanks to fast temperature enhance and stepping, in neutral and oxidative atmospheres Rock-Eval parameters were calculated with to the

Rock-Eval 6 software (Lafargue et al., 1998). Four parameters were interesting for the characterization of the starting material: the total organic carbon (TOC), the hydrogen index (HI, mg HC /gTOC), the oxygen index (OI, mg CO2 /gTOC) and the thermal maturity estimation based on the S2 band (T_{max}). The combination of the hydrogen and oxygen index plotted in the Van Krevelen diagram drives to discriminate the type of CM that composes the starting material. The T_{max} is used as an indicator of the thermal maturity of the CM (Espitalié et al., 1985a, 1985b). The %wt TOC reveals the total amount of CM in the starting material.

III.3.2.2 Vitrinite reflectance (%VR)

Vitrinite reflectance is defined as the percentage of reflection of an incident monochromatic light by the surface of a polished fragment vitrinite, a maceral particle of carbonaceous matter present within the metasediment. This measurement has been calibrated with the thermal maturity of CM contained in rocks from the early diagenesis until the early metamorphism stage (Tissot and Welte, 1984). In addition, vitrinite reflectance has been used as a new calibration of thermometers in early maturation stage of the CM (Barker, 1988). Kinetics models based on the vitrinite reflectance have also been proposed on the correlation between the vitrinite reflectance and the atomic H/C ratio (Burnham and Sweeney, 1989; Sweeney and Burnham, 1990). This kinetics model can follow the maturation from 0.3 to 4 %VR, approximately from 20 to 300°C based on the thermometer introduce by Barker (1988).

Vitrinite reflectance has been used in this work in order to characterize the CM contained in the starting materials before experiments. In addition, to follow the maturation evolution during the hydrostatic experiments on existent kinetics calibration, the vitrinite reflectance was measured on vitrinite concentrate from Candiota (Silva and Kalkreuth, 2005) added to sample.

Due to the low amount of natural vitrain in our two starting materials, upstream preparation before the analyses has to be done. This step consists in separating the CM from the whole rock sample. First, samples are crushed finely and the CM is separated using dense liquor. The residual CM obtained is included in epoxy resin and polished. Mean vitrinite reflectance was measured using a Leica DMR XP microscope equipped with a photometer and an oil-immersion objective on at least 50 particles. Glass-reflectance standards were used for the calibration of the method (Bertrand et al., 1993; Robert, 1971).

III.3.3 Structural analysis of the carbonaceous material crystalline organization

III.3.3.1 Raman Spectroscopy of Carbonaceous Material high resolution mapping

Raman Spectroscopy of Carbonaceous Material (RSCM) has been used to constrain the crystallinity of the carbonaceous material (CM). Sample sections were analyzed with ReniShaw InVIA microspectrometer at ISTO-BRGM, Orléans, using argon laser beam of 514 nm focused on the sample by DM2500 Leica microscope equipped with x100 objective. These apparatuses are coupled with Renishaw software Wire 4.0 which was used for data acquisition. Further explanations on the RSCM functioning are detailed in Chapter II.

Acquisition time varies from 30 to 200 seconds (Spectrometer opening time was around 5s with a maximum of 40 spectra accumulation). Laser power was maintained at less than 0.5mW on the surface of the sample to avoid heating of CM grain during analyses. To avoid defect bands generated during thin section polishing all analyses were performed on subsurface grains by focusing laser beam through transparent or translucent minerals (Ammar and Rouzaud, 2012; Katagiri et al., 1988; Pasteris, 1989). Based on the literature, the lithology could have an effect on the RSCM signal by adding structural defects (Pasteris and Wopenka, 1991; Wada et al., 1994). RSCM results and especially the intensity ratio, on shales and sandstones from the Shimanto Belt, did not show important deviation one from to another, except for advanced graphitization (Figure III.12). In the literature, studied zones are in higher maturation stage of the CM with important deformation, these points could explain the measured deviation. However, to prevent a possible lithological control of the RSCM signal, we decided to analyze only shale layers. Two approaches have used depending on the scale of the strain gradient. The first approach corresponds to the classic approach of Beyssac et al. (2002) of the RSCM geothermometry with a minimum of 20 punctual points of analysis randomly localized in the entire sample. This approach is particularly adapted to large-scale strain gradient in which a single thin section allows studying only one type of microstructure. The second has been used for mm-scale strained structure where analyses were processed across a series of cross-sections perpendicular to the main structure. In this case, the approach is particularly adapted to small-scale strain gradient where microstructures are significantly smaller that the size of a thin section. Spacing between analyses was drastically reduced and

concentrated, from few tens of micrometers to less than 10 µm, when approaching the deformed zone. X-Y coordinates of the punctual analyses were taken for georeferencing the analyses on maps or profiles.

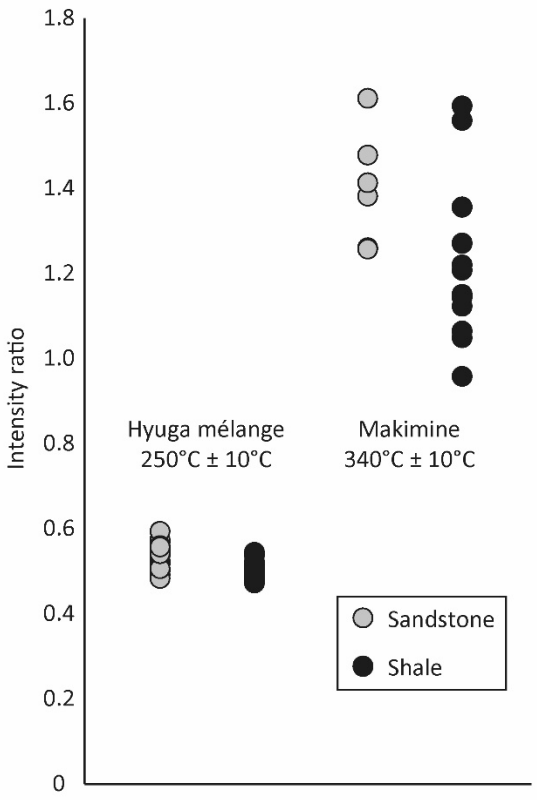

Figure III.12 : Variations of the intensity ratio depending on the lithology (sandstone vs. shale) measured on samples from the Shimanto Belt at 250°C (Hyuga tectonic mélange unit) and 350°C (Makimine unit)

Raman spectra processing was done using PeakFit v4.12. In order to get the best comparison between carbonaceous material spectra from the sheared-domain and the poorly deformed-domain, only spectra with flat baseline were considered and linear baseline subtraction function was applied. To determine the baseline, two bands of 100cm^{-1} wide were selected around 900 and 1900cm^{-1}. To interpret Raman spectra and obtain Raman spectra parameters, Lahfid et al.'s (2010) procedure was used for deconvolution. This approach is well adapted to low metamorphic grade and consist in a deconvolution of 5 bands (D1, D2, D3, D4 and G) using Lorentzian functions (Figure III.13a). These bands form one Defect massif made of the D4, D1 and D3 bands (D band) centered around 1350cm-1 and one Graphite band (G sl. Band) composed of D2 + G bands centered around 1600cm-1 and are attributed, respectively, to the vibrational and A1g and E2g (Beny-Bassez and Rouzaud, 1985; Tuinstra and Koenig, 1970). By using area ratio RA1 = (D1+D4)/(D1+D2+D3+D4+G) it is possible to obtain a temperature estimate in

the range of 200 to 330°C with a ± 25°C uncertainty (RA1 = 0.0008. T_{max} + 0.3758). In some cases, carbonaceous particles have higher crystallinity (i.e. Black Fault Rock spectra) so that the deconvolution using 5 bands described above was not possible in the absence of D4 or even D3 bands. In such cases, we used the procedure and calibration defined by Beyssac et al. (2002) using a 3 bands deconvolution (Figure III.13a). However, in contrast with the classic deconvolution proposed by Beyssac et al. (2002), for convenience, the deconvolution function used was not the Voigt function but the Lorentzian function. The difference between the calculated temperatures for 150 analyses with the Voigt and the Lorentzian function is always inferior to 10°C, much below the error made on the calibration (Figure III.14). The main Raman spectra parameter used in this work was the intensity ratio (i.e. R1 in Beyssac et al. (2002)) which consists of comparing the height of the defect band (D band) and the raw graphite band (G sl. Band).

After the processing phase, using the GIS software ArcMap 10.6, each analysis was precisely located on microstructural pictures. Such high-resolution mapping allowed to compare micro-textures and the corresponding Raman spectra distribution.

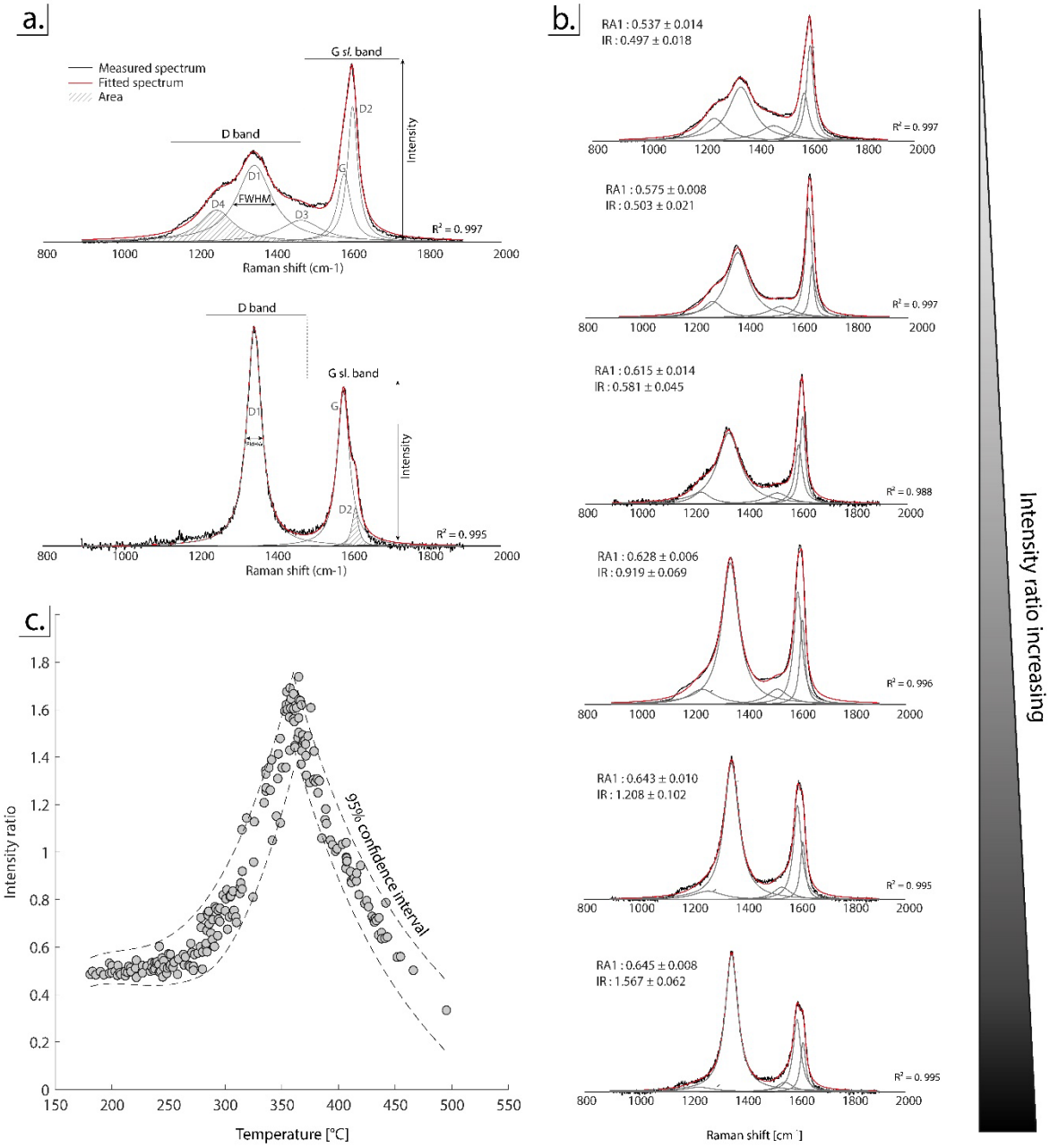

Figure III.13: Raman Spectra of Carbonaceous Material ***a.*** *Typical Carbonaceous Material spectra and their respective parameters obtained through the deconvolution processes described in (Beyssac et al., 2002; Lahfid et al., 2010)* ***b.*** *Spectrum shape evolution during the carbonization phase (200 to 360°C) and intensity ratio increasing* ***c.*** *Calibration obtained with a 95% interval of confidence from the analyzes of undeformed or poorly deformed samples from the Shimanto Belt and from the Montagne Noire (this study calibration).*

III.3.3.2 Intensity ratio (IR) and evolution of the CM crystallinity

The ratio between the height of each D band and G sl. Band is also an important parameter to describe the crystalline of CM, and the intensity of this ratio (intensity ratio -IR) has been used as the main Raman parameter in this study. Indeed, this IR parameter reflects the crystalline structure of the Carbonaceous

Material (Pasteris and Wopenka, 1991; Tuinstra and Koenig, 1970; Wopenka and Pasteris, 1993) and evolves in all along metamorphic temperature range. First, during the carbonization stage and early stage of the graphitization (i.e. from 200 to 360°C), heteroatoms (H, O, S) are expulsed and the formation of Basic Structural Units (BSU) begins by the construction of C-C link. The first appearance of polyaromatic structures is described. During this phase the IR increase from 0.5 to 1.6 (Figure III.13b). Then during the graphitization stage (i.e. from 360°C to 600°C), polyaromatic structures are stacked, crystallites extend and begins to be thicker. The IR response corresponds to a decrease of RI from 1.6 to 0.2. However, based on our experience during the Raman acquisition, the IR also showed to be a sensitive parameter that evolves with strain during the carbonization and the early graphitization stage. Other RSCM parameters have been tested as well to reveal the strain effect on the crystallinity of the CM such as the FWHM of the G band and the distance between the D and G bands. However, these parameters show ambiguous and inconsistent evolution along strain-gradients. Finally, we focused our results on the IR evolution which is considered as the main strain sensitive RSCM parameter. Further studies have shown the same conclusion but during the graphitization stage on natural (Kedar et al., 2021) and experiment sheared samples (Bustin et al., 1995; Ross et al., 1991a).

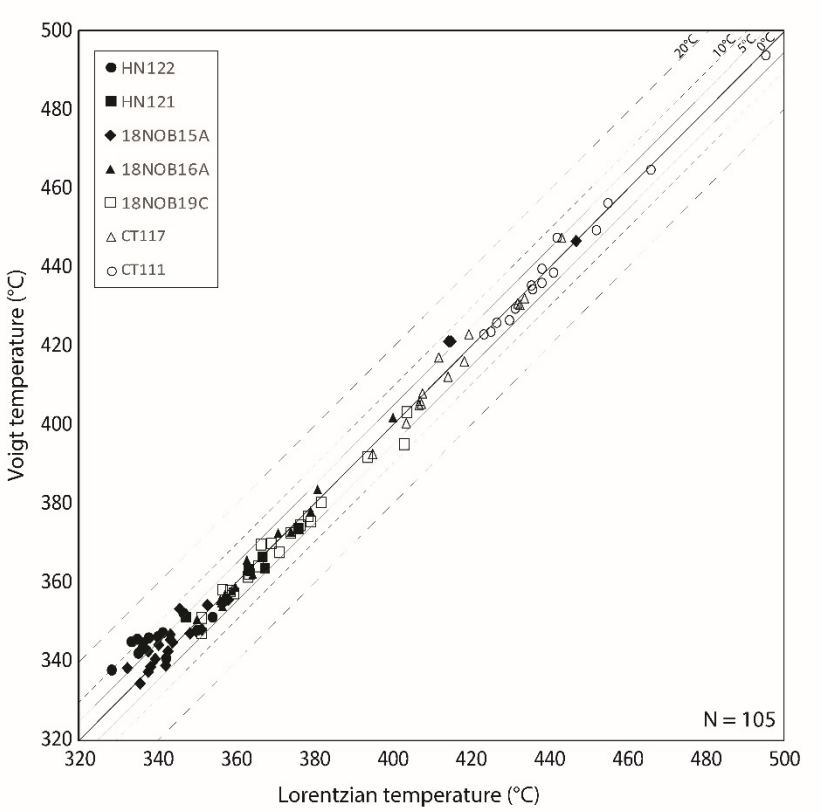

Figure III.14:Calculated temperature by the (Beyssac et al., 2002) calibration using deconvolutions with a Voigt function and Lorentzian function.

III.3.3.3 Intensity Ratio (IR) calibration from undeformed samples

Based on this strain sensitivity, we proceed our own calibration between the IR measured for undeformed - poorly deformed and the temperatures calculated using geothermometers (Beyssac et al., 2002; Lahfid et al., 2010) (Figure III.13c). 210 Raman analyses have been used on poorly deformed samples sampled from the Shimanto belt (Japan) and the Montagne Noire (France). A 95% confidence interval envelope from 180°C to 500°C was calculated based on these measurements (Figure III.13c). This calibration shows a poor evolution of the IR from 180°C to 240°C around 0.5 and then increases abruptly until to 1.6 from 250°C to 360°C. After 360°C, during the graphitization stage IR decreases from 1.6 to 0.2 very quickly until the perfect crystallization of graphite where the IR will sole down to zero.

III.4 Characterization of the microstructures

III.4.1 Microscopy

III.4.1.1 Optical microscopy (OM)

Optical microscopy has been applied using a reflected light in addition to macro observation in order to distinguish textures and micro-textures, especially for 'hard' minerals like quartz, plagioclase and carbonates composing the rocks clasts wrapped in a shaly matrix. Reflected light high-resolution mapping has been realized thanks to the automatized microscope of the CL focused on the mm-scale strain-gradients.

III.4.1.2 Scanning Electron Microscopy (SEM)

In addition to the optical microscopy, SEM has been used to characterize the microstructures at lower scales and the phase using a semi-quantitative method on polished and carbon-coated (±20nm) samples. SEM imagery is based on the re-emission after an excitation through electron-sample interaction. An electron gun enlightens the sample and, in response, it reemits several waves such X-ray, secondary electron (SE) or back-scattered electron (BSE). Depending on the phase heaviness, a certain quantity of back scattered electrons are emitted by the matter and appear white for the heavier to black for the lighter phases. Thanks to the BSE imaging, a semi-qualitative repartition of the phases and associated microstructures can be observed. In addition, the energy-dispersive X-ray spectroscopy (EDS) analysis allows obtaining a semi-quantitative information and defining the phase spotted by the detector. SE consists of low energy electron emitted by surface of the sample. Therefore, the SE imaging permits to observe electronically the surface texture of the sample.

At ISTO, Orléans, SEM analyses were carried out using a SEM Merlin Compact Zeiss, equipped with BSE, SE and EDS Quantax detectors, at 15kV with a working distance of 10mm. At BRGM-ISTO, Orléans SEM analyses were carried out using a TESCAN MIRA 3 XMU at 15kV with a working distance of 15mm.

III.4.1.3 Cathodoluminescence (CL)

CL has been used for the characterization of microstructures for the mm-scale deformed zone in order to distinguish mineralogical and textural evolution along the strain gradient based on the luminescence

of minerals like quartz, plagioclase and calcite because of the low/absent luminescence of clays and phyllosilicates of the matrix. The CL method is based on the semi-conductivity of certain minerals which, when excited by an electron gun, emit photons in the visible spectrum wavelength. The luminescence mechanism is explained by the interaction between the semi-conductive material and an incident electron, which hands a part of its energy to another electron of the valence band of the material and emit a photon in response. The wavelength of the emitted photon is characterized by the type of material and can reveal the internal structure, the growth history of mineral or the evolution of composition. CL was ran with a Cathodyne-Newtec apparatus using an automatized stage and coupled with a Leica microscope and a low light Qimaging Retica R1 camera, at ISTO, Orléans. Thick-section placed in a vacuum chamber at an Argon pressure ~ 50 x 10^{-3} mbar and irradiated by a cold cathode source electron gun titled at 18° with the sample. Standard voltage-current beam conditions were maintained at 15kV and 150 µA during the acquisition time around 1 to 5 second per image. Every X10 magnification images snapped were stitched using the Image J software in order to obtain a high-resolution map.

III.4.2 Micro-compositional evolution - Electron probe micro-analysis (EPMA)

Punctual, few micron-scale mineral compositions and element mapping have been carried out through EPMA analyses on carbon-coated samples. The EPMA is mainly based on the same excitation-material method used by the SEM. In response to the bombardment of the incident electrons produced by Tungsten head, X-rays are emitted and each wavelength is characteristic of a chemical element. Emitted wavelengths are analyzed thanks to the Wavelength Dispersive X-ray Spectroscopy detector (WDS) which is based on the Bragg diffraction law. EPMA analyses were performed using a CAMECA SX Five equipped with 5 WDS spectrometers, at BRGM-ISTO, in Orléans. Punctual quantification analyses were acquired under a voltage acceleration of 15kV and a 10 nA current beam on focused beam of ca. 1µm. Element mapping acquisition was done with operating conditions of 15kV, a beam current of 100 nA, 150 ms per pixel for the dwell time and1µm for the step. In this study, 10 oxides have been quantified (Si, Ti, Al, Fe, Mg, Mn, Ca, Na, K and Cl). Processing of element mapping has been

processed and thanks to the XMapsTools software (Lanari et al., 2014), developed for reconstructing the phase maps.

III.4.3 Micro-textural evolution - Electron Back-Scattered diffraction (EBSD)

The crystallographic information that allows determining the strain mechanisms has been obtained using an Electron Back Scattered Diffusion apparatus. The EBSD detector is composed of a phosphor screen and a low light condition camera. After being excited by the SEM column electron gun, some electrons are diffracted on the planes of the crystal lattice and form two diffraction cones. Due to the low angle of diffraction and following the Bragg's law, these cones are flattened and will be projected as lines on the phosphor screen of the EBSD detector. These bands are called Kikuchi bands. The addition of several diffraction planes forms on the screen a diffraction diagram (EBSP). Thanks to the EBSP indexation through the Hough transform, Miller indexes are obtained. Based on the last cited, the orientation of the crystal is defined for each point of measurement. In a first time, samples were polished using a colloidal silica suspension and then carbon-coated with a thin 2nm coat. EBSD data were performed via an EDAX PEGASUS EDS/EBSD system coupled with the OIM DC 6.4 software at ISTO-BRGM, Orléans, installed on the TESCAN MIRA 3 XMU SEM. Operating conditions involved an accelerating voltage of 20-25 kV and a working distance of 20mm for each map with a one micrometer resolution. Processing was made firstly on OIM using the cleaning option that consists in removing extra points. Internal misorientation and sub-grain boundary maps and lower hemisphere pole figures were obtained using the MTEX script developed by Jacques Précigout (available at: https://www.jacques-precigout.fr/ressources). Crystallographic Preferred Orientation (CPO) and J-index of texture strength (Bunge, 1982) are also obtained in addition which permitted us to discuss of the deformation mechanisms.

Preface

In this chapter, the effect of the non-seismic deformation on the CM crystallinity is presented for the temperature range covering the carbonization and early graphitization stages (i.e. 200 to 360°C). Strain gradients from different scale and finite strain have been sampled from three accretionary complexes (Shimanto Belt, Kodiak Accretionary Complex and Infrahelvetic complex). The CM crystallinity response to the strain has been analyzed thanks to the RSMC high-resolution approach and especially the IR sensitive to the strain and natural increasing under temperature stress. The CM crystallinity evolution has been linked with microstructures obtained by classic petrological approach. The results suggest that the non-seismic deformation leads to a CM crystallinity enhance irrespectively of the regime of deformation and from the millimetric to the regional scales. In addition, the strain quantity and the CM crystallinity increase are correlated and the ductile deformation has shown a stronger effect on the CM crystallinity than the brittle deformation. The use of the RSCM geothermometry is still acceptable for limited strain but should be used carefully for high quantity of strain.

This work aims to be published in Tectonophysics journal in the following weeks. Therefore, it has been adapted in order to prevent repetition.

Chapter IV – The role of non-seismic deformation on the carbonaceous material crystallinity enhance: Raman Spectroscopy and microstructural analyses of strain gradients from ancient accretionary complexes

IV.0 Abstract

Carbonaceous Material is a common component of metasediments in subduction and collision belts, mainly deriving from the diagenetic and then the metamorphic evolution of the organic matter initially present within the sediment. During the burial history, the crystallinity of carbonaceous material increases by rearrangement of the aromatic carbon sheets led by a heat stress. However, additional external factors could enhance the crystallinity such as the pressure, the fluid-interactions or the deformation. The effect of the last cited remains poorly studied and especially at low temperatures, from 200 to 360°C. Here we propose to explore the effect of the deformation during the carbonization stage along natural strain gradients at different scales, from millimetric to metric scale. Samples of different strain gradients elected from three ancient accretionary complexes have been analyzed using the Raman spectroscopy. Intensity ratio, a sensitive Raman parameter to strain, shows a significant enhance of the carbonaceous material crystallinity at all scales. Evolution is observable for low strain energy while the strain quantity and the CM crystallinity increase are correlated. These results bear major consequences of the strain influence on the carbonaceous material crystallinity and on the interpretation of the Raman Spectroscopy of Carbonaceous Material temperature obtain through the calibration in strained zones. In addition, they reveal the usefulness of the Raman spectroscopy as a new tool to evaluate the strain quantity.

IV.1 Introduction

The Raman Spectroscopy of Carbonaceous Material (RSCM) allows quantifying the degree of crystallinity of carbonaceous material (CM), which increases upon geological heating through the carbonization and graphitization processes. It is considered as a reliable indicator of metamorphic grade (Pasteris and Wopenka, 1991; Wada et al., 1994), the quantitative evolution of crystallinity of CM has been proposed as new geothermometers for a wide range of geological peak-temperature between 200 and 650°C (Beyssac et al., 2002; Kouketsu et al., 2014; Lahfid et al., 2010; Rahl et al., 2005). It is now widely used in metamorphic petrology as an innovative, quick and non-destructive method (Beaudoin et al., 2015; Clerc et al., 2015; Lanari et al., 2012). However, the fine understanding of carbonization and graphitization processes is limited, particularly concerning the loss of functional groups and the

formation of a lattice of graphene. The effect of deformation is often proposed to explain local anomaly of RSCM temperatures. Nevertheless, the effect of deformation remains poorly studied except for fast seismic deformation '. Indeed, the intensity ratio (i.e. R1 in Beyssac et al., 2002) has been used to detect evident CM crystallinity enhance or worsen from Black Fault Rocks (Ito et al., 2017; Ujiie et al., 2021) or on fault gouges and breccia (Furuichi et al., 2015; Kouketsu et al., 2017; Kuo et al., 2018). Unfortunately, this new application assumes that CM spectra reflect only the thermal record irrespectively of the potential impact of geological strain on CM crystallinity (Bonijoly et al., 1982a; Bustin et al., 1995; Ross and Bustin, 1990; Tagiri and Tsuboi, 1979). Besides, numerous questions remain unexplored such slow non-seismic deformation from the brittle deformation (*i.e.* brecciation) to the ductile deformation (*i.e.* mylonitization). Non-seismic deformation has also been explored in order to understand the effect on the CM crystallinity in high temperature grade. Preexistent results have shown the increase of the CM crystallinity using RSCM or Vitrinite Reflectance and HTREM in highly strained rocks. However, these results have been focused on the finale graphitization transformation at high temperatures through natural examples (Suchy et al., 1997) or slow creep experiments (Bonijoly et al., 1982a; Bustin et al., 1995; Ross et al., 1991a; Ross and Bustin, 1990). Ambiguous results have been obtained and complex scenarios have been proposed to explain the effect of deformation. Indeed, the strain effect is difficult to dissociate to the short-life frictional movements (Bustin, 1983a; Suchy et al., 1997) generating pulse of temperature. In addition, these experimental studies are difficult to compare to each other, because several experimental conditions differ like the confining pressure, that evolves from ambient pressure up to 1 GPa (Bustin et al., 1995), or temperatures that evolve from 300°C to HTT at 3000°C. However, the CM kinetics are highly dependent to the pressure, which has a direct effect on the activation energy needed (Nakamura et al., 2020). Finally, the effect of deformation on the CM crystallinity during the carbonization stage, from 200°C to 360°C, remains poorly studied while it represents the temperature range where deformation mechanisms and microstructures are most diversified and where the effect of deformation is the most complex (Nakamura et al., 2015). The RSCM method, widely accepted by the geoscience community, is a powerful tool but the strain effect, which may have an effect of the CM crystallinity, has to be better understood and precisely during this range of temperature where few other thermometers are available.

Here we present new insights on the effect of the deformation on the crystallinity of the poorly-organized CM during the carbonization and early graphitization stages along strain gradients from the millimeter scale up to the metric scale. Samples from the Shimanto Belt, the Kodiak Accretionary Complex and the Glarus Thrust area have been selected in order to characterize microstructures evolution, obtained from optical and electronic microscopy and from EBSD, along these strain gradients. In a second time, the CM crystallinity has been linked with the microstructure evolution. The CM crystallinity has been evaluated revealing the quantitative information on the lattice organization of the CM thanks to the Raman Spectroscopy and a new innovative high-resolution approach. Finally, we discuss in one hand the effect of the deformation of the CM crystallinity and the possible error deviation affixed to the thermometer calibration and, in another hand, the difference between the effects of the non-seismic deformation and the seismic deformation on the Raman signal evolution.

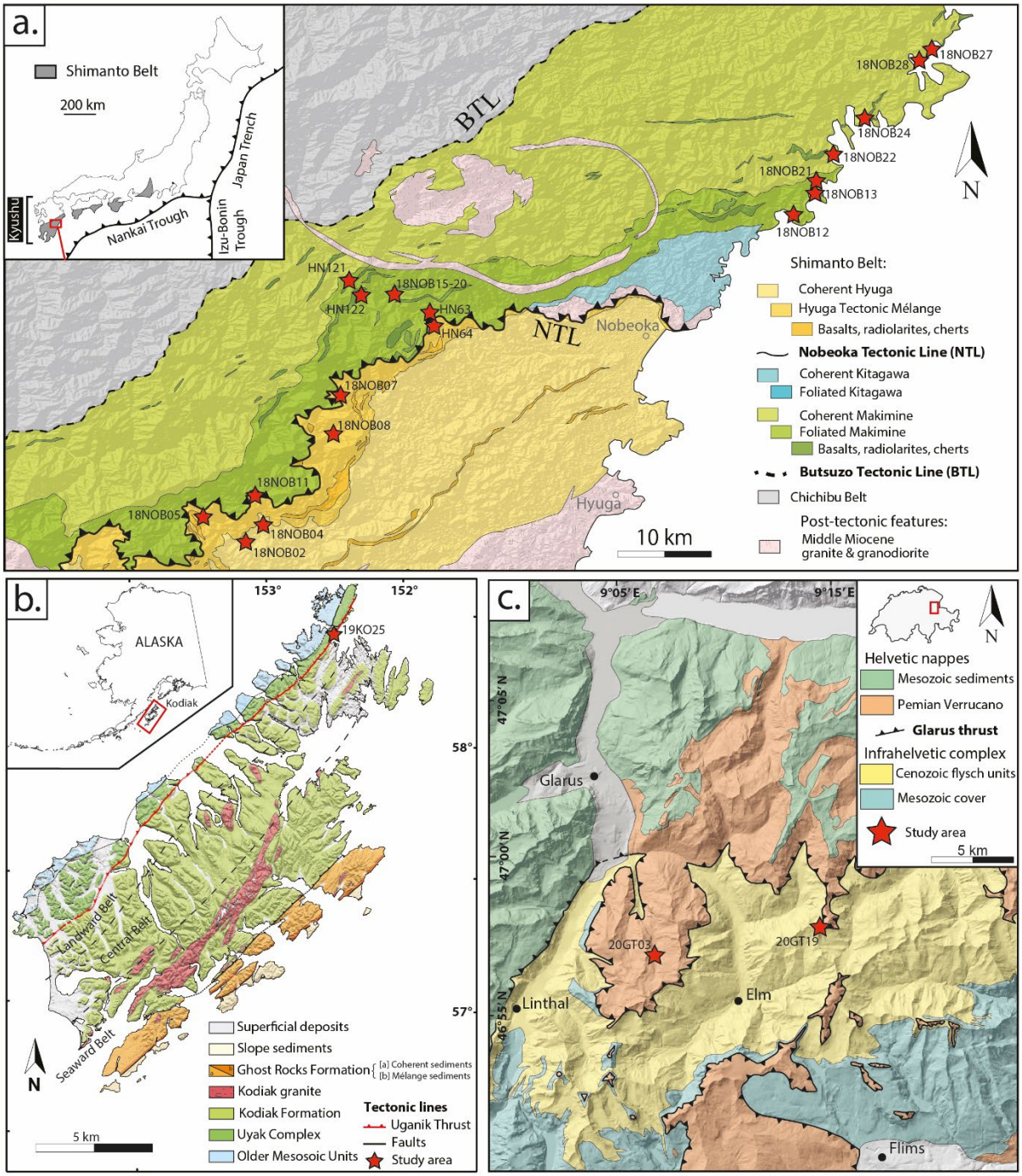

Figure IV.1: Geological maps of the three studied areas. ***a.*** *Geological map of the Shimanto Belt (Japan)* ***b.*** *Geological map of the Kodiak Accretionary Complex (Alaska, USA)* ***c.*** *Geological map of the Glarus Thrust area (Switzerland) modified from Akker et al. (2018) and Dielforder et al. (2016); Red stars localized the sampled outcrops or samples.*

IV.2 Geological setting and sampling strategy

IV.2.1 The Shimanto Belt accretionary complex

The Shimanto Belt accretionary complex (or the Shimanto Belt) is an exhumed subduction complex that runs over 800 km from Tokyo to Okinawa passing through Shikoku and Kyushu Islands. To the north, the Shimanto accretionary complex is separated from the Chichibu Belt by the Butsuzo Tectonic Line (Figure IV.1a), a main thrust zone (Saito et al., 1996). It extends southward off the coast line and is locally unconformably overlain by Neogene sediments of the Miyazaki group on the east that escaped significant burial (Charvet and Fabbri, 1987; Taira et al., 1988). The subduction complex is characterized by an accumulation of NW dipping coherent sedimentary units and tectonic mélanges, thrust bounded, from Cretaceous to the Tertiary that shows a southeastward younging and is parallel to the current Nankai trench. The Shimanto complex is divided into Cretaceous subbelt and Tertiary subbelt by a low dipping out-of-sequence fault, the Nobeoka Tectonic Line (Kondo et al., 2005; Mukoyoshi et al., 2009) in Kyushu and Aki Tectonic Line in Shikoku (Sakaguchi, 1999), marked by a significant jump in the metamorphic peak-conditions on the Kyushu Island (Raimbourg et al., 2014).

In Kyushu Island, two Cretaceous units and one Eocene-Oligocene unit are distinguished: Makimine unit, Kitagawa unit and Hyuga unit, respectively. Each unit is composed of coherent sediments, composed of an alternation of shale and sandstone, bounded with foliated tectonic mélanges (i.e. Coherent Hyuga and Hyuga mélange; Coherent Makimine and Makimine mélange). The latter is composed of exotic boudins of metasandstones and metabasalts wrapped in a shaly matrix more or less foliated. The Nobeoka Tectonic Line separates foliated Hyuga with foliated Kitagawa on the east and both coherent and foliated Hyuga with foliated Makimine on the west (Raimbourg et al., 2014) (Figure IV.1a). Burial RSCM temperatures obtain are 215 ± 20°C, 260°C ± 10°C, 320 ± 10°C and 330 to 360°C, respectively for Coherent Hyuga, Hyuga mélange, Kitagawa mélange and Makimine mélange (Palazzin et al., 2016; Raimbourg et al., 2014, 2017a).

IV.2.2 The Kodiak accretionary complex

The Kodiak Accretionary Complex (Figure IV.1b), southeast Alaska, is a Triassic to Tertiary NE-SW trending accretionary wedge. It is composed of five northwest dipping stacked sedimentary units, thrust-

bounded, and shows a straitgforward younging toward the southeast in the direction of the current Aleutian Trench (Byrne, 1982). The Kodiak Accretionary Complex has been described as a major décollement-faults zone dividing overscraped and overthrusted sediments which preserved early deformation of underthrusting during the accretion (Fisher and Byrne, 1987, 1992). The younger outcropping unit, Paleocene Ghost Rock Formation, in the southeast of the Kodiak Island, is mostly composed of mélange sediments characterized as products of décollement zone (Fisher and Byrne, 1987). Mélange zones are increasing toward the southeast (ie. the structural base) and are composed of big blocks of coherent, thinly bedded and massive sandstones, layers underlayered with sheared and disrupted black shale (Meneghini et al., 2010). The Kodiak Formation, which covers over 70% of the island, is a coherent unit mostly composed of late Maastrichian turbidite sediments. This unit presents folds and thrust structures and the development of the Greenschist facies (Sample and Fisher, 1986; Sample and Moore, 1987). A late deformation formed a large anticline which created relief in this unit. The Kodiak Formation is separated in three tectonic subbelts with respectively, from the southwest to the northwest, Lanward Belt, Central Belt and Seaward Belt (Figure IV.1b). The late Cretaceous Uyak Complex, on the northwest of the Kodiak Formation, is characterized by a tectonic mélange unit composed of sandstones, basalts and cherts clasts in an argillite matrix (Connelly, 1978). The contact between each unit is fault-bounded. The interface between the Uyak Complex and the Kodiak Formation is marked by the Uganik thrust, well exposed in the Big Waterfull Bay. In this place, the Kodiak Formation and Uyak Complex are both intensely sheared and veined. Fluid inclusions (Vrolijk et al., 1988) and RSCM (Rajic et al., in prep/personal com.) have used to evaluate depth and maximum temperature of the three described units at between 10 to 14km and temperatures ranging from 210°C to 330°C, respectively. RSCM shows temperature respectively, 215 ± 15°C and 270 ± 10°C, for the Ghost Rocks Formation and Uyak Complex. Temperatures calculated for the Kodiak Formation are 280 ± 15°C in the Landward Belt and up to 330°C ± 10°C for the Central and Seaward belts.

IV.2.3 The Infra-Helvetic Complex flysches

The Glarus Thrust is an Oligo-Miocene Out-Of-Sequence thrust in the eastern part of the Swiss Alps covering a surface of a 600km² in the Glaris Canton in the southeast of Zürich, Switzerland (Figure

IV.1c). This accident splits tectonic units into an Helvetic Complex above para-autochtonous units and the Infra-Helvetic Complex (Pfiffner, 1993, 1981). The Helvetic Complex, also called the Glarus Nappe Complex, is composed of a Permian volcanic sediment unit, the Verrucano, overlain by a concordant Triassic and Jurassic sediment units. The last discordantly overlies on the complex Infra-Helvetic Complex. This unit is composed of crystalline basement followed by Mesozoic carbonate units and Cenozoic flysch units, itself complexly composed of autochtonous flysches and imbricated flysches during the Pizol phase in early Oligocene (Akker et al., 2018; Burkhard et al., 1992; Pfiffner, 1977). The Infra-Helvetic flysch shows a gradual North to South thermal metamorphism from the anchizone to a low grade Greenschist (*i.e.* 200°C to 320°C) (Ebert et al., 2007; Lahfid et al., 2010; Rahn et al., 1995). This overlain complex was folded and imbricated during the Calanda phase before the thrusting of the Helvetic Complex (Pfiffner, 1977). The Glarus thrust represents a minimum of 30 km displacement to the north (Pfiffner, 1985). The thrusting began at the end of the Oligocene (30-35Ma) with an important ductile deformation at the metamorphic peak conditions (Lihou, 1996; Pfiffner, 1977). Offset of metamorphic boundaries has been described (Milnes and Pfiffner, 1977) in addition to Miocene K-Ar and $^{40}Ar/^{39}Ar$ ages on micas (Hunziker et al., 1986) that both indicate that the Glarus thrust was still in motion after the metamorphic peak until the early Miocene (*i.e.* 20-25Ma) during the Ruchi phase.

IV.2.4 Sampling strategy

The sampling strategy aims to answer different scientific questions (1) the effect of deformation on the crystallinity of CM, (2) the effect of the strain energy quantity and (3) an auxiliary question which is the jump of scale. For that, we proceeded to an imbricated sampling strategy where outcrop and mm-scale shear zones were observed. In Shimanto and in Kodiak, we selected samples directly along shear zone with the C-plane on this sample. Then we selected poorly deformed or undeformed samples in a preserved zone, severed as ‘references’. In the Glarus Thrust zone, the strain gradients were meter-thick so we selected samples at different distance from the thrust in order to have a continuous strain gradient.

For this study, we selected three sampling areas. The Shimanto Belt in Japan because the distributed deformation through a network of shear zones was perfect to lead to work. In order to rule out the local effect to a certain region, we decided to compare the results obtained in Shimanto with an analogue in

terms of thermal and tectonic history. Thanks to the same strategy applicated to the Kodiak Accretionary Complex samples, we were able to compare these results on a mm-scale and on outcrop-scale. In addition, we sampled the Glarus Thrust strain gradient. It corresponds to a meters-thick strain gradient, and permits us to sample a continuous gradient with a large amount of strain. Thanks to these three sampling areas, we could discuss about the effect of deformation on the crystallinity of CM, the effect of the strain energy quantity and the jump of scale effect.

Table IV.1: Outcrop locations and information from the Shimanto Belt, the Kodiak Accretionary Complex and the Glarus Thrust area

Accretionary Complex	Unit	Outcrop	Location		Samples	Scales
			Latitude	*Longitude*		
Shimanto Belt	Coherent Hyuga	18NOB02	32,386000	131,298639	3	Outcrop
		18NOB04	32,412639	131,320917	4	Outcrop
	Hyuga mélange	18NOB05	32,408333	131,256056	3	Outcrop
		18NOB07	32,521972	131,384222	2	Thin section
		18NOB08	32,490444	131,381472	2	Thin section
		18NOB11	32,427722	131,314694	-	Outcrop
		HN64	32,594419	131,462973	2	Thin section
	Foliated Makimine	18NOB12	32,699250	131,833972	1	Regional
		18NOB13	32,721083	131,855583	-	Outcrop
		18NOB15	32,612389	131,451000	3	Regional
		18NOB16	32,613358	131,451758	1	Regional
		18NOB19	32,61875	131,449917	2	Regional
		18NOB20	32,621389	131,450556	1	Regional
		18NOB21	32,731388	131,857889	1	Regional
		HN63	32,6029473	131,477571	1	Regional
		HN121	32,635283	131,400816	1	Regional
		HN122	32,622843	131,4162388	1	Regional
	Coherent Makimine	18NOB22	32,755194	131,876667	1	Thin section
		18NOB24	32,791278	131,906472	1	Regional
		18NOB27	32,862722	131,976083	1	Regional
		18NOB28	32,853111	131,970778	2	Regional
Kodiak Accretionary Complex	Kodiak Formation / Uyak Complex	19KO25	58,430472	-152,514833	4	Outcrop / Thin section
Glarus Thrust	Infra-helvetic Complex	20GT03	46,996830	9,091400	6	Outcrop / Thin section
		20GT19	46,954310	9,237210	6	Outcrop

IV.3 Zooming in from large-scale structures and microstructures

IV.3.1The Shimanto Belt accretionary complex

IV.3.1.1 Large-scale architecture

Three units have been sampled in the Shimanto Complex: the coherent Hyuga unit, the Hyuga mélange unit and the coherent Makimine unit; 'coherent' is referred to as turbiditic dominant units. Local peak-temperatures obtained for these units show a straightforward increase of the temperature conditions from 215 to 360°C further complicated by a ca. 60°C temperature jump across the NTL. It is noteworthy that this range of geological temperatures covers all the carbonization and the early graphitization stages and shows different structures. All outcrop locations and main information are given in Table IV.1.

The Coherent Hyuga unit is composed of mostly undeformed series of turbidite with alternation of shales with sandstone layers from 5 cm to meters thick. Two distinctive deformation structures have been observed. In one hand, when the outcrop is composed mainly of sandstones (18NOB02) the deformation is concentrated in shaly interlayers between two layers of sandstone. Shales are squeezed and show a cataclasite texture with angular clasts of sandstones wrapped by a dark shaly matrix (Figure IV.5a and 5b). In another hand, when the outcrop is mostly composed of shales with centimeters-thick sandstone layers, shear zones are observed (18NOB04). These shear zones are composed of a thin layer of gouge or cataclasite, thinner than 1 millimeter, and are partially recrystallized into quartz. Along these shear zones, crushed texture of shale with weakly elongated quartz are observed and the thicker sandstone layers are parallelized to the shear zones showing a top-to-the-SE kinematics. A similar shear-zone distribution is also present in the Makimine Coherent unit (Figure IV.14b). In the Coherent Hyuga unit the deformation is mostly brittle as we could expect for a low temperature.

The Hyuga mélange unit is composed of tectonic mélange including intensely recrystallized sandstones and basalt clasts of various yet generally modest sizes (*i.e.* mm to decimeter), sometimes boudinaged and wrapped in a shaly matrix poorly to finely foliated (Figure IV.6). According to Fukuchi et al. (2014) and based on relative XRD peak intensity, quartz is the main component of mélange (*i.e.* 60 to 80%) while the rest corresponds to phyllosilicates. The foliation is marked by chlorite or flattened clasts and shows a gentle and consistent 30-40° dip to the north (Raimbourg et al., 2014). The NW-SE lineation is

marked by the stretching of the quartz veins and the deformation is strongly non-coaxial as shown by metric shallow shear zones connected in an anastomosed network (Figure IV.6). This distributed deformation forms a typical C-S-C' like structure and sigmoids, both showing a Top-to-the-SE kinematics. In a closer view, same textures are observed with micrometric shear zones at the sample-scale (Palazzin et al., 2016). The deformation is mainly brittle but shows brittle-ductile transition along the network of shear zones.

The Cretaceous part of the Shimanto belt is subdivided into two sub-units: the coherent Makimine sub-unit lying structurally above the foliated Makimine sub-unit. The first cited is composed of an alternation of sandstone layers of variable thickness interbedded with thin layers of shales where the bedding is preserved (Figure IV.14b). In these shaly layers, the deformation is marked by a conspicuous lineation marked by chlorite, white mica and stretched quartz grains. Clasts, when present, show a clear preferential orientation indicating the direction of stretching. Most of the deformation is localized along ductile shear-bands mostly concentrated at the base of the sandstone layers (Figure IV.14b). In these ductile deformation zones, lenses of sandstone and basalt show asymmetric boudinage and sigmoidal deformation of the foliation planes, which indicate a top-to-the-SE kinematic (Raimbourg et al., 2014). Brittle deformation is also described in the large sandstone lenses, especially near to the boundary between the coherent and foliated units, marked by a normal fault network. Raimbourg et al. (2014) indicate that no evidence of chronology has been observed between the ductile and the brittle deformations.

The foliated Makimine sub-unit can be distinguished on the coast where it crops out spectacularly and on-land along the riverbanks. The unit corresponds to a richer-phyllitic lithology, compared with the coherent Makimine, where isoclinal folds and metamorphic foliation are developed (18NOB16). The distribution of the deformation structures, in contrast with the Hyuga mélange unit, shows evidences of intense vertical thinning. However, associated with this rather coaxial deformation, sets of small-scale shear zones are observed showing a low angle with the metamorphic foliation (Figure IV.14c). The particularity of these shear zones is the presence of top-to-the-NNW kinematic, only visible on this unit of the Shimanto Belt. The Top-to-the-SE kinematic is also described but never associated with the NNW

shear-bands (Fabbri et al., 1990; Raimbourg et al., 2014). Locally, the foliated Makimine is composed of tectonic mélanges with stretched and boudinaged clasts of basalts, sandstones and silts (Saito et al., 1996; Teraoka and Okumura, 1992) (18NOB13 and 18NOB21). Deformation is also localized through a network of shear zones, identical to the ones identified in the Hyuga mélange unit, forming metric-lenses and themselves crossing over by thin shear-bands until to the centimeter-scale. Sigmoids generated by the ductile shearing show a top-to-the-SE kinematic.

IV.3.1.2 Shimanto Belt microstructures

The Coherent Hyuga unit is affected by two main deformation structures both acquired in the brittle regime. The first one corresponds to squeezed shale in narrow shear-zones stuck between large sandstone lenses. The material is composed of few millimetric angular clasts of sandstone embedded in a shaly matrix near the main shear-plans, typically as cataclasite (Figure IV.5b). The second type of structure is observed in the shaly rich turbidites of the coherent Hyuga unit. It corresponds to shear-band where a clast-size diminution is observed associated with the acquisition of a clear preferred orientation parallel to the shear direction. Along the few shear-bands cutting across the turbidite layers a thin gouge or cataclasite is observed. The sheared-material is characterized by an intense reduction of the grain-size and the development of very thin truncated quartz ribbons. No precise texture can be distinguish in the matrix. These shear zones are partially recrystallized by quartz, which show orthogonal fractures.

The Hyuga mélange unit is characterized by a micro-scale foliation planes marked by fined grained phyllosilicates (clay and white micas) (Palazzin et al., 2016). Many quartz ribbons have been described and are composed of several elongated hundred micrometers length quartz crystals. These quartz ribbons show an undulose extinction associated with bulges described as a result of pressure solution (Palazzin et al., 2016). Shear-bands are thin, following the base of the quartz ribbons, and are marked by the clay and white mica crystal alignments (Figure IV.8a). In the shear-zones and the very close surrounding, the white mica crystals become the majority phase and a major shear-band is accompanied by tiny secondary shear-bands (Figure IV.8c). The network of shear zones is also observed at the thin section-scale and formed the typical S-C-C' like fabric. The deformation is marked by an intense grain-size reduction (e.g. quartz grain measured from 150µm to 10µm), apparition of new bulging and sub-grains,

respectively, around and inside the relict grains (Palazzin et al., 2016). The very fine material also shows a parallelization to the shear-direction and the development of local sigmoids inside the shear zones. EBSD analysis of the quartz ribbons has been done by Palazzin et al. (2016) and shows in the whole sample a strong Crystallographic Preferential Orientation (CPO) in the direction of the lineation and a Shape Preferential Orientation (SPO) is either parallel or perpendicular to the stretching lineation. In contrast, CPO in the shear zones shows a concentration almost perpendicular to the foliation and to the shear-zone boundaries. In the shear zones, EBSD illustrates the dynamic recrystallization leading to a grain-size reduction below 10 μm, promoting by the grain boundaries mobility.

The Coherent Makimine unit is defined by a preserved bedding crossed over by shear zones. Sheared materials are characterized by a fine blend of shale and clast of sandstones more or less stretched or boudinaged (Figure IV.13). As a major difference with the coherent Hyuga unit, sandstone clasts show a ductile deformation.

The Foliated Makimine unit appears either as phyllite rich sediment deformed co-axially or as tectonic mélange. Typical samples of the tectonic mélange sediment show a mélange texture, sharing almost identical micro-textures described for the Hyuga mélange unit with the difference that the quartz ribbons show more plastic deformation as expected with the increasing regional temperature (i.e. here ca. 330 to 360°C). The phyllite-rich layers of the foliated Makimine unit show the development of a metamorphic foliation and are characterized as a very thin alternation of phyllite-rich layers and extremely stretched quartz ribbons where a conspicuous stretching lineation is marked by white mica and chlorite (Raimbourg et al., 2014). Quartz veins are locally abundant and are often completely transposed to the foliation. Palazzin et al. (2016) described the quartz ribbons with the typical ‘core and mantle’ structure, with relict grains from 250 μm to 1 mm showing an undulose extinction and a subgrain domain and surrounding domains composed of 5-10 μm recrystallized grains elongated in the stretching direction. EBSD data obtained by Palazzin et al. (2016) in the quartz ribbons show lobate external rims of the quartz relicts, a weak CPO and an intense dynamic recrystallization triggered by bulging and subgrain rotation.

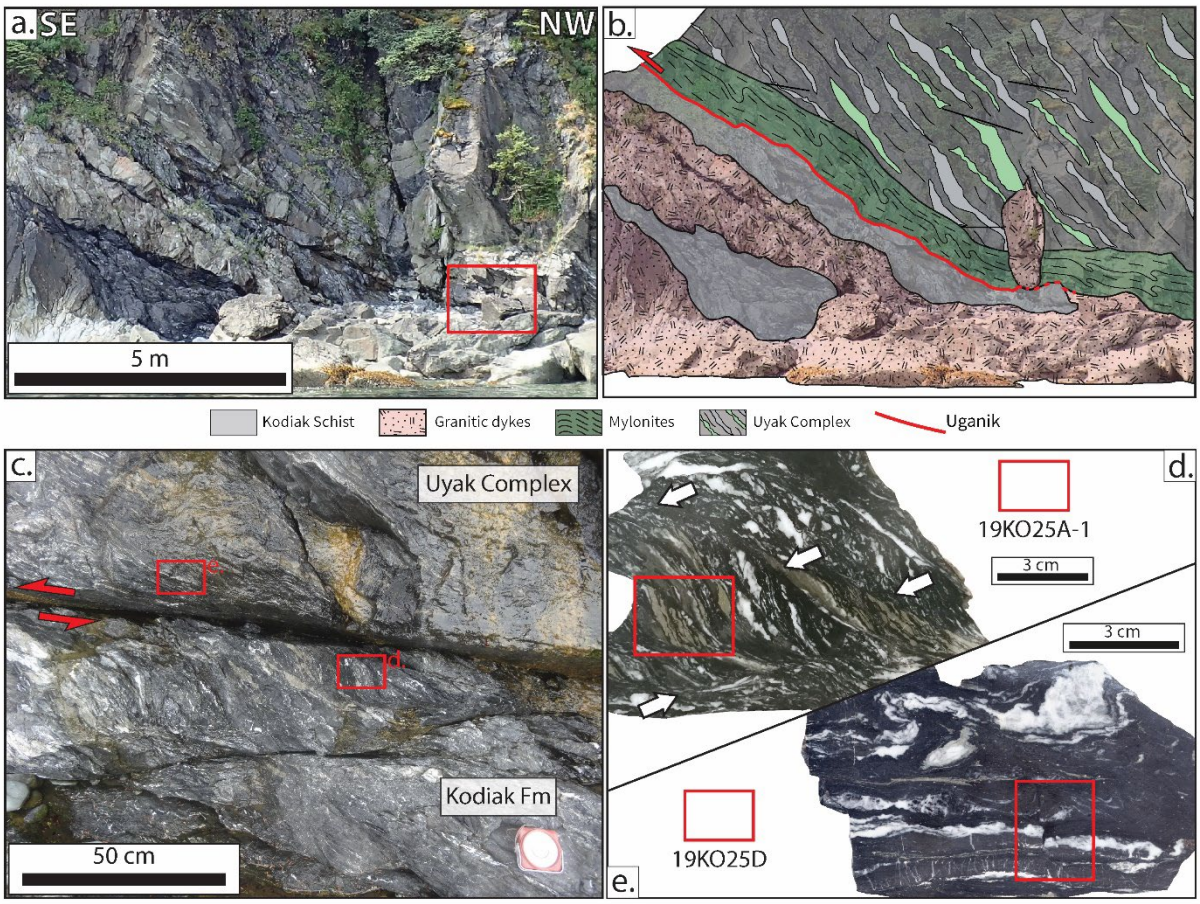

Figure IV.2: Structure of the Uganik Thrust in the Kodiak Accretionary Complex. ***a. and b.*** *Close up on the outcrop 19KO25 that show the structure of the Uganik Thrust separating the Kodiak Formation and the Uyak Complex and the description of the rocks observed on this outcrop.* ***c.*** *Zoom in the Uganik Thrust itself which show a damaged zone in the Kodiak Formation and a mylonitization of the Uyak Complex.* ***d.*** *Scan of the polished slate sampled in the damaged zone cross-cut by a network of shear-zones and in the mylonitized zone. Red rectangle localized sample 19KO25A-1 and 19KO25D analyzed.*

IV.3.2 The Kodiak accretionary complex

IV.3.2.1 Large-scale organization of the accretionary complex

The Kodiak Accretionary Complex samples analyzed in this study come from the Uganik thrust. The Uganik thrust is a tectonic contact separating the Kodiak Formation (footwall) and the Uyak Complex (hangingwall) (Figure IV.2a and 2b). The Kodiak Formation, more precisely the Landward Belt, is characterized by a damage zone in the footwall. This damage zone is observed as a mélange of chert lenses, quartz and calcite veins in a shaly matrix intensely overprinted by a dense and complex network of shear zones indicating a simple shear top-to-the-SE kinematic (Figure IV.2c). Clasts of chert and shared veins show elongated and boudinaged shapes in the narrow space between two shear zones while these clasts show an angular shapes when the space between two shear-bands becomes wider (Figure

IV.2d). When the distance with the thrust increases, the density of veins and shear-bands decreases and the damage zone is replaced by a coherent turbidite. The hangingwall on the NW-block, the Uyak Complex, is characterized to a 1 to 1.5 meter-thick mylonite with asymmetric folds indicating a top-to-the-SE kinematic identical to the footwall (Figure IV.2c). Further on the NW, typical tectonic mélange with block-in-matrix texture is observed and composed of chert and sandstone clasts.

IV.3.2.2 Kodiak microstructures

Samples analyzed in this study have been selected along the Uganik thrust and its vicinity in order to make a comparison with the deformed zones (Figure IV.2d). One in the damaged zone (19KO25A-1) and two poorly deformed local references selected at tenth of meters below the deformation zone. Samples used as references show very basic features of black shale layers and appear devoid of prominent deformation structure.

The sample from the damaged zone in the Kodiak Formation footwall (Figure IV.2d) is composed of quartz, albite and greenish clasts in a shaly black matrix crossed over by a network of mm-shear zones. Poly-aggregates of sandstone are intensely recrystallized. They show plastic stretching, boudinage with irregular contour and are traversed by a dense array of calcite veins (Figure IV.3b). These aggregates are composed of large quartz grains from 200µm up to 1mm that show undulose extinction. Irregular grain boundaries are observed with lobate contact and evidence of bulging (BLG). In the center of large quartz grains, sub-grains are observed and sometimes new recrystallized grains by sub-grain rotation (SGR) are visible. Greenish clasts, mostly composed of chlorite, show a softer behavior with boudinage and stretched shape with more regular contour. The matrix is mainly composed of chlorite and white micas that marked the main foliation. In the shear-zone, the shear foliation is carried by white micas and chlorite, in narrow zones up to 100µm, parallel to the stretching direction (Figure IV.3a).

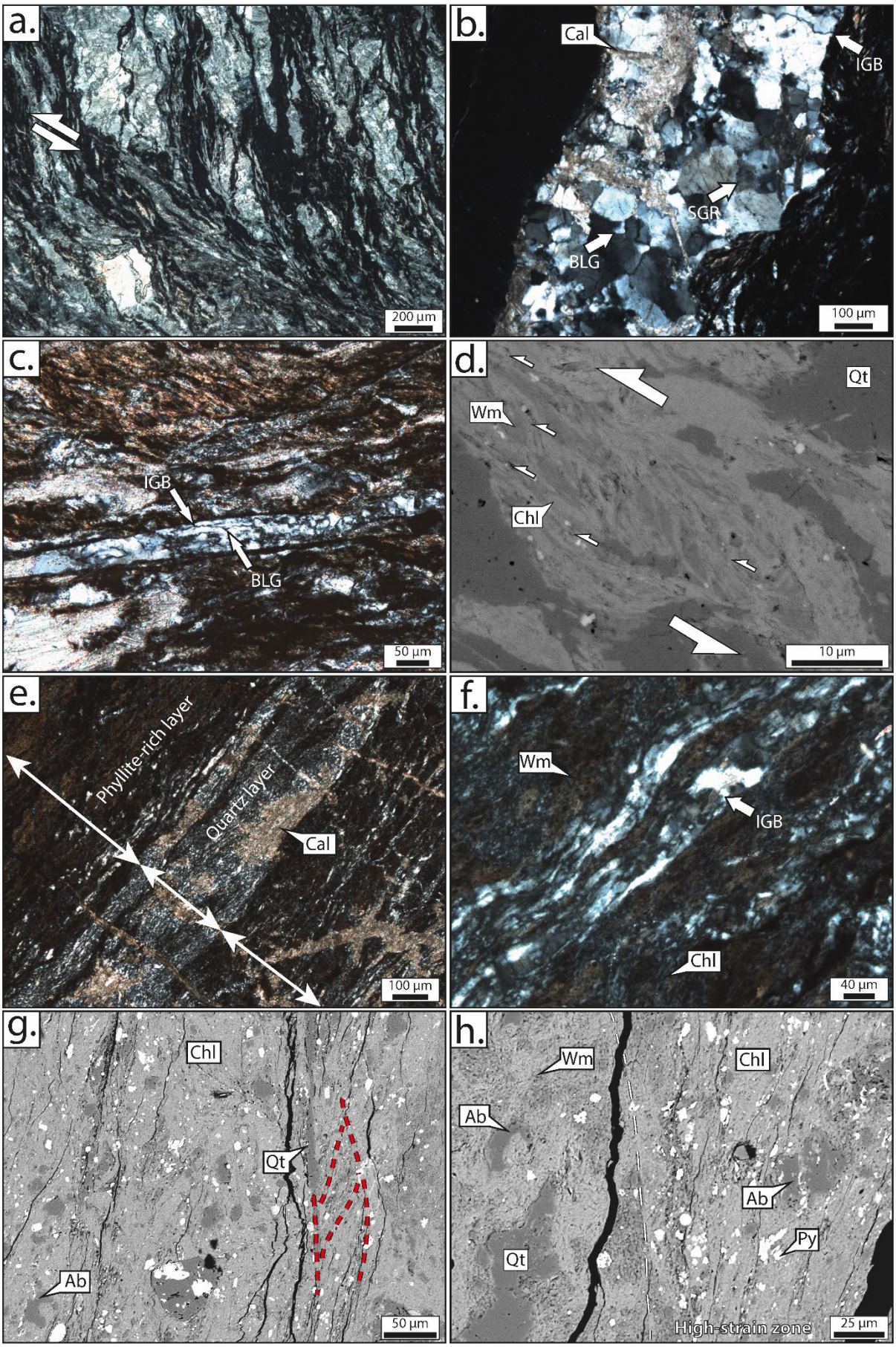
a.
200 µm
b.
Cal
IGB
SGR
BLG
100 µm
c.
IGB
BLG
50 µm
d.
Qt
Wm
Chl
10 µm
e.
Phyllite-rich layer
Quartz layer
Cal
100 µm
f.
Wm
IGB
Chl
40 µm
g.
Chl
Qt
Ab
50 µm
h.
Wm
Chl
Ab
Ab
Py
Qt
High-strain zone
25 µm

Figure IV.3: Microstructures of the sample 19KO25A-1 ***a. to d.*** *and 19KO25D* ***e. to h.*** *from the Uganik Thrust outcrop.* ***a.*** *Shear-band marked by white micas, chlorite and elongated quartz.* ***b.*** *Poly-aggregates of quartz from the matrix, partially recrystallized, that show large grains with internal deformation with irregular grain boundary (IGB) and recrystallization by bulging (BLG) and sub-grain rotation (SGR).* ***c.*** *Elongated quartz grain from the shear-zone that shows an intense grain size reduction with recrystallization by BLG and parent grains with undulose extinction and IGB.* ***d.*** *Imbrication of white micas and chlorite in the shear-zone showing a C-S structures separate by a multitude of shear-bands in the main shear-zone.* ***e.*** *Alternation of phyllite-rich and quartz-rich defining the layering of the sample 19KO25D.* ***f.*** *Quartz ribbons elongated presenting IGB and undulose extinction associated with chlorite and white mica.* ***g.*** *S-C structures, elongated quartz and corroded albite in a chlorite matrix in the high-strain zone.* ***h.*** *High-strain zone and surrounding limit showing the evolution mineralogy and microstructures.*

Moreover, white mica and chlorite shear zones show a complex imbrication and the formation of micrometric sigmoids crosscut by several micrometers shear-bands (Figure IV.3d) showing a C-S deformation structure. Albite clasts that show eroded shape in the main foliation zone tend to disappear in the shear zones. Quartz ribbons within the shear zones are elongated and composed of two families of quartz that have experienced an important grain-size reduction (Figure IV.3c). Elongated 50 µm grains with undulose extinction and irregular grain boundaries (IGB) have been identified as parent grains and recrystallized grain with a sharp extinction and linear contact. These recrystallized quartzs present a Shape Preferential Orientation (SPO) parallel to the stretched direction and a grain-size around 10µm. The process that conducts to the recrystallization seems to be a bulging process (Figure IV.3c). Amount of calcite veins and more generally calcite crystallization seem to be correlated with the amount of finite strain and the distance with the core of the deformed zones.

The mylonitized sample from the Uyak Complex is composed of a fine alternation of phyllite layers with sandstone layers (Figure IV.3e). This alternation appears lately cut (or overprinted) by calcite veins and normal faults. The phyllite layers are composed of white micas often replaced by chlorite (Figure IV.3f). Sandstone layers are composed of poly-aggregates of angular quartz and plagioclases where the clast sizes measured varying around 50 to 100µm in the preserved zone from the deformation. In the more sheared zones, an important grain-size reduction is observed with grain size as small as 10µm. On the rim of the ribbons, grains show a clear preferred linear orientation and a SPO parallel to the stretching direction. Hundreds of micrometric ribbons have also been observed and show undulose extinction (Figure IV.3f). In addition, calcite veins are sometimes parallel to the main foliation. Sheared calcite veins indicate a clear top-to-the-SE kinematic consistent with the overall asymmetry of the deformation.

In addition, the sample shows a high-strain zone marked by a thin black layer (Figure IV.11a) well identifiable by CL (Figure IV.11b and 11c). This layer is composed mainly of recrystallized and oriented chlorite and a very low amount of quartz, when observed, are intensely stretched (Figure IV.3g). Albite clasts are almost absent from the high-strain zone or present a corroded shape. S-C like structures are sometimes observed in the high-strain zone (Figure IV.3g).The phyllosilicate matrix of this high-strain zone is composed of scattered Fe-rich and Ti-rich sulfides and oxides often elongated and characterized by a low porositywith respect to the lower strain zone cited above (Figure IV.3g and 3h)

IV.3.3 The Glarus Thrust

IV.3.3.1 Large-scale structure of the Glarus Thrust

The Glarus Thrust consists in a pluri-kilometric thrust that separates the Helvetic Nappes from the Infrahelvetic complex. The concentration of this displacement is characterized by a meters-thick strain gradient, in the flysch of the Infrahlevetic complex, with the development of an intense foliation and mylonitization (Figure IV.7). This thrust is characterized by an asymmetric mylonitic foliation almost absent after 5 to 10 meters below the thrust and still present after tens of meter in the hanging-wall in the Verrucano unit (Badertscher and Burkhard, 2000; Schmid, 1975). The thrust is marked by a 20cm to 5 meter-thick (in rare case) strongly deformed rocks often characterized as calc-mylonites. These mylonites are composed of a complex imbrication of para-autochthonous carbonates and flysch from the Infra-Helvetic Complex (Badertscher and Burkhard, 2000). This layer of calc-mylonite shows a large boudinage deformation in addition to the mylonitization and lobate contact with the underneath flysch (Figure IV.7). The deformation is very important in the last centimeters of the flysch in contact with the calc-mylonite (Figure IV.7 closer view). A fine mylonite composed of a thin alternation of carbonates and flysch layer is observed. Further above the contact, a consistent foliation is observed in the flysch and in the zone 1 - 2 meters away from this contact, moreover, this foliation is predominant without any influence of the thrusting. In addition, rare auxiliary shear-bands are observed in the flysch, in the thrust vicinity. Sometimes, a very fine gouge has been described in sharp shear zones, called ‘septum’, and has been interpreted as late movement of the Glarus Thrust (Schmid, 1975). In the sampled outcrop (20GT19), at the Foostock, this gouge has not been observed. To finish, internal strain gradients have

been described in the flysch units far from the main tectonic contact based on the concentration of veins (Akker et al., 2018) and on subordinate faults (20GT03).

IV.3.3.2 The Glarus Thrust micro-structures

In the Glarus Thrust area, a sampling profile, composed of 6 samples, has been collected in the Foostock zone (Herwegh et al., 2008). This profile corresponds to a 6 meters thick sampling vertical profile from the flysch unit until to the contact between the flysch and the intensely deformed calc-mylonite (Figure IV.7) with an increasing finite strain. Along this profile the composition between the shale and the carbonate clasts evolves, and seems to control the behavior of the rock. The sample selected at 6 meter from the contact (20GT19F) show a regular alternation of shale and carbonate layer that do not show prominent deformation features. The two next samples selected at 2 and 1 meter below from the contact (20GT19E and 20GT19D) show a more complex texture with well observable micro folds in the carbonate layers. The sample selected at 15 centimeters from the contact (20GT19C) is a carbonate rich-sample that shows isoclinal folds. In the zone richer in shale, we can distinguish an alternation with stretched carbonate clasts cut by a locally dense array of perpendicular calcite veins. The two last samples, selected at 2 centimeters and within the contact zone (20GT19B and 20GT19A), correspond to intensely deformed mylonite. They are, rich-shale samples, composed of a fine alternation between calcite bands and an association of chlorite and white micas intensely stretched. Calcite veins are also deformed by the mylonitization deformation and show an important elongation in the stretching direction and show undulose extinction. These calcite veins were analyzed using the EBSD to determine the deformation processes (Figure IV.4a and 4d). Misorientation maps show large crystals of calcite with an important strain energy and subgrains formation (Figure IV.4c and 4f). In addition, rims of parent grains are irregular and show bulges with an important misorientation, leading to the idea of recrystallization by bulging. A higher misorientation and a higher amount of sub grains have been noticed in the sample selected within the contact zone (*i.e.* 20GT19A), which also shows more recrystallization (Figure IV.4c and 4f). Additionally, little recrystallized grains on the rim of the veins and between two large parent grains are observed with a low intern misorientation. New grains and misorientation show a trend of 45° with the stretching lineation in the core of the veins while on the rim

grains they show a trend parallel to the stretching direction. This organization reminds C-S like structure observed in shear zones at all scales. Pole figures (Figure IV.4b and 4e) indicate a c-axis cluster perpendicular to the foliation for 20GT19B and show a low angle with the perpendicular to the foliation for 20GT19A. J index and M index calculated, respectively at 2.31/0.10 and 2.18/0.08, for the 20GT19A and 20GT19B show a weak CPO slightly higher for the closer sample to the contact.

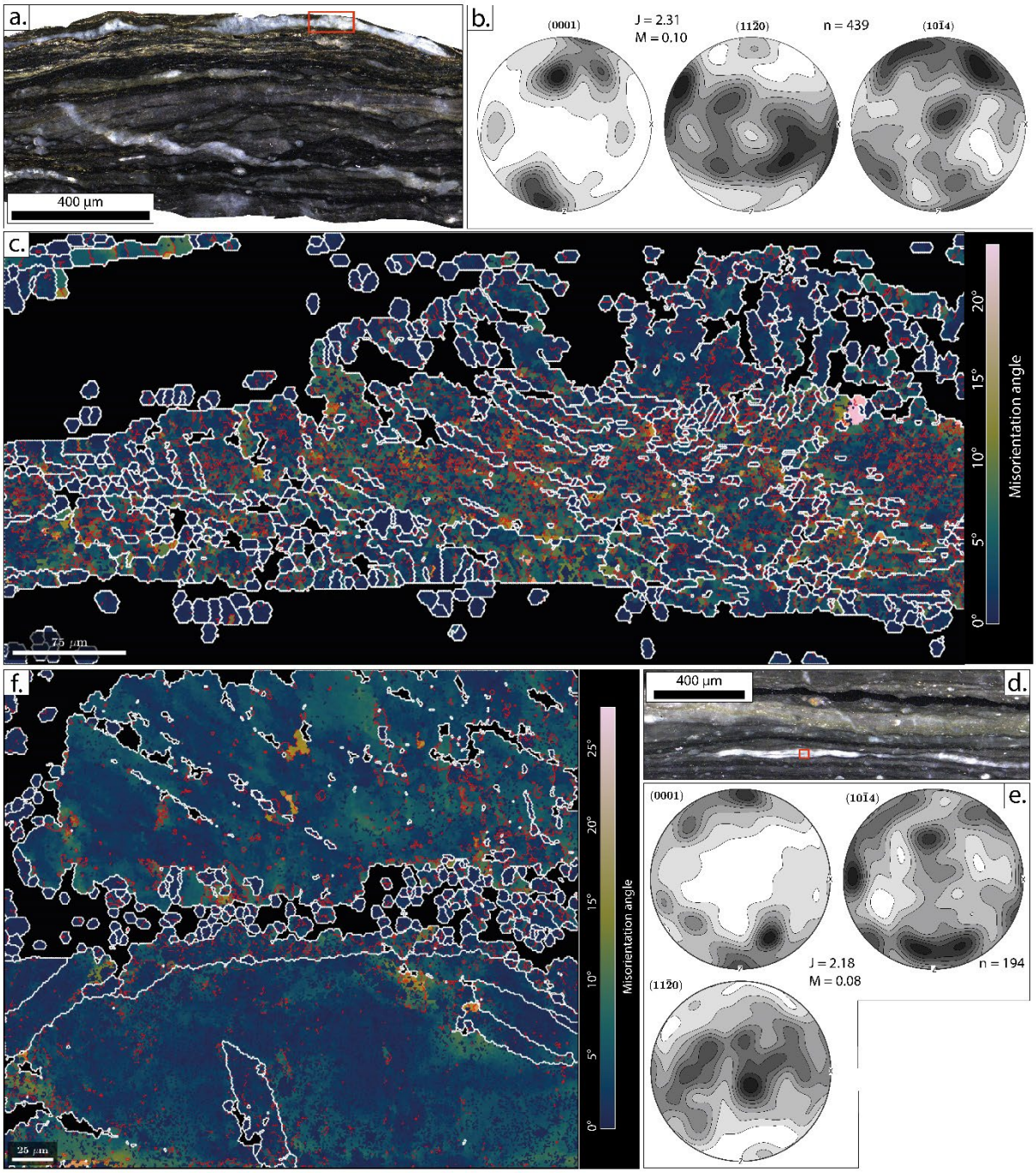

Figure IV.4: EBSD data obtain on the sample 20GT19A ***a. to c.*** *and 20GT19B* ***d. to f.****.* ***a. and d.*** *Scan of the samples and location of the EBSD mapping area.* ***b. and e.*** *Lower hemisphere pole figures of the c-axis, a-axis and r-axis, and indicative J and M index.* ***c. and f.*** *Internal misorientation maps with sub-grains limits of the ZX plan (ie. Z in West and X in North).*

For the subordinate internal strain gradient (20GT03), samples show an evolution from an alternation of shale and carbonate layers, which are progressively folded and near the contact develop an intense crenulation cut by the foliation (Figure IV.10a). The crenulation zone is marked by a majority of chlorite associated with white micas (Figure IV.10b). In the parallelized layer that crosscut this crenulation, the foliation is carried by white micas and chlorite. In opposition with the crenulation zone, the foliated zone is composed mainly of white mica and concentrates oxides and sulfides (Figure IV.10c). A grain-size reduction of the phyllosilicates is also observed in the foliated zone (Figure IV.10c). The micro-structures of the sample in contact with the main slipping (shear) zone is characterized by intensely folded and stretched clasts of carbonates in a shaly matrix with a grain-size reduction in comparison with previous samples of the strain gradient (Figure IV.12b). A thin comminuted black layer of few hundreds of microns composed of shale and micrometric sub-angular clasts characterizes the core of the deformed zone (Figure IV.12a and 12c). This sheared layer is characterized by a higher concentration of micro- scale clasts experienced an intense grain-size reduction and mixed with shaly phases, and these clasts are embedded also by smashed calcite clasts of tens of microns (Figure IV.12a).

IV.4 RSCM results

A very detailed Raman Spectroscopy of Carbonaceous Material (RSCM) approach has been applied to analyze the potential effects of the deformation on the crystallinity of carbonaceous material at different scales: decametric outcrop-scale strain gradients based a series of samples and at mm to µm-scale strain gradients at the scale of a single thin-section. The results are presented in the next sections.

IV.4.1 Outcrop-scale shear zones

We selected three outcrops, two from the Shimanto Belt and one from the Glarus thrust, in order to examine the effect of deformation on the crystallinity of carbonaceous materials at different regional temperatures from 200 to 280°C. To do that, we sampled rocks in deformed zone and from poorly or undeformed zone through strain gradients until the core of the deformed zone.

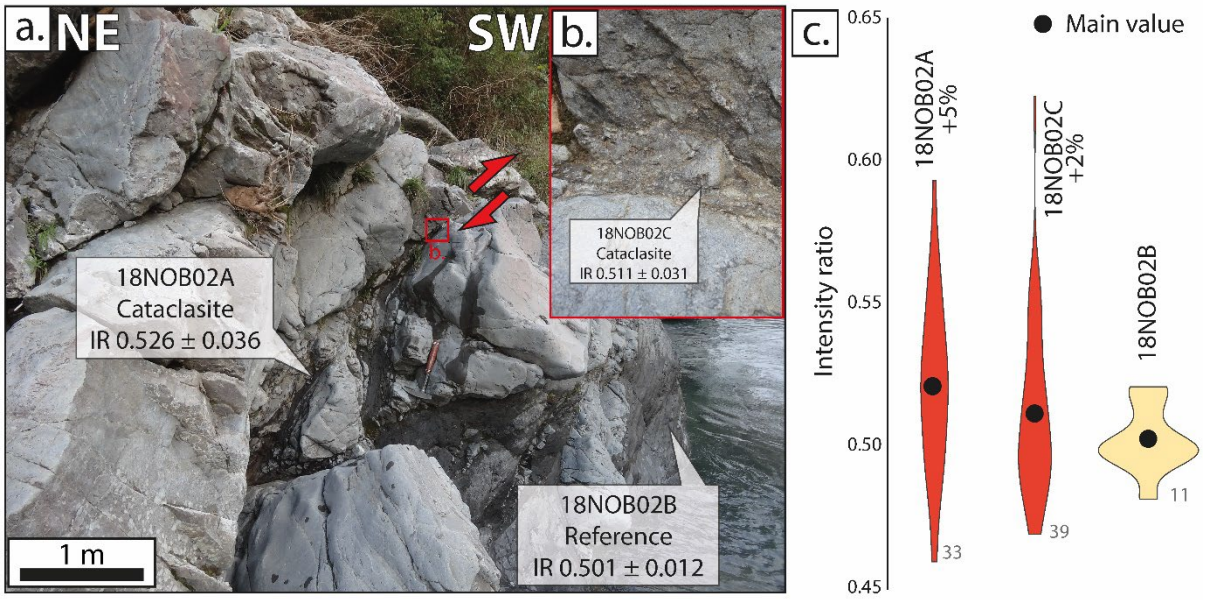

Figure IV.5: 18NOB02 outcrop from the Hyuga Coherent unit of the Shimanto Belt. ***a.*** *Structure of the outcrop with large lenses of sandstones elongated along shear-zone located in shaly zone.* ***b.*** *Zoom in the shear-zone where the material is composed of angular quartz grain in a squeezed shaly matrix.* ***c.*** *Intensity ratio measurements from the three analyzed samples.*

The first outcrop comes from the Hyuga Coherent unit (i.e. 200°C regional temperature). This outcrop is mainly composed of sandstone layers separated by thin shale layers. Shear bands crosscut these layers where the deformation is mainly characterized by brittle deformation through cataclasite composed of angular sandstone clasts embedded in a shaly matrix (Figure IV.5b). In the poorly deformed zone, used as reference, the intensity ratio measured is 0.501 ± 0.012. RSCM intensity ratio shows values of 0.511

± 0.031 and 0.526 ± 0.036 in these deformed zones, being respectively an increase of 2% and 5% (Figure IV.5). A higher dispersion of values in the deformed zones is also noticed.

The second selected outcrop is composed of tectonic mélange sediments, from the Hyuga mélange unit (*ie.* 260°C), that shows a network of metric ductile shear zones. Samples have been selected along these shear-bands and in a non-foliated zone. Intensity ratio measured in the sheared-zone is included between 0.528 ± 0.028 and 0.571 ± 0.048 with an important heterogeneity and dispersion of values (i.e. regarding to the standard deviation). In the poorly deformed zone the intensity ratio is 0.505 ± 0.015. This evolution between the deformed and undeformed zones represents an increase between 5 to 13% with a twice increase of dispersion (Figure IV.6).

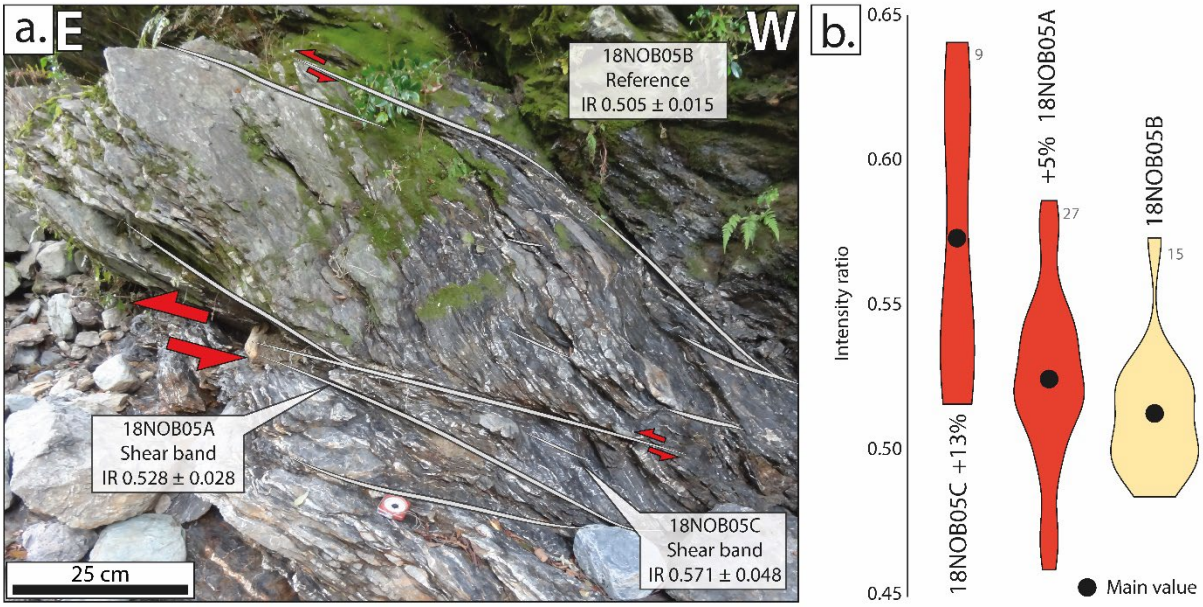

Figure IV.6: 18NOB05 outcrop from the Hyuga mélange unit of the Shimanto Belt. ***a.*** *Structure of the outcrop cross-cut by an anastomosed network of shear-zones with top-to-the-SE and imbricated shear-zone at different scales.* ***b.*** *Intensity ratio measurements from the three analyzed samples.*

The last outcrop selected is the Foostock in the Glarus thrust area. In this specific location, the regional temperature is around 280°C, close to the ones measured for the previous outcrop in the Hyuga tectonic mélange unit. By comparison with the last outcrop, the Glarus Thrust in this area shows an important strain with a deca-kilometric displacement concentrated in a metric strain gradient. Six samples have been selected along a profile from a poorly foliated zone until to the contact between the footwall and the hangingwall, respectively at 6 meters, 2 meters, 1 meters, 15 centimeters, 2 centimeters and on the

contact (Figure IV.7). Along this sampling profile, intensity ratio shows a weak increase from 1 to 5% until to the last centimeters with the dispersion close to the ones obtained in the reference sample. In the two last centimeters, where mylonitization defined the deformation, we can distinguish an important increase of the intensity ratio of 39% at 2 centimeters from the contact and of 52% on the contact (Figure IV.7). These values show a very high heterogeneity reaching up to +200% on the contact with respect to the results obtained at 6 meters to the contact.

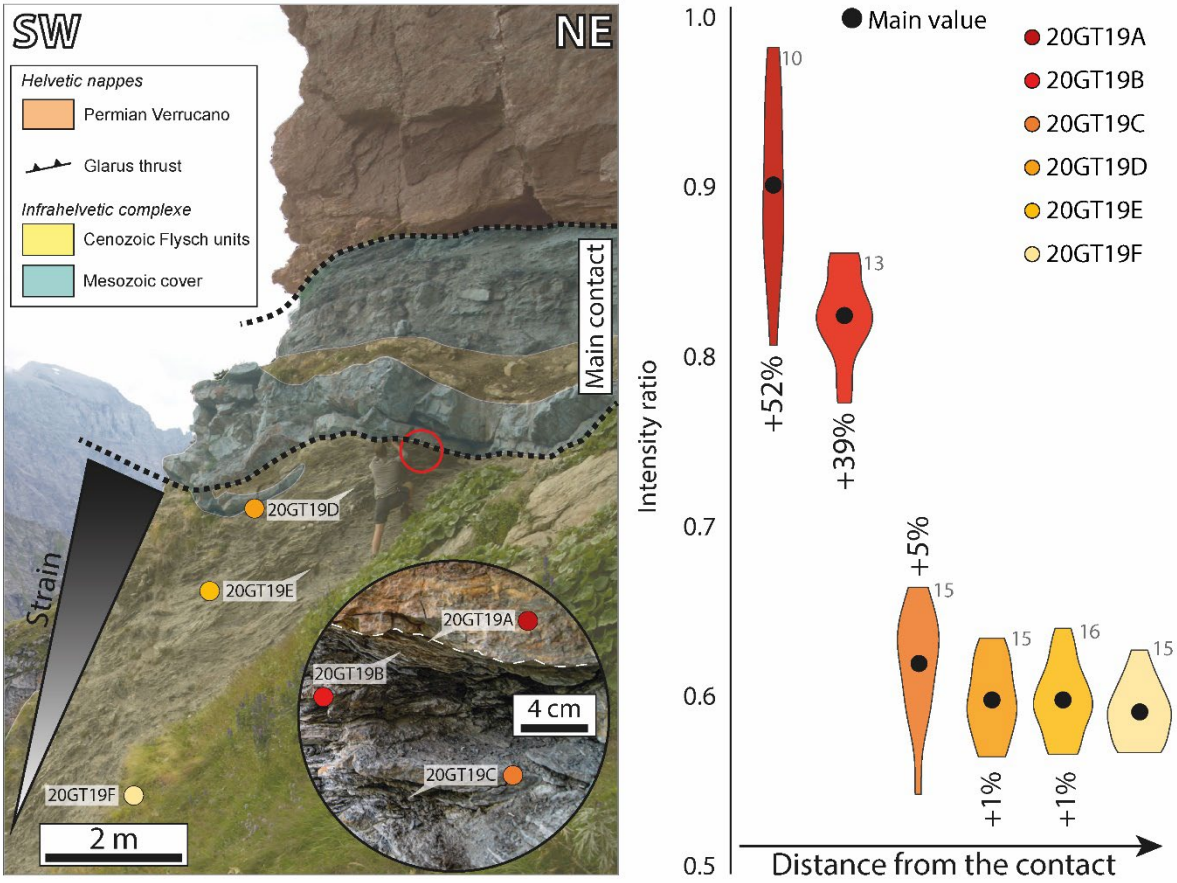

Figure IV.7: 20GT19 outcrop from the Foostock in the Glarus Thrust area. ***a.*** *Structure of the sampling gradient in the flysch above the main contact of the Glarus Thrust and location of the analyzed samples. Zoom in the contact with mylonitized material just above the contact.* ***b.*** *Intensity ratio measurements from the 6 samples of the gradient.*

IV.4.2 mm-scale shear zones

In this section, we focused in the effect of the deformation at the smaller scale. In fact, at the millimeter-scale, we can distinguish in our samples thin shear-zone. Thanks to a new high-resolution method using the RSCM we can trace the evolution of the intensity ratio through these sheared structures with a micrometric step between each analyzed spot.

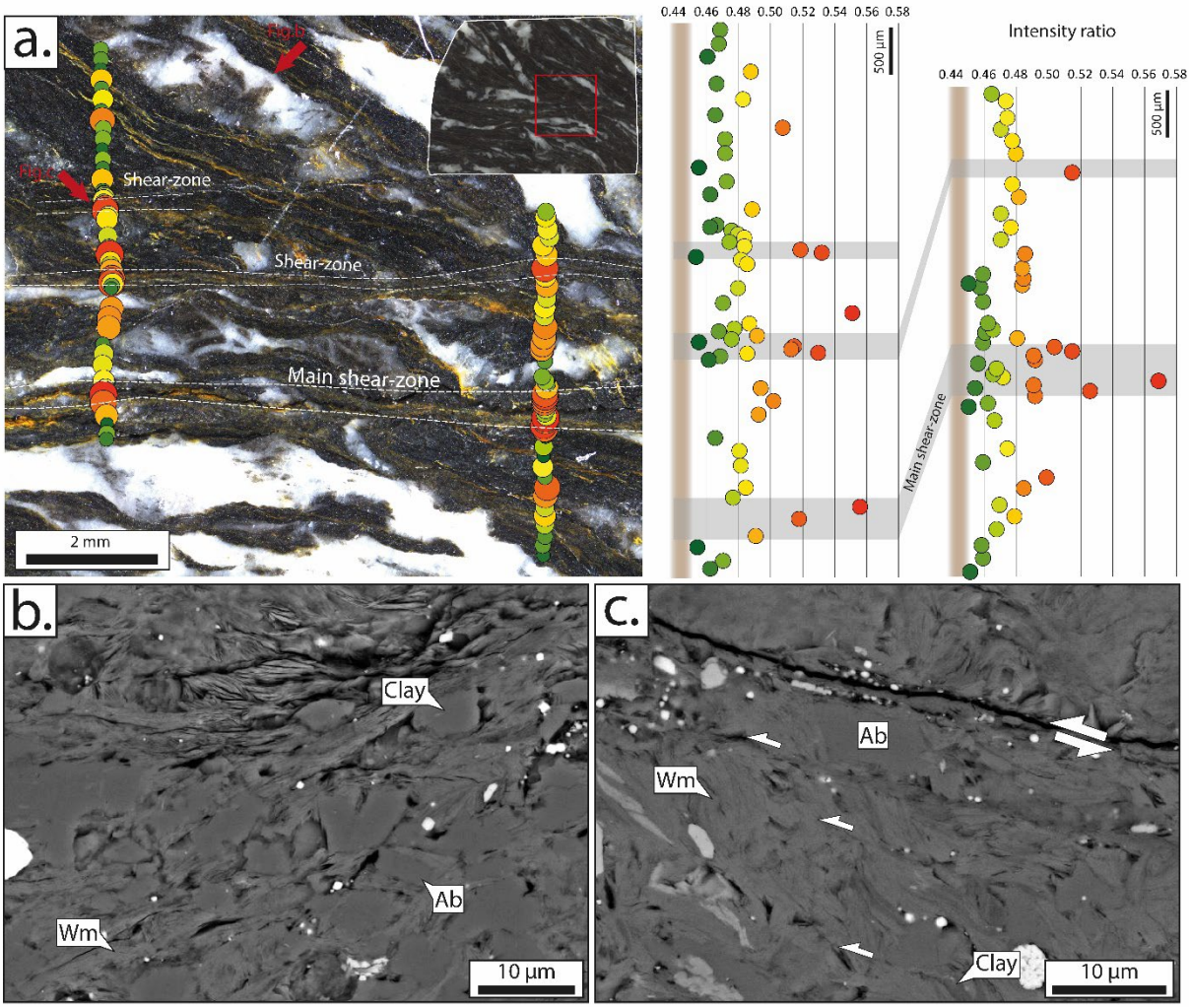

Figure IV.8: Raman profiles along shear-zones of the sample HN64 (Shimanto Belt) and SEM images of the micro-structures. ***a.*** *Raman intensity ratio profiles along shear-zones and respective diagrams. Grey areas represent the sheared-zone and brown rectangle the intensity ratio values measured for the references.* ***b.*** *Clay and white micas marking the main foliation of the host-rock.* ***b.*** *Majority of white micas and intercalated clays showing an alternation of shear-bands in the deformed zone.*

Three samples have been selected to study this evolution, one from each of three studied zones presented above. For a sake of comparison, these samples (Figure IV. 8 to 10) come from zones where the regional temperature is approximatively identical, between 260 and 270°C. These three sheared samples are characterized by the same type of microstructures, hundredth micrometers ductile shear-zone crosscutting the main foliation where the material is parallel to the shear direction. The sample from the Glarus Thrust (Figure IV.10) is a little bit different because a parallelized layer that crosscuts a crenulation characterizes the deformed zone. Due to the narrow scale of the shear zones, it is difficult to distinguish a clear evolution along the strain gradient that is why we decided to separate these samples in two zones: the deformed zone (grey colored rectangles in figures) and the less deformed zones as the

host-rock. Each of these three samples shows the same evolution with an increase, at different intensity, of the intensity ratio in the deformed zone of certain points.

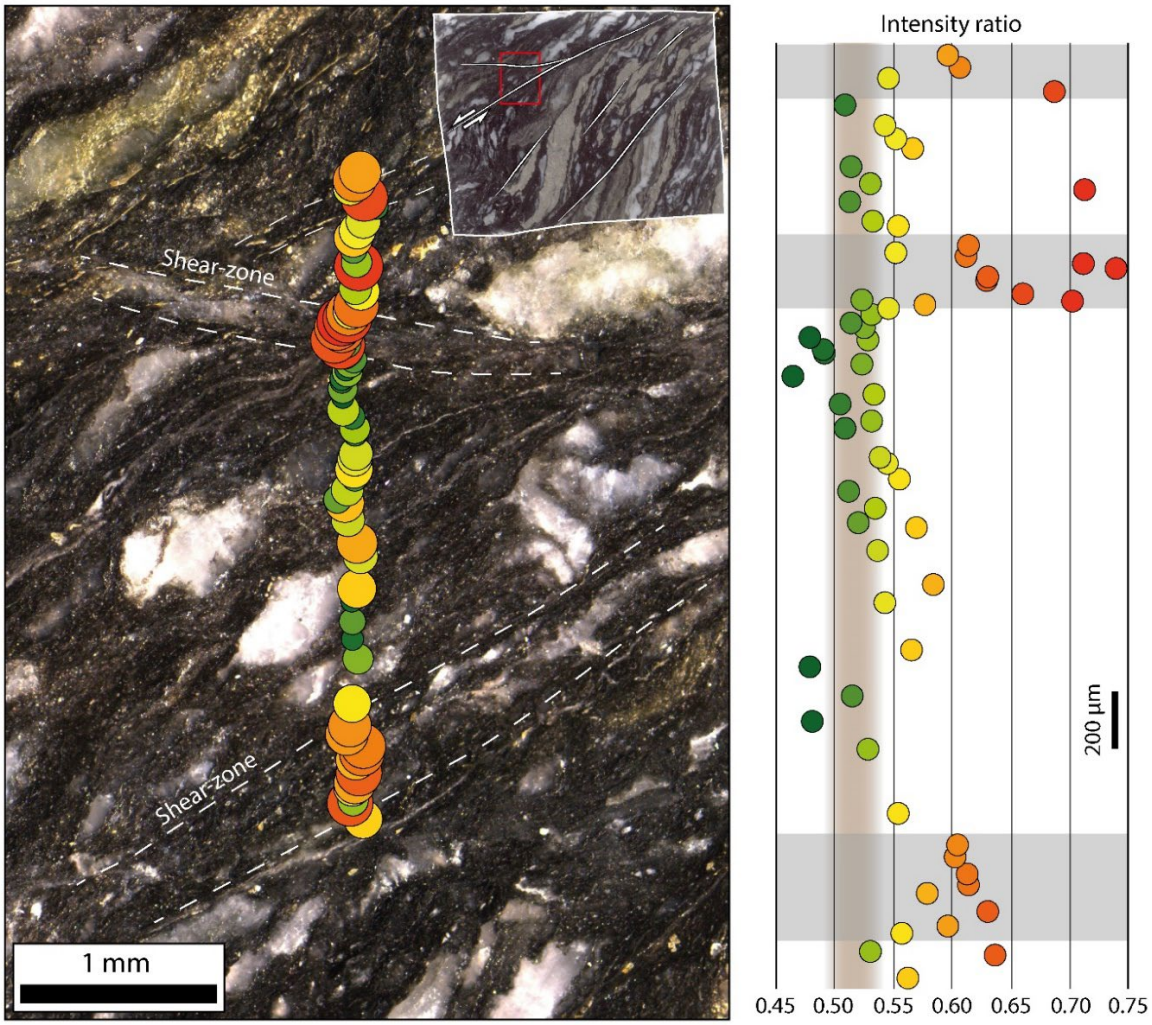

Figure IV.9: Raman profiles along shear-zones of the sample 19KO25A-1 (Kodiak Accretionary Complex) and associated intensity ratio diagrams. Grey areas represent the sheared-zone and brown rectangle the intensity ratio values measured for the references.

Values obtained, respectively from the samples from the Shimanto, the Kodiak Accretionary Complex and the Glarus Thrust, range from 0.46 to 0.57, from 0.53 to 0.75 and from 0.57 to 0.66, (Figures IV. 8 to 10). Not all the measurements show the same evolution and a large dispersion of the values is observed from the intensity ration measured in the host-rock to +50% of increasing (0.54 to 0.75) in the highest cases in the Kodiak Accretionary Complex sample (Figure IV.9) when the maximum of evolution is +23% (0.46 to 0.57) in the Hyuga mélange sample (Figure IV.8a). Moreover, in the Hyuga mélange sample (Figure IV.8a and 8c), we can distinguish two thicknesses of shear zones without distinction on

the quantity of strain which is difficult to estimate. Increase of the intensity ratio in both deformed zones is quasi-identical and results are similar. In addition, higher intensity ratios have been measured in the surrounding of shear zones in comparison with the host-rock on each sample. These weak increases, from 4% to 5%, are more constant and a low disparity of values is observed.

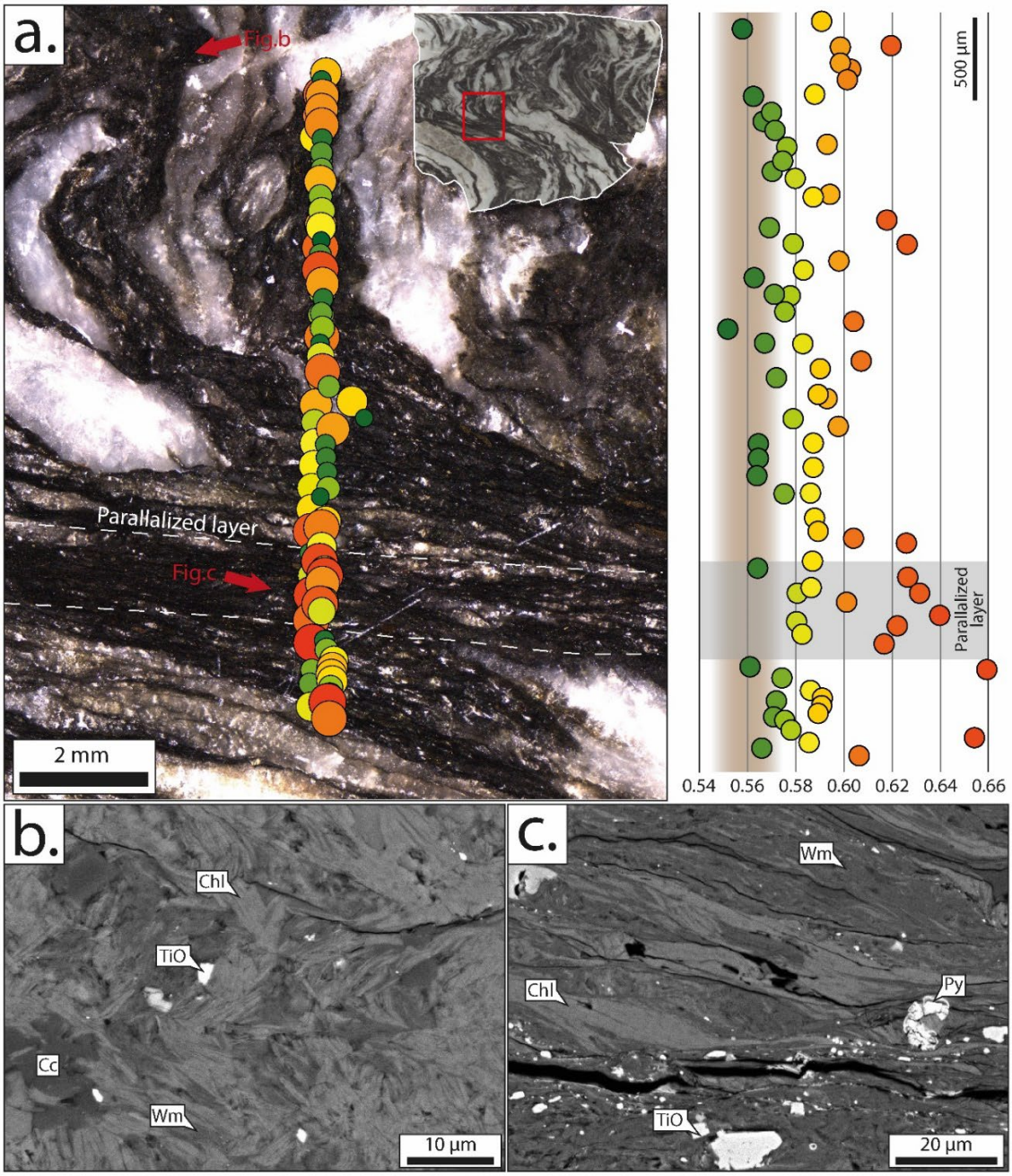

Figure IV.10: Raman profiles along shear-zones of the sample 20GT03C (Glarus Thrust) and SEM images of the micro-structures. ***a.*** *Raman intensity ratio profiles along shear-zones and respective diagrams. Grey areas represent the sheared-zone and brown rectangle the intensity ratio values measured for the references.* ***b.*** *Chlorites and white micas marking the crenulation of the host-rock.* ***c.*** *Majority of white micas and intercalated chlorite showing an intense stretching in the parallelized zone.*

Very localized strain samples have been analyzed through the samples 19KO25D and 20GT03A selected respectively in the Kodiak Accretionary complex and in the Helvetic complex (Glarus Thrust). Both samples have been analyzed using the high-resolution approach producing orthogonal profiles to the localized structures. These profiles are characterized by a consequent increase of IR in the strain zones from 0.58 to 0.65 (Figure IV.11) and from 0.62 to 0.86 (Figure IV.12), i.e. +12% and +40% respectively to samples from the Kodiak Accretionary complex and the Glarus thrust. The values can reach up to 0.97, equivalent to +57% of increase, in the 20GT03A (Figure IV.12d). The profiles shape a rectangular function when going through the high strain zone with a sharp increase of the IR but a slight shouldering is observable on the outer part near rim of the strained zone (Figure IV.11d). The IR profiles in the high strain zone show a plateau of IR values without a large dispersion of values as observed in the ductile shear zones described above.

To go further to the millimetric to micrometric scale shear-zone, we decided to apply the same high-resolution approach on the sample from the Makimine where the regional temperature is a little bit higher (*ie.* 340°C ± 10°C). Figure 13 shows the results obtained from this sample. Intensity ratio shows a large dispersion of values inside and outside of the deformed zone, from 0.8 to 1.2. These results are observed on each sample form the Makimine we analyzed, and due to this large dispersion, it is difficult to see a clear evolution of the intensity ratio along these shear zones. However, we can reveal two behaviors of the intensity ratio in the shear-zone. In one hand, we can observe the similar IR values as the ones measured in the host-rock. In other hand we can observe a diminution of IR values when approaching the rim of the sample richer in irons hydroxides and irons oxides. In addition, this sample shows an evolution of the lithology between the deformed and the undeformed zones and these evolutions could be associated to the rock-type change (Pasteris and Wopenka, 1991; Wada et al., 1994). Based on this observation, we will discuss the effect of deformation for higher temperature in the discussion section comparing poorly deformed samples with intensely stretched and sheared ones.

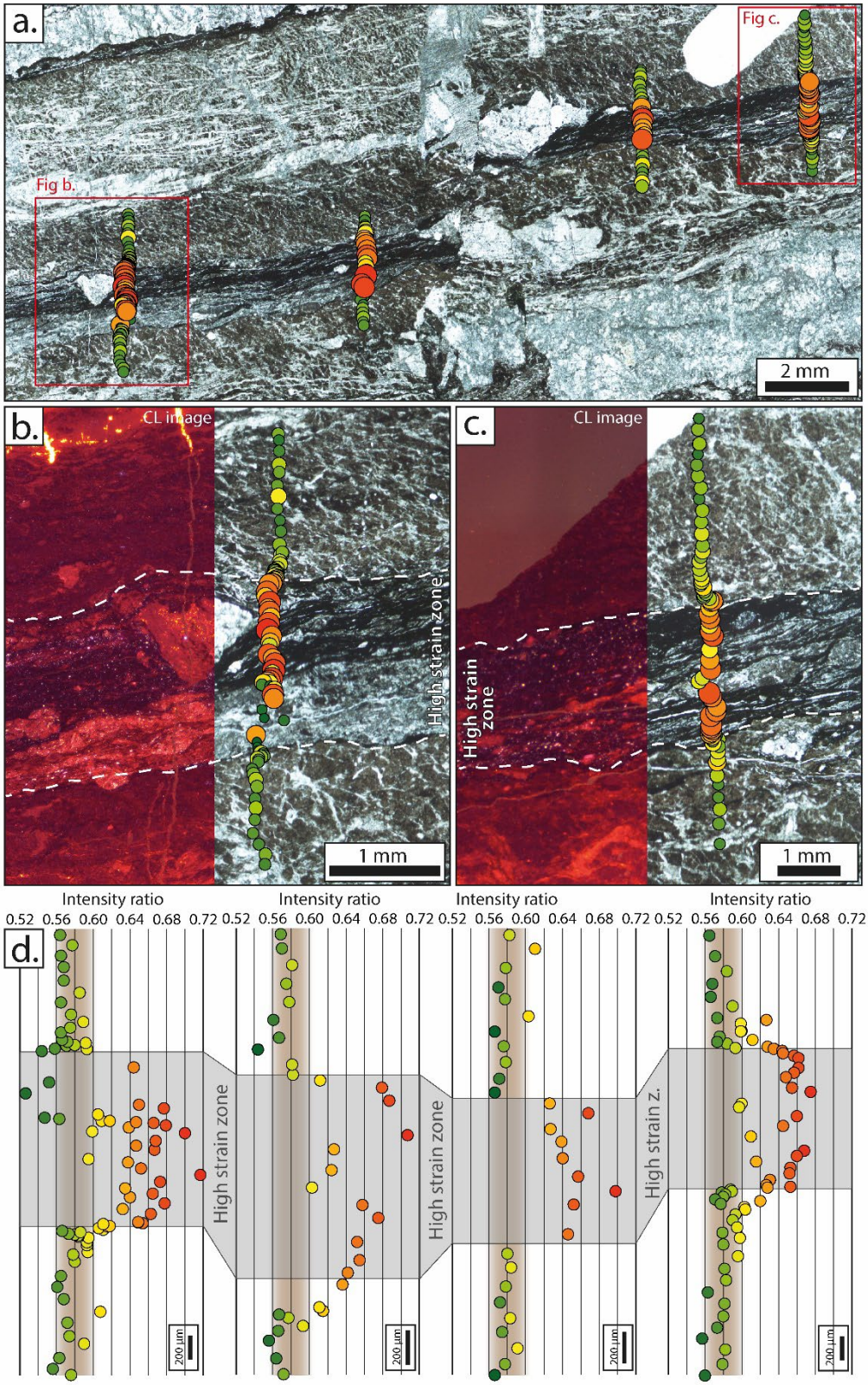

Figure IV.11: ***a.*** *Raman profiles along high-strain zone and surrounding of the sample 19KO25D (Kodiak Accretionary Complex) and associated intensity ratio diagrams. Grey areas represent the sheared-zone and brown rectangle the intensity ratio values measured for the references.* ***b. and c.*** *Close up of two profiles showing the evolution of microstructures using light microscopy and cathodo-luminescence.* ***d.*** *IR diagrams along the four profiles*

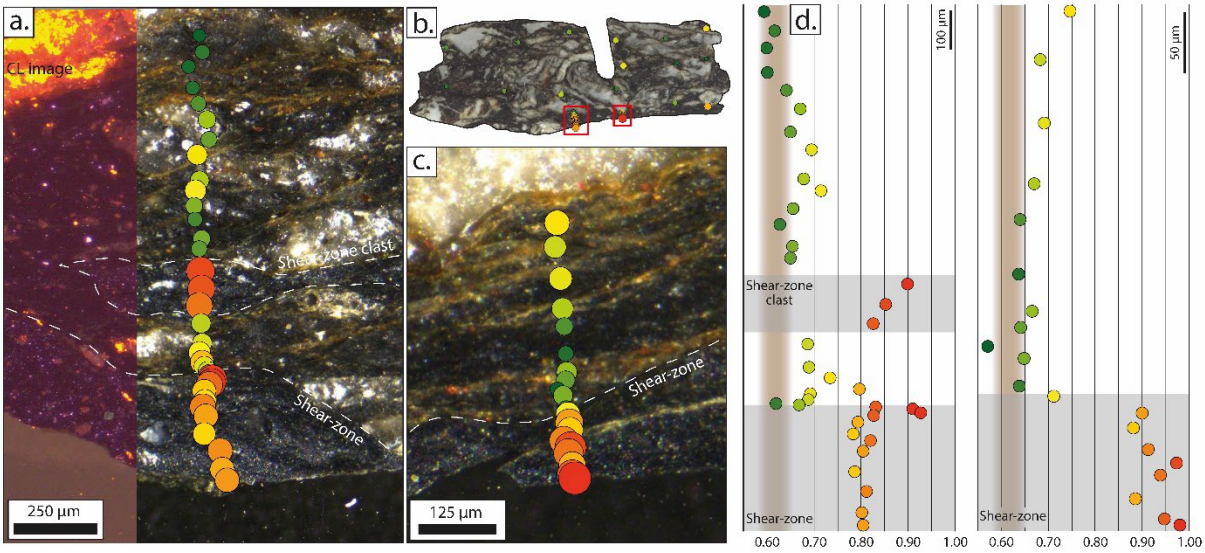

Figure IV.12: Raman profiles along localized shear-zone and surrounding of the sample 20GT03A (Glarus Thrust) and associated intensity ratio diagrams ***(d.)*** *Grey areas represent the sheared-zone and brown rectangle the intensity ratio values measured for the references.* ***b.*** *Overview of the sample and random RSCM point of analyzes.* ***a. and c.*** *Close up of two profiles showing the evolution of microstructures using light microscopy and cathodo-luminescence.*

IV.5 Discussion

In this study, we compare non-seismic deformed zones at several scales in order to reveal the effect of the deformation in the CM crystallinity during the carbonization and the early graphitization stages and the very beginning of the graphitization window. To make this exploration, intensity ratio parameter that appears as a relevant indicator of the crystallinity statement of the CM (Pasteris and Wopenka, 1991) and is relatively reactive to the deformation (Kedar et al., 2021) has been used.

IV.5.1 Effects of deformation on the CM crystallinity

We used two different approaches depending on the scale of the strain-gradients. In each case, the non-seismic shear shows an increase of the intensity ratio in the deformed zones either at millimeter scale or at outcrop scale. This increase is often weak, but is important enough to be confidently detected by the RSCM approach. Brittle deformation, as observed in the Hyuga coherent unit, the IR increase is often less than 5%. At variance, ductile strain gradients show in average an increase between 10 and 20% for both millimetric and outcrop scales. Therefore, both scales (i.e. millimetric and outcrop scales) show the same evolution of the CM crystallinity. This result is particularly important as it participates in the scale-transfer that is mandatory in structural geology and simply to be taken into account either for the RSCM geothermometry approach or for the detection of strain in the absence of classical strain markers.

However, each scale has drawback, in the analyses at the millimeter scale it is difficult to get a clear linear evolution through the structure, while at the outcrop scale, lithology heterogeneity will have a direct effect on the deformation partitioning and will make higher dispersion, so it is difficult to define larger strain gradients from embedded smaller scale gradients. In addition, it highlights that a weak strain energy is necessary to distinguish crystallinity evolution. However, the comparison between the Shimanto Belt and the Kodiak Accretionary Complex with the Glarus Thrust at the outcrop scale gives new insights. In the Glarus Thrust area, the total amount of displacement reaching to 30km (Pfiffner, 1985) is located in a narrow shear-zone of 5 to 10 meters below the thrust. Thereby its quantity of strain is much higher than those in Japan and in Alaska, and its evolution of IR shows dramatic increase (*i.e.* up to 70%). By consequence, the crystallinity observed in the more deformed zone of this strain gradient is directly correlated to the strain quantity. Finally, a low quantity of strain is necessary to observe the effect of the deformation on the crystallinity of carbonaceous material, but this evolution is closely linked with the strain energy.

In addition, an important dispersion is observed within the sheared zones with respects to the host-rocks, as the one described during the graphitization stage. In a simplistic mind, we could define two dominant groups with a sheared group that shows an increase of IR and a group that preserved the background lower crystallinity. The same phenomenon has already been described for high strain deformation during the graphitization stage at higher temperatures (Suchy et al., 1997). This dispersion has been interpreted as the remnants of preexistent structure such as the bedding for example (Bustin et al., 1995). A speculative explanation for this phenomenon could be local overpressure caused by a difference of stress at the micrometer scale. Driven by the mineralogical difference in the shear-zone, different pressures could be observed in the different parts of the deformed zone. Moreover, due to the pressure dependence of the CM kinetics, the mechanical wear could be improved by this overpressure phenomenon and lead to this dispersion of crystallinity. In addition, the CM crystallinity, interpreted thanks to the intensity ratio Raman parameter, shows a similar evolution during the carbonization and the graphitization stage (*i.e.* crystallinity enhance, dispersion). Therefore, it would be acceptable to define the mechanical effect of deformation during the carbonization stage as the same that occur during the graphitization stage at

higher temperature. Indeed, simple shear is responsible of the parallelization of the Basic Structural Unit (BSU) and of the flattening and coalescence of the preexistent pores of the carbonaceous material (Bustin et al., 1995; Ross and Bustin, 1990). Due to this mechanical work, aromatic carbon sheets will grow and therefore the crystallinity will increase. However, as the Raman spectroscopy is only an indicator of the crystallinity of carbonaceous material, a nanoscale study, using HTREM, would be necessary to characterize the proper effect of ductile shear on the carbonaceous material lattice.

Another external factor, in addition to the mechanical wear, which could have a catalytic effect on the crystallinity of carbonaceous material, could be the fluid content. Actually, shear zones may be envisioned as drains and free water could circulate in these preferential paths. The water content could have a possible catalytic effect as the one described during the metamorphism reactions (Früh-Green, 1994; Rubie, 1986). In addition, fluids may also create local overpressure in these shear zones (Raimbourg et al., 2017b). Nakamura et al. (2000) described the dependence to the pressure of the carbonaceous material kinetics that will be catalyzed by higher pressures. Therefore, an overpressure generated by circulation of fluids in the shear zones could catalyze the transformation of the carbons and increase the crystallinity of the carbonaceous material in the deformed zone as well.

IV.5.2 Ductile shear zones vs. very localized ductile shearing

Several new insights are provided by comparing the three samples selected from the Shimanto Belt (HN64), Kodiak Accretionary Complex (19KO25A-1) and Glarus thrust (GT03C) with the high-strain localized samples (19KO25D and GT03A) from one thin deformed zone. In highly strained samples, the shape of the IR profiles obtained using the RSCM is different and less continuous with respect to those from the previous ductile sheared samples (Figures IV.11 and IV.12). Indeed, the profiles shape a rectangular function, interpreted as the important strain contrast, with a plateau in the sheared zone and weak shouldering approaching to the high strain zone. This evolution of the IR is consistent with a microstructural and mineralogical evolution in the high strain zones where a larger amount of phyllosilicates and lower amount of “hard” clasts (albite, quartz and calcite) are observed. This evolution conducts to a strong control of the rheology and the localization of the strain, which affects the CM crystallinity. In addition, IR that shows a large dispersion in the ductile shear-zone is much lower in

high strain zone, where all CM grains show a higher value, and where the strain is more homogeneous. Moreover, IR presents a large evolution close to +20% and could reach up to 40% in the high strain zones. Therefore, the correlation between the IR increase and the quantity strain, observed at the outcrop scale, is also valid in mm-scale strained zones.

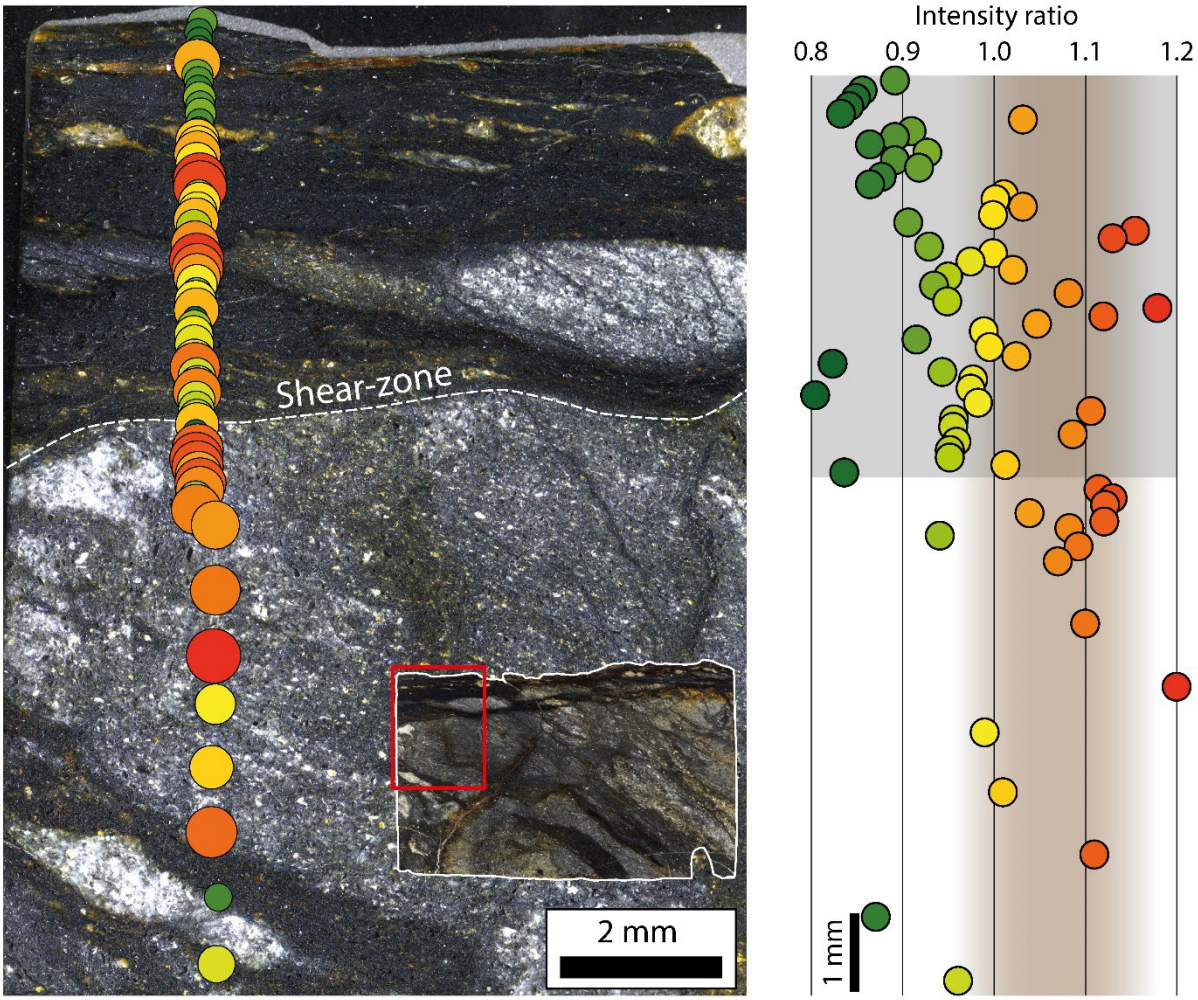

Figure IV.13: Raman profiles along shear-zones of the sample 18NOB22A (Shimanto Belt) and associated intensity ratio diagrams. Grey areas represent the sheared-zone and brown rectangle the intensity ratio values measured for the references.

IV.5.3 CM crystallinity enhance at regional-scale

In order to check the possible effect of the deformation on the intensity ratio at different scales we used our own calibration between the IR and the temperature retrieved from classical RSCM geothermometry (Beyssac et al., 2002; Lahfid et al., 2010) (Figure III.13c in Chapter III). Both millimetric and outcrop scales plotted in this calibration do not show deviation and are included in the 95% confidence interval. In certain cases, as the one described in the Glarus Thrust with an important finite strain quantity, few

points show a deviation and misfit with this calibration when the increase is very important. Based on these results, we apply our model to a regional scale deformation in order to asses it. The Makimine unit, in the Shimanto Belt, is composed of two different sub-units with almost similar temperatures, one preserves the turbidite alternation and another highly stretched and elongated (Figure IV.14). Based on structural criteria, we discriminate two groups of samples with the undeformed/poorly deformed group and the deformed group. In Figure III.14, we plotted Raman measurements of these two groups in our calibration with a 95% confidence interval. We can observe from 320 to 360°C that the deformation has an important role on the intensity ratio with a quasi-systematic increase. Due to this evolution, deformed samples misfit with this calibration, and for the most intensely deformed samples a clear overshoot of the calibration is observed with intensity ratio values that can reach to 2.2 when the maximum measured IR for undeformed samples was 1.6. This increase of IR is ca. +38%, similar to the increasing percentages observed for high strain zones (e.g. Glarus Thrust). However, poorly deformed samples only exposed to geological burial/heating show a different trend and follow the calibration. Therefore, it seems that the results we obtained from millimetric to metric strain gradients are applicable to regional scales. It means that the results measured with the RSCM have to be discuss cautiously when deformation is evident in the studied area. In addition, above 360°C, the distinction between poorly deformed and deformed samples is impossible and both groups follow the calibration. An explanation to this phenomenon could be the behavior change of quartz with the plasticity activation at low temperature in presence of water in the system (Palazzin et al., 2016). Due to this behavior change, the majority of the deformation localized in the shale previously is now shared everywhere in the rock and accommodated by the quartz, by partitioning. Finally, based in these observations it looks that during the graphitization stage, above 360°C, there is no effect of the deformation on the crystallinity. However, previous results from the literature (Bonijoly et al., 1982a; Bustin et al., 1995; Suchy et al., 1997) on high strain lead us to follow our research during this stage of evolution of the crystallinity of carbonaceous material.

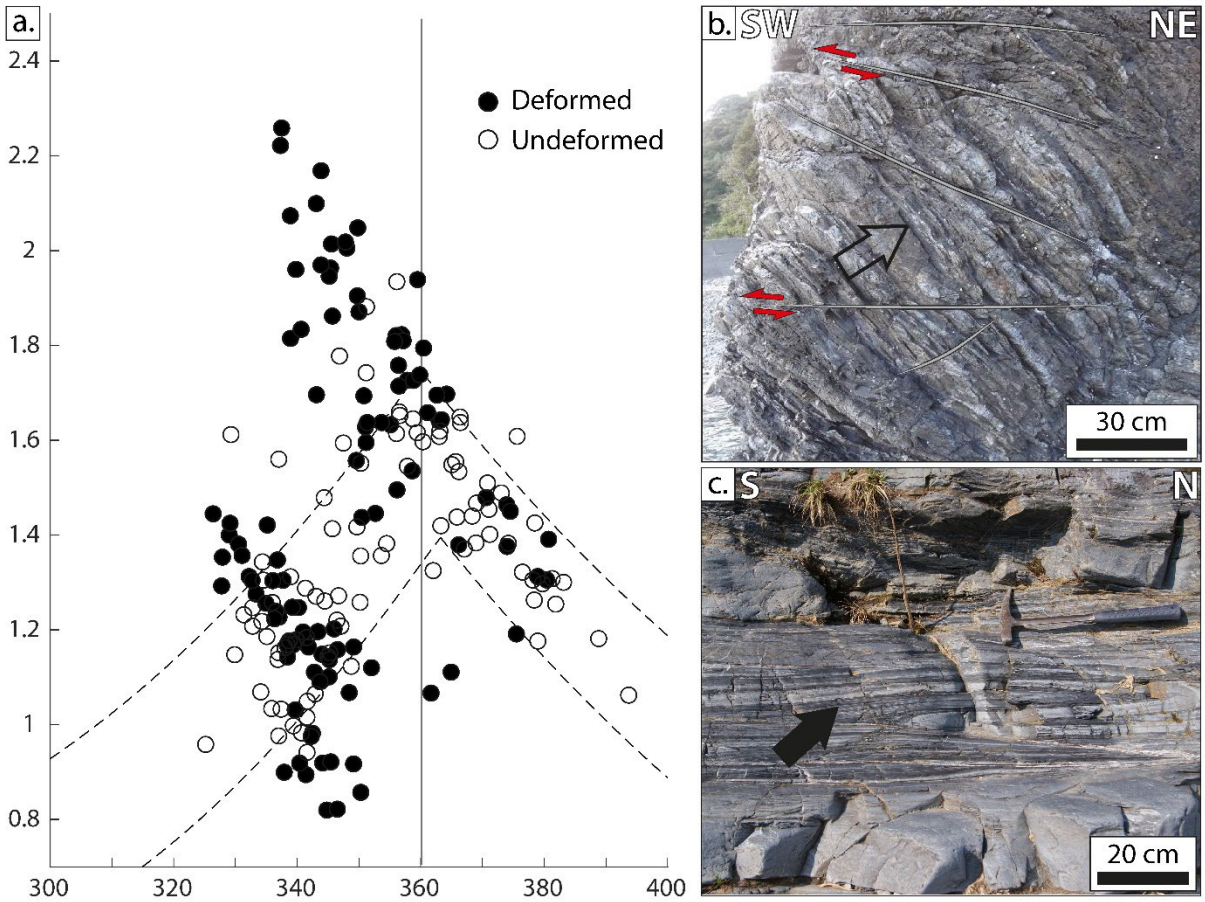

Figure IV.14: Intensity ratio obtained from the Makimine unit. ***a.*** *Intensity ratio measurement from undeformed and deformed samples of the Makimine unit on the calibrated 95% confidence interval. The vertical line represents the end of the carbonization and the beginning of the graphitization phase.* ***b.*** *Structure of the Coherent Makimine composed of turbidite and crosscut by shear-zones.* ***c.*** *Structure of the foliated Makimine composed of co-axially deformed rocks.* ***b. and c.*** *Examples of undeformed and deformed samples used in the diagram* ***a.****.*

IV.5.4 The effect of deformation and temperature breakdown

Finally, we can discriminate ranges of finite temperature during the carbonization and beginning of the graphitization stages when the deformation will have different influences. From 200 to 240°C, the results are ambiguous and the deformation effect is very weak. Actually, at these temperatures the deformation mechanisms are very complex and the partitioning between the ductile and the brittle deformation is difficult. Indeed, the crystallinity evolution suffers of this complexity. In addition, it is difficult to get a clear evolution because the intensity ratio is almost the same between 200 and 240°C, i.e. around 0.5. The deformation effect becomes however the maximum between 240 and 300°C. In this interval, the deformation is more ductile and the evolution of the IR as a function of temperature is not too quick (Figure III.13c). Ductile deformation is observed even at these temperatures and can be

explained by the high content of water that generates a softening effect on the rheology as described by Palazzin et al. (2016). After 300°C and up to 360°C, the evolution is complex and the intensity ratio evolves very quickly even without deformation. Indeed, a lot of heterogeneity is observed, even for poorly deformed sample, and it is difficult to see a clear evolution of the crystallinity due to this natural dispersion. Therefore, it is impossible to discuss the strain effect at the mm-scale and metric scale except for a very important strain energy as shown in the Makimine unit (Figure IV.14). After 360°C, the intensity ratio behavior is different and no distinction between deformed and undeformed samples has been observed. We interpret this phenomenon as the consequence of the activation of the quartz plasticity at in this temperature range. Therefore, the deformation is now generalized in the entire sample and not only on the shaly matrix where we analyzed the carbon grains.

IV.5.5 Impact on the RSCM geothermometry

Finally, the simple tool of the Raman Spectroscopy thermometer (Beyssac et al., 2002; Kouketsu et al., 2014; Lahfid et al., 2010) based on the evolution of the crystallinity is questionable. The impact of deformation on the intensity ratio until to 360°C, and on the crystallinity of the carbonaceous material could generate substantial deviation on the calculated temperature. Indeed, during the maturation from poorly organized to organized CM, the deformation will increase the D band intensity and after deconvolution processes the area and FHWM under this band will increase as well. Geothermometers are based on these RSCM parameters measured under the Raman spectra. Because of the deformation, these calibrations will be directly impacted by the creation of an artefact. By consequence, the calculated temperature will be overestimated. However, samples used to calibrate these thermometers have been selected along strain gradients, so a part of the deformation is already included into these thermometers. To illustrate the effect of strain on RSCM geothermometers, we applied the Lahfid et al. (2010) RSCM calibration to the Glarus thrust that show a gradual strain gradient from a poorly foliated to a mylonitized zones (Figure IV.15). For weak deformation (i.e. until 20% of increase) the response on the calculated RSCM temperature will be no more than few tens of degrees. In this case, the deviation is accommodated by the standard deviation of the method, which is comprise between 25°C (Lahfid et al., 2010) and 50°C (Beyssac et al., 2002). However, a large dispersion of the values could mislead the interpretation of the

results. In the case of high strain, like in the Glarus Thrust area, the increase of the D band area is very important and the calculated temperature could increase up to 70°C, which is not negligible (Figure IV.15). Therefore, in the case of high strain, when the IR increases more than 20%, the RSCM thermometer should not be used and replaced with other thermometers, because the ductile shear could generate very intense overestimation.

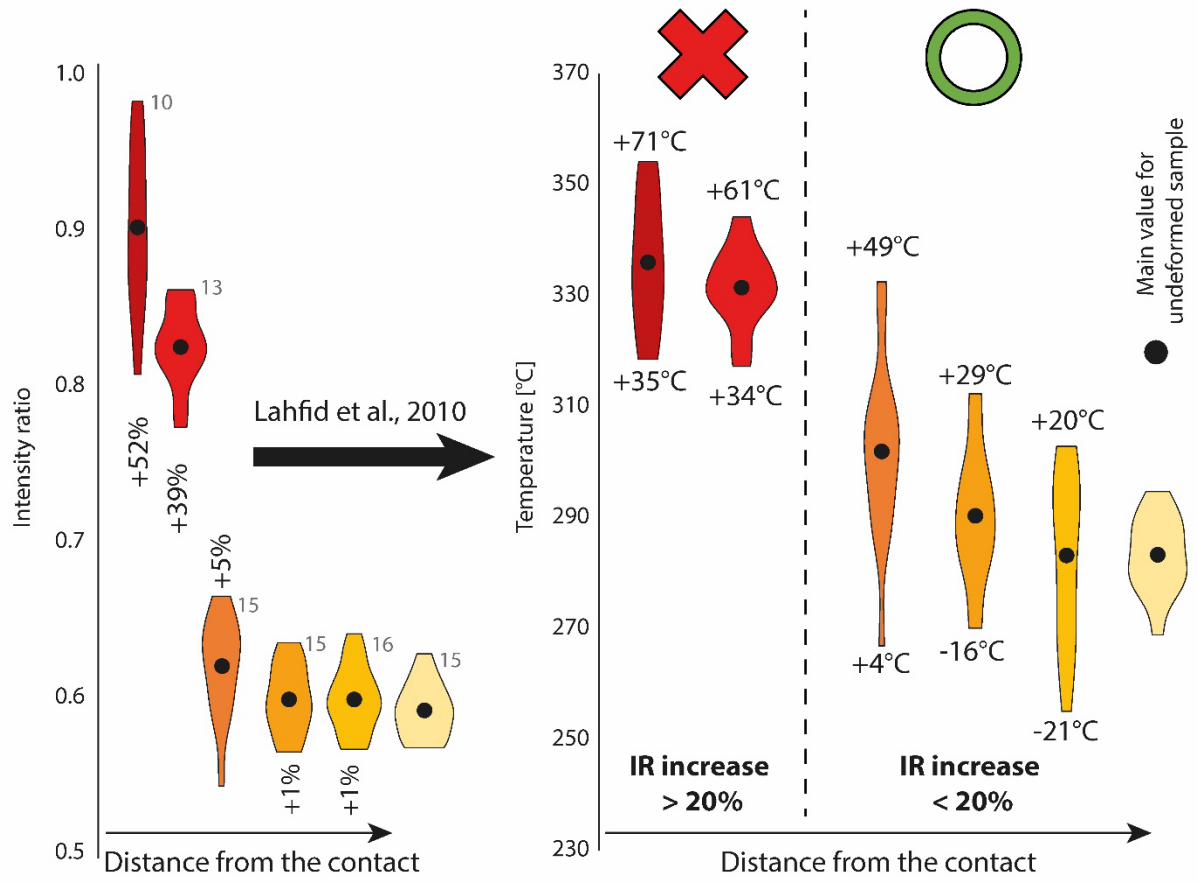

Figure IV.15 : Intensity ratio evolution and equivalent apparent temperature obtained using Lahfid et al. (2010) geothermometer along the Glarus Thrust strain gradient.

IV.5.6 Non-seismic long-term deformation vs. seismic deformation

The ductile non-seismic deformation that occurs during a very slow shearing in the accretionary complexes reveals an increase of the crystallinity of the carbonaceous materials during the carbonization phase. This point has been shined on light thanks to the Raman Spectroscopy, and more precisely thanks to the intensity ratio parameter. However, in previous publications, the effect of deformation has already been shown during a fast and brittle deformation through the study of faulting using the Raman Spectroscopy (Furuichi et al., 2015; Ito et al., 2017; Kouketsu et al., 2017; Kuo et al., 2018) in order to

detect the possible frictional heating generating during the faulting. Conclusions on the effect of seismic deformation on the carbonaceous material are ambiguous and in opposition with intensity ratio increase (Ito et al., 2017; Ujiie et al., 2021) and decrease (Kouketsu et al., 2017; Kuo et al., 2018). However, in this study it is always difficult to discriminate the proper strain effect from a possible frictional-heating effect generated during the slip. Recent studies on Black Fault Rocks suggest that the CM crystallinity enhance measured in the fault veins is dominantly due to mechanical wear rather than the frictional heating (Moris-Muttoni et al., in prep.). Here we will discuss the difference observed between the seismic and non-seismic deformation effects on the CM crystallinity. To do that, we compare profiles obtained from the Shimanto Belt sample with a profile from Black Fault Rocks in the same area (Moris-Muttoni et al., in prep.) (Figure IV.16). Both profiles show, in the deformed zone an increase of the intensity ratio, but the shape of the profile and the amplitude of the increase are different. Indeed, the seismic profile shows a rectangular function evolution through the structure with a very sharp evolution when in the non-seismic profile and the evolution is more abstractive. In addition, for the non-seismic deformation, the average of increase of the intensity ratio is often between 10 to 20% when the seismic deformation shows very consistent values of 40%. Moreover, the non-seismic shear deformation shows a high dispersion of values, from the background IR to a 20% increase, while in the Black Fault Rock sample all the values inside the vein show higher IR. Finally, the shear deformation shows a weak and diffuse evolution, in comparison with the seismic deformation. These differences are interpreted as the result of a large strain intensity which is definitely higher and more localized during the seismic deformation events and conducts to amorphization by intense comminution. The only way to observe the same increase amplitude of the intensity ratio in the non-seismic deformation is to look at high strain deformation as the one studied in the Glarus Thrust area (20GT19 sampling profile) or in localized high strain samples. The latter cited shows very similar features with the seismic deformation in terms of microstructures and RSCM evolution. Indeed, the evolution of the microstructures is very contrasted and sharp between the high strain zones and the surrounding and is localized along a fine layer. In addition, a rectangular function shape is observed for the IR profiles through the high strain zone where all the CM grains are affected by the deformation. However, slight differences are also identifiable, such as the presence of a slight shouldering outer of the high strain zone, the maximum values are measured

in the center of the sheared zone whereas in seismic deformation structure the highest values are measured on the rim of the strained zone. To finish, the average IR increase is weaker in the high strain zone produced by non-seismic deformation.

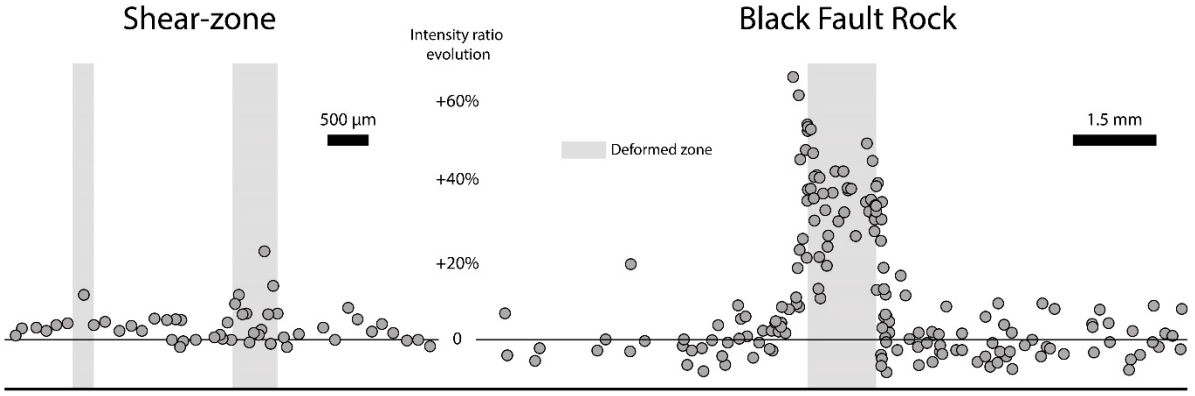

Figure IV.16: Percentage increase comparison of intensity ratio profiles of non-seismic deformation (non-seismic shear-zone) and seismic event deformation (Black Fault Rock) in terms of percentage with respect to the host-rock values.

IV.6 Conclusions

The non-seismic shear deformation is visible at different scales in the accretionary complexes, from the thin section until to decametric strain gradients. In this study, we focused potential effects of the deformation on the crystallinity of the carbonaceous material that experienced upper carbonization – incipient graphitization low-grade conditions (i.e. 200-360°C). To describe quantitatively changes in the crystallinity of the carbonaceous material, we used the intensity ratio RSCM parameter that appears as a reliable indicator of the CM lattice. At all scales, the crystallinity of CM is increasing by the deformation with 20% of evolution in average. This evolution is associated with a higher dispersion of values observed in the deformed zone. Bimodality of CM crystallinity is observed in the deformed zone with either no evolution (i.e. similar to the host-rock CM crystallinity) or higher crystallinity. This evolution of the crystallinity does not require a large quantity of strain but seems correlated to the strain energy, which appears as the main controlling factor of the increase in the deformed zone. Interestingly, the effect of the deformation appears closely linked to the type of microstructure and to the deformation mechanisms, which is primarily controlled by the background temperature and pressure. Brittle deformation shows a weak increase of the CM crystallinity whereas the ductile deformation generates a higher evolution of the CM crystallinity. In addition, the evolution of the CM crystallinity for poorly to

organized CM is similar to the ones observed for well-organized CM during the late graphitization stage. Therefore, the interpretation of the shearing mechanical effect on the CM during the graphitization can be transposed to the carbonization and the early phases of the graphitization.

Comparison between non-seismic and seismic deformation (Chapter VI) shows a significant difference in crystallinity of the carbonaceous material. As the microstructures are different for these two objects, the intensity ratio shows lower increase, more value dispersion in the ductile shear zones mainly due to the quantity of strain less important in shear-zones.

Finally, thanks to the RSCM method and especially the IR, the effect of strain has been highlighted on the CM crystallinity. RSCM geothermometry is based on the CM crystallinity and could generate deviation in the calculated temperature during the carbonization and early graphitization stages. However, this study has shown that the deviation induced by the deformation is absorbed by the method error of the machine even a large dispersion of the values will be obtained. For high strained terranes, a large deviation is observed and it overpasses the machine error. In this case, RSCM geothermometry should be used very carefully and paired with another thermometer.

Preface

This chapter presents the study of the effect of the non-seismic deformation on the CM crystallinity through deformation experiments. Experimental approach shows its advantage to control some strain parameters such as the quantity of strain and the strain rate that are not always possible to obtain in natural shear-zones. Deformation experiments have been carried out thanks to Paterson Rig and solid-medium Griggs type apparatuses and immature has been deformed at various strain rate, quantity of strain and confining pressure. Microstructures and RSCM response in strained zone have been compared and linked with mechanical data. This study highlights the strain effect that conducts to an increase of the CM crystallinity in the experimentally deformed zone, identified thanks to the microstructural evolution, irrespectively of the regime of deformation. Compared with natural non-seismic deformed zone, similar qualitative and quantitative results have been noticed.

Chapter V – Effect of strain on carbonaceous material crystallinity: insights from deformation experiments at low strain-rate on immature shale

V.1 Introduction

The evaluation of the degree of crystallinity of the carbonaceous material is accessible through the Raman Spectroscopy of Carbonaceous Material (RSCM) analyses. Upon geological heating, the degree of crystallinity increases through the thermal maturation by the carbonization and graphitization stages during the low grade metamorphism up to the granulite metamorphic facies. The first correlation qualitatively linked the degree of metamorphism to the CM lattice organization (Pasteris and Wopenka, 1991; Wada et al., 1994). Later on, quantitative calibration of these correlations resulted into the development of geothermometers based on the RSCM parameters, applicable to the temperature range from 200 to 600°C (Aoya et al., 2010; Beyssac et al., 2002; Kouketsu et al., 2014; Lahfid et al., 2010; Rahl et al., 2005). Well-accepted by the geoscientist community and easy to apply, these geothermometers are widely used in ancient wedge and collisions zones (Beaudoin et al., 2015; Clerc et al., 2015; Lanari et al., 2012).

However, amongst regional-scale temperature trends, anomalous temperatures, i.e. temperatures strongly deviating from the trend, are sometimes observed (Barzoi and Guy, 2002, 2002; Scharf et al., 2013). These anomalous temperatures are interpreted as an effect of strain, but the relationship between strain and CM crystallinity (hence on RSCM parameters) is not well understood. The strain effect has been poorly studied up to now and the previous studies mainly focused on the well-organized CM in the advanced or late graphitization processes of natural (Kedar et al., 2020; Nakamura et al., 2015; Suchy et al., 1997) or experimental (Bonijoly et al., 1982a; Bustin et al., 1995; Ross et al., 1991a; Ross and Bustin, 1990) samples. In addition, at lower degree of crystallinity the study of the effect of strain is very limited and focused on the seismic deformation analyzing the intensity ratio (IR ; i.e. R1 in Beyssac et al. (2002)) in Black Fault Rocks (Ito et al., 2017; Ujiie et al., 2021) or fault gouges (Furuichi et al., 2015) to detect evidence of crystallinity increase as a consequence of seismic slip. These low-grade and high strain rate examples are problematic: in those samples, the CM crystallinity reflects potentially a combination of high strain, as well as high temperature pulses as a result of seismic frictional heating. Finally, the effect of non-seismic and slow strain rate deformation, is still unknown, despite the fact that such kind of deformation covers the whole range of crustal conditions, from the brittle to viscous regime.

In Chapter IV of this study, the effect of non-seismic deformation on CM crystallinity has been explored along natural strain gradients from the mm-scale to the regional scale using the RSCM (in particular IR parameter). The results suggest a crystallinity enhancement in the strained zone, with an intensity that depends on the strain amplitude, similarly to the results obtained at higher maturation grade (i.e. late graphitization). Nonetheless, the quantification of the strain parameters is very limited in natural samples such as the strain quantity, the strain rate, the quantity and nature of fluids. Moreover, deformation is often the result of successive deformation stages for variable conditions of pressure, temperature and strain rate.

Here we propose to use an experimental approach aiming to reproduce the natural non-seismic deformation structures in laboratory, in order to explore the strain effect on the CM crystallinity and control the majority of the strain factors. The Paterson Rig and the solid-medium Griggs apparatuses have been used to reproduce these structures, targeting a range of CM crystallinity during the carbonization and the early stage of graphitization (i.e. from 260 to 300°C). RSCM analyses have been carried out to characterize the IR, relevant to the CM-organization.. With careful observations of the microstructures, these analyses make possible to link the RSCM parameters to their respective microstructural domain. In parallel thermal maturation experiments, at hydrostatic constant pressure and temperature, have been performed in order to understand the quantitative influence of duration-temperature pair on the CM crystallinity. The calculation of CM kinetics during the early maturation stages, until now inexistent, can be compared with Paterson Rig experimental CM crystallinity, based on the IR, to highlight the effect of stress during deformation experiments. Finally, we discuss the strain effect on the CM crystallinity for non-seismic deformation by comparing natural and experimental samples and its implications on external controlling factors (i.e. free water, maturity of the CM and pressure) during the CM crystallinity evolution in the carbonization and the early graphitization stages.

V.2 Geological settings and starting materials

Samples used for both experiments, thermal maturation in autoclaves and deformation experiments using Paterson Rig and Solid-medium Griggs apparatuses, have been selected in the Shimanto Belt in Japan. The description of the Shimanto Belt has been made in detail in the previous chapter. Two shales have been sampled as starting materials, based on the maturity of their carbonaceous materials. Characterization of the rock chemistry and mineralogical composition has been obtained respectively by XRF and XRD analyses. Microscopy technics have not been used due to the small size of particles contained in both samples. In addition, the degree of maturity and the lattice organization have been investigated using a set of tools, such as RSCM, vitrinite reflectance (%VR) or RockEval pyrolysis. All these methods are presented in Chapter III.

The first starting material, 18NOB01A, is a non-metamorphosed shale sampled in the Miyazaki Group in the Shimanto Belt. The Miyazaki Group is a Pliocene non-accreted forearc basin composed of a thick sequence of turbidites (Murata, 1997; Shuto, 1961). This sample has been selected as an immature sediment containing non-organized and immature CM. This rock has been sampled in a thick layer of shale in the turbidite unit and is composed of a fine assemblage of Quartz – Albite – K-feldspar – Calcite – Mullite – Illite – Pyrite. Semi-quantitative estimation based on the Rietveld method shows a majority of Qt and Ab (ca. 60%), calcite represents about 5% of the rock, and the rest is composed of clays (ca. 35%). The maturity of the CM contained in this sample, about 0.60% TOC, is estimated thanks to the RockEval pyrolysis, vitrinite reflectance and RSCM. RockEval pyrolysis shows a T_{max} at 435°C and the combination between the oxygen and hydrogen index corresponds to an organic matter of type III (i.e. plant origin) in the modified Van Kravelen diagram (Figure V.1). Vitrinite reflectance average obtained for NOB01 a is 0.54 ± 0.04 and corresponds of a temperature of 84 ± 7 °C based on Barker's (1988) calibration (Table V.1) and a thermal maturity between the end of the diagenesis and the beginning of the catagenesis. RSCM parameters have been measured but the evolution of the Raman parameters at these degrees of maturity is still debated and is ambiguous.

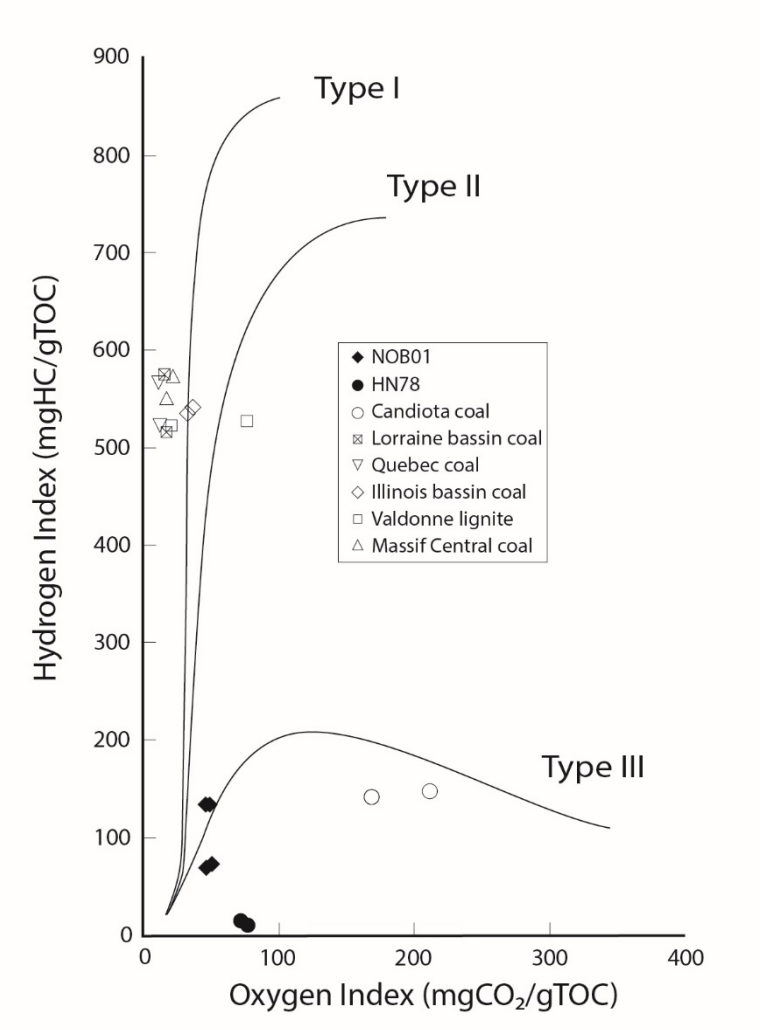

Figure V.1: Modified Van Krevelen diagram showing the types of organic matter contained in the starting material and selected additional vitrain.

The second starting material, HN78, is a shale from the coherent Hyuga unit in the Shimanto Belt. This sample has a similar composition to NOB01A but is considered as a poorly mature sediment. This sample is composed approximately of 45% Quartz – 16% Albite – 33% Illite – 5% Chlorite based on the XRD results and the semi-quantitative Rietveld method. Chemical composition and water content can be observed in Table (V.1). In this sample, the CM, from plant land, is poorly organized and has reached a thermal maturity at the transition between the metagenesis and the metamorphism. Calculated temperature obtained thanks to the RSCM calibration of Lahfid et al. (2010) is approximately 201 ± 11°C. No vitrinite reflectance has been measured, and because of the lack of advanced thermal maturity, no T_{max} can be calculated due to the absence of S2 peak using the RockEval pyrolysis.

With respect to preexistent studies, we used an additional well-studied vitrinite in hydrostatic thermal maturation experiments to trace the maturation of CM. Vitrinite of B12 from Candiota (Bresil) (Silva and Kalkreuth, 2005), presenting similar degree of maturity and type of CM, has been chosen based on the vitrinite results (i.e 0.43 ± 0.03) and RockEval pyrolysis (Table V.1).

Table V.1 Characterization of chemistry and degree of crystallinity of the carbonaceous material of the starting materials (18NOB01A – HN78 and B12).

Sample	*Raman spectroscopy*										*Vitrinite Reflectance*		*RockEval pyrolyse*
	D1 band (cm^{-1})	*D1 band FWHM*	*G band (cm^{-1})*	*G band FWHM*	*R2 ratio*	*RA1 ratio*	*Intensity Ratio*	*Width ratio*	*D/G dist. (cm^{-1})*	*Estimated temp. [a][b]*	*Rm%*	*Estimated temp. [c]*	T_{max}
18NOB01A	1358 ± 7	105 ± 13	1610 ± 7	69 ± 18	0.48 ± 0.09	0.47 ± 0.10	0.60 ± 0.08	1.66 ± 0.62	252 ± 7	-	0.54 ± 0.04	84 ± 7°C	437°C
HN78	1350 ± 2	116 ± 6	1603 ± 3	52 ± 5	0.53 ± 0.01	0.53 ±0.01	0.49 ± 0.02	2.25 ±0.14	254 ± 2	201 ± 11	-	-	-
B12	-	-	-	-	-	-	-	-	-	-	0.43 ± 0.03	60 ± 7°C	445°C

[a] Lhafid et al., 2010 ; [b] Beyssac et al., 2002 ; [c] Barker, 1988

wt%	**LOI**	**SiO_2**	**TiO_2**	**Al_2O_3**	**FeO**	**MgO**	**MnO**	**CaO**	**Na_2O**	**K_2O**	**P_2O_5**	**SO_3**
NOB01A	4.36	64.08	0.72	16.73	5.82	1.9	0.04	0.29	1.49	3.26	0.23	0.17
HN78	8.38	58.77	0.66	14.87	4.81	2.06	0.07	4.67	1.68	2.83	0.15	0.61

All samples have been prepared for different experiments (thermal maturation, deformation experiments and flash heating), as solid or powder samples. We took care to conserve the original degree of crystallinity of the CM in each preparation. Thanks to two different degrees of crystallinity, we can follow the evolution of CM crystallinity against temperature or deformation and pressure for different degree of crystallinity from the non-organized to the poorly organized CM.

V.3 Hydrostatic maturation and kinetics calculation

V.3.1 Hydrostatic maturation

Hydrostatic thermal maturation has been carried out using autoclaves in order to understand the CM evolution under constant temperature and pressure during the carbonization and early graphitization stages. Powdered samples, sealed in gold capsules, have been matured at 1.5 kbar and from 500 to 800°C for a duration between 3 hours to 45 days in order to stabilize and cover the CM crystallinity organization between CM poorly organized to the organized CM (i.e. Polyaromatic structures stack by 2 or 3). Additional water has been added in some experiments in order to discuss the role of fluid during maturation. The detailed explanations of the sample preparation and choices of experimental conditions are presented in Chapter III.

After experiments, the CM crystallinity is observed by the RSCM analyses of the samples. 20 points have been measured on each sample and each experiment is doubled. All the results obtained are presented in Table V.2. Parameters used to follow the maturation are mainly focused on the D- and G-band positions, FMHW, intensity ratio and distance between the D and G bands (i.e. RBS in Henry et al. (2019)). In addition, area ratios used for thermometric calibrations (Beyssac et al., 2002; Lahfid et al., 2010) have been analyzed. The different parameters studied show ambiguous evolution through the maturation stage (Figure V.2), except for the intensity ratio (IR) (Figure V.2g) that shows a monotonous evolution for each maturation temperature. In addition, the IR covers all the range of crystallinity from the carbonization to the early graphitization stages (i.e. from 0.5 to 1.6), as we discussed above in Chapter III. Therefore, in order to follow the maturation and the CM crystallinity evolution, as in previous studies at higher range of maturation (Pasteris and Wopenka, 1991), the IR has been selected for our study.

Thanks to the IR evolution, we are able to calculate the CM kinetics through the carbonization and the early stage of graphitization. The relative explanation is presented in the next section.

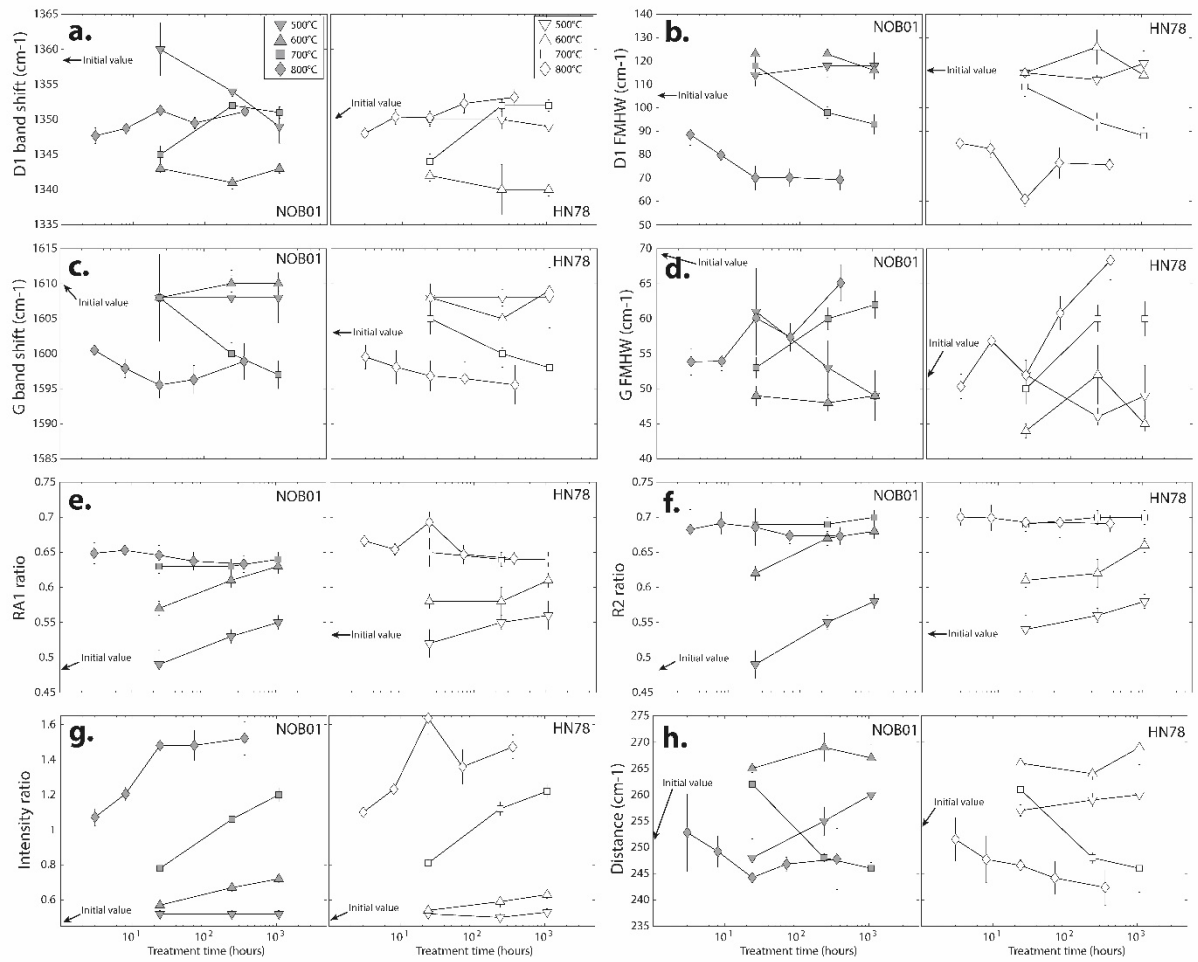

Figure V.2 : Evolution of the RSCM parameters through the carbonization and early graphitization stages for 18NOB01A and HN78. ***a.*** *D1-band shift.* ***b.*** *D1-band FMHW.* ***c.*** *G-band shift.* ***d.*** *G-band FMWH.* ***e.*** *RA1 area ratio (Lahfid et al., 2010).* ***f.*** *R2 area ratio (Beyssac et al., 2002).* ***g.*** *Intensity ratio (R1 in (Beyssac et al., 2002)).* ***h.*** *D- and G-band distance (RBS in (Henry et al., 2018).*

Table V.2 : Summary of the RSCM parameters measured for all maturation experiments for the immature (18NOB01A) and poorly mature (HN78) starting materials.

Sample	Temperature (°C)	Time (hours)	***Raman spectroscopy***																					
			D1 band (cm^{-1})	*SD*	*D1 band FWHM*	*SD*	*G band (cm^{-1})*	*SD*	*G band FWHM*	*SD*	*R2 ratio*	*SD*	*RA1 ratio*	*SD*	*Intensity Ratio*	*SD*	*Width ratio*	*SD*	*D/G dist. (cm^{-1})*	*SD*	*Gss/D2 dist.(cm^{-1})*	*SD*	*Estimated temp. [a][b]*	*SD*
NOB01A	*Starting materials*		1358	7,0	105	13,0	1610	7,0	69	18,0	0,48	0,09	0,47	0,10	0,60	0,08	1,66	0,62	252	7,0	29,7	9,5	-	-
	500	24	1360	3,8	114	4,8	1608	0,7	61	6,2	0,49	0,02	0,49	0,02	0,52	0,02	1,87	0,22	248	3,6	25,7	2,6	-	-
	500 [1]	24 [1]	1355	1,4	110	6,1	1607	0,4	54	1,4	0,50	0,02	0,50	0,02	0,50	0,02	2,03	0,12	252	1,9	23,5	0,9	-	-
	500	240	1354	3,0	118	5,0	1608	1,0	53	3,9	0,55	0,01	0,53	0,01	0,52	0,02	2,23	0,12	255	2,7	21,4	2,3	201	16,3
	500	1080	1349	2,4	118	5,8	1608	0,5	49	3,6	0,58	0,01	0,55	0,01	0,52	0,02	2,42	0,09	260	2,5	19,7	3,1	224	13,6
	600	24	1343	0,6	123	1,9	1608	0,6	49	1,4	0,62	0,01	0,57	0,01	0,57	0,01	2,51	0,10	265	0,8	19,6	1,6	249	9,0
	600 [1]	24 [1]	1343	0,6	122	3,9	1608	0,3	48	1,4	0,61	0,01	0,57	0,01	0,58	0,02	2,51	0,05	265	0,5	19,2	1,1	247	10,8
	600	240	1341	0,9	123	3,8	1610	2,6	48	1,2	0,67	0,01	0,61	0,01	0,67	0,02	2,54	0,07	269	2,7	17,4	0,5	297	9,3
	600	1080	1343	0,7	116	3,6	1610	2,3	49	1,1	0,68	0,01	0,63	0,01	0,72	0,02	2,36	0,08	267	2,5	17,3	0,4	313	8,4
	700	24	1345	1,2	118	3,6	1608	3,5	53	1,5	0,69	0,01	0,63	0,01	0,78	0,01	2,23	0,05	262	3,5	18,4	0,4	320	11,0
	700	240	1352	1,0	98	2,5	1600	1,6	60	1,6	0,69	0,01	0,63	0,01	1,06	0,02	1,63	0,04	248	0,8	21,9	0,5	317	15,7
	700	1080	1351	0,8	93	4,2	1597	0,9	62	2,0	0,70	0,01	0,64	0,01	1,20	0,04	3,84	0,23	246	1,1	23,0	0,6	328	4,1
	800	3	1348	1,1	89	4,6	1600	6,7	54	1,9	0,68	0,03	0,65	0,01	1,07	0,05	1,65	0,10	253	7,4	20,4	1,0	337	12,6
	800 [2]	3 [2]	1348	0,7	87	3,3	1598	2,5	54	1,9	0,69	0,02	0,65	0,01	1,10	0,03	1,61	0,10	250	2,9	20,4	1,7	333	8,3
	800	8	1349	0,7	80	2,1	1598	3,0	54	1,3	0,69	0,02	0,65	0,01	1,21	0,04	1,48	0,06	249	2,9	21,2	0,9	333	7,1
	800 [2]	8 [2]	1350	0,7	78	3,7	1597	2,0	55	1,8	0,69	0,02	0,65	0,01	1,23	0,04	1,41	0,08	247	2,2	21,8	1,0	335	7,1
	800	24	1351	0,8	70	5,2	1596	2,4	60	1,9	0,69	0,03	0,65	0,01	1,48	0,09	1,17	0,08	244	2,8	23,3	0,7	336	11,9
	800 [2]	24 [2]	1352	0,4	73	2,4	1597	0,5	59	1,7	0,69	0,01	0,64	0,01	1,39	0,04	1,24	0,05	245	0,7	23,9	0,6	334	4,0
	800	72	1349	0,8	70	3,9	1596	0,9	57	2,0	0,67	0,01	0,64	0,01	1,48	0,09	1,22	0,05	247	1,3	22,6	0,7	341	5,1
	800 [2]	72 [2]	1349	0,9	78	4,6	1599	5,3	59	2,2	0,68	0,01	0,64	0,01	1,29	0,06	1,33	0,09	250	5,6	21,9	1,0	339	6,6
	800	360	1351	0,7	69	4,3	1599	5,6	65	2,6	0,67	0,01	0,63	0,01	1,52	0,09	1,06	0,05	248	5,8	24,4	1,0	341	5,6
	800 [2]	360 [2]	1352	0,5	72	3,4	1598	5,1	66	2,3	0,68	0,01	0,63	0,01	1,49	0,09	1,09	0,06	246	5,1	24,3	1,0	341	4,2
HN78	*Starting materials*		1350	2,0	116	6,0	1603	3,0	52	5,0	0,53	0,01	0,53	0,01	0,49	0,02	2,25	0,14	254	2,0	21,4	0,9	201	11,0
	500	24	1350	1,0	115	3,2	1608	0,6	52	2,0	0,54	0,02	0,52	0,02	0,52	0,02	2,21	0,07	257	1,1	23,1	1,4	178	20,8
	500	240	1350	1,4	112	2,0	1608	0,3	46	1,2	0,56	0,01	0,55	0,01	0,50	0,02	2,43	0,05	259	1,3	18,6	1,3	213	16,8
	500	1080	1349	2,6	119	5,3	1608	0,5	49	4,3	0,58	0,01	0,56	0,02	0,53	0,02	2,47	0,14	260	2,8	19,3	2,3	230	24,6
	600	24	1342	0,8	115	0,5	1608	5,0	44	1,0	0,61	0,01	0,58	0,01	0,54	0,02	2,60	0,02	266	0,7	16,3	0,7	254	9,8
	600 [1]	24 [1]	1340	3,6	126	7,5	1605	4,1	52	4,2	0,62	0,02	0,58	0,02	0,59	0,03	2,44	1,16	264	1,2	20,7	2,3	246	24,4
	600	240	1340	0,9	114	4,1	1609	3,4	45	1,1	0,66	0,01	0,61	0,01	0,63	0,02	2,51	0,07	269	3,3	16,6	0,3	299	14,9
	600	1080	1342	1,0	107	5,1	1604	3,8	47	1,7	0,68	0,01	0,63	0,01	0,76	0,02	2,92	0,09	263	3,9	17,0	0,5	321	16,6
	700	24	1344	1,1	109	4,1	1605	3,8	50	2,2	0,69	0,01	0,65	0,02	0,81	0,02	2,18	0,10	261	4,5	18,0	0,7	332	10,9
	700	240	1352	0,8	94	3,7	1600	1,0	60	1,9	0,70	0,01	0,64	0,01	1,12	0,04	1,58	0,05	248	1,0	21,7	0,7	333	13,4
	700	1080	1352	0,8	88	3,4	1598	4,2	60	2,5	0,70	0,01	0,64	0,01	1,22	0,04	3,87	0,34	246	4,5	23,2	1,3	330	6,0
	800	3	1348	0,7	85	2,1	1600	3,8	50	1,7	0,70	0,01	0,67	0,01	1,10	0,03	1,69	0,07	252	4,1	20,0	1,1	329	5,5
	800 [2]	3 [2]	1349	0,6	84	3,1	1599	1,0	51	1,7	0,71	0,01	0,67	0,00	1,13	0,03	1,64	0,04	250	0,9	20,3	0,4	326	2,4
	800	8	1350	1,0	83	3,9	1598	4,2	57	2,4	0,70	0,02	0,65	0,01	1,23	0,04	1,45	0,08	248	4,5	21,9	1,2	330	8,0
	800 [2]	8 [2]	1350	0,4	79	1,8	1598	1,1	53	1,5	0,71	0,01	0,67	0,01	1,25	0,03	1,50	0,04	249	1,1	21,0	0,5	327	3,4
	800	24	1350	0,9	61	3,1	1597	0,9	52	2,1	0,69	0,01	0,69	0,01	1,64	0,09	1,17	0,07	247	1,0	22,8	0,9	333	6,6
	800 [2]	24 [2]	1352	0,7	72	1,4	1597	0,5	57	1,7	0,72	0,01	0,67	0,01	1,49	0,05	1,27	0,03	245	0,8	22,8	0,5	320	3,2
	800	72	1352	1,4	76	6,6	1596	3,2	61	2,4	0,69	0,02	0,65	0,01	1,36	0,1	1,26	0,12	244	3,1	23,5	0,8	333	9,5
	800 [2]	72 [2]	1351	1,2	76	4,7	1597	3,8	59	3,1	0,68	0,02	0,65	0,01	1,31	0,05	1,28	0,1	246	4,5	23,2	1,1	338	9,6
	800	360	1353	1,2	76	2,4	1596	3,5	68	2,8	0,69	0,01	0,64	0,01	1,47	0,07	1,11	0,05	242	3,3	26,1	0,8	334	5,3
	800 [2]	360 [2]	1352	0,9	68	3,1	1596	4,2	64	2,8	0,70	0,02	0,66	0,02	1,61	0,09	1,07	0,03	243	4,5	25,7	1,1	331	9,1

[1] wet 1:2 wt% H2O [2] we[a] Lhafid et al., 2010 ; [b] Beyssac et al., 2002 ; [c] Barker, 1988

V.3.2 Kinetics calculation

As shown above, the IR ratio evolution is monotonous in the range that we are interested in. In this section, we will explain in detail how to obtain the kinetic laws that link the duration to temperature, following the method presented in Nakamura et al. (2020, 2017) for higher degree of crystallinity (i.e. late graphitization stage). Previous studies for simple evolution proposed to use a power rate model or the Johnson-Mehl-Avrami (JMA) model (Huang, 1996; Muirhead, 2012), however, carbonization, similar to graphitization, is not a simple chemical reaction but the result of simultaneous reactions (formation of BSU, devolatilization or crystal growth). Therefore, in order to model the complex chemical evolution of the CM evolution, we preferred to use the method proposed by Nakamura et al. (2017), using a sigmoidal function with the following equation:

$$f(T,t) = \frac{IRmin + (IRmax - IRmin)}{1 + \left[\frac{thalf}{t}\right]^h} \quad (1)$$

Where t_{half} and h are respectively the inflection point and the order of reaction, called "Hill coefficient" of the sigmoid function. The parameter t_{half} could be described following an Arrhenius relation as:

$$thalf = A \exp\left(\frac{-m}{T}\right) \quad (2)$$

Combining the equations (1) and (2), we obtained:

$$f(T,t) = \frac{IRmin + (IRmax - IRmin)}{1 + \left[\frac{A \exp\left(\frac{-m}{T}\right)}{t}\right]^h} \quad (3)$$

Where IRmin and IRmax are respectively, the minimum and maximum IR values (i.e. 0.5 and 1.6), A is the intercept and m the slope of the Arrhenius plot, T and t are the temperature and the time of heating, respectively.

After analyzing samples using the RSCM and obtaining the IR the first step consists in a superposition model. In others words, all the data, obtained for different temperatures, have to be transposed to a single reference temperature. This transposition step has to be repeated for at least two different reference

temperatures. In our case, we chose 500°C and 600°C and obtained two diagrams that show a sigmoid evolution of the IR as a function of the temperature (Figure V.3). Using Matlab and the fitting toolbox, the fit of the two functions (3) is obtained and respective parameters presented above are defined (i.e. t_{half} and h). This fit is called master curve (Figure V.3). The final step consists in plotting the Arrhenius relation for each temperature and the straight-line obtained gives the A and m parameters of this relation. In possession of all the parameters needed in the equation (3) (Table V.3), it is now possible to calculate for each pair heating temperature and time the corresponding IR.

Table V.3 : Constants obtained from the Arrhenius plot for the calculation of kinetics for 18NOB01A and HN78

Constant	**Value**	
	18NOB01A	HN78
IR_{min}	0.5	0.5
IR_{max}	1.6	1.6
A	7.289E-10	1.049E-08
m	-30921	-27905
h	0.42	0.45

Thanks to this relation, isoplots of IR, varying from 0.5 to 1.6 values, have been drawn with natural temperature and time values for these two samples (Figure V.III). Plotting natural data of IR and respective calculated metamorphic peak temperature, we tested our kinetics models for both starting materials. Modelled geological times obtained are in agreement with the natural data measured in the field. In this chapter, the kinetics calculated for the immature shale (18NOB01A) have been used to predict in experiments the evolution of CM as a result of application of temperature. Furthermore, the comparison on low-strain and high strain domain was carried out to assess the effect of strain on CM. In Chapter VI, the kinetics model from the poorly mature shale (HN78) has been adapted for short exposition time of heat generated by seismic events in poorly mature CM.

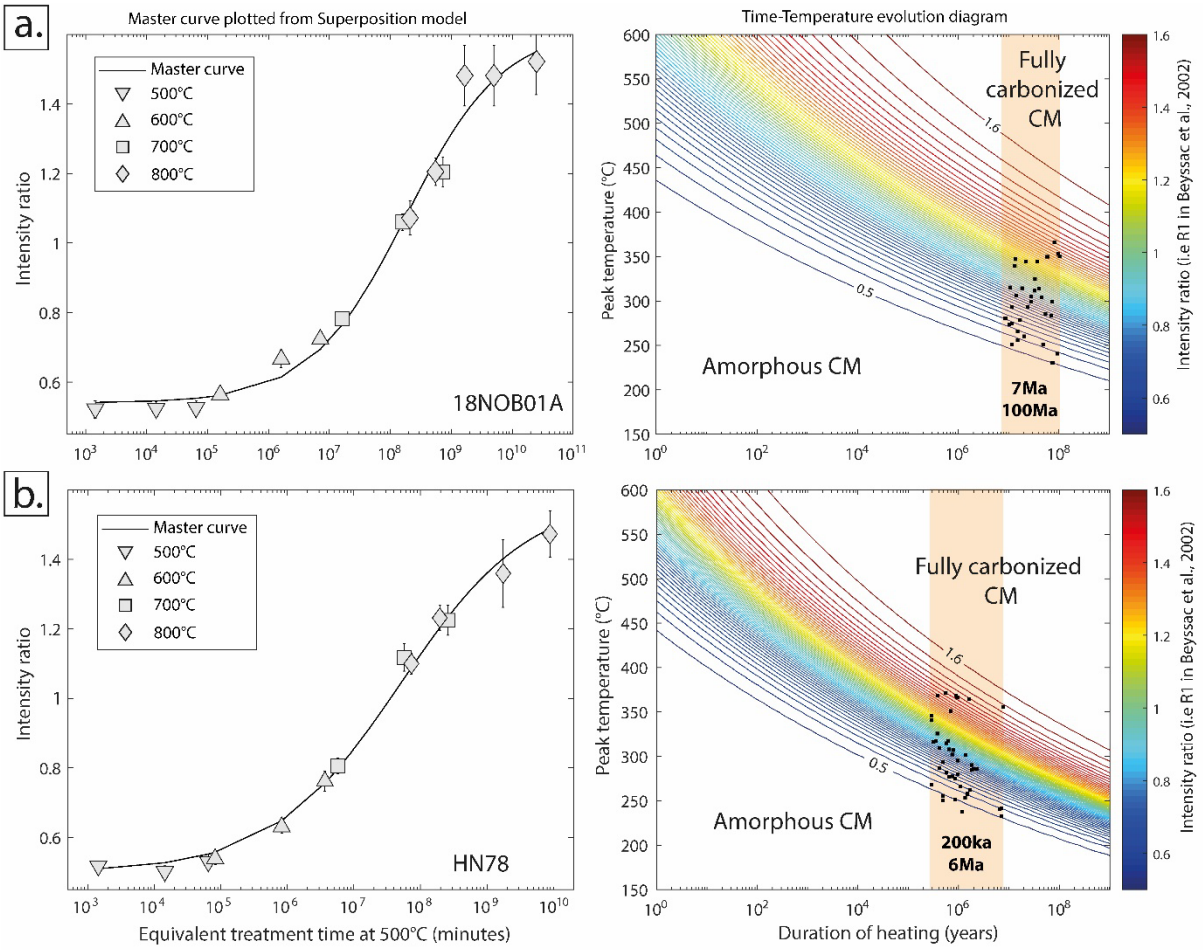

Figure V.3: Master curves resulting for the superposition model and isoplot of the intensity ratio for 18NOB01A ***(a)*** *and HN78* ***(b)****. Black squares represent IR measured on natural samples from the Shimanto Belt with respective calculated RSCM temperatures. Orange rectangle is the range of time necessary to reach this IR for the temperature given used to control the kinetics model.*

V.4 Results

This study includes 8 Paterson Rig apparatus and 4 solid-medium Griggs apparatus experiments with the aim of reproducing non-seismic deformed zones at very slow deformation rate. With Paterson Rig apparatus, 5 experiments have been carried out in shear assembly and 3 in co-axial mode on cylinder based on several problems met during the deformation experiments. With the Griggs apparatus, 2 experiments have been carried out at constant deformation rate in the "Tullis-modified" Griggs apparatus and 2 supplementary in the new Griggs apparatus at constant load. The detailed description of these apparatuses, the deformation assemblies and the experimental conditions are provided in Chapter III.

Proceedings, failures and refinement are explained in the following apparatus by apparatus on the mechanical data section. In the microstructural and RSCM sections, the focus has been made on 4 Paterson Rig apparatus (PP633, PP636, PP638 and PP641) and 4 Griggs apparatus experiments (T609BM, T610BM, OR87BM and OR92BM).

V.4.1 Mechanical data

The first part of the mechanical data will describe succinctly the deformation experiments of the Paterson Rig apparatus and the second part the Griggs apparatus experiments. The assembly and the deformation mode will be described with the respective mechanical data and eventually failures that occurred in the course of experiments.

V.4.1.1 Paterson Rig experiments

All experiments carried out using the Paterson Rig apparatus have been done using the co-axial deformation mode of the machine. However, the sample assembly evolved along experiments in order to reproduce shear or co-axial deformation using respectively 45° cut alumina pistons or cylinders. Experiments have been run at 150MPa of confining pressure and 600°C or 700°C with a heating rate of 4.5°C/min similar to the one used in the thermal maturation experiments. Experiments PP629 to PP636 are in shear-mode while PP638 to PP649 are in co-axial mode. All experimental conditions and settings are summarized in Table V.4.

PP629

The first experiment consists in a column assembly in shear. Powdered sample has been placed between two 45° cut pistons in porous alumina and manually compressed. When the required temperature was reached, the deformation started and the deformation rate was set at 0.1 $\mu m.s^{-1}$. A large amount of compaction is observed in this sample (Figure V.4a), which represents the half of the vertical displacement. In addition, at the end of the experiment the stress reached to ca. 300MPa, being approximately 65kN in terms of axial force, close to the theoretical maximum value accepted by the apparatus. The deformation has been stopped after 5 hours and 1.4mm of displacement, corresponding to ca. 2mm of shear displacement. After cutting the sample, we observed that the quantity of powder was insufficient and needed to be increased.

PP630

The second experiment in shear-mode is similar to the previous but with a higher quantity of powder. To focus mainly on the deformation and compact quickly the powder, the deformation rate has been set at $1\mu m.s^{-1}$ until the straight curve shows signs of bending. This displacement was linear and the stress reached to high values around 350MPA. After reaching the first signs of bending, the deformation rate was reduced to $0.1\mu m.s^{-1}$ for the rest of the experiment (Figure V.4b). The stress continued to increase gently until it reached a plateau after ca. 2 hours and 30 minutes at 400MPa, equivalent to an axial force of 68kN. After 6 hours of deformation the load cell is stopped and the shear displacement reached to 3.43mm. However, no deformation was observed along the sample assembly but the porous alumina 45° cut plan showed an undulose plan on the contact (Figure V.4b).

In summary, the two first experiments using the Paterson Rig apparatus have shown the limits of our assembly. Indeed, the porous alumina let the water go out from the sample and the dehydration of clays in the powder generated a ceramic-like material that turned out to be stronger than the porous alumina used for the shear pistons. We decided to improve our assembly using non-porous alumina pistons which are stronger than the porous ones as shear pistons. In addition, we flushed the sample with argon pore

fluid, in order to prevent the oxidation of CM. The explanation of the last point is made in detail in Chapter III.

PP632

During this experiment the powdered sample is placed between two shear pistons cut at 45° and compacted by hand using a specific manufactured tool. When the required temperature is reached the deformation is set at 0.1µm.s^{-1}. The stress curve showed a steep slope (Figure V.4c). The value of stress reached is lower than the one in the previous experiments using porous alumina when a first sharp stress drops to 40MPa that corresponds to a 27µm displacement occurred at around 70MPa (Figure V.4c). A second 15 µm quick displacement, corresponding to a 20MPa stress drop occurred and the stress began to increase drastically that suggested a rupture of the iron jacket. The jacket rupture produced a dehydration process of the sample and an important hardening. After a third rupture, the experiment was stopped after 7 hours of deformation with a 3.5mm of shear displacement. The sample assembly was cut at the middle and we observed that slip localized along the boundary between the sample and the top shear piston, without any deformation in the core of the sample. Therefore, all the deformation was concentrated in a very thin zone, accordingly, extremely fine-grained material could be observed (Figure V.4c).

PP633

Based on the brittle behavior of the previous experiment, it was decided to reduce the deformation rate by half. During loading, the deformation rate was set at 0.5µm.s^{-1} and before the value of sharp stress drop observed in the experiment PP632, it was reduced at 0.05µm.s^{-1}. However, even at this deformation rate, at approximately 65MPa, an instantaneous drop of the stress occurred with the same amplitude of stress drop with a displacement of 45µm. The stress stayed constantly at 35 MPa after this rupture and a second drop occurred 3 hours and 30 minutes after (Figure V.4d). To avoid dehydration, the experiment was stopped with a total shear displacement of 1mm. The sample column presented a very slight deformation, and after cutting the sample, a rupture plan has been observed between the sample and the bottom shear piston where fractured and crushed structures are noticed.

PP636

In order to reduce the occurrence of slip between the sample and one of the shear pistons, the plans at 45° have been made rough. The same experimental conditions than in the PP633 have been set. After 1 hour and half, at a stress of 130MPa a first stress drop of 50MPa occurred with a displacement of ca. 90µm. The stick-slip event was been followed by continuous deformation of 1.2 mm along localized along the rupture plan with a constant stress that slightly increase from 70 to 80MPa (Figure V.4e). A second drop occurred with a short displacement of 20µm and the experiment was stopped. Here the shear displacement reached was 1.6mm. The sample showed a shear plan localized between the top shear piston and the sample and very little deformation distributed in the sample itself. In addition, thanks to the rough plan, twice value of stress reached in previous experiments (PP632, PP633) has been reached but we did not avoid the rupture.

In summary, due to the low confining pressure used during the shear experiments with the Paterson Rig apparatus, we observed systematically stick-slip events, and shear was always localized in very thin zones, often at the limit between pistons and sample, where grain size reduction was extreme. Based on these results, and in order to avoid the occurrence of stick-slip events, we decided to work on co-axial mode using ca. 30 mm cylinders drilled perpendicular to the main bedding of the immature shale.

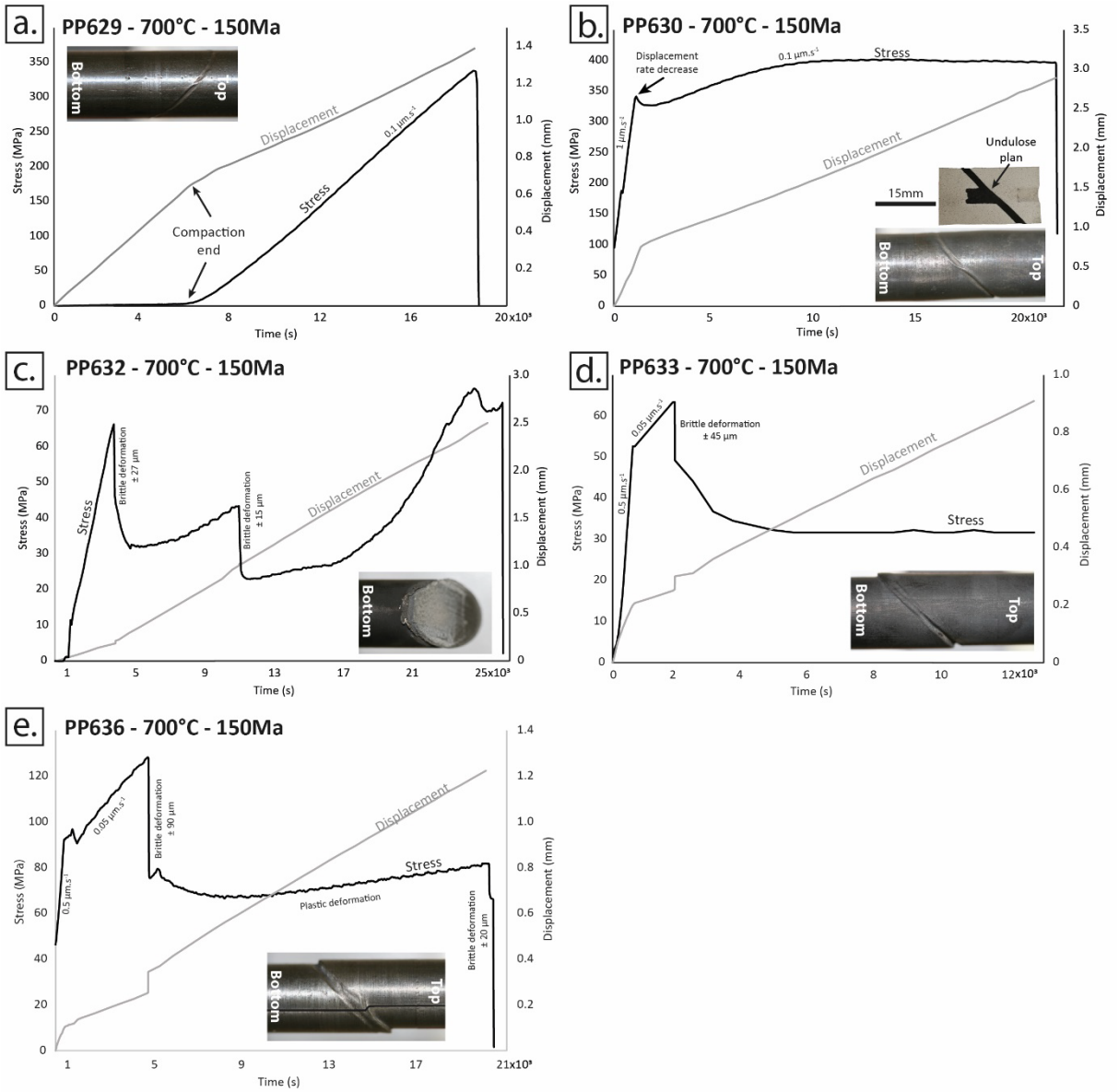

Figure V.4 : Paterson Rig mechanical data obtained for shear assemblies deformed at 700°C and 150MPa representing the vertical displacement and the σ_1 stress as a function of time.

In opposition to the shear-mode assemblies, used in the 5 previous experiments, here the sample is a cylinder of 15mm in diameter and approximately 30mm in length placed between full alumina pistons. The same preparation consisting in removing the oxygen from the column before the experiment has been done.

PP638

This first experiment in the co-axial mode of deformation has been realized on the same conditions as the previous ones in shear. Along the initial stage of loading, the deformation rate was set at 0.5 µm.s^{-1}

and when we reached the critical stress value (i.e. ca. 70MPa) where ruptures occurred in the previous experiments, it was reduced at 0.1 $\mu m.s^{-1}$. Through times, the stress increases, becoming more and more flat, up to reach to a maximum value in stress, then, which was followed by a slight weakening. During this phase, the displacement rate remained constant. Few minutes before the 5^{th} hour of deformation a sharp stress drop of 50 to 60MPa occurred at 120MPa corresponding to a 60µm displacement (Figure V.5a). The stress remained constant until the end of the experiment utile a second drop occurred generating a 20µm displacement. The result of this 2.5mm deformation experiment indicates the generation of complex conjugate deformed fractures which do not show any distributed deformation zone. Macrostructures observed along these fractures concern mainly crushed rocks showing a bimodality of grains sizes. Therefore, we concluded that the deformation rate needed to be drastically reduced.

PP641

In the PP641 experiment, the deformation rate has been reduced by 2.5 times at 2 to 0.025 $\mu m.s^{-1}$. However, the reduction of the deformation increases importantly the time of experiment and therefore the temperature has to be adapted and reduced to 600°C in order to keep the required degree of CM crystallinity. During this experiment, the motor of the load cell has been set in order to maximally reduce the deformation rate. After the stress consistently increases up to 160MPa, we reduced the deformation rate to 0.015$\mu m.s^{-1}$. However, at 180MPa, a stress drop of 110MPa occurred with a displacement of 135µm (Figure V.5b). This rupture is followed by a new phase of 1mm deformation at constant stress before a second stress drop, then the experiment was stopped. This sample shows complex conjugate shear zones with an angle of 60° to the long axis of the sample (i.e. vertical) with a width of 10 to 40µm. During this experiment, a shortening of 3 mm is observed on the sample and the strain rate estimated during the first phase of constant stress is in the order of 10^{-7} s^{-1}. Taking in consideration the angle between the vertical displacement and the shear plans, the width of the shear zones and the general strain rate, the local strain rate that occurred during two stress plateau is in the order of 10^{-4} s^{-1} (local strain rate = (Vertical strain rate / Cos(angle Vv and Vt)) / Shear-zone width). The sample after the experiment

shows a complex conjugate network of shear-zones. These shear-zones combined crushed rocks in opened fractures with stretched clasts along these fractures.

PP649

In the last experiment PP641, stick slip events occurred. In order to minimize the occurrence of such stick-slip events, we decided to carry out a further experiment under constant load on a cylinder sample. The stress was set in such way to be enough close to similar deformation rate as in the last experiment but below the stress level at which rupture occurred. The stress was successively set at 115, 130, 140 and 155MPa in order to continue to deform the sample (Figure V.5c). No rupture has been observed during the experiment. A total shortening of 2.3mm has been measured at the end of the experiment, however, no localization of the deformation has been observed along shear plan.

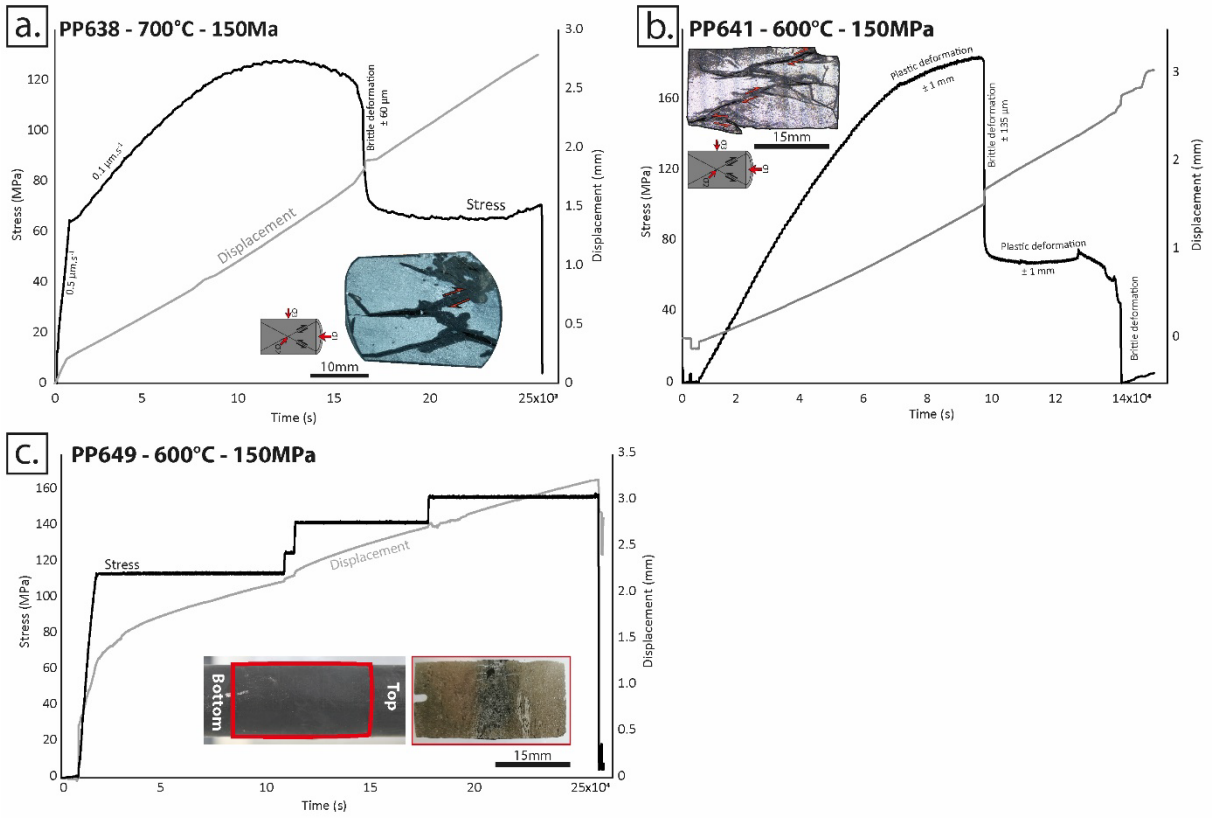

Figure V.5: Paterson Rig mechanical data obtained for co-axial assemblies deformed at 600°C or 700°C and 150MPa representing the vertical displacement and the σ_1 stress as a function of time.

In summary, all but one experiments in the Paterson rig showed stick slip events. Suppressing these brittle deformation events requires to reduce drastically the deformation rate, up to a point where the

duration of experiments increased unreasonably. Indeed, the Paterson Rig apparatus is composed of several rubber O-rings and the long exposition to heat and argon gas causes leak of gas and uncontrolled decrease of the confining pressure. Therefore, this apparatus is not adapted to long experiments and the complexity of the apparatus requires a constant monitoring. In order to enhance our chances to reproduce distributed shear-zones, without microfaults, as the ones observed in natural samples, we decided to carry out experiments using the solid-medium Griggs apparatus. This apparatus provides advantages comparing with the Paterson Rig: (1) the fH2O is higher than in the Paterson rig, so that the clays in the assembly do not dehydrate, or at a slower rate than in the Paterson rig, (2) a solid-medium confining pressure that allows users to proceed long time experiments without leak, hence enabling lower strain-rate experiments. In addition, using the Griggs apparatus it would be possible to explore the catalytic effect of pressure on the CM kinetics comparing experiments with similar conditions of work except the pressure. However, in these experiments, the catalyzing effect of deformation could not be compared with our CM kinetics calculated previously. In the next section, all mechanical data of the Griggs experiments are presented.

V.4.1.2 Griggs apparatus experiments

Four Griggs experiments have been carried out during this study. First two (T609BM and T610BM) at constant deformation rate are realized in the "Tullis modified" apparatus and other two (OR87BM and OR92BM) at constant load in the new-generation apparatus. These experiments have been carried out at a temperature range from 400 to 600°C and at 1GPa. Sample assemblies correspond to a slice of immature shale between two shear-piston cut at 45° and sealed in a Pt-Jacket. Detailed descriptions about the method, sample assembly and experimental conditions are provided in Chapter III. All experimental conditions and settings can be found in Table V.5.

T609BM and T610BM

T609BM and T610BM have been carried out respectively at 600°C in a NaCl solid medium and at 400°C in a KI solid medium (Figure V.6a) and an equivalent strain rate of $10^{-5}s^{-1}$ has been set to deform samples. In T609BM from the beginning of the experiment until to strain $\gamma = 2$, the differential stress increased consistently during the loading phase. From the $\gamma = 2$ until to the end of the experiment, when

$\gamma = 3$ is reached, the differential stress curve softened. However, due to the hardening occurred during the experiment he peak stress was not reached during this experiment but approached around 350MPa (Figure V.6b). In opposite, at 400°C in the experiment T610BM, the peak stress was attained at lower strain ($\gamma = 1.5$) around 950MPa. This peak stress is followed by the drastic reduction of the differential stress until to 600MPa (Figure V.6b). After the stabilization of the differential stress at 600MPa and when $\gamma = 3$ was reached the deformation was stopped and the sample was quenched.

After the preparation of the samples for microstructural and RSCM observations, we noticed that the deformation was mostly brittle and localized along a major slipping zone of 10 to 50µm, in agreement with the rupture of the Pt-jacket that we observed when we took the sample out of the rig. Based on these observations we decided to carry out experiments in constant load in order to reduce the strain rate.

OR87BM

This experiment has been carried out at 600°C – 1GPa and stabilized for 17 hours after reaching the required conditions. Constant load of 200MPa has been applied to the sample and progressively increased in order to find a good ratio between the strain rate and the duration of the experiment. The final constant load applied corresponded to a differential stress of 500MPa that progressively increased until to 700MPa due to the area evolution of the sample (Figure V.6c). At the end of the experiment, the strain reaches to $\gamma = 5.34$ with a constant rate of $10^{-6}s^{-1}$ in average. Deformation observed mostly occurred during the stage when the constant load was set at 500MPa. This deformation is localized along a main shear band where fractured material is observed. In addition, in the surrounding of the main localized deformed zone C-S ductile structures are observed.

OR92BM

This experiment has been realized at the same conditions as the previous except for the stabilization time at 600 – 1GPa reduced at 30 minutes. At the beginning of the deformation stage, the constant load was set at 500MPa. However, due to the time of stabilization shorter than before and as a consequence a softer sample, the deformation was so quick. Indeed, the strain rate was measured at approximately

$10^{-4}s^{-1}$ and the Goetze criterion has been overpassed at $\gamma = 7$. The distribution of the deformation and the thickness of the sample are very heterogeneous, therefore only the condition of bulk stress on the limits of the sample will be described in the following. Due to the large displacement, the rupture of the Pt-jacket was total, separating the sample in two distinct pieces. Therefore, after this total rupture, mechanical data are no more representative. However, beforehand the stress showed more and more increasing values until to $\gamma = 11$ (Figure V.6d). After $\gamma = 11$, the stress increases sharply until reaching to 2500MPa of differential stress, due to the intense diminution of the contact surface of the sample on each forcing bloc. Finally, the experiment was stopped when the strain reached a value of $\gamma = 15$ and a differential stress of 2500MPa. The rupture in the sample was total and separated in two parts: the top and bottom pieces. On the rupture plans, in the middle of the sample, a vitreous localized plan has been observed on the top surface of the bottom piece of the sample. Under the vitreous plan, ductile strain gradient is observed from very stretched minerals to undeformed clasts.

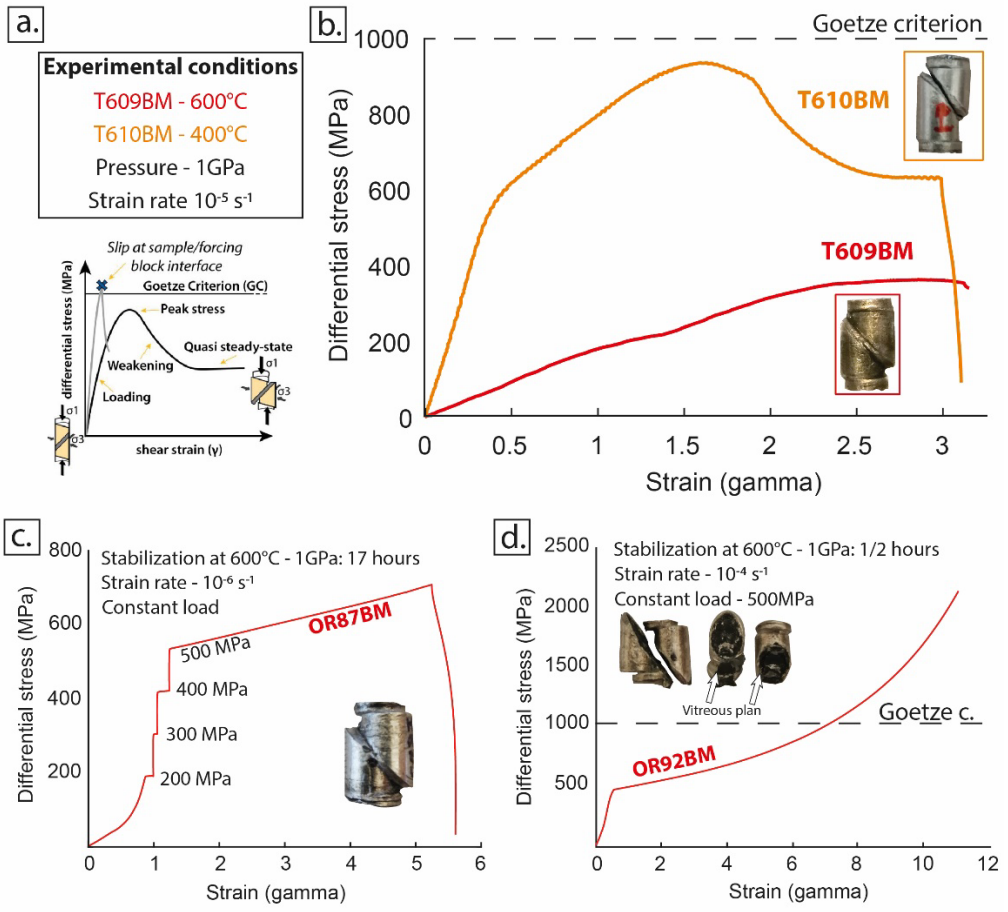

Figure V.6 Mechanical data from the solid-medium Griggs apparatus experiments. ***a.*** *Experimental conditions used in the "Tullis-modified" apparatus and set of terms using to described the mechanical data (from (Mansard, 2019).* ***b.*** *Differential stress versus strain (gamma) curves obtained for deformation experiment at constant strain rate for the experiments T609BM and T610BM.* ***c.*** *and* ***d.*** *Differential stress versus strain (gamma) curves obtained for deformation experiment at constant load obtained for the OR87BM and OR92BM experiments.*

In summary, Paterson Rig and Griggs apparatuses experiments have been carried out in order to reproduce viscous shear-zones. Many results have been obtained through these experiments with the localization of the deformation along conjugate or narrow shear-zones. Viscous behavior associated with brittle behavior is spotted along these deformed zones showing crushed zone and elongated mineral in viscous shear-zones. Paterson and Griggs rig experiments have shown in many instances stick-slip events, and the differential stress was always very high, close to the Goetze criterion (but for the constant load experiment). The microstructures of deformation show systematically very large gradients of strain, with very thin zones of localized deformation cutting across completely undeformed domains. Experiments PP633 and PP636 are associated with a rupture plan at the interface between the sample and the shear piston where the deformation is located. PP633 and PP638 show a brittle deformation

located along fractures of crushed zones. PP636 and PP641 show important stretching in the deformed zone. Griggs apparatus experiments OR87BM and OR92BM also show intense stretching on the sample when the deformation is mostly brittle in the two samples created using the “Tullis-modified” Griggs apparatus (T609BM and T610BM).

In the following, we will be interested in the microstructures, mineralogical and chemical evolutions of these samples and the associated response in terms of CM crystallinity using the RSCM.

Table V.4: Experimental conditions, settings and associated deformed structures of the Paterson rig experiments.

Experiments	Name	Deformation mode	Pistons	Time	Temperature	Pressure	Displacement rate	Displacement	Stick-slip	Ss. displ.	Stress drop	Strain rate	Conditions	Deformed structure
Paterson Rig	PP629	Shear	Porous alumina	5 hours	700°C	150MPa	0.1 µm.s^{-1}	1.4 mm	No	-	-	-	Pore fluid connected	Compaction only
	PP630	Shear	Porous alumina	6 hours	700°C	150MPa	0.1 µm.s^{-1}	3.5 mm	No	-	-	-	Pore fluid connected	Compaction only
	PP632	Shear	Non-porous alumina	7 hours	700°C	150MPa	0.1 µm.s^{-1}	3.5 mm	Yes	27µm / 15µm	40MPa / 20MPa	-	Pore fluid connected / Argon flushing	Vitreous plan along piston
	PP633	Shear	Non-porous alumina	4 hours	700°C	150MPa	0.05 µm.s^{-1}	1.0 mm	Yes	45µm	30MPa	-	Pore fluid connected / Argon flushing	Breccia layer along piston
	PP636	Shear	Non-porous rough alumina	6 hours	700°C	150MPa	0.05 µm.s^{-1}	1.6 mm	Yes	90µm	50MPa	-	Pore fluid connected / Argon flushing	Vitreous plan and foliated zone along piston
	PP638	Co-axial	Non-porous alumina	7 hours	700°C	150MPa	0.1 µm.s^{-1}	2.6 mm	Yes	60µm	50 to 60MPa	-	Pore fluid connected / Argon flushing	Conjugate micro-breccia fault
	PP641	Co-axial	Non-porous alumina	42 hours	600°C	150MPa	0.015 µm.s^{-1}	3.0 mm	Yes	110 µm	135MPa	5.7E10^{-7} s^{-1}	Pore fluid connected / Argon flushing	Conjugate fractures and shear-zones
	PP649	Co-axial	Non-porous alumina	72 hours	600°C	150MPa	Constant load	2.3 mm	No	-	-	2.7E10^{-7} s^{-1}	Pore fluid connected / Argon flushing	Homogeneous shortening

Table V.5: Experimental conditions, settings and associated deformed structures of the solid-medium Griggs type apparatus experiments.

Experiments	Name	Deformation mode	Apparatus	Type of displacement	Time	Temperature	Pressure	Peak stress	Displacement	Strain rate	Gamma	Pt-jacket rupture	Localized def.	Microstructures
Solid medium Griggs type apparatus	T609BM	Shear	Tullis-modified	Constant strain rate	34 hours	600°C	1000MPa	350MPa	1.5 mm	2.6E10^{-7} s^{-1}	3.1	No	Yes	Micro-breccia in narrow 20 to 50µm shear-zone
	T610BM	Shear	Tullis-modified	Constant strain rate	72 hours	400°C	1000MPa	950MPa	2.3 mm	2.2E10^{-7} s^{-1}	3.0	Yes	Yes	Micro-breccia in narrow 5 to 20 µm shear-zone
	OR87BM	Shear	New generation	Constant load	175 hours	600°C	1000MPa	-	3.1 mm	9.9E10^{-6} s^{-1}	5.3	No	Yes	S-C ductile structures / Fractured main shear-zone
	OR92BM	Shear	New generation	Constant load	20 hours	600°C	1000MPa	-	8.1 mm	5.0E10^{-4} s^{-1}	16	Yes	Yes	Ductile µm-strain gradient / Crushed zones

V.4.2 Microstructural analyses

In this section, the microstructural observations will be presented separating the main occurrence of brittle deformation (PP633, PP638, T609BM and T610BM) or ductile deformation (PP636, PP641, OR87BM and OR92BM) irrespective of the experimental apparatuses.

V.4.2.0 Starting material

The starting material 18NOB01 is an immature shale composed of a fine assemblage of Quartz – Albite – K-feldspar – Calcite – Mullite – Illite – Pyrite. The sample does not present any atypical microstructures and shows a non-organized structure without preferential orientation.

V.4.2.1 Brittle deformation

PP633

The PP633 experiment has been characterized by a rupture between the bottom piston and the sample interface. The sample assembly is composed on a plan where the powdered sample is placed at 45° and a furrow is drilled in the bottom shear piston in order to preserve undeformed sample during the experiment. The rupture occurred between this furrow and the sample and left an irregular plan at this place (Figure V.7a), whereas the contact with the top shear piston is straight. Hundreds-of-microns large zones are consolidated (i.e. preserved from brecciation) and separated by finer material composed of quartz and albite clasts in a matrix composed of phyllosilicates (Figure V.7a and 7d). In the contact with the top shear piston, a slight parallelized layer is observed where clasts and phyllosilicate sheets are reoriented parallel to the main shear direction (Figure V.7d). Between the furrow and the bottom of sample ~~limit~~, a 200µm-wide zone is observed with crushed material (Figure V.7b) that shows angular clast in a matrix composed of micrometer scaled acicular phyllosilicates and pieces of hard clasts with an important grain size reduction but without preferred orientation (quartz or albite) (Figure V.7c).

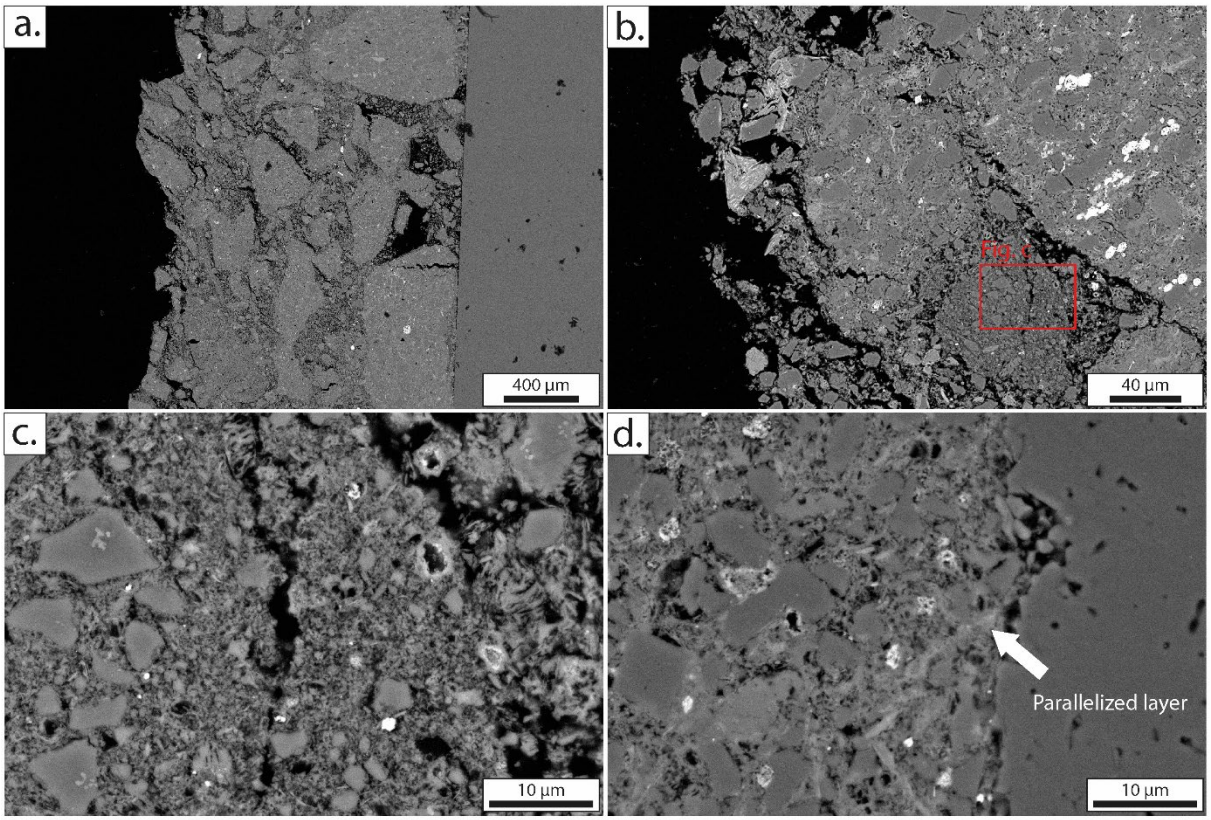

Figure V.7: Microstructures observed for the Paterson Rig experimental sample PP633. ***a.*** *General view from the top shear piston (right) to the rupture plan between the bottom shear piston and the sample.* ***b.*** *Close up view on the rupture plane showing a 200µm-wide brittle deformed zone* ***c.*** *Close up view in the last microns in the rupture plan showing angular clasts in a micron-size matrix composed of clasts and phyllosilicates* ***d.*** *Contact between the sample and the top shear piston showing a slightly preferential orientation of clasts and phyllosilicates with the alumina piston.*

PP638

The deformed cylinder obtained in the experiment PP638 is crosscut by a network of conjugate fractures characterized by a blackened zone (Figures V.5a and V.8b). Undeformed zones are composed of grains of quartz, albite and calcite in a phyllosilicates matrix where the porosity is important (Figure V.8a). The blackened zones are open because of decompression cracks that occurred at the end of the experiment and external limits with the undeformed zones are irregular. Blackened zones are characterized by almost similar mineralogical assemblages as the undeformed zones and do not show a clear preferential shape orientation of the clasts (Figure V.8b). However, in contrast with the undeformed rocks, the center of these blackened zones shows a lower porosity due to probably the recrystallization of micro-scale acicular phyllosilicates (Figure V.8c). In some locations, unload cracks are not observed along the slipping plans and the deformed zone is characterized by a micro-breccia

(Figure V.8d). These micro-breccias are composed of fractured clasts with more or less bimodal grain sizes of 2 to 4 µm wide and these clasts are embedded in a hundredth nano-scale clasts zone with angular shapes (Figure V.8e). In few locations (Figure V.8f), this micro-breccia could show a slight foliation but not significant comparing to the non-oriented zones.

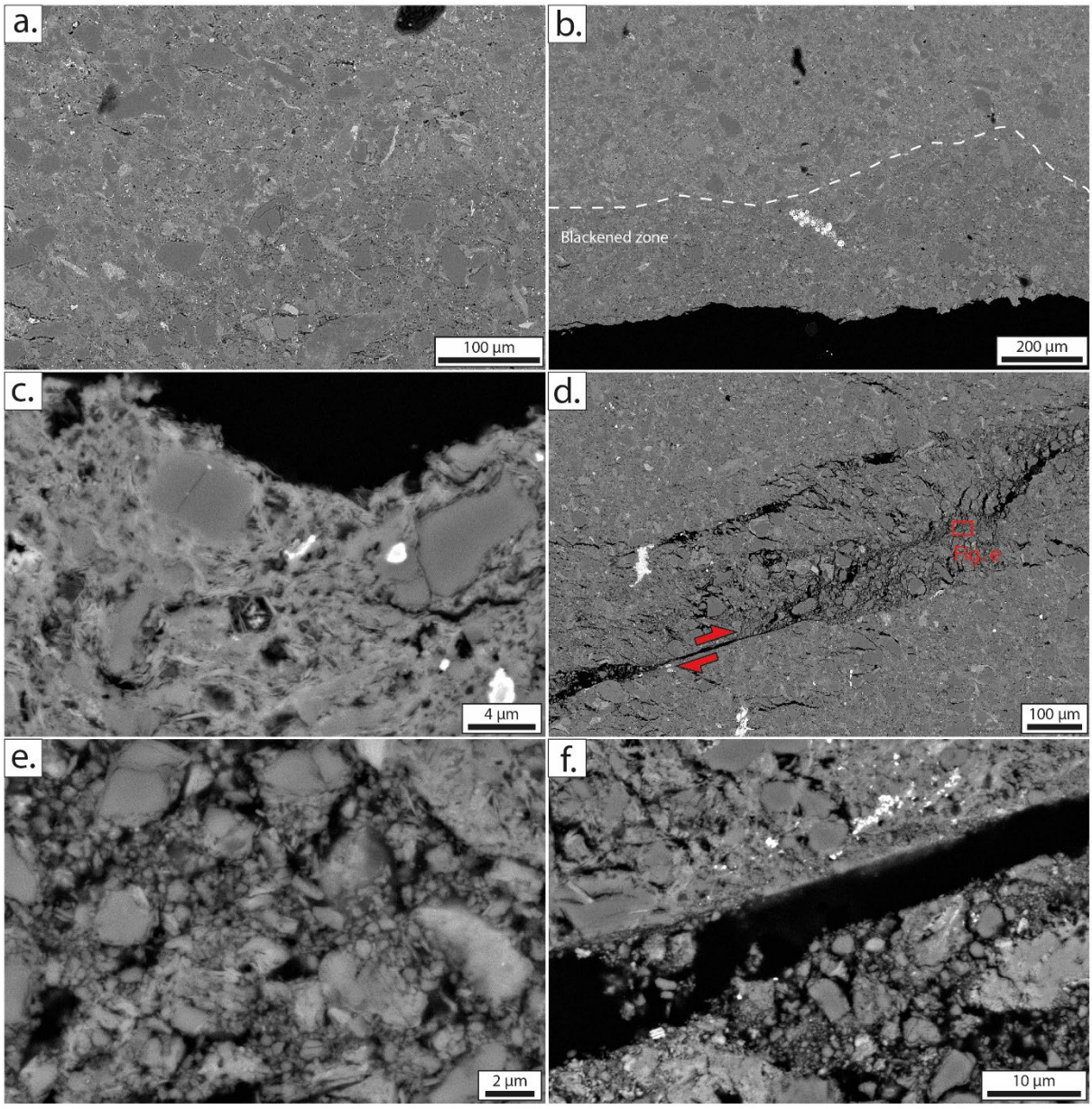

Figure V.8 : Microstructures observed for the Paterson Rig experimental sample PP638. ***a.*** *General view of the undeformed zone* ***b.*** *Limit between the blackened zone and the undeformed rock showing a diminution of the porosity.* ***c.*** *Internal zone of the blackened zone where recrystallization of phyllosilicates are observed.* ***d.*** *Micro-breccia located in zone preserved from the unload-cracks.* ***e.*** *Close up view in the micro-breccia showing a bimodal grain size distribution.* ***f.*** *Slightly reorientation of the micro-breccia.*

T609BM

In the sample T609BM, the deformation is localized along a main 20µm-wide fractured zone, which is associated with second-order fractures forming a conjugate network (Figure V.9.c). The main deformed zone is characterized by an important grain size reduction and is composed of clasts of quartz or albite, sometimes slightly reoriented at 45° from the main slipping direction (Figure V.9d). These clasts are embedded in a very fine matrix parallel to the rims of the fractures whereas no specific orientation is observed in the core of this zone (Figure V.9d). At the very near proximity of the fractured zones, clasts also show a preferential shape orientation. While going away from the fracture, a set of fractures parallel to the alumina forcing blocks are observed (Figure V.9c). The material between each fracture shows a weak sigmoid behavior forming S-C structure. In the undeformed zone, located on the extremities of the sample, the primary structure (i.e. ante-deformation) is characterized by sub-rounded grains with size ranging from 20µm to hundredth of microns, sometimes fractured, in a shaly matrix composed of clays, white micas and chlorites (Figure V.9a and b).

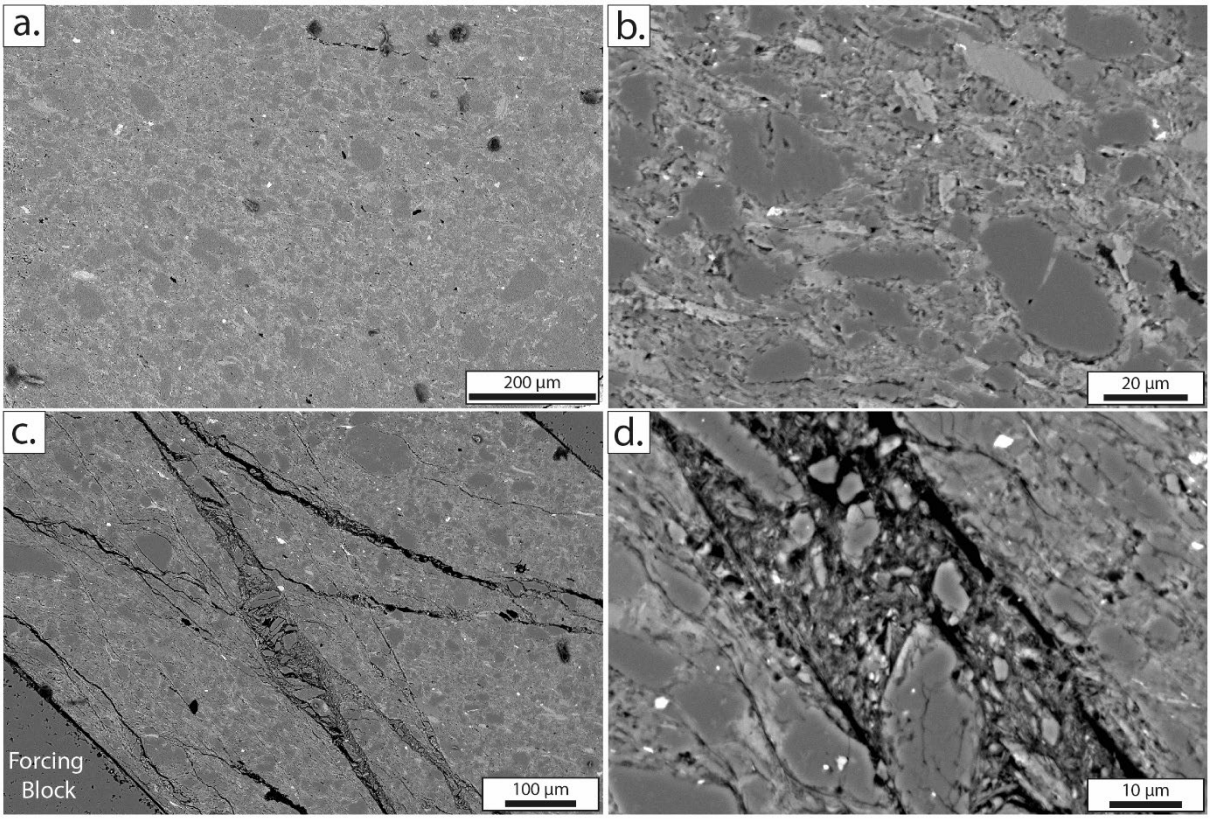

Figure V.9: Microstructures observed for the solid-medium Griggs apparatus experimental sample T609BM. ***a.*** *Undeformed zone large view* ***b.*** *Close up view of the undeformed zone showing the sub-rounded clasts of quartz or albite in a shaly matrix* ***c.*** *Main fracture where the deformation is located and surrounding from each shear forcing blocks* ***d.*** *Close up view in the main fracture showing the grain size reduction and the slightly preferential shape orientation of the clasts.*

T610BM

In the sample T610BM experimentally deformed at 400°C, the location of the deformation and the contrast between the deformed and undeformed zone is well marked (Figure V.10). The undeformed zone is characterized by the same material presented above, with tens of microns scaled sub-rounded grains in a shaly matrix (Figure V.10a). Similar to the Griggs experiments for the sample T609BM, the deformation is located along a main slipping zone of 10 to 20µm long. However, in comparison with this sample two deformation features are observed. In the close surrounding of the deformed zone a foliation at 45° is developed and tends to 0° at the contact with the deformed zone. This foliation is underlined by the phyllosilicates and calcite ribbons and by the shape preferential orientation of the clasts (Figure V.10b and 10c). In the core of the deformed zones, the deformation is characterized by a fine micro-breccia composed of angular clasts embedded in a shaly matrix showing an intense grain size reduction and a chemical evolution based on the BSE image (Figure V.10c). Sometimes the development

of a foliation is observed separated by shear planes forming slight S-C structures marked by soft mineral such as calcite (Figure V.10d).

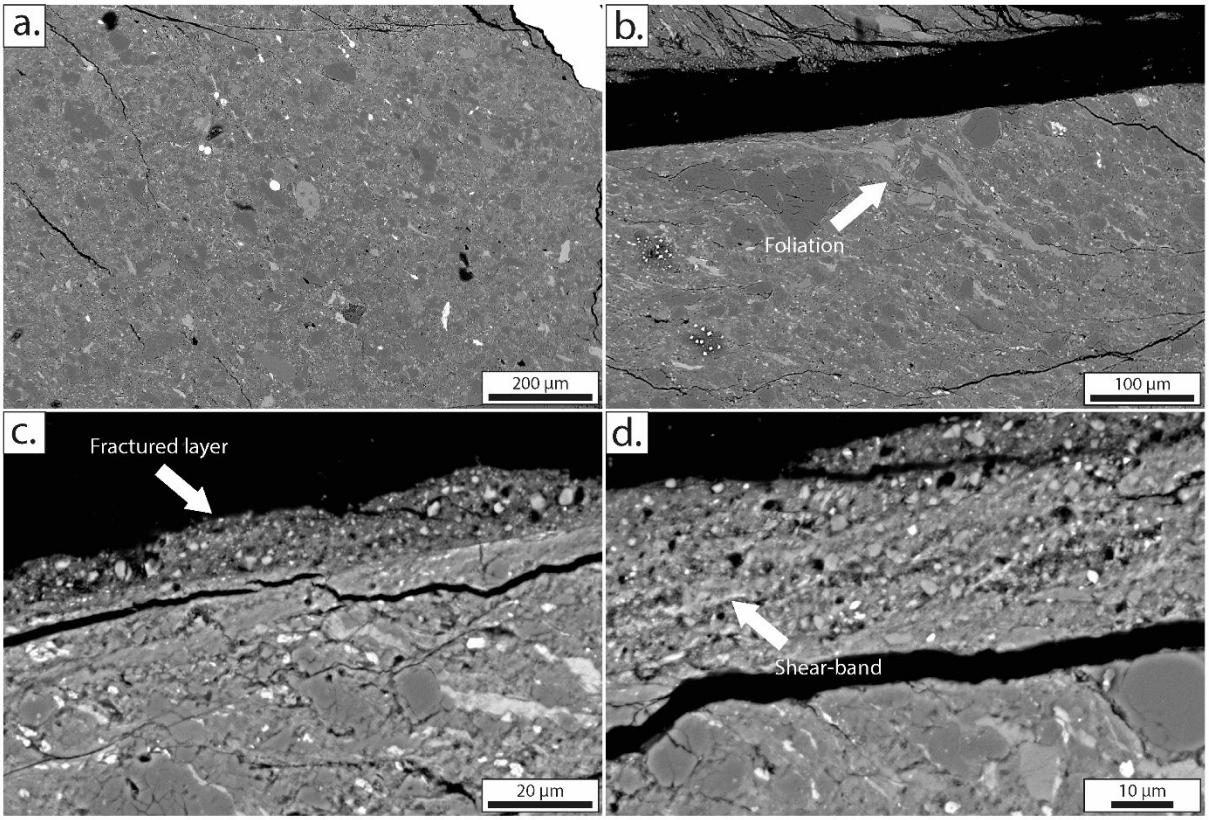

Figure V.10 : Microstructures observed for the solid-medium Griggs apparatus experimental sample T610BM. ***a.*** *Undeformed zone composed of sub-rounded clasts in a shaly matrix* ***b.*** *Vicinity of the main fractured zone showing the foliation development marked by phyllosilicates and calcite ribbons* ***c.*** *Close up view on the fractured layer on the rim of the deformed zone* ***d.*** *Development of S-C structures in the fractured zone.*

In summary, the brittle deformation observed in these four samples is characterized by the formation of micro-breccia composed of angular clasts in a more or less preferentially orientated matrix. The matrix is composed of micrometric clasts and phyllosilicates suffering of an important grain size reduction. The main difference between the low pressure (Paterson Rig experiment) and high pressure (solid-medium Griggs apparatus) is, in the Griggs-type experiments, the local development of S-C structures in the main deformed zone. In addition, the strain is more localized in the high pressure than in the low pressure experiments. In the following, the deformation microstructures, chemical and mineralogical evolution are presented for the ductile deformation.

V.4.2.2 Ductile deformation

PP636

The sample PP636 has been generated during an experiment where stick slip occurred. However, this rupture has been followed by a long displacement along this rupture plan that conducted to the formation of a narrow deformed zone presented in the following (Figure V.4e). The sample is composed of a homogeneous layer on all the width from the two shear pistons composed of large clasts of quartz and albite, sometimes fractured, embedded in a phyllosilicate matrix without preferential orientation (Figure V.11a and 11d). Approaching to the rupture interface between the sample and the top shear piston, a foliated zone of 10µm, richer in phyllosilicates, is observed where clasts show a lightly bending and the phyllosilicates reoriented from 45° to the parallelization to the slipping zone (Figure V.11b and 11c). We can notice the absence of angular clasts in this zone. On the contact between the sample and the alumina piston, a luminescent 2µm wide zone is observed where the material is totally parallelized and intensely stretched (Figure V.11b and 11c).

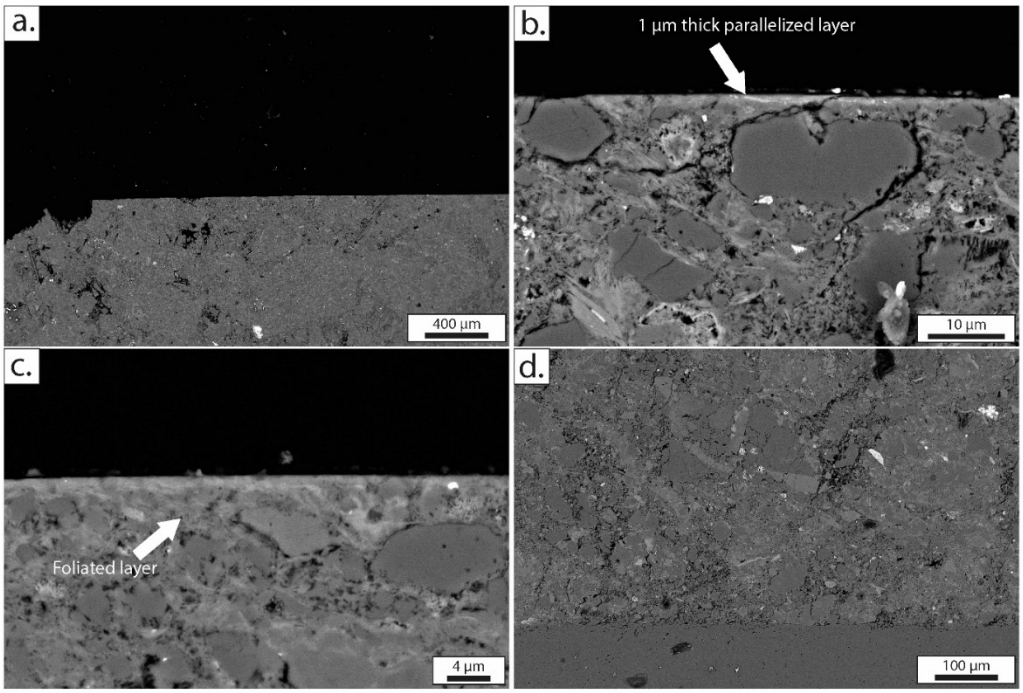

Figure V.11: Microstructures observed for the Paterson Rig experimental sample PP636. ***a.*** *General view of the sample from the bottom shear piston to the top shear piston (absent here)* ***b.*** *Close up view of the luminescent parallelized layer on the contact between the sample and the top shear piston* ***c.*** *Close up of the narrow foliated layer following the parallelized layer and the undeformed rock* ***d.*** *Close up view on the undeformed zone near the bottom shear piston composed of large clasts in a shaly matrix*

PP641

The sample PP641 has been generated from the co-axial deformation of a cylinder and the deformation is characterized by the development of a network of conjugate slipping zones. This network is often composed of unload-crack that conducted to the opening of the deformed zones. The deformation is characterized by the presence of brittle deformation through the formation of fractured zones (Figure V.12b and 12c). However, on the extremities of the deformed zones on four locations, shear-zones have been observed (Figure V.12) and look like anterior to the brittle deformation. These shear-zones are localized in narrow 20 to 40µm-wide zones and show an important development of foliation and the absence of porosity. The foliated layers present an intense stretching and grain size reduction, with grain size of the order of the micron (Figure V.12a to 12f). In some cases, S-C structures are observed with successive shear plans parallel to the main slipping zone and foliation, and sigmoid shapes are formed in between (Figure V.12d). EPMA maps have been obtained using XMapTools software, phase reconstitution has been done as well (Figure V.13). These maps indicate that in the shear-zone elements are mobile and show a diminution of Ca, Al and Fe whereas Na, K are concentrated (Figure V.13c). Based on phase maps, shear zones are characterized by the recrystallization of white micas and chlorite. In addition, the grain size and the concentration of the quartz and calcite clasts drastically decrease and the absence of albite is noticed (Figure V.13b). When quartz or albite clasts are still present in the deformed zone, the shape shows intense stretching and formation of ribbons. Juxtaposed to the shear-zone, sometimes, fractured zones are observed composed of micron-scale angular clasts of quartz, albite or phyllosilicates (Figure V.12b). Finally, the undeformed part of the sample, comprised between the conjugate slipping zones, is characterized by quartz, albite and calcite grains in a matrix composed of calcite, clays and phyllosilicates with an important porosity (Figure V.12g and 12h).

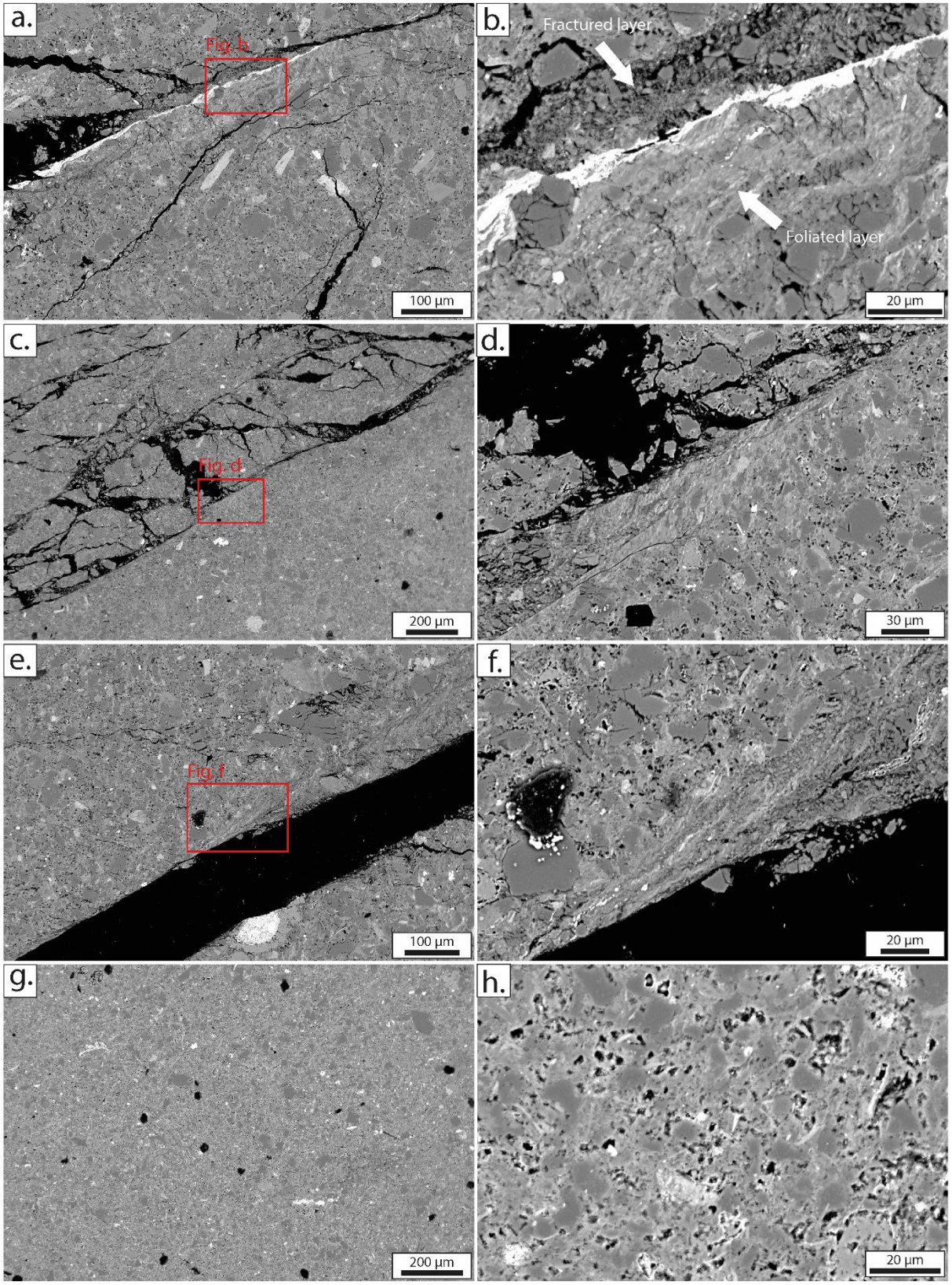

Figure V.12 : Microstructures observed for the Paterson Rig experimental sample PP641. ***a.-c.-e****. General view of the shear-zones and their respective surroundings* ***b.-d.-f.*** *Close up on the shear-zones showing a grain size reduction and the foliation development in narrow deformed zone* ***g.*** *General view of the undeformed rock* ***h.*** *Close up on the undeformed rock composed of clasts in a phyllosilicates matrix presenting an important porosity.*

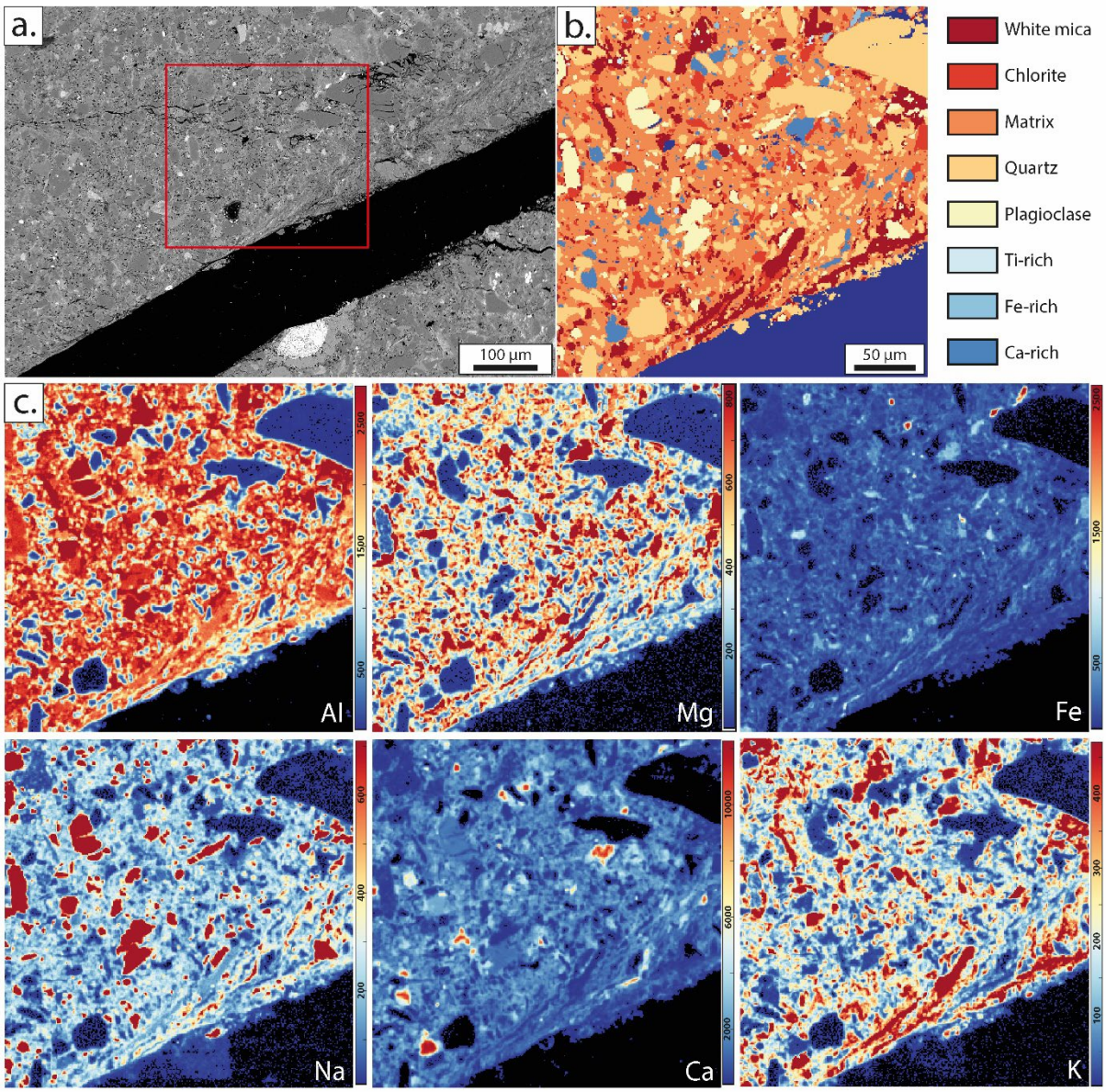

Figure V.13: EPMA elements and phases maps of PP641. ***a.*** *Location of the EPMA maps* ***b.*** *Reconstruction of the phases maps using the software XMapTools showing the mineralogical evolution through the strain gradient* ***c.*** *Elements maps obtained using EPMA showing the evolution of major elements : Al, Mg, Fe, Na, Ca, K.*

OR87BM

Sample OR87BM has been obtained thanks to a solid-medium Griggs apparatus deformation experiment at constant load with successive steps. Similar to the two first Griggs apparatus experimentally deformed samples described above, the deformation is localized along a main deformed zone with two microstructures (Figure V.14a). Indeed, the SEM observations indicate the cohabitation of fractured layer and foliated layer within this main deformed zone. Unfortunately, unload-cracks are present and hide the clear evolution without the preservation of the complete strain gradient. The foliated zone has

a width of ~ 10µm and is characterized by the reorientation of soft phases such as phyllosilicates or calcite ribbons (Figure V.14d and 14e). Fractured zones are observed juxtaposed to the foliated layers with a width of a few microns (Figure V.14f and 14g). Fractured zones can be identified with the intense grain size reduction where the distinction of the clasts is no more possible using FEG-SEM. However, a low angle foliation development is observed in these micro-breccia layers (Figure V.14g). In addition, it is important to notice that the whole sample is affected by deformation even if the main deformed zone is located along this main shear-plan. This rock is crosscut by several tiny shear-zones forming S-C structures separated by 10 µm and with the development of sigmoid shapes (Figure V.14c). In this foliated zone, clasts show grain sizes between few microns up to 20µm. The preserved zone from the deformation is located on the extremities of the sample where quartz and albite grains ranging from 20 to 100µm are observed and embedded in a shaly matrix that does not show any preferential orientation.

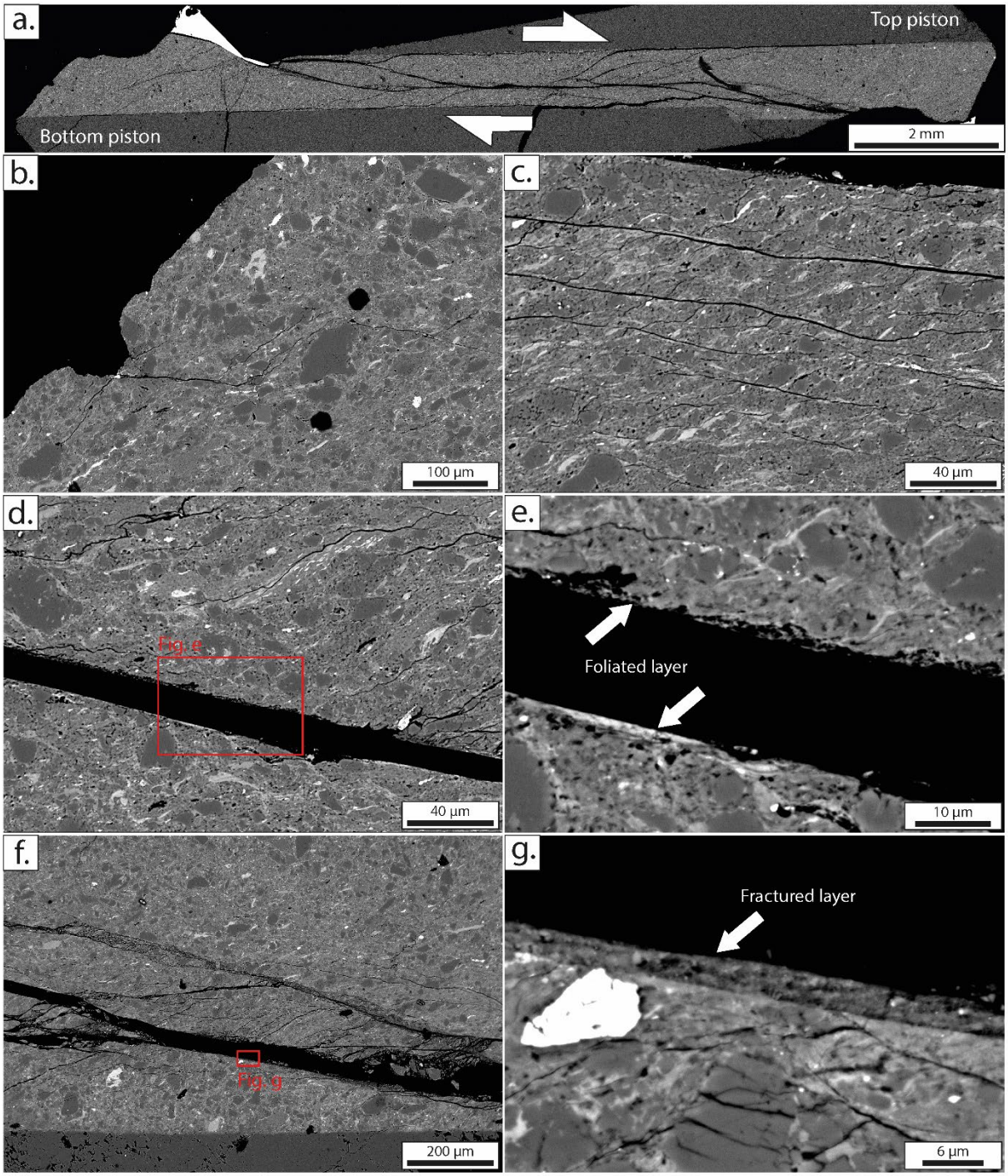

Figure V.14: Microstructures observed for the solid-medium Griggs apparatus experimental sample OR87BM. ***a.*** *Overview of the sample OR87BM showing the localization of the deformation along a main plane* ***b.*** *Undeformed zones at the extremity of the sample showing quartz and albite clasts in a matrix composed of phyllosilicates* ***c.*** *Surrounding of the main deformed zone with the formation of S-C structures* ***d.*** *Location of the foliated zone along the main deformed zone* ***e.*** *Close up on the narrow foliated layer* ***f.*** *Location of the fractured zone along the main deformed zone* ***g.*** *Close up on the fractured layer showing a foliation development in the crushed material.*

OR92BM

OR92BM sample corresponds to an experiment in which large values of strain were achieved. Unfortunately due to the intense deformation applied to the sample, the Pt-jacket broke and the sample was separated in two pieces where a vitreous plans were formed on the surface of each piece. However, it means that the localization of the deformation was in the center of the sample. On the bottom of the piece the deformation shows a strain gradient from the bottom forcing block to the other border (Figure V.15a). This strain gradient can be separated in 3 zones including the undeformed zone, the foliated zone and the parallelized zone that corresponds to the vitreous plan described above. The undeformed zone is characterized by the presence of clasts of quartz and albite, from 10 to 30µm in size, embedded in a phyllosilicate matrix. The foliated zone shows a narrow zone of 40 µm with a foliation at low angle with the main shear direction. The foliation is defined by the elongation of several phases, including quartz clasts (Figure V.15b). In addition, the grain size reduction is important in the foliated zone with quartz clast size inferior to 10 µm. The parallelized layer is luminescent and presents a maximum width of 3µm where no phases are distinguishable (Figure V.15b). Element mapping shows an increase of the Na and Fe concentration in the deformed zone while Al, K and Ca decrease (Figure V.16c). The reconstruction of phases using XMapTools software indicates the recrystallization of a second generation of white mica less rich in potassium associated with chlorite in the foliated and parallelized zones (Figure V.16b). The occurrence of chlorite is increasing with the quantity of deformation up to the parallelized layer. In addition, the quantity of quartz clasts decreases and, once again, the albite is absent. Element map of chlorine made with the EPMA indicates an important pollution by solid-medium salt identified through the concentration on the rim of the sample on few microns, as well as the sodium. Therefore, sodium measurements are questionable, as they might correspond to intrinsic variations in the proportion of phases as a result of deformation, as well as percolation of confining medium into the sample through fractures.

In addition, on the top piece of the sample, the deformation is even more concentrated (Figure V.15e). In this zone, an intense foliation, parallel to the main shear direction, is developed with an intense stretching and the formation of S-C structures of few microns (Figure V.15f). No any phase can be

identified in this intense foliated zone but looks like phyllosilicates in majority. EPMA maps obtained in this intensely deformed zone show a strain gradient from a foliated amplitude equivalent to the one described in the bottom piston up to an intensely foliated one (Figure V.17). In the intensely deformed part, the salt pollution is very important based on the concentration of chlorine (Figure V.17b). However, the intensely foliated layer is characterized by the quasi-absence of hard clasts as quartz or calcite and remains its major composition of phyllosilicates. The white mica of the first generation is almost replaced by the second generation and the quantity of chlorite is very important (Figure V.17a). The low amount of Fe-, Ti-rich clasts is also noticed. This main deformation is associated with a tardive deformation in the thinner part of the sample (Figure V.15c). This second deformation is expressed by nanometer angular clasts forming a intensely comminuted micro-breccia (Figure V.15d).

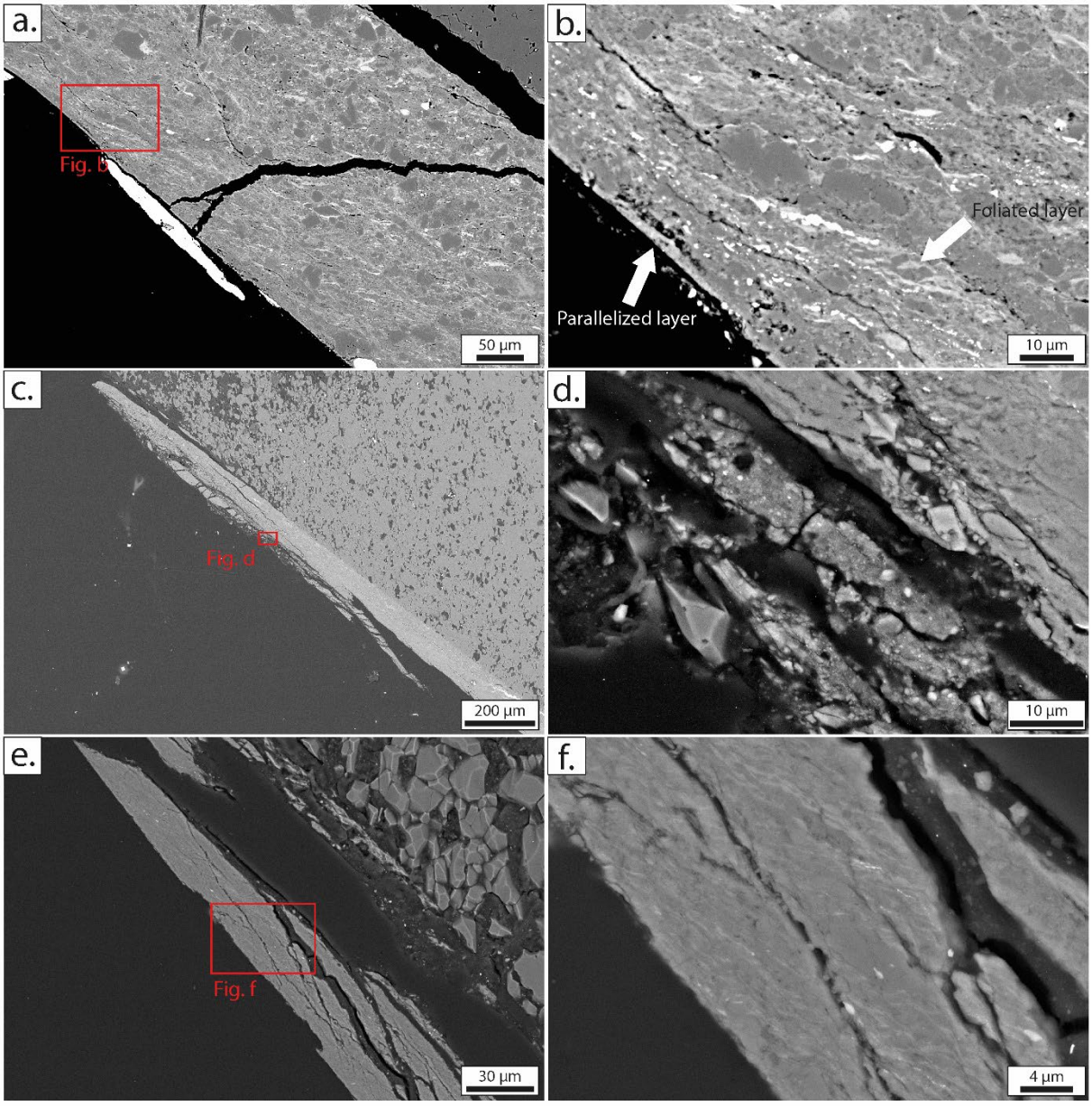

Figure V.15 : Microstructures observed for the solid-medium Griggs apparatus experimental sample OR92BM. ***a.*** *Overview on the strain gradient from the undeformed to the parallelized layer in the bottom piece* ***b.*** *Close up on the foliated zone at 20° to the main shear direction and parallelized zones* ***c.*** *Overview of the thinner zone of the bottom piece and location of brittle deformation* ***d.*** *Close up on the brittle deformation showing nano-scale clasts comminuted* ***e.*** *Overview of the intense foliated layer in the top piece* ***f.*** *Close up on the intense deformed layer where the foliation is almost parallel to the main shear direction underlined by a majority of phyllosilicates phases*

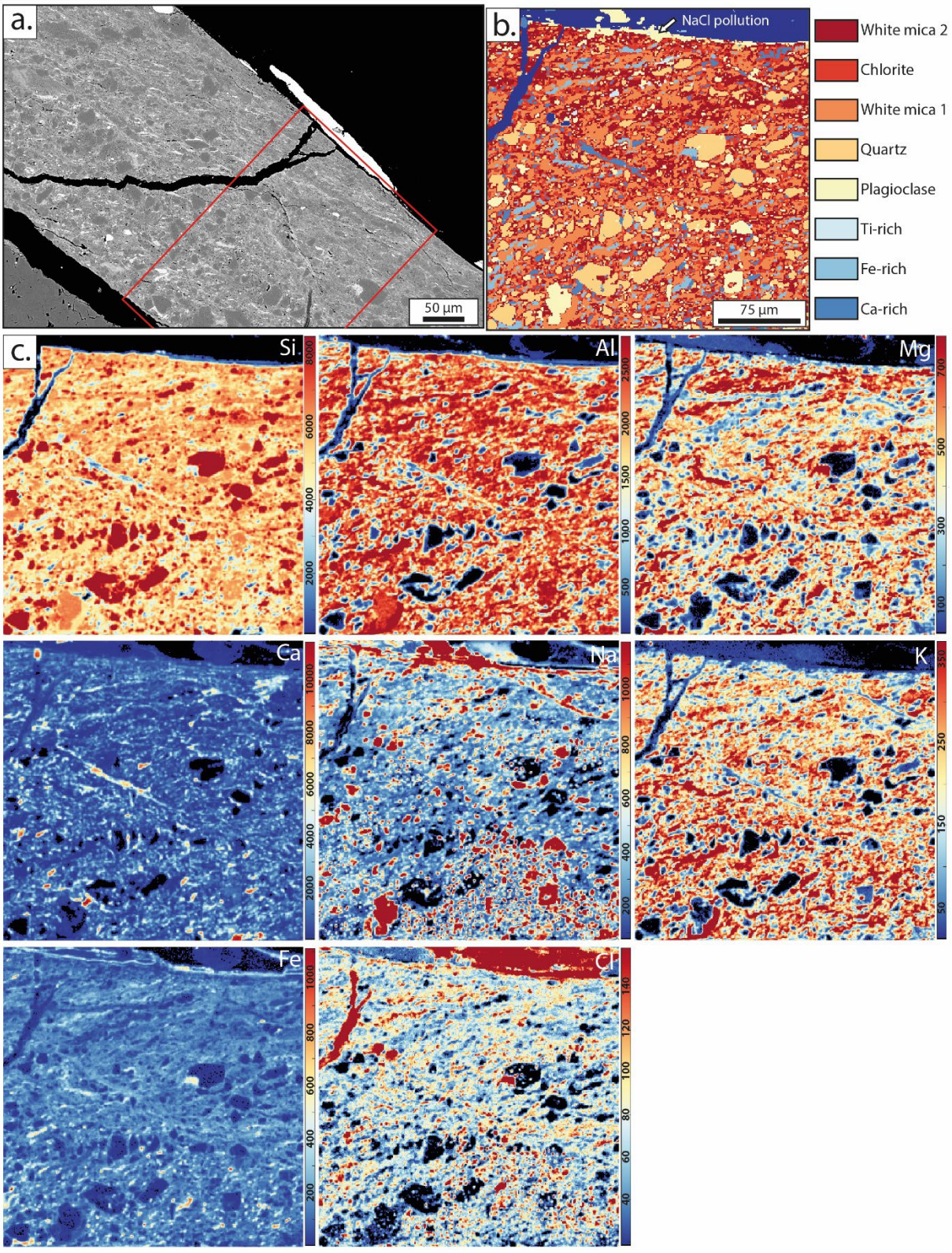

Figure V.16 : EPMA elements and phases maps of OR92BM bottom piece. ***a.*** *Location of the EMPA maps* ***b.*** *Phases maps obtained using XMapTools showing the recrystallization of a second generation of phyllosilicates and the NaCl pollution* ***c.*** *Elements maps obtained using EPMA showing the evolution of major elements: Si, Al, Mg, Na, Ca, K, Fe, Cl.*

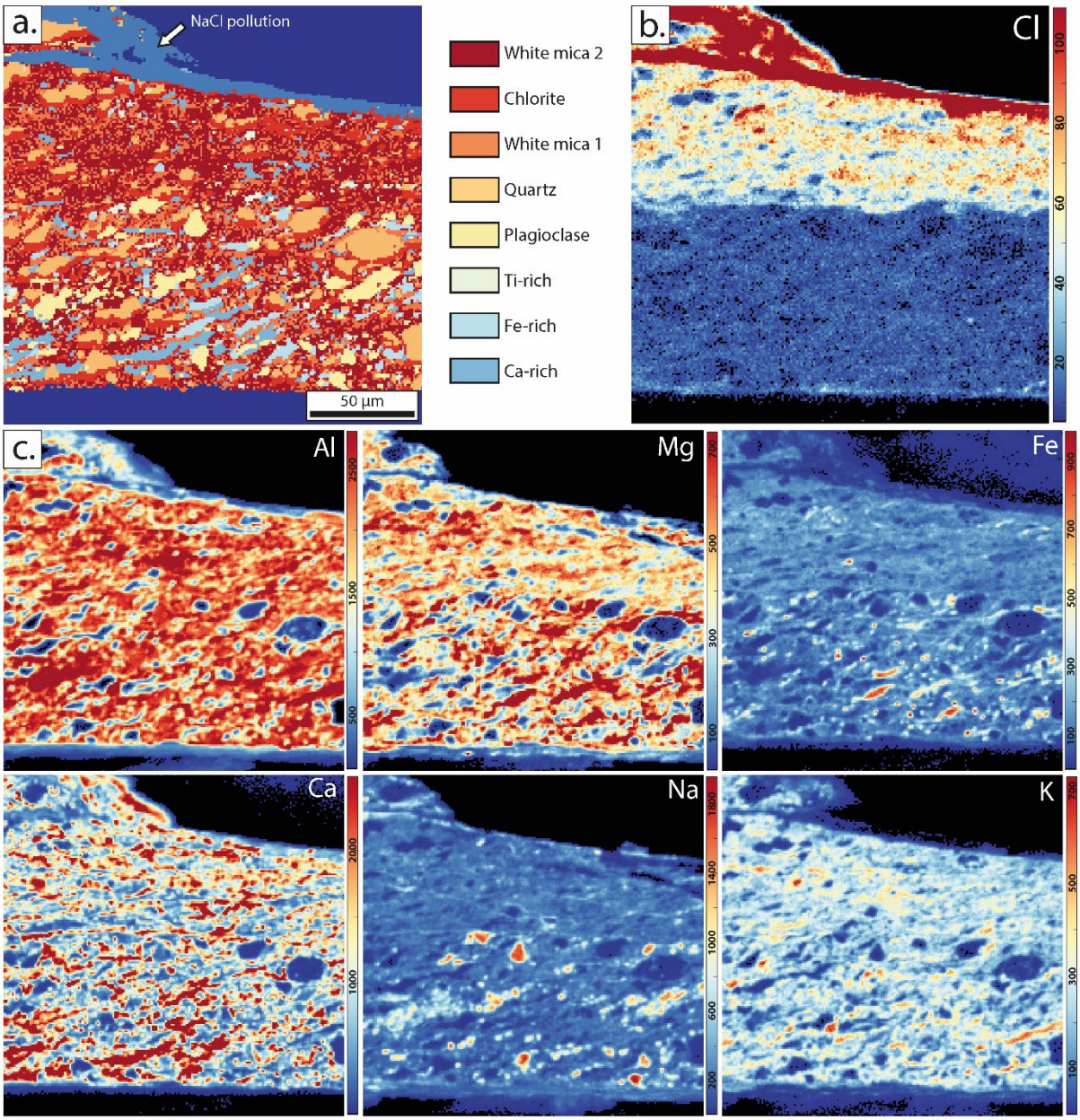

Figure V.17: EPMA elements and phases maps of OR92BM top piece. ***a.*** *Phases maps obtained using XMapTools showing the recrystallization of a second generation of phyllosilicates and the NaCl pollution* ***b.*** *Chlorine map showing the pollution correlation with the strain quantity* ***c.*** *Elements maps obtained using EPMA showing the evolution of major elements: Al, Mg, Fe, Ca, Na, K.*

V.4.2.3 Microstructure interpretation and link with mechanical data

In this study, two types of microstructures can be distinguished. On one hand, micro-breccia characterized by an intense grain size reduction and angular clasts from various sizes are observed. On the other hand, foliated zones are observed where minerals are elongated and oriented in the stretching direction. In addition, recrystallization of phyllosilicates is observed associated with the decreasing amount of the hard clasts (i.e. quartz and albite). In terms of deformation mechanisms, these two

microstructures can be identified as the products of brittle deformation for micro-breccia produced by mechanical comminution, whereas for ductile deformation, chemicophysical processes are responsible of the microstructures observed in the foliated zone. In the following, the description of the RSCM results will be made based on the microstructure observations and deformation mechanisms.

Based on the stress evolution, it is possible to attempt to interpret the mechanism of deformation that have been produced. Indeed, stick-slips observed thanks to the sharp stress drop in Paterson rig experiments (i.e. PP633) can be interpreted as fracturing. Moreover, it is also possible to produce brittle microstructures such as micro-breccia without stick-slip mechanism and important stress drops observed during the Griggs apparatus experiments T609BM and T610BM. In the opposite, after a stress drop, plastic deformation can occur along the produced fracture with long creep and finally appears such ductile microstructures such in PP636. In addition, when the stress becomes flatter, the interpretation is oriented in a plastic deformation that would produce ductile deformation. However, to be sure of the ductile de formation, the presence of such stretched mineral is necessary in order to quantify the deformation with the record displacement during this phase. In the experiment PP641, a Fe-rich sulfide is stretched on 2mm and the associated displacement during the deformation experiments where the stress curve is flat. In this case it is possible to link the flat slope of the stress curve with plastic deformation and ductile deformation.

Therefore, based on all these examples and discussion above, the interpretation of the link between the microstructures and the experimental mechanical data is complex and needs the presence of well-established clues. In the discussion section, the link between mechanical data, microstructures and RSCM response is more detailly discussed.

V.4.3 RSCM results

The RSCM has been used in order to explore the effect of strain on CM crystallinity evolution along experimental strain gradients. Two analyzing approaches have been used: (1) high resolution profiles when the size of the strain gradients allows it or (2) analyses on microstructure zones (e.g. undeformed, foliated, parallelized, and fractured) of the intensity ratio. The RSCM data will be presented in the same order as it has been done in the microstructures section.

V.4.3.1 RSCM effect of brittle deformation

PP633

The deformation in the sample is located on the interfaces between the sample and the shear pistons with an interface of weak parallelized layer on the top piston and a 200µm wide fractured zone on the interface of bottom piston (Figure V.18a). The parallelized layer shows a slight increase of the intensity ratio from 0.657 ± 0.014, in the undeformed zone, to 0.674 ± 0.013 in average in the deformed zone (Figure V.18b). The same results are observed in the fractured zone with a slight trend that shows an increase in the deformed zone at 0.683 ± 0.014, so ca. 4%. In addition, a slight trend from 0.669 to 0.712 is observed from the limit of the undeformed zone to the rim with the shear piston. However, on the extreme rim of the sample in contact with the bottom piston, totally immature CM have been analyzed (Figure V.18c). The Raman spectra obtained are comparable to the ones analyzed in immatures sediment from the Ninetyeast Ridge.

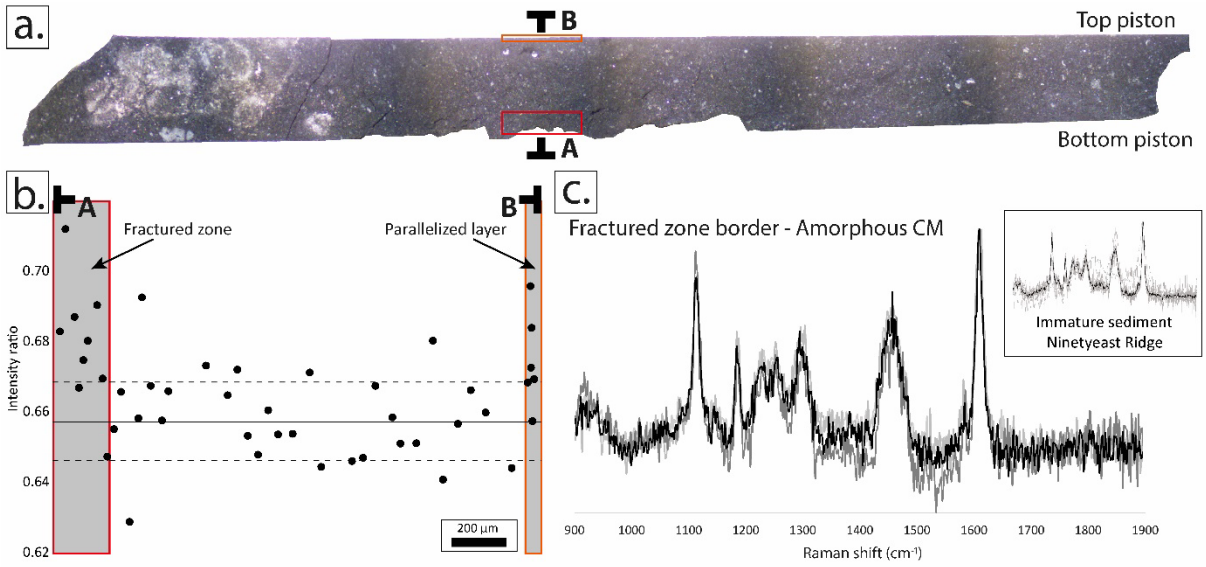

Figure V18 : RSCM results obtained for the sample PP633. ***a.*** *Reflection image obtained for the sample PP633 showing the locations of the two deformed zones* ***b.*** *Intensity ratio profile from the fractured zone to the parallelized zone across the sample* ***c.*** *Amorphous CM spectra analyzed on the rim of the fractured zone compared with immature sediment from the Ninetyeast Ridge IODP drilling.*

PP638

The sample PP638 is characterized by the location of the deformation along the blackened zone described in the microstructure section above. Along a profile passing through the blackened zone and

the undeformed rocks, no significant evidence of evolution in the intensity ratio has been highlighted, i.e. 0.719 ± 0.04 in the undeformed zone against 0.707 ± 0.03 in the blackened zone. It is impossible to distinguish these areas due to an important dispersion of the data observed in both zones. However on the extreme rim of the blackened zone where cracks are opened amorphous CM have been analyzed (Figure V.19), similarly to the previous sample.

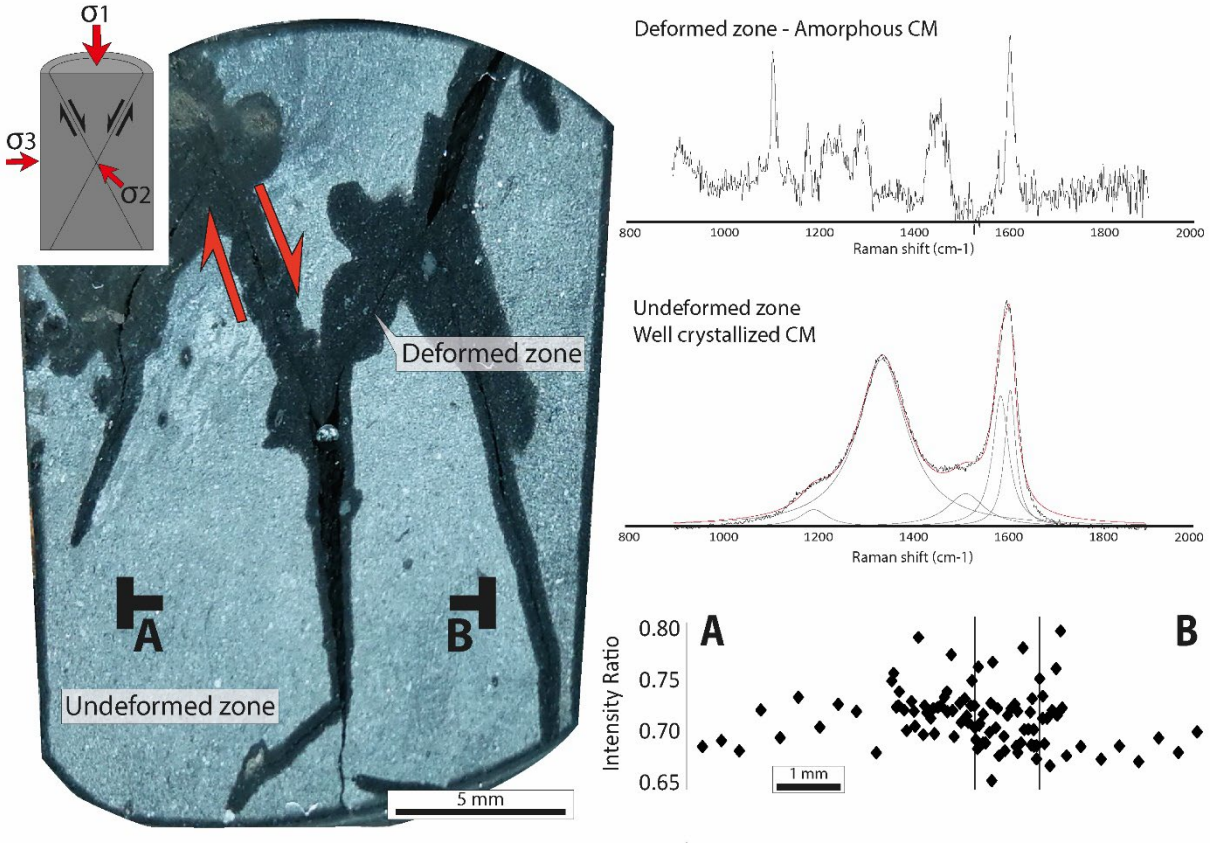

Figure V.19 : RSCM results obtained for the sample PP638 showing the profile across the undeformed zone and the blackened zone and typical RSCM spectra measured in the sample.

T609BM

Both analytical approaches have been used in this sample in order to follow the effect of deformation, high-resolution profile and analyses of different zones. Three zones have been determined, the undeformed zones that correspond to the extreme rim of the sample, the fractured zone where the deformation is localized as well as the surrounding zone of the fracture, which consists in the 100µm-wide domain around the fractured zone. The two extreme rims of the sample have been separated due

to the large difference observed in the IR measurement revealing an important experimental temperature gradient (Figure V.20a). In addition, no distinction could be makd between the fractured and poorly deformed surrounding zones, which are both around 0.90. The same results are observed in the high resolution profile through the fractured zone, a large dispersion is observed, from 0.86 to 1.06, without constant and clear evolution of the IR in the deformed zone.

T610BM

Due to the duration-temperature pair used during this experiment, the crystallinity of the CM is less organized than we expect. However, we proceed the same approaches that have been used in the sample T609BM. The IR profile along the foliation development does not show a clear evolution from the poorly deformed rock to the foliation development in the few micrometers. Once again, a large dispersion irrespective of the strain quantity is observed from 0.56 to 0.79. In addition, analyses of zones have been made in two different zones comparing the fractured zones and their surrounding (Figure V.20b). For both zones, no distinction has been observed between the fractured zones and their surrounding. However, the zone 1 shows IR mainly between 0.60 and 0.65 when in the zone 2 the IR varies from 0.65 to 0.70 (Figure V.20b). In this experiment, the experimental temperature gradient is still present.

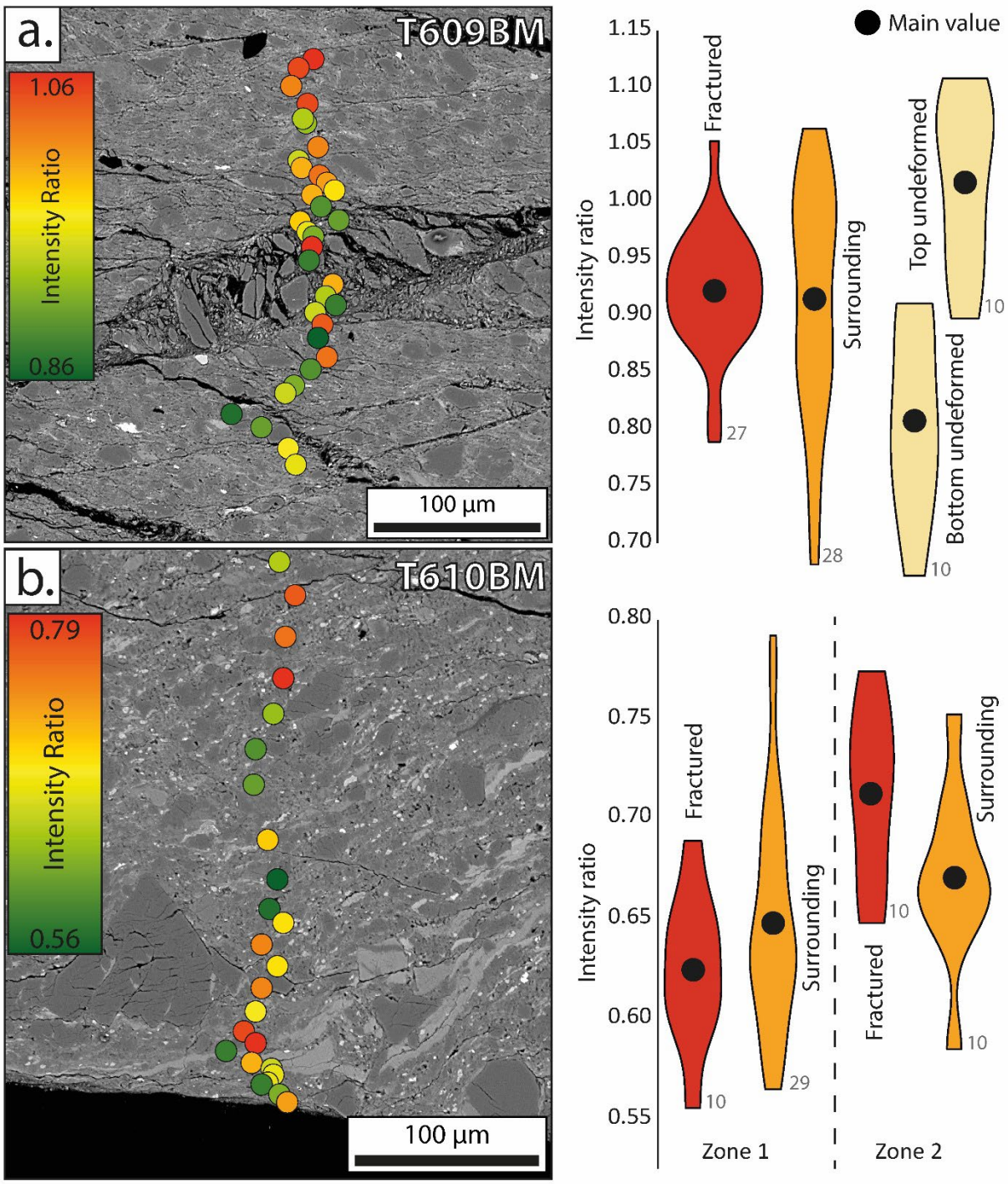

Figure V.20 : RSCM results obtained for the samples T609BM and T610BM. ***a. and b.*** *RSCM results obtained from high-resolution IR profile through the surrounding and the fractured zone and intensity ratios of the different microstructural zones of the sample T609BM.* ***a.*** *T609BM.* ***b.*** *T610BM.*

V.4.3.2 RSCM signal in ductile shear zones

PP636

Limited by the too small size of different microstructural domains, analyses by zones have been used for the sample PP636. Three microstructural zones can be distinguished, the undeformed zone, the foliated layer and the parallelized layer. The undeformed layer shows an IR of 0.673 ± 0.02, whereas in the foliated layer and the parallelized layer a respective increase of 8% and 17% is measured, i.e. 0.726 ± 0.03 and 0.784 ± 0.05, respectively (Figure V.21). It is worthy to notice that the increase of dispersion in the deformed zone is also important. Finally, a correlation between the strain quantity and the IR increase is observed with a higher IR in the parallelized layer than in the foliated layer.

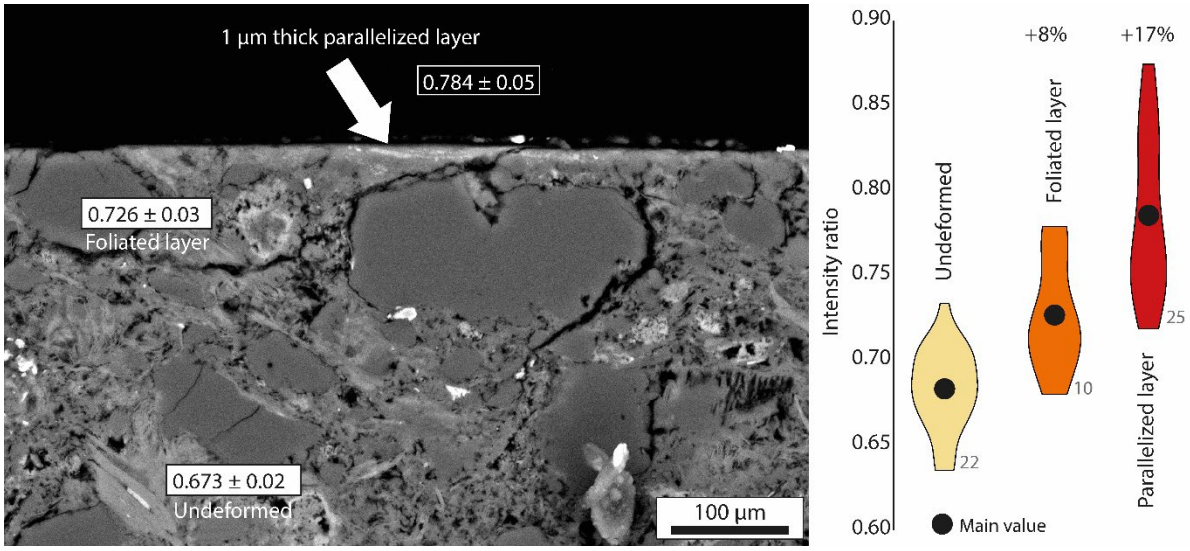

Figure V.21 : RSCM results obtained for the sample PP636. IR evolution in three microstructural zones: undeformed, foliated and parallelized layers that shows an increase in the deformed zones.

PP641

The sample PP641 shows the coexistence of two microstructures, the micro-breccia and the shear zone. The focus was made here on the latter, through high resolution profile (Figure V.22a and 22b). The first shear zone is 30 µm wide; inside, the IR shows a clear increase trend with respect to undeformed surrounding material, with average IR of 0.74 and 0.66, respectively (Figure V.22a). In addition, a single point has been measured in the micro-breccia, which runs along the foliated zone and also shows a high IR. In the second micrometer-scale strain gradient the same evolution is observed with a clear gap in IR,

from ~0.53 in the undeformed host rocks to ca. 0.70 (locally up to 0.83) in the shear zone (Figure V.22b). In addition, comparing the IR obtained in the undeformed zones with the slightly deformed and the foliated zones shows an increase of the IR in the deformed zone. Indeed, the surrounding of the foliated layer (i.e. slightly deformed zone), where the first traces of the deformation are visible, shows an increase of 6% and in the foliated layer an increase of 14% is measured (Figure V.22c). In both last cited deformed layers, the dispersion of the results is more important than in the undeformed zone where the IR are very constant.

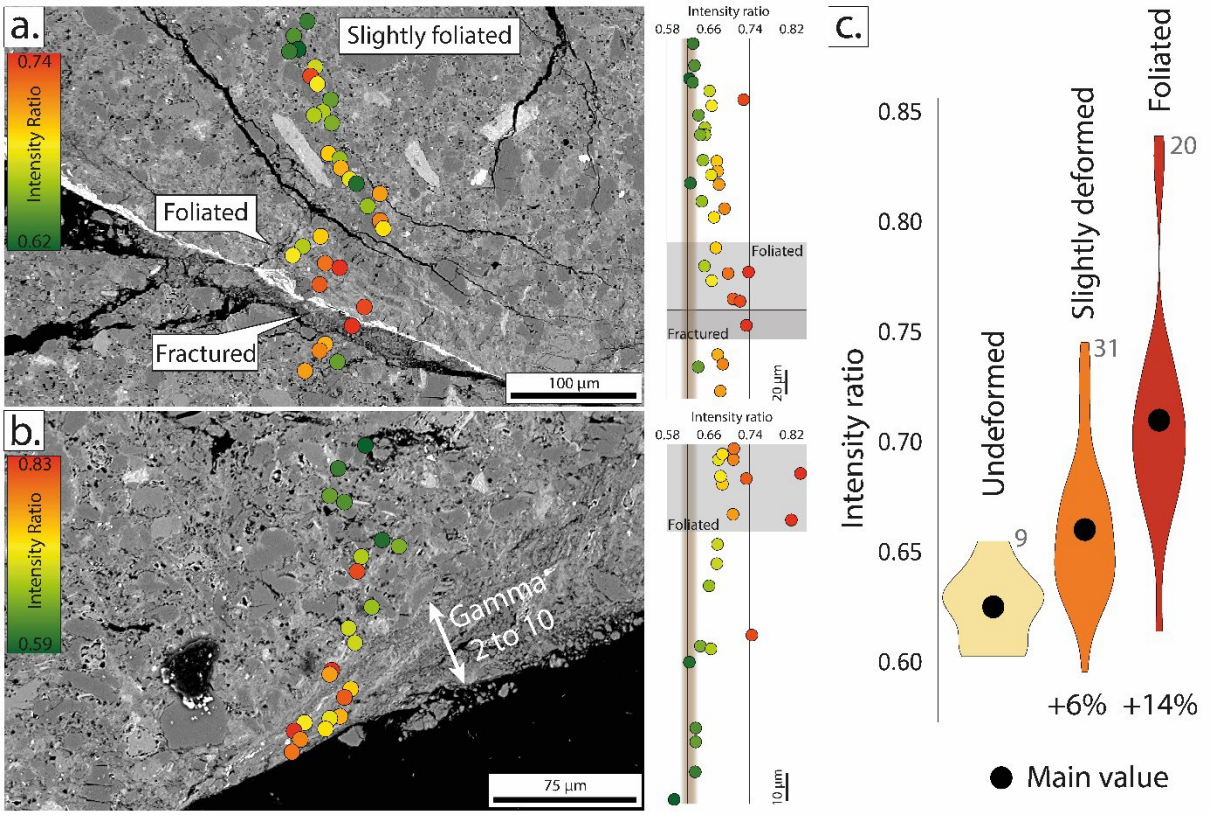

Figure V.22 : RSCM results obtained for the sample PP641. ***a. and b****. high-resolution IR profiles obtained along the viscous shear-zones developed during the experiment* ***c.*** *IR diagram by zones showing the evolution of the IR in the undeformed, slightly deformed and foliated zones.*

OR87BM

This sample has been deformed under high confining pressure comparing to the two last samples described above. Due to the size of the S-C structures developed in surrounding of the main localization structure it is impossible to work using a high-resolution approach, therefore the focus was made on the deformed zone along the main structure (Figure V.23b). The two extreme rims of the sample have been

analyzed and show similar values on the bottom and top of undeformed zones, respectively 0.726 ± 0.034 and 0.712 ± 0.033 (Figure V.23a and 23c). In comparison, the foliated layer analyzed in the middle of the sample shows an increase of the IR at 0.858 ± 0.058, equivalent to 19%, with an important dispersion of the values visible on the increasing of the standard deviation (Figure V.23c).

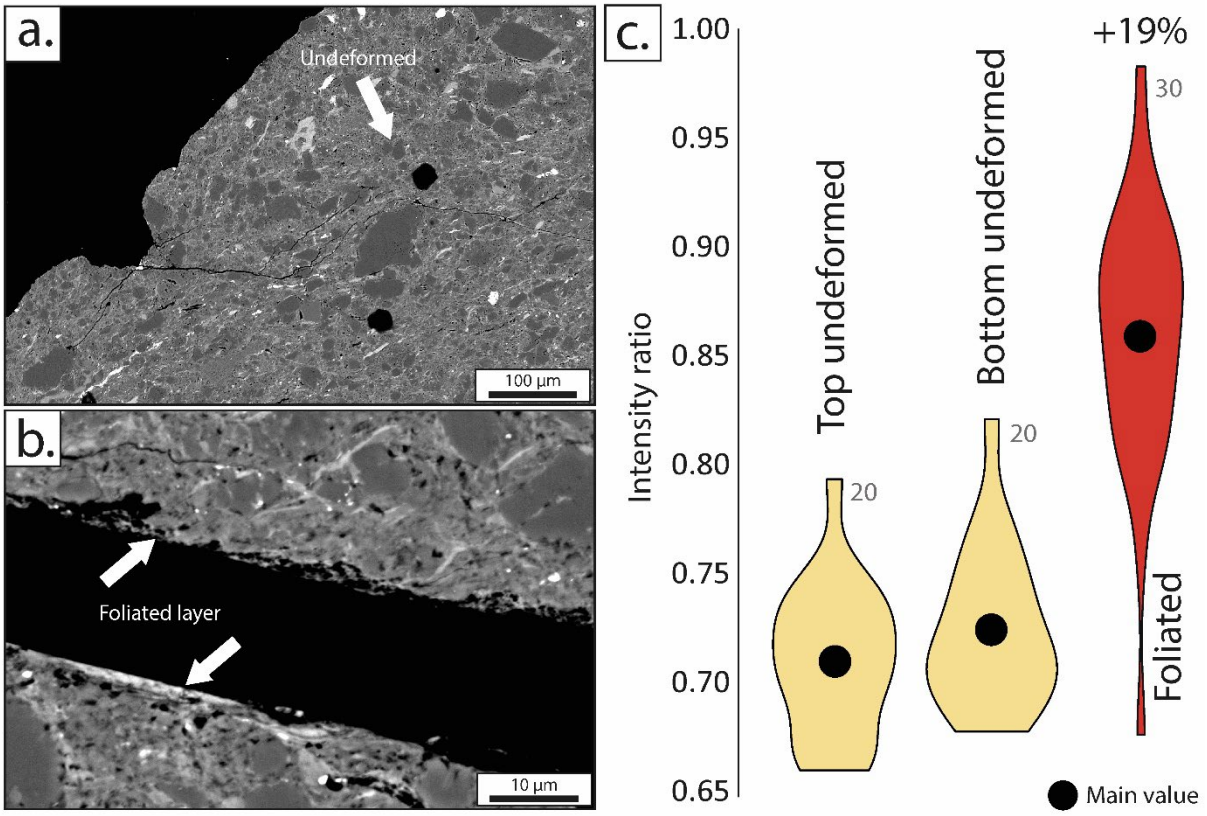

Figure V.23 : RSCM results obtained for the sample OR87BM. ***a.*** *Location of the undeformed zone used* ***b.*** *Location and microstructure of the foliated zone used* ***c.*** *IR diagram showing the increase IR in the foliated zone comparing with the undeformed zones.*

OR92BM

The last sample analyzed is characterized by a large quantity of strain of certain zones due to the important displacement induced during the experiment. On the bottom of piston, two zones have been analyzed, (1) a strain gradient from a poorly deformed up to the parallelized layer in the few last micrometers (Figure V.24c) and (2) the undeformed layers in the extreme border of the sample and a fractured zone that occurs in the surrounding (Figure V.24d). The zone (1) shows an increasing trend of IR from the poorly deformed zone to the parallelized zone. Indeed, the IR increases from 0.729 ± 0.041 to 0.837 ± 0.034 (+12%) in the foliated zone and 0.856 ± 0.033 (+15%) in the parallelized zone (Figure

V.24a). The zone (2) shows a very slight increase of 3% between the two undeformed zones and the fractured zone with IR 0.740 ± 0.029, 0.751 ± 0.025 and 0.769 ± 0.04, respectively (Figure V.24a). The IR measured in the two undeformed zones show similar values and comparable to the ones measured in the poorly deformed layer of the zone (1). On the top piston of the sample, three microstructural zones have been distinguished: the undeformed, the poorly foliated (Figure V.24e) and an intensely foliated zone (Figure V.24f). The undeformed zone shows an IR of 0.716 ± 0.078 that is very similar to the other undeformed zones of this sample. However, in the poorly foliated zone, an IR of 0.718 ± 0.031 is measured corresponding to a slight increase of 4% comparing with all the undeformed IR obtained. The most significant increase has been measured in the intensely foliated layer where the IR reaches to 0.980 ± 0.356 corresponding to a 41% increase (Figure V.24b). Finally, comparing the IR measured in the strain gradient in the zone (1) of the bottom piston and the intensely deformed layer in the top piston, a clear increasing IR trend is shown correlating with the quantity of strain.

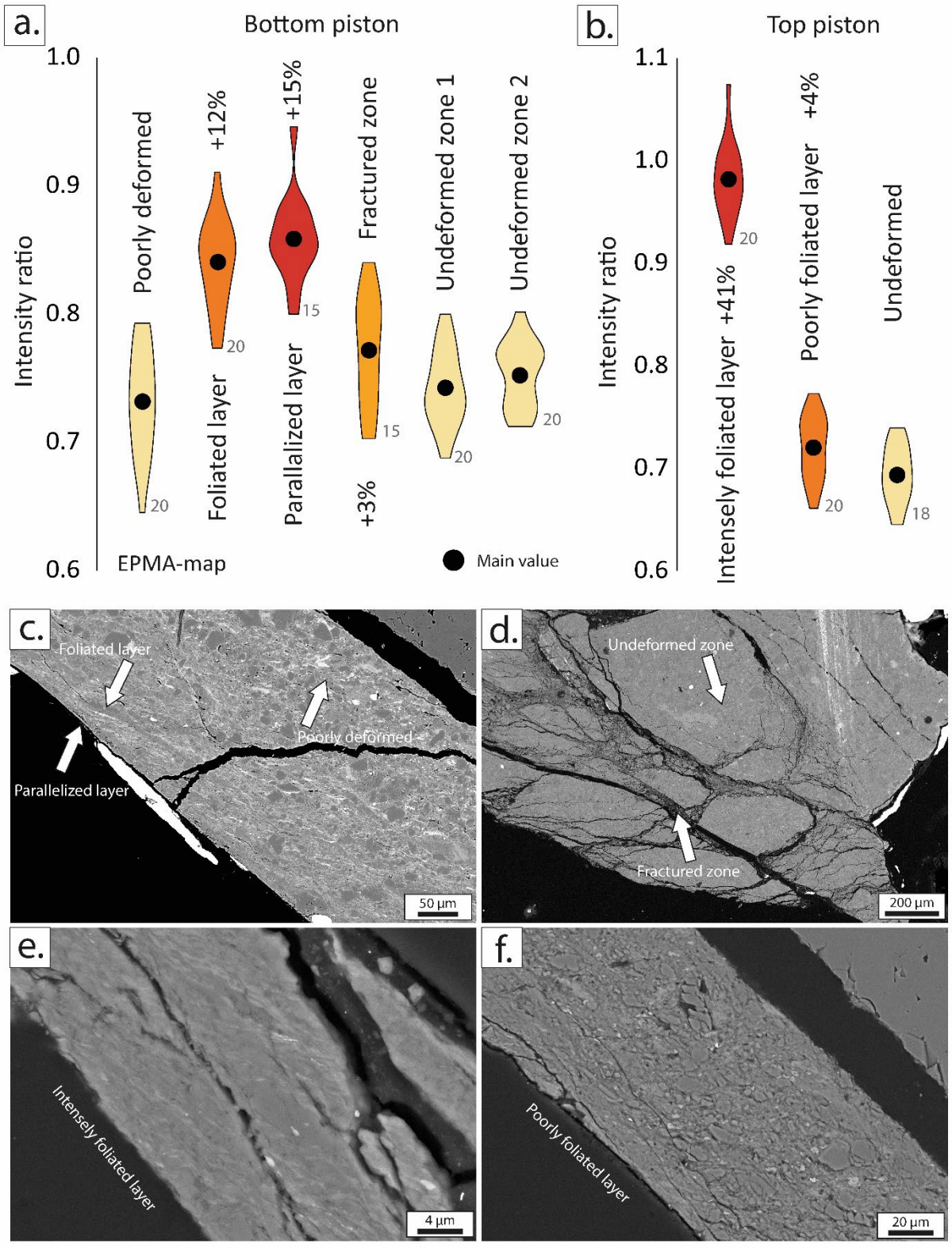

Figure V24 : RSCM results obtained for the sample OR87BM. ***a. and b.*** *Diagram representing the IR evolution in microstructural zones defined and increase of the IR in deformed zones (a. bottom piston ; b. top piston)* ***c. to f.*** *Microstructural zones division based on the grain size reduction, considered as a proxy for the quantity of strain.*

V.5 Discussion

V.5.1 Link among mechanical data – microstructures – RSCM

In order to illustrate the link between the mechanical data and the microstructures we will focus on two samples: PP633 and PP641, corresponding respectively to the brittle deformation and the ductile deformation.

The first, PP633, mechanical data show a quick and steep stress increase followed by a stress drop. After this stress-drop, the stress remains constant until the end of the experiment. Now, regarding the microstructures of deformation, when it was pulled out from the deformation column, the sample PP633 presented a very thin (ca. 2 μm) vitreous layer where the rupture occurred, i.e. on the interface between the bottom shear piston and the sample. In addition, a 200 μm wide crushed zone is observed parallel and juxtaposed to the vitreous layer. The stress-drop observed corresponds to the rupture that occurred between the sample and the forcing block and the constant stress that follows this rupture generated the vitreous plan by the displacement along this localized sliding zone. Another example of a long localization on the rupture plan of the deformation is shown by the sample PP636. Due to the presence of a continuous sample between the powdered included on the shear plan and the furrow, the deformation is localized in this zone and shows a brittle fractured zone.

The sample PP641 shows shear zones crosscut by cataclastic zones. Mechanical data show two stages of deformation where the stress curve is almost flat (Figure V.26a), which corresponds to a 2mm displacement. Based on the shear-zones development the quantity of strain is difficult to be estimated. However, thanks to the stretching of a Fe-rich sulfide observed along a slipping zone it possible to measure the plastic displacement that corresponds also to a 2 mm displacement. This first plastic deformation phase is followed by a stress-drop. On the basis of microstructural record, we interpret this first stage of deformation (constant stress, 2mm displacement) as the strain accumulated in the shear zone, and the subsequent stress drop as the formation of the cataclastic zone. In addition, the formation of shear-zone conducted to the ductile deformation of phases included in this foliated zone and the recrystallization of new phases controled the rheology (Figure V.26c). This foliation induced an

increasing of the CM crystallinity based on the IR increase (Figure V.26b). The link between the microstructures and the IR signal is described below in detail (V.5.1.3).

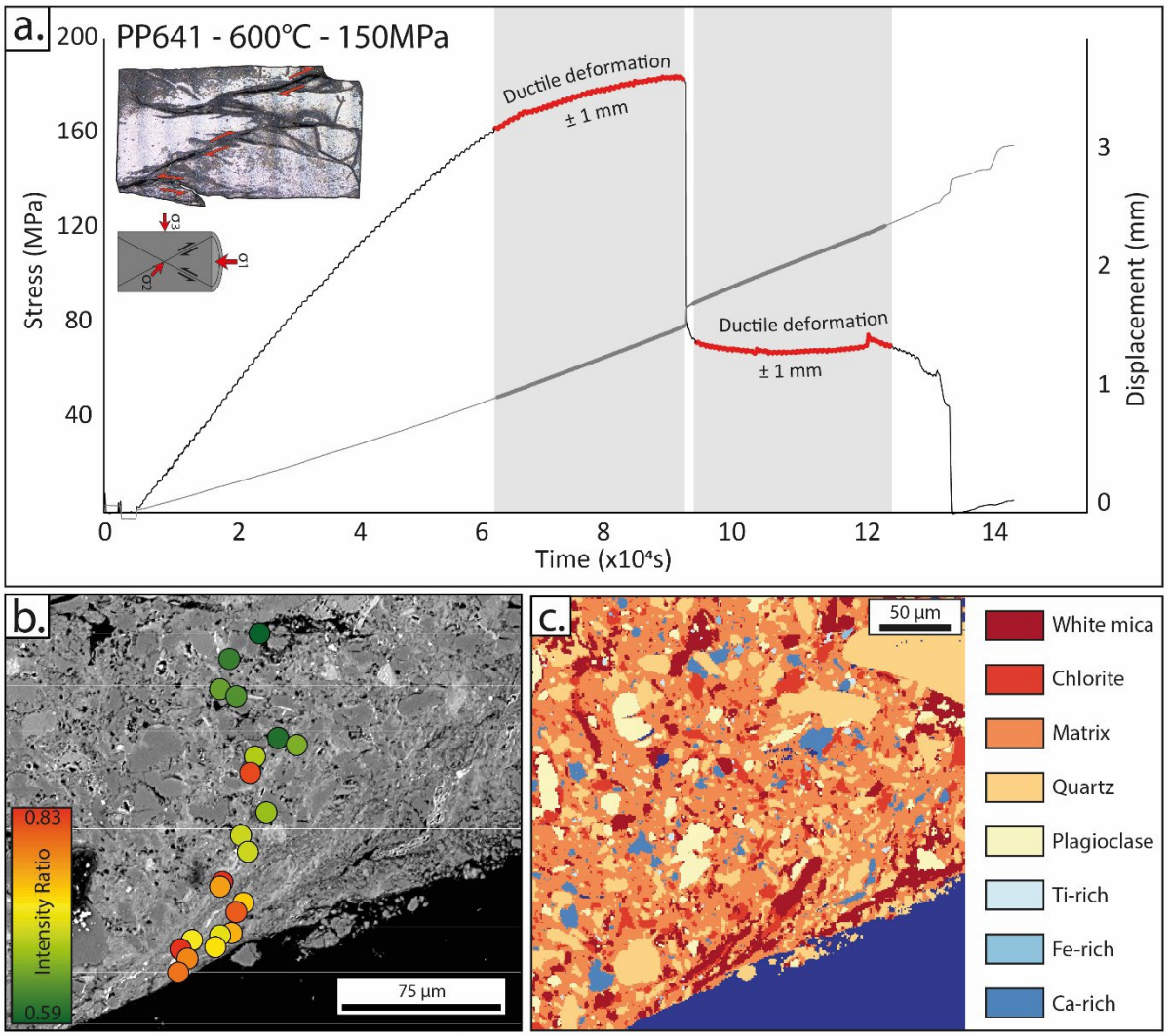

Figure V.25 : Composite results of the mechanical data, RSCM profiles and microstructures evolution within shear-zone in the PP641 Paterson Rig experiments. ***a.*** *Mechanical curves showing in red the stress flattening during the experiment and in grey rectangle the plastic deformation induced* ***b.****IR profiles showing the increasing CM crystallinity in correlation with the quantity of strain* ***c.****Phases map showing the evolution of microstructures and mineralogical composition in the shear-zone created during the plastic deformation phase.*

V.5.1.1 Dehydration effect on the sample strength

The two first Paterson Rig experiments PP629 and PP630 just as the solid-medium Griggs apparatus experiments OR87BM and OR92BM have given important information on the strength evolution of the sample during experiments and the link with the dehydration. As a reminder, the sample used in this study is an immature shale containing around 4.36 wt% of water. In the experiments PP629 and PP630,

porous alumina was used as forcing blocks. This sample assembly allows removing the water from the sample and the stress reached at the end of the experiment was very important, up to 400MPa. In comparison, the sample deformed in the same sample assembly using full alumina forcing bloc, avoiding the dehydration, has shown the first weaknesses around 60 to 70 MPa. In addition, the sample PP630 shows an undulose plan in the contact between the porous alumina and sample. It means that the dehydration of the powdered sample has recrystallized in very strong alumina, stronger than the shear pistons. In addition, based on the stabilization time, which corresponds to the moment without deformation at required temperature and pressure, in the Griggs apparatus have shown similar results. Unlike the Paterson Rig, Griggs assembly is welded in a strictly airtight Pt-jacket and no water could go out from the system. However, for a stabilization time at 600°C of several hours against 30 minutes, the strength of the sample is very different. Indeed, in OR87BM and OR92BM, the same constant load at differential stress of 500MPa was applied but a shorter stabilization time on OR92BM was applied. However, the displacement of the deformation piston is at least 100 times quicker in OR92BM, compared with OR87BM due to the lower strength of this sample.

Once again, the longer heating of the sample at 600°C has conducted to the dehydration and the hardening of the sample. To summarize up, the dehydration of the sample during the experiments is a main factor controlling the strength of the material and the deformation style during experiments. Samples that experienced dehydration became much stronger and no deformation are observed for Paterson rig experiments. In opposite, when no dehydration occurred, the sample is very weak and for the same differential stress the stress is intensely transferred to the sample with an important deformation.

V.5.1.2 Continuous deformation vs. stick-slip deformation

In the sample PP632, PP633 and PP636, stick-slip deformation occurred with an important stress-drop corresponding to the rupture at the interface between the sample and shear piston, followed by a constant stress corresponding to the localized deformation along these deformed plans. Unlike the continuous deformation, the deformation is characterized by the localization in a narrow vitreous plan recognizable by a strong stretching of soft phase (i.e. calcite, sulfide, phyllosilicate) and luminescent micron wide

plan on the interface. Apart from the narrow and intense localized deformation, microstructures are similar to the ones observed in deformed sample in ductile regime such as PP641 or OR87BM and OR92BM.

However, due to the stick-slip events, frictional heating could be generated and the observation of CM crystallinity enhance in these zones, the strain and the heat induced could not be separated. In order to assess this hypothesis the frictional heating will be modeled using the equation from Carslaw and Jaeger (1959):

$$T = \frac{2F0}{\kappa}\left[\left(\frac{kt}{\pi}\right)^{\frac{1}{2}} e^{-\frac{x^2}{4kt}} - \frac{x}{2} erfc\left(\frac{x}{2\sqrt{kt}}\right)\right] \quad (4)$$

Where T, Q, κ, k, t and x are respectively, the induced temperature, the heat flux, the thermal diffusivity, the thermal conductivity, the time and the distance from the source, all in SI units. In this equation (4) all the parameters are known, expect for the heat flux. This parameter can be estimated as $F_0 = Q_{th} / t_w$, respectively the fracture energy and the sliding time. The linear relation obtained in Aubry et al. (2018) allows to link the displacement and the fracture energy (Figure V.27a). The maximum stress-drop observed in the Paterson Rig experiments corresponds to a displacement of 135µm according to this correlation to a fracture energy of $3.0x10^2$ J.m^{-2}. The second uncertainty is about the sliding time because during experiments the time step was set at 1 second. According to Koizumi et al. (2004) and Passelègue et al. (2016) this sliding time is always included between 10 to 100 µs but should be in average around 20µs. In order to test all possibilities, sliding time has been set at 2, 20 and 200µs. Respective increasing temperatures induced by frictional heating are 93°C, 30°C and 10°C for a few of microseconds due to the heat diffusion. Therefore, the frictional heating generating during this rupture events is not enough sufficient to interfere with the strain effect and is negligible for the experimental temperature (i.e. 600°C). RSCM differences between the deformed zone and the undeformed zones could be interpreted only in terms on strain effect on the CM crystallinity.

In addition, the slip displacement and the stress-drop of Paterson Rig experiments have been plotted and shown a good correlation ($R^2 = 0.944$) (Figure V.27b), with a slope controlled by the stiffness of the experimental apparatus used in this study.

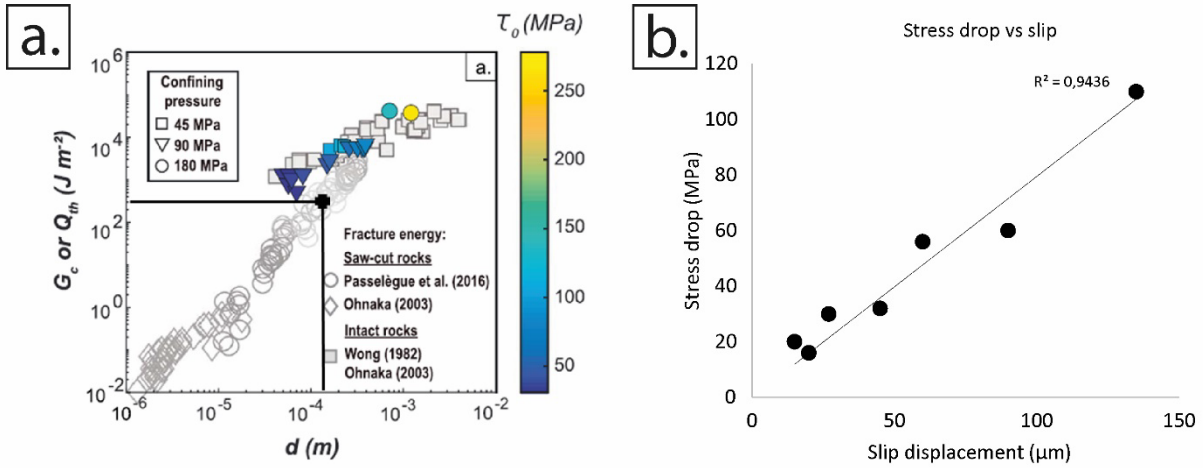

Figure V.26 : a. Fracture energy versus the slip displacement (Modified from (Aubry et al., 2018)). b. Stress drop versus slip displacement measured during Paterson Rig experiments

V.5.1.3 Strain localization and CM crystallinity evolution

Along strain gradients, it is possible to follow the mineralogical and microstructural evolutions that conduct to the strain localization. In this section, we will focus on the shear zones observed in the sample PP641, OR87BM and OR92BM. These samples present the same mineralogical and microstructural evolution despite of the difference of confining pressure used during deformation experiments. In the shear-zones, from 10 to 40µm wide, the grain size is reduced importantly until to those inferior to the microns and S-C structures are developed. Chemical transfers have been revealed with the decrease of Ca and Al whereas the Na increases. The mobility of the K is more ambiguous with an increase in the low pressure experiments and a decrease in the high pressure experiments. The mineralogy shows the development of new phyllosilicates (i.e. white micas and chlorites) oriented parallel to the main shear direction, the progressive replacement of sulfides and oxides, the drastic diminution of the quartz amount and the absence of albite. Due to the recrystallization of anisotropic phases, such as phyllosilicates, and the absence of hard clasts, the rheology of the sample is affected and becomes softer in the shear-zones. Therefore, the deformation is localized in these shear-zones. Finally, due to the strain localization in the viscous shear-zones through these processes, the CM grains are affected by the deformation and a

crystallinity enhance is observed. This evolution is described in detail in the next section V.5.2 of the discussion.

V.5.2 The effect of deformation and pressure on the CM crystallinity

V.5.2.1 the IR evolution in the strained zone

The microstructural observations have highlighted the coexistence in the experiments of two regimes of deformation, a brittle one and a viscous one. On both cases, RSCM, and especially the IR, has been used to evaluate the evolution of the crystallinity of the CM along these strain gradients. The brittle deformation has shown an increase of the CM crystallinity in the strained zone (Figures V.18 V.24). Similarly, in the viscous shear-zones the same evolution of the CM is observed. However, comparing these two evolutions of the CM crystallinity the one generated by brittle deformation is very small and always inferior to 5%, whereas the viscous deformation generates at least an evolution of 10% to 20% and could reach intense values of 40% in case of intense deformation. Therefore, the effect of deformation on the CM reorganization is real and its detection is amplified in Griggs experiments where the temperature is gradually decreasing toward the center of the sample whereas the IR and the crystallinity increase. In this case, another controlling factor occurs and is interpreted as the effect of deformation. In addition to the IR increase, the dispersion of the values is very important in the deformed zones. This heterogeneity has been observed in higher degrees of metamorphism on CM (Suchy et al., 1997) and interpreted as the interaction of previous structures such as bedding or strain shadows (Bustin et al., 1995). Pasteris and Wopenka (1991) described the dispersion of the values as a response of the defects generated by the polishing wear. However, in this study, all analyses have been carried out in sub-surface to avoid this artefact. Moreover, along the different viscous microstructures and the estimation of the strain quantity, an evolution of the CM crystallinity has been observed. Indeed, a correlation between the increasing IR, and as consequence the crystallinity, and the increasing strain quantity is observed with the poorly foliated layers where the IR increases about 10%, ~ 20% and ~40% for foliated and intensely foliated layers (OR92BM), respectively. However, even for a lot amount of strain, the effect of deformation is observed on the CM crystallinity. All these results lead to the same conclusion, i.e. the viscous deformation is an important controlling factor of the CM crystallinity.

In the brittle deformed samples (PP633 and PP638) at low pressure, amorphous CM have been measured on the extreme rim of the sample. However, in these places, the microstructures seem to be similar to the one in the strained zones. Therefore, the interpretation of the formation of this amorphous material cannot coincide with the deformation that occurs under pressure and temperature. We interpret this deformation effect as a late event in link with the depressurization and friction between the border of the sample and the shear piston. Kirilova et al. (2018) show that increasing strain at ambient pressure and without heating conducts to an amorphization of the CM.

To finish, in T609BM and T610BM no evidence of the deformation effect has been recorded on the CM crystallinity. However, in this apparatus, important horizontal and vertical temperature gradients exist. The response on the IR is a repartition of the values from 0.70 to 1.10 only for the two undeformed zones on each side of the sample. Therefore, because of the dispersion of the data in the undeformed zones comparing the IR from the strained layer is not rigorous and not deviation or evolution could be interpreted. In addition, the duration-temperature pair of the experiment T610BM was not sufficient to reach the required degree of crystallinity and the CM contained in the sample remain non-organized (inferior < 200°C). In this range of crystallinity the evolution of the RSCM parameter is still debated, the evolution of the IR is very slight and does not show a clear evolution. Finally in this range of degree of maturation, the IR is not the best parameter to observe the evolution of the crystallinity (Henry et al., 2019).

V.5.2.2 Catalyzing effect of deformation and deviatoric stress

During experiments, even in the undeformed zone, a large deviatoric stress is applied on the sample. Paterson Rig experiments and thermal maturation in autoclaves have been carried out at the same pressure, so it is possible to compare the results from the Paterson rig with the calculated kinetics. The average IR and standard deviation as well as experimental temperatures from the 8 Paterson Rig experiments have been plotted on the duration and peak temperature diagram (Figure V.28). Adding the IR measured in average in undeformed zone, the theoretical time of annealing is obtained based on the kinetics (in grey in Figure V.28). For all experiments, in the shear or co-axial assembly, the calculated duration is equal to the actual experimental duration when considering the lowest values of IR measured

in the sample, but the calculated duration is twice, or even larger, the actual duration when considering the highest IR measured. In other words, CM crystallinity increases faster than that in hydrostatic experiment (on which the kinetic laws were established). The sample PP641, which is homogeneously deformed, illustrates nicely this effect: the calculated duration is at least two times with respect to the real duration (i.e. 100 hours) and reaches in the highest duration of an average of 8 times (i.e. 320 hours against 42 hours of experiments). In addition, the sample PP649 was homogeneously shortened, so the deformation is generalized and no undeformed zone could be plotted in this T-t-IR diagram. Indeed, the viscous deformed sample shows a very important increase of the expected time until to 8 times the experimental duration for the maximum IR range. During PP638 experiment, the mechanical data show a shallow curve of the stress followed by a drop stress. This shallow part consists in the plastic deformation of the sample before the localization of brittle slip planes. The expected duration, as the one for PP649, is longer than the experimental duration, from 4 additional hours up to 5 times of this experimental time.

Therefore, the effect of deviatoric stress is important and catalyzes the kinetics of transformation of the CM during the carbonization and the early graphitization processes. The observation from these two samples strengthens our interpretation of the deformation increasing effect of the CM crystallinity debated above.

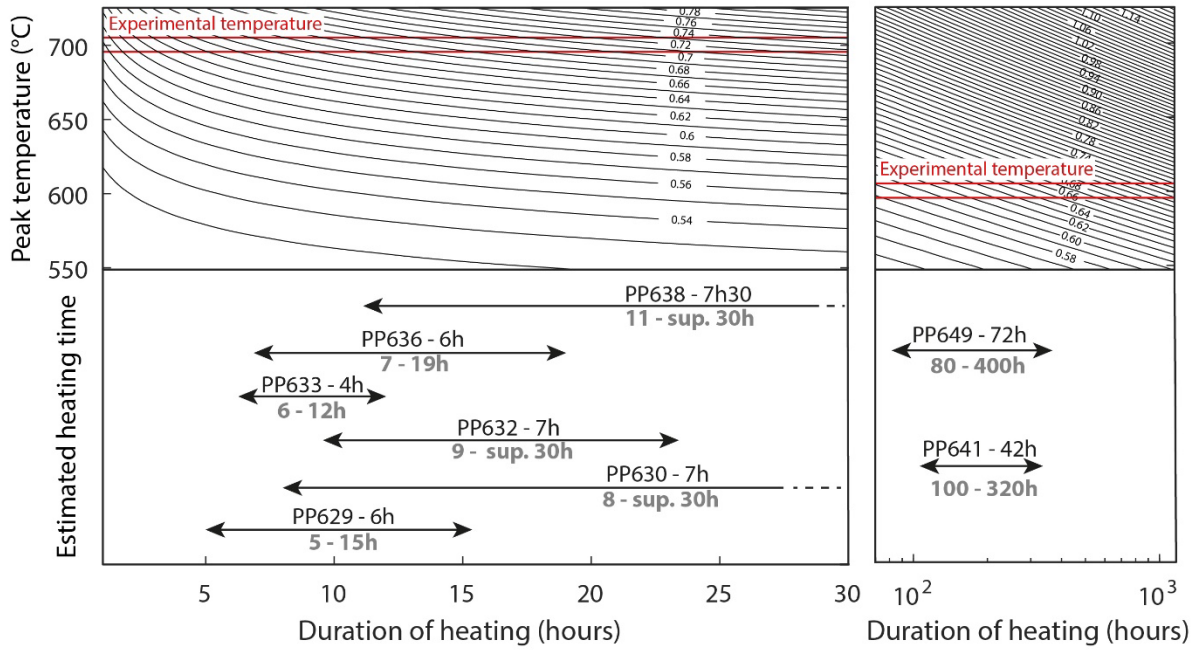

Figure V.27 : Comparison between the experimental exposition times (black) and the necessary times of heating (grey) based on the calculated kinetics, experimental temperatures and measured IR in undeformed zone.

V.5.2.3 Griggs apparatus vs. Paterson Rig: the pressure effect

The use of two different experimental apparatuses permits to deform starting materials at two different confining pressure. As shown by previous studies, the effect of pressure should have a catalytic effect on the kinetics of graphitization for well-organized carbonaceous material. Indeed, experiments have been carried out in order to reproduce graphitization processes from ambient pressure up to 1GPa (Bustin et al., 1995) and show the correlation between the increasing pressure and the decreasing activation energy. In addition, kinetics laws have been established at different pressures in order to understand the effect of pressure during the graphitization processes (Nakamura et al., 2020). However, this hypothesis stays unexplored for the poorly organized CM. Two experiments from the Paterson Rig (PP641) and from the solid-medium Griggs apparatus (T609BM) have been carried in very similar experimental conditions such as experimental temperature (600°C) and duration (34 and 38 hours). The only parameter that changes during these experiments is the pressure set at 150MPa and 1000MPa respectively for the Paterson Rig and the Griggs apparatus. In order to avoid bias, the IR measured in undeformed zones have been used and are 0.624 ± 0.017 in the low pressure experiment and 0.804 ± 0.082 (+29%) or 1.013 ± 0.075 (+62%) for high pressure experiments. The deviation of values of the two undeformed zones is explained by an important vertical temperature gradient in the “Tullis-

modified" Griggs apparatus. Notwithstanding this technical issue, the important deviation between the low and the high pressure experiments cannot be explained only by this temperature gradient. Therefore, as during the late graphitization stage, the pressure has a major control on the kinetics of transformation of the CM during the carbonization and the early graphitization stages and should be taking in consideration before using the RSCM.

In addition, the local strain rates of the two experiments are very similar with values ranging from 10^{-3} to $10^{-4}s^{-1}$. Therefore, this parameter allows comparing the microstructures developed during experiments. However, during the PP641 experiment, the mechanical data curve shows a first plastic deformation followed by a brittle deformation forming fractures. Due to this evolution, the focus will be made only on the first part of the mechanical data when the deformation is plastic. Microstructural results show two different regimes of deformation. In the Paterson Rig experiment, the localization of the deformation along 30 to 50µm wide shear-zones whereas the Griggs experiment shows the localization of the deformation on a 20µm wide fractured zones. The passage from the brittle to the viscous deformation could be explained by the quantity of strain localization. Indeed, when the pressure increases, the deformation is more localized and at this strain rate and this temperature conditions, closed to the brittle-viscous limit, the concentration of deformation more important could play a role on the type of deformation.

V.5.2.4 Local variation of the IR

In experimental samples, a dispersion of the values is observed on the deformed zones. In addition, in some samples, such as T609BM and T610BM (Figure V.20), a large dispersion of values at very short scales is described and makes difficulties on the interpretation of the evolution of the CM crystallinity. As explained above, the possible influence of previous structures can control the evolution of the crystallinity (Bustin et al., 1995). However, the disks of sample used in these experiments have been cut at 45° of the bedding and the evolution of the IR does not fit with the bedding stratification. Therefore, the bedding influence is rejected. In addition, Bustin et al. (1995) discussed about strain shadows generated by the mineralogical changes in the sample. Our samples are mainly composed of "hard" clasts such as quartz and albite and could create this kind of strain shadows. In addition, the evolution

of the mineralogy at small scale could generate preferential paths for fluids and these fluids could conduct to local overpressures (Raimbourg et al., 2017b). As the pressure is a controlling factor of the CM kinetics (see the discussion section V.5.4), the over-pressurized zones could catalyze the maturation of the CM.

V.5.2.5 Comparison with natural data

Similar to the natural strained zone presented in Chapter IV, CM crystallinity measured thanks to the RSCM in strained zones has shown the same evolution and in the same proportion. Indeed, in natural and experimental strained samples (Figures V.18 to V.24), a very slight increase of the CM crystallinity is observed in brittle deformed zone (Figures V.18 and V.24) whereas viscous deformation leads to an increase of around 20% in average (Figure V.21 to V.24). In addition, the quantity of strain is controlling the response in terms of intensity of increase of the CM crystallinity for both sample types and the same dispersion in strained zones is observed. Therefore, the evolution of the CM is the same for natural and experiment strained zones and could be explained by the same phenomena: the shear is responsible of the parallelization of the Basic Structural Unit (BSU), the flattening and the coalescence of the pores of the CM. These processes are associated with crystallite growth and all together leads to the CM crystallinity increase (Bustin et al., 1995; Ross and Bustin, 1990).

V.5.3 External factors catalyzing CM transformation

Several external factors could influence and catalyze the crystallinity of the CM. Here, the effect of water, degree of maturity of the starting material and the pressure effects are discussed.

V5.3.1 Water effect on the kinetics and link with the shear-zones

In order to explore the effect of water on kinetics, 10 %wt water has been added in gold capsules during thermal maturation experiments for experiments run at 500, 600 and 800°C with different durations. The evolution of the IR and the distance between the D- and G-bands (RBS in Henry et al. (2019) have been used in order to compare the results from the dry and wet maturations. Naturally, from 200 to 360°C the IR increases and the RBS decreases. The evolutions of these parameters are identical for both starting materials and will be presented together. For very short experiments (i.e. 3 and 8 hours) the IR and the RBS show a very small or negligible increase of the crystallinity on wet samples. For

experiments lasting 24 and 72 hours, the crystallinity enhance is less important in wet samples for high temperature of maturation (800°C) whereas it is catalyzed for lower temperatures (500 and 600°C). For long-term experiments, the crystallinity is the same as that at 800°C (Figure V.29). It is important to notice that all the evolutions are very small or negligible (i.e. less than 1%). Finally, the effect of water is negligible and could not explain the important evolution of crystallinity measured in strained zone. This results is in agreement with the study conducted at higher temperature during the graphitization, where no evolution of the CM kinetics has been observed after adding water (Huang, 1996).

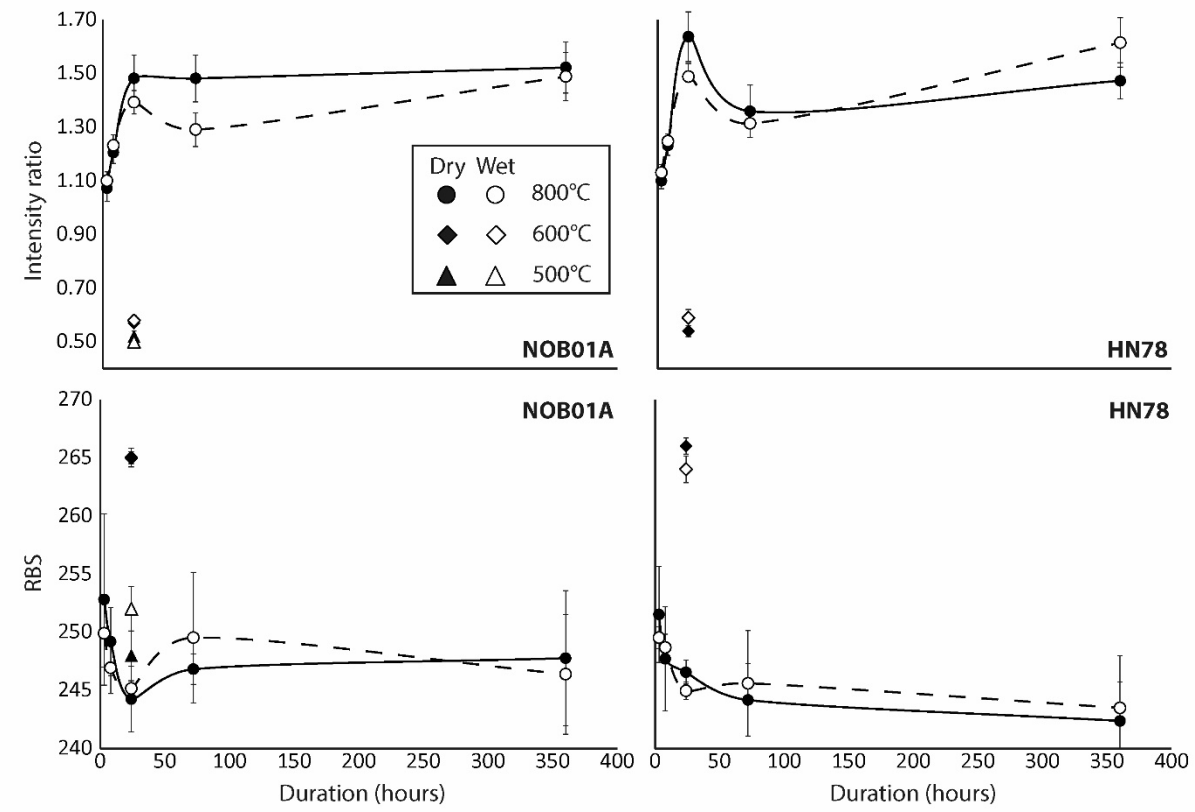

Figure V.28 : Intensity ratio and RBS evolution during thermal maturation experiments for dry and wet powdered samples 18NOB01A and HN78.

V.5.3.2 Maturity of the starting material

The maturity of the starting material, as the type of CM, is an important factor that controls the kinetics transformation of the CM. This point has still been debated for graphitization stage when a metamorphic event occurred before a second more important one that controls the CM maturation. Results suggest that a preexistent metamorphism could delay the crystallization of the CM for higher metamorphic peak temperature (Beyssac et al., 2019). However, this point has never been debated for the carbonization

and the early graphitization stages. Comparing the immature shale (18NOB01A) and poorly mature shale (HN78), used as starting materials, in the thermal maturation experiments could answer this question. On the two master curves presented above (Figure V.3), a similar or slight quicker maturation is observed for the immature shale in comparison with HN78. In addition, the carbonization maturation of HN78 seems to be slower than that for 18NOB01A based on the steepness of the master cruves (Figure V.3). Finally, regarding to the geological time transformation of the CM, the crystalline organized state of the CM, reached when the IR is equal to 1.6, is observed with a shorter time in the case of the poorly mature shale. Therefore, similarly to the graphitization stage, during the carbonization and the early graphitization stages (Beyssac et al., 2019), the maturation of the CM is delayed because a larger quantity of energy is necessary due to the pre-organization of the CM. However, when the quantity energy needed is reached, the crystallinity evolution becomes quicker than the one of the non-organized CM.

V.6 Conclusions

In Chapter IV, we were describing the effect of the non-seismic deformation on CM crystallinity through natural samples presenting strain gradients at several scales during the carbonization and early graphitization stages of maturation. In this study, we were interested in the non-seismic deformation effect on the CM crystallinity using experimental approach in order to reproduce these structures in laboratory. The RSCM has been used to characterize the evolution of the CM crystallinity based on the IR, a sensitive parameter to the deformation reflecting the CM lattice organization. Before deformation experiments, thermal maturation experiments under isotropic stress, without strain (but for initial compaction) have been conducted in order to contrast kinetics transformation of the CM from the non-organized to the poorly organized CM (i.e. during the carbonization and early graphitization stages of maturation). These static maturation experiments provide the basis to compare the evolution of the CM when adding strain or deviatoric stress during experiments. In a second time deformation experiments have been carried out using the Paterson Rig and the solid-medium Griggs apparatuses, respectively at low and high confining pressure to reproduce strained zones with a degree of crystallinity of the CM close to the ones observed in natural samples. Experiments have conducted to the formation of two types of deformed samples with in one hand brittle deformation and in other hand viscous deformation. Mechanical data, microstructures and RSCM results are concordant and show an evident evolution of the CM crystallinity in both cases. Brittle deformation is localized in narrow zone, with angular clasts and a matrix with a large grain size reduction. The IR measured show a slight increase, inferior to 5%. In contrast, ductile deformation is characterized by narrow 10 to 40µm wide foliated to intensely foliated zones. Shear-zones produced by deformation at low and high pressures show a localization of the deformation based on the development of new anisotropic phases and the diminution of hard clasts such as quartz and albite. Concurrently, the CM crystallinity reflected by the IR evolution in the deformed zones shows a consequent increase from 10 to 20% even up to 40% in the mostly deformed zone. In addition, the comparison between hydrostatic maturation and Paterson Rig experiments has shown a constant increase of the CM crystallinity, emphasized in homogeneously plastically deformed samples, induced by deviatoric stress and deformation. A little amount of deformation is necessary to be detectable on the CM crystallinity analyses but we observed a strong correlation between the strain

quantity and the CM crystallinity increase. In addition, an important dispersion of the values has been observed in the zones where CM crystallinity was increased by strain.

All these results are very similar, in terms of CM crystallinity evolution, to the ones observed for the natural non-seismic deformed zone at all scales. It looks reasonable to use the results obtained experimentally to interpret some results on natural samples in the future. In addition, experimental results on the CM crystallinity are similar to the results obtained on natural and experimental analyses during the late graphitization stage (Bonijoly et al., 1982a; Bustin et al., 1995; Kedar et al., 2020; Nakamura et al., 2015; Ross et al., 1991a; Suchy et al., 1997). The CM crystallinity enhance processes observed during the graphitization are akin to those ones demonstrated here, which operate on CM with a lower crystallinity (hence in the stage of "carbonization" and not "graphitization"). Finally, similarly to natural samples, the experimental sample results support the hypothesis that the effect of strain is one of the main controlling factors of the CM crystallinity.

In addition, we paid a special attention to the external controlling factors of the CM kinetics (i.e. water saturation, pressure and crystallinity of the starting material). Through the Paterson Rig compared to the solid-medium Griggs experiments, the effect of pressure has been highlighted in the lower range of crystallinity of the CM and remains one of the main controlling factors on the CM crystallinity. The degree of crystallinity of the starting material is still important for long term heating, similar to the natural ones, and pre-ordered CM (i.e. in carbonization phase) conducts to a faster evolution towards well-organized CM. Finally, additional water in the system does not catalyze the carbonization and early graphitization processes.

Preface

This chapter is dealing with the effect of the seismic deformation, often associated to quick and brittle mechanisms, on the CM crystallinity. In this study, Black Fault Rocks, interpreted as pseudotachylyte in literature, have been analyzed using RSCM high resolution profiles paired with microstructural observations. In addition, numerical modelling of the heat diffusion and the CM kinetics during the carbonization and early graphitization stages (i.e. IR from 0.5 to 1.6) has been developed for molten layer similar to pseudotachylyte in order to compare the CM crystallinity evolution in a molten layer with the one from BFR. Results suggest that the increasing of the IR in the BFR cannot be associated with molten or frictional heating origin but with a mechanical wear control on the CM crystallinity.

This work has been submitted in the "Scientific Reports" journal under the title of "**Pseudotachylyte veins in accretionary complexes: melt or mechanical wear?".** It has been adapted avoiding the repetition in the thesis manuscript. In addition, this work has been presentend during two international congress first on the 29th of March 2021 at the European Geosciences Union (EGU) online congress and on the 5th of November 2021 at the Réunion des Sciences de la Terre (RST) congress in Lyon (France).

Chapter VI – The role of seismic deformation on the carbonaceous material crystallinity: pseudotachylyte veins in accretionary complexes: melt or mechanical wear?

VI.1 Abstract

Whether seismic rupture propagates over large distances to generate mega-earthquakes or is rapidly aborted mainly depends on the slip processes within the fault core, including in particular frictional melting or intense grain-size reduction and amorphization. The record of seismic slip in exhumed fault zones consists in many instances in Black Faults Rocks, dark and glass-like-filled aphanitic veins that have been interpreted as resulting from the quenching of frictional melts, i.e. pseudotachylytes. Such interpretation has nevertheless been questioned as similar macro to nano-textures have been observed either on intensely comminuted natural fault rocks or on slow creep experiments on crustal rocks, where melting is absent. Here, we report a new dataset of Raman Spectroscopy of Carbonaceous Material analyses, aimed at discriminating the slip weakening processes operating in the fault core during slip. Using high spatial resolution profiles on natural Black Fault Rocks from accretionary complexes and an experimentally calibrated modelling of Raman intensity ratio evolution with temperature, we assessed different scenarios of temperature evolution during fault slip. In the three studied Black Fault Rocks interpreted so far as natural pseudotachylytes, Raman Spectroscopy of Carbonaceous Material results are not consistent with a molten origin and therefore rather reflect mechanical wear during deformation. These results bear major consequences on the dynamics of faulting, as the slip-weakening processes that occur during seismic slip rely on the extreme grain-size reduction and fluidization rather than melting.

VI.2.1 Introduction

Pseudotachylytes have been described for the first time at the beginning of the XXth century as veins filled with black and aphanitic to glassy material (Shand, 1916). They are considered as resulting from frictional melting produced by landslide, meteor impact, or fault rupture (Grunewald et al., 2000; Masch et al., 1985; Reimold, 1995), most often in the shallow and brittle domain of the lithosphere, but in some instances at important depths until to the eclogite facies conditions (Austrheim and Boundy, 1994; Sibson, 1975; Wenk, 1978). Many pseudotachylyte veins are described within fault systems in crustal rocks and are associated with different types of brittely deformed rocks such as cataclasite or fluidized gouge. Pseudotachylyte veins present typical features such as injection structures, amorphous matrix or microlites (Sibson, 1975). More recently, Black Fault Rocks have been described in sedimentary

accretionary prisms (Hasegawa et al., 2019; Ikesawa et al., 2003; Kitamura et al., 2005; Meneghini et al., 2010; Mukoyoshi et al., 2006; Rowe et al., 2005; Ujiie et al., 2007) with macro- and micro-structures similar to the pseudotachylytes reported in crustal rocks (Sibson, 1975). These Black Fault Rocks are described as fault core filling material in zones of intense deformation of the host-rock at low to very low temperature conditions ranging from 160°C to 320°C.

VI.2.2 Ambiguity of the microstructures

Whether Black Fault Rocks originate from friction melting or mechanical wear and drastic grain-size reduction is a long-standing issue, due the ambiguity of some of the microstructures associated with pseudotachylytes (Sibson, 1975). Indeed, micro-textural features, such as fluidization and flow textures, amorphous and aphanitic textures, or corroded clasts were considered as a result of ultra-comminution (Lin, 1996; Marti et al., 2017; Pec et al., 2012b, 2012c; Spray, 1995; Wu et al., 2020) or intense fluid-rock interaction within the fault core (Yamaguchi et al., 2014), without melting. This issue is even more acute in the Black Fault Rocks hosted in low-grade metasediments, which contain large amounts of mineral-bound water: upon slip and temperature increase, thermal pressurization of released water might reduce friction and prevent from further temperature increase and ultimately from melting (Brantut et al., 2010, 2008; Rice, 2006).

VI.2.3 Insights from RSCM on fault slip processes

Raman Spectroscopy of Carbonaceous Material is a powerful geothermometer widely used in metamorphic petrology to constrain peak-temperature conditions for both regional and contact metamorphism (Aoya et al., 2010; Beyssac et al., 2002; Raimbourg et al., 2014). Raman Spectroscopy has been also used in order to evidence frictional heating during seismic events on natural Black Fault Rocks from accretionary complexes (Furuichi et al., 2015; Ito et al., 2017; Kouketsu et al., 2017; Kuo et al., 2018) and on experimentally deformed samples (Ito et al., 2017; Kuo et al., 2017). However, crystallinity of carbonaceous material in intensely deformed rocks may be also influenced by parameters other than temperature. In particular, shear has been shown to be responsible for a large increase in crystallinity of carbonaceous material (Bonijoly et al., 1982b; Bustin et al., 1995) even if in some other examples, the relationship between strain and Raman spectrum evolution is more ambiguous (Ito et al.,

2017; Kedar et al., 2021; Kouketsu et al., 2017; Kuo et al., 2018). Therefore, in Raman Spectroscopy studies on both naturally and experimentally damaged rocks, it is difficult to disentangle thermal and mechanical effects.

A way out of this conundrum relies on the fundamental difference between temperature and deformation as the strain field might be discontinuous, while the temperature field, because of diffusion, is not. Based on this straightforward idea, we developed a new high-resolution spatialized approach to Raman Spectroscopy (*i.e.* spot size < 2µm), to unravel how the carbonaceous material crystallinity is distributed in space within rock samples. We applied this approach to three Black Fault Rocks described as pseudotachylyte in two exhumed accretionary complexes, two in the Shimanto Belt (Hasegawa et al., 2019; Ikesawa et al., 2003) in Japan and one in the Kodiak Accretionary Complex (Meneghini et al., 2010; Rowe et al., 2005) in Alaska, in order to discriminate the respective effect of temperature increase and strain, and eventually to decipher the mechanical processes at the origin of the Black Fault Rocks.

VI.3 Results

VI.3.1 Structures

The two exhumed accretionary complexes investigated here were both formed of stacks of units composed either of coherent turbidites or tectonic mélange units, both mostly composed of shales and bounded by thrust faults (Byrne, 1982; Taira et al., 1988). Some of these fault zones (two in Shimanto and one in Kodiak Accretionary Complex), contain Black Fault Rocks bearing characteristic features of pseudotachylytes (Hasegawa et al., 2019; Ikesawa et al., 2003; Meneghini et al., 2010; Rowe et al., 2005). Black Fault Rocks are black and aphanitic thin veins, which cut sharply across, with straight boundaries, the host-rock that often contains itself brittle microstructures (Figure VI.1). The two Black Fault Rocks from the Shimanto Belt are millimeter-thick or less but in Kodiak, the Black Fault Rock described by (Rowe et al., 2005) reaches up to 30 centimeters in thickness. In addition, in contact with meter-sized sandstone lenses, some Black Fault Rocks show structures interpreted as injection structures of a fluidized material perpendicular to the fault core (Ikesawa et al., 2003; Meneghini et al., 2010) (Figure VI.3a, 3b and 3c). The filling material is also black and has an aphanitic texture (Figure VI.1).

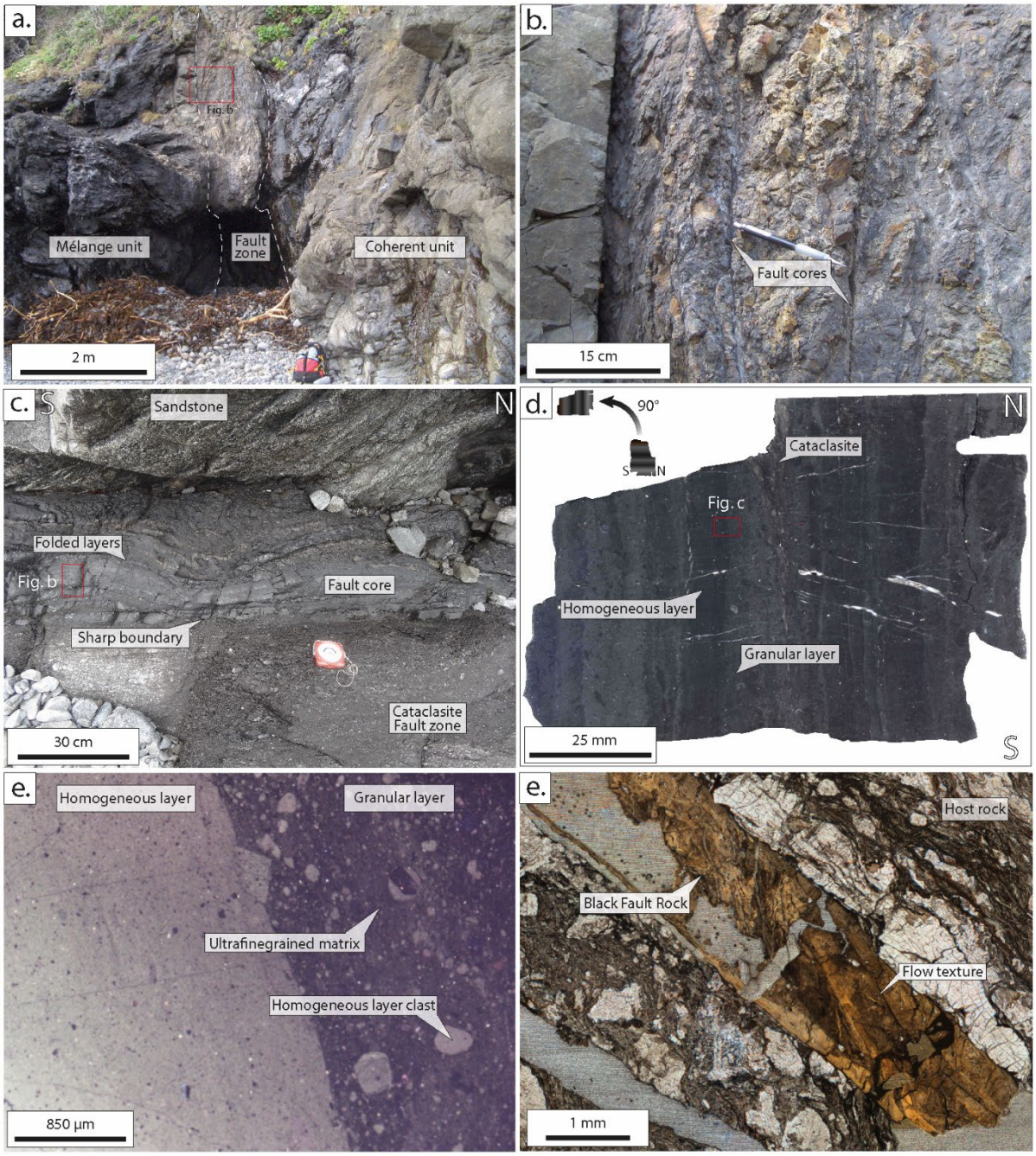

Figure VI.1 : Structures and micro- to nano-structures of the Black Fault Rocks observed in fossil accretionary complexes. ***a.*** *Meter-thick fault zone between the Mugi mélange unit and a coherent unit in the Shimanto Belt* ***b.*** *Close-up view of the fault zone with two fault cores* ***c.*** *Outcrop in the Kodiak Accretionary Complex showing the aphiric fault core sharply cutting the host rock and folded in a later stage* ***d.*** *Internal structure of Kodiak Black Fault Rocks showing alternations of homogeneous and granular layers* ***e.*** *Cathodoluminescence image of Kodiak Black Fault Rock, highlighting the difference between the granular and the homogeneous layers and showing clasts of the homogeneous layer embedded in an ultrafine-grained matrix.* ***e.*** *Flow textures inside the Nobeoka Black Fault Rock*

VI.3.2 Microstructures

The Black Fault Rock material is characterized by sub-rounded to rounded quartz grains, feldspars and sometimes calcite (Ikesawa et al., 2003), less than 100µm in size, embedded in a vitreous black matrix. Grains, sometimes, show embayment, corroded and fractured structures (Hasegawa et al., 2019). Grains are wrapped in a matrix (Figure VI.2a and 2b). Under SEM, the matrix seems composed of a ultra fine-grained material composed mostly of phyllosilicates, with the notable occurrence of pores (Mukoyoshi et al., 2006; Rowe et al., 2005), micrometer scale scattered euhedral iron sulfides or titanium oxides (Hasegawa et al., 2019; Ikesawa et al., 2003; Meneghini et al., 2010) and scattered angular clasts (Figure VI.2c). For example, the Kodiak Black Fault Rock is composed of 1 to 2µm euhedral zoned plagioclases, in a matrix composed of acicular chlorite (Meneghini et al., 2010) (Figure VI.2b). Iron sulfides and titanium oxides present euhedral to sub-euhedral shapes and sizes ranging from ca. 0.5 to 1 µm (Figure VI.2b and 2c). Titanium oxides are mostly observed in the homogeneous layers, whereas iron sulfides are more abundant in the coarse-grained layers. In the Nobeoka fault zone, Black Fault Rock observed in optical microscopy and SEM show flow textures, where the layering is defined by the evolution of the amount of sulfide grains (Hasegawa et al., 2019) and the quantity and the shape of pores (Figure VI.2a and Figure VI.1), when the main material (*i.e.* ultrafinegrained matrix and clasts) remains homogeneous. This texture evolution is also observed in Okitsu and Kodiak Black Fault Rocks. However, on the extreme rim of the Black Fault Rocks, a thinner grain size of the clasts in the ultrafinegrained matrix is observed.

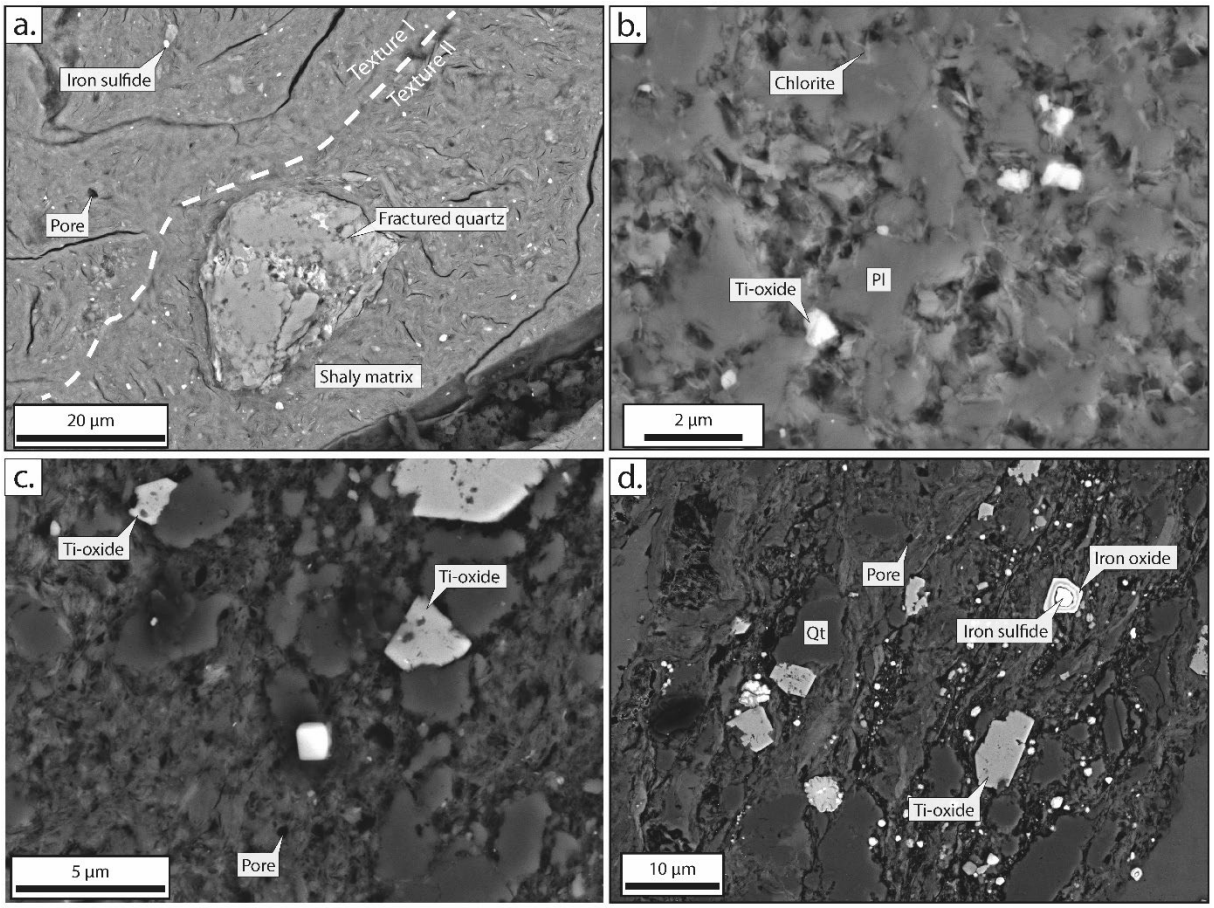

Figure VI.2 : SEM illustrations of the microstructures observed in the Black Fault Rocks and its host-rock. ***a.*** *Fractured quartz in a shaly matrix containing scattered iron sulfides and pores and showing two textures ;* ***b.*** *(Sub)euhedral titanium oxydes in a Black Fault Rock composed of plagioclase clasts and a chlorite matrix* ***c.*** *Shaly matrix of the Black Fault Rock containing euhedral titanium oxydes and pores* ***d.*** *Host-rock shaly matrix containing quartz clasts and iron sulfides replaced by titanium oxydes on the rim Location* ***a.*** *Nobeoka Black Fault Rock ;* ***b.*** *Kodiak Black Fault Rock ;* ***c. and d,*** *Okitsu Black Fault Rock*

The host-rock of the Black Fault Rocks (Figure VI.2d), is also composed of quartz and albite clasts embedded in a matrix composed of phyllosilicates with scattered iron sulfides and titanium oxides, the latter with a much lower abundance than in the Black Fault Rock. The grain size of quartz and albite clasts is larger than in the Black Fault Rock. Clasts embedded in the matrix show angular shapes and internal fractures. Titanium oxides have euhedral shapes, while the iron sulfides have either euhedral or framboïdal shapes. Iron sulfides show a clear metamorphic reactional corona composed of titanium oxides (Figure VI.2d).

Table VI.1 : Location, structural and micro-structural observations of the three Black Fault Rocks analyzed in this study.

Sample	Location	Latitude	Longitude	Geological unit	*Textures* Fault core width	Single/Multi tectonic event	Fluidization structure	Glassy matrix
Okitsu	Japan	33.219433	133.244452	Okitsu mélange	1 mm	Single	Yes	Yes
Nobeoka	Japan	32.592666	131.735357	Hyuga mélange	1.2 - 1.5 mm	Single	No	Yes
Kodiak	USA	57.422027	-152.480361	Ghost Rocks formation	5 - 30cm	Multi	Yes	Yes

Sample	*Micro- to nano-textures* Rounded clasts	Clasts grain size	Corrosion / Embayment structure	Flow texture	Matrix grain size	Fine-grains within matrix	Nature of fine-grains	Fine-grains size	Pores in the matrix	References
Okitsu	Yes	< 100 µm	Yes	Yes	-	Yes	Rutiles	100 nm - 3 µm	Yes	Ikesawa et al., 2003
Nobeoka	Yes	< 0.1 mm	Yes	Yes	-	Yes	Fe-rich particles	10 - 20 µm	No	Hasegawa et al., 2019
Kodiak [a]	Yes	0.1 - 1 mm	Yes	Yes	< 2 µm	Yes	Tabular zoned plagioclases, Ti/Fe-rich particles	1 - 2 µm	Rare	Rowe et al., 2005 Meneghini et al., 2010

[a] The description corresponds to the homogeneous layer

VI.3.3 Polystaged vs single-staged

Moreover, two types of microstructures have been observed for these Black Fault Rocks. Samples from the Shimanto Belt are composed of a single homogeneous layer. In contrast, the thicker Black Fault Rock from Kodiak has a multi-layered structure, with “homogeneous” or “granular” layers, visible in both proportion and size of the clasts embedded in the vitreous matrix (Figure VI.1d and 1e). Homogeneous layers are composed principally of an ultrafinegrained matrix, bright in cathodoluminescence imaging, embedding scattered, micron-size, particles. Granular layers are composed of an ultrafinegrained matrix, dark in cathodoluminescence imaging, embedding a large proportion of clasts of various sizes from the homogeneous layer (Figure VI.1e). These features support the hypothesis of a polystaged formation process for the Kodiak black Fault Rock.

VI.3.4 RSCM profiles

In this study, the Raman Spectroscopy intensity ratio of carbonaceous material (i.e., R1 in (Beyssac et al., 2002)) and area ratio (i.e., RA1 in (Lahfid et al., 2010)) were measured over high-resolution cross-sections through the Black Fault Rocks and bounding host-rock. Intensity ratio evolutions, along each cross-section (straight lines or synthetic cross-sections compiling the projection of distinct segments), show a significant increase, revealing a higher crystallinity inside the veins (Figure VI.3 to VI.5). The median intensity ratio in the host-rock and the Black fault Rock is 0.500 and 0.600 (Okitsu – Figure VI.3), and 0.500 and 0.682 (Nobeoka – Figure VI.4), respectively. In Kodiak, the median intensity ratio in the host-rock is 0.454, while it reaches 0.497, 0.490, 0.507, 0.508 and 0.505 in the five layers forming the Black Fault Rock, labelled I to V, respectively. In the Kodiak Black Fault Rock (Figure VI.5), the highest median intensity ratio values were not analyzed on the homogeneous layer II but on the granular layers with clasts-and-matrix structures layers III to V. Most importantly, intensity ratios profiles show a discontinuity at the boundary between the Black Fault Rocks and the host-rock jumping from 0.530 to 0.620 in Okitsu, from 0.520 to 0.680 in Nobeoka and from 0.490 to 0.530 in Kodiak (using a local median on zones a few micrometers-wide on each side of the boundaries). Within the Black Fault Rock, the highest values are mostly observed near the boundary with the host-rock, within a zone a few micrometers wide (Figure VI.3 to VI.5). Moreover, intensity ratio values measured inside the Black

Fault Rocks show an important scatter marked by a higher standard deviation, from 0.010, 0.004 and 0.009 in the host-rock to 0.063, 0.052 and 0.017 in the Black Fault Rocks of Nobeoka, Okitsu and Kodiak respectively. Accordingly, extremely high intensity ratios are present inside the Black Fault Rocks, up to 0.92 for the Nobeoka Black Fault Rock, 0.72 in Okitsu and 0.55 in Kodiak. Finally, fluidization structures described as injection veins show similar intensity ratios and standard deviation values 0.529 ± 0.019, as the ones in the host-rock, hence a lower intensity ratio than the Black Fault rocks (Figure VI.3).

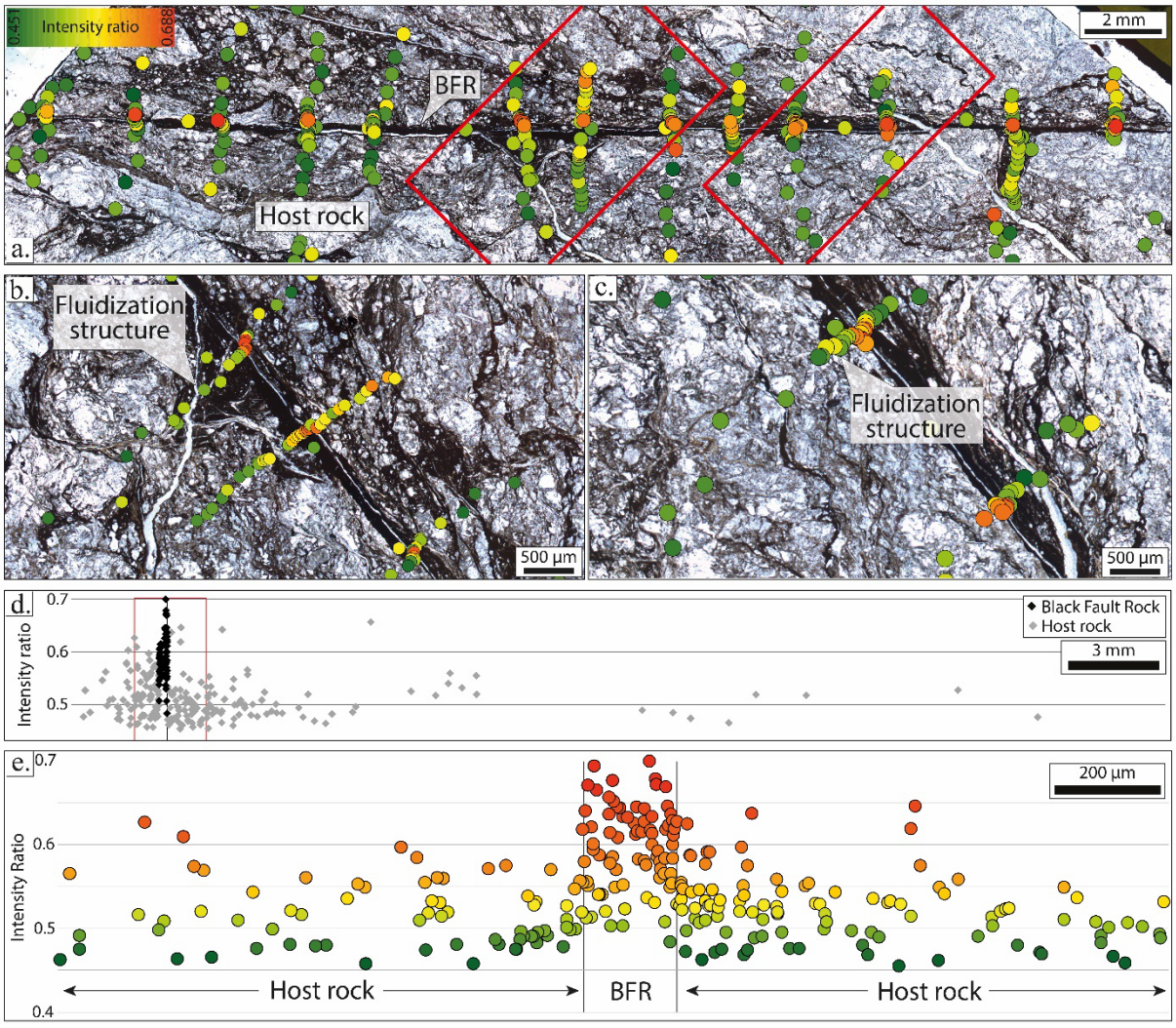

Figure VI.3 : Raman spectroscopy results obtained for the Okitsu Black Fault Rock and its host rock. ***a.*** *Intensity ratio evolution along high-resolution cross-sections of the Black Fault Rock ;* ***b. and c.*** *Close-up views of the fault core and the fluidization structure.* ***d.*** *Integrated cross-section showing RSCM intensity ratio evolution.* ***e.*** *Close-up view (red square in (d)) which shows the sharp evolution of the RSCM intensity ratio near the fault core. RSCM = Raman Spectroscopy of Carbonaceous Material*

Table VI.2 : Statistics on the intensity ratio obtained from the three Black Fault Rocks (BFR) analyzed in this study compared with their respective host-rock, used as a local reference (HR) and underformed references outside of the fault zone.

		Minimum	*Maximum*	*Median*	*Mean*	*SD*
Nobeoka	BFR	0,556	0,924	0,682	0,682	0,063
	HR	0,452	0,835	0,500	0,516	0,058
	Ref.	0,440	0,472	0,455	0,454	0,010
Okitsu	BFR	0,483	0,720	0,600	0,598	0,052
	HR	0,454	0,656	0,500	0,511	0,040
	Ref.	0,459	0,474	0,467	0,468	0,004
Kodiak	BFR	0,478	0,549	0,506	0,506	0,017
	HR	0,424	0,526	0,460	0,462	0,009

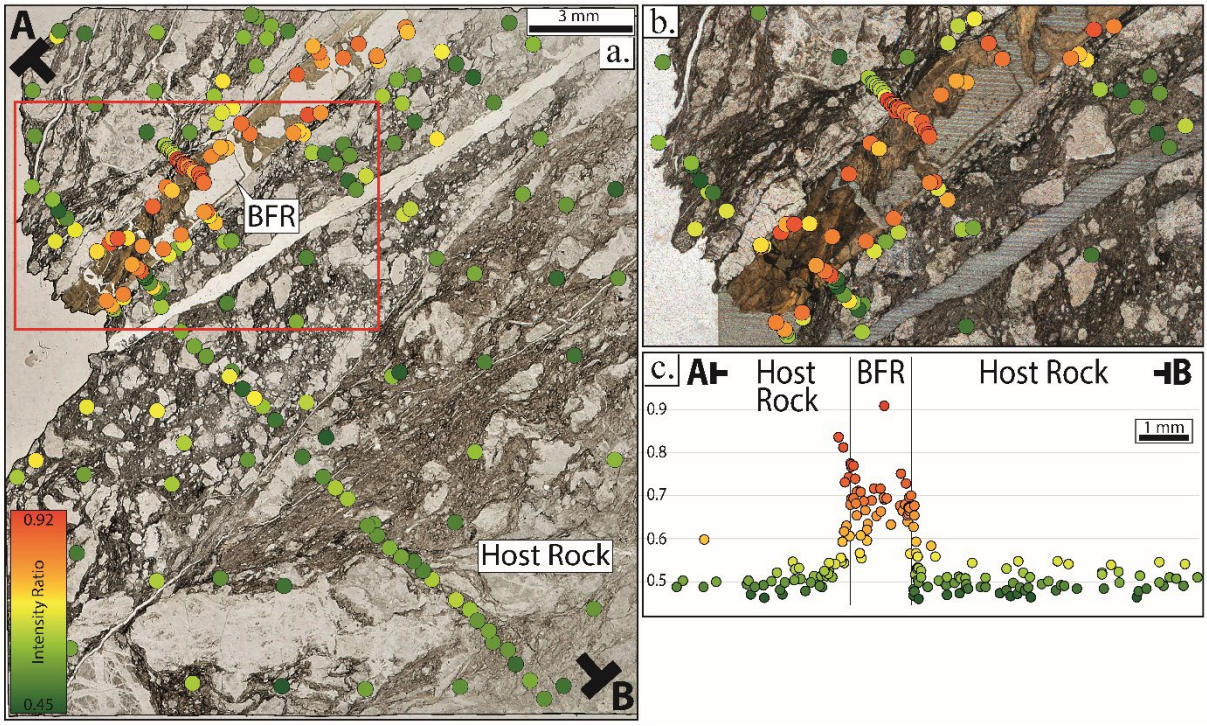

Figure VI.4: Raman Spectroscopy results obtained for the Nobeoka Black Fault Rock ***a.*** *Distribution of intensity ratio over the sample – each dot corresponds to a carbonaceous particle measured by Raman spectroscopy* ***b.*** *Zoom in the contact of the Black Fault Rock with the host rock which shows discontinuity in the intensity ratio* ***c.*** *Cumulative cross-section showing the evolution of the intensity ratio perpendicular to the Black Fault Rock*

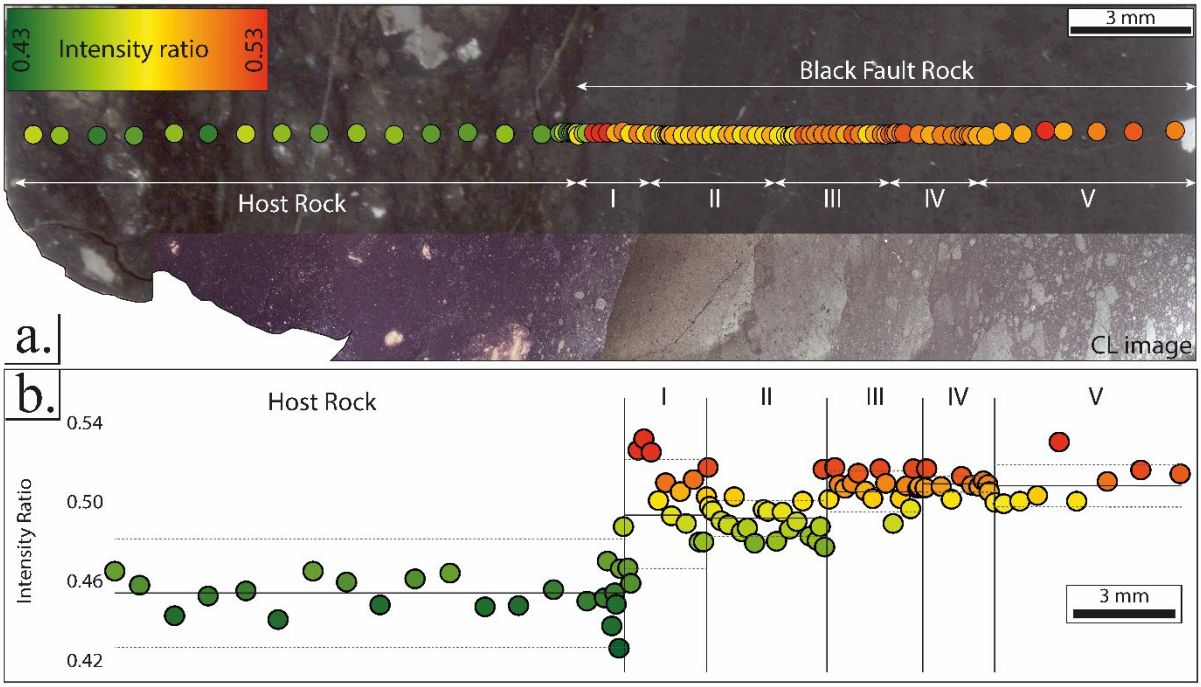

Figure VI.5 : Raman spectroscopy results obtained for the Kodiak Black Fault Rock ***a.*** *Distribution of the intensity ratio measured across the different microstructures and CL image that allows differentiating the multiple layers composing the Black Fault Rock* ***b.*** *Cross-section showing the evolution of the intensity ratio and area ratio through the sample. The largest discontinuities in intensity ratio coincide with the boundaries between the Black Fault Rock and host rock. Solid lines represent the mean intensity ratio and the dotted lines standard deviation of each unit.*

VI.3.5 Thermal modelling of RSCM evolution

VI.3.5.1 Model description

In order to interpret the Raman Spectroscopy ratio profiles across Black Fault Rocks, we developed a model to evaluate the contributions of the effects of heat production and temperature increase during fault slip on carbonaceous material crystallinity. This model combines (1) heat diffusion and (2) kinetics of carbonaceous material evolution during carbonization and early graphitization processes.

Kinetics of Raman Spectroscopy of Carbonaceous Material signal evolution as a function of temperature was calibrated on the basis of thermal maturation experiments, following (Nakamura et al., 2017) procedure. The detailed explanations of the kinetics calculation has been made in the Chapter V.

Heat diffusion modelling is based on the heat equation applied to a 1D system (0), composed of an infinite matrix embedding a molten layer of thickness h(= the current thickness of the Black Fault Rock), with a laminar flow controlled by the Reynold number included between 5.3 and 8.9×10^{-3} (i.e. below 2000). We considered three idealized end-member cases to model the evolution of the system before

and after melting. Case (1) corresponds to a fault zone of thickness h, where heat is dissipated by mechanical work, up to melt the central portion of the fault. Heat production is described as $\dot{E} = \tau . \left(\frac{u}{h}\right)$, with τ (shear stress) and u (slip velocity) inferred from geodetic and seismological models (Yoshida et al., 2012). Cases (2) and (3) describe the temperature field in a molten layer of thickness h, without/with viscous shear heating, respectively. Heat production is modelled as $\dot{E} = \mu \left(\frac{u}{h}\right)^2$, where μ is the melt viscosity.

$$\frac{\partial T}{\partial t} = \kappa . \frac{\partial^2 T}{\partial z^2} + \frac{S}{\rho . Cp} \quad where\ \kappa = \frac{k}{\rho . Cp} \tag{0}$$

Slip parameters are subject to large uncertainties, even if mechanical and seismological data provide some constraints on the orders of magnitude. Different slip models, in terms of velocity u and total duration, were considered, in order to fit the intensity ratio measured in natural rocks.

The geometry and boundary conditions of the model were adjusted on the natural case study of the Nobeoka Black Fault Rock. The thickness of the molten layer of the modelling is fixed to 1mm. The initial temperature and intensity ratio field are very uniform and equal to 200°C and 0.50, respectively. Based on the interpreted melting temperatures for Black Fault Rocks in accretionary complexes in the literature (Meneghini et al., 2010; Ujiie et al., 2007), the temperature of the molten layer is estimated at 1400°C.

Table VI.3 : Constants and respective values used in the heat diffusion modelling.

Constant	Value	Unit	References
Host rock size	0.1	m	-
Molten layer size	1.10^{-3}	m	-
Host rock temperature	200	°C	-
Molten layer temperature	1400	°C	-
Thermal conductivity – k	2.0700	W/m/K	Cermak and Rybach, 1982(Cermak and Rybach, 1982)
Heat capacity – Cp	1180	J/kg/K	Cermak and Rybach, 1982(Cermak and Rybach, 1982)
Density – ρ	2660	Kg/m^3	Schön, 1996(Schön, 1996)

VI.3.5.2 Assumptions of the thermal model

The largest uncertainties in the thermal model lies in the heat production related to mechanical work, which constitutes a large fraction of the total faulting work (Scholz, 1990).

Heat production might in some cases be so large as to melt the slipping fault and form pseudotachylytes, as summarized in (Di Toro and Pennacchioni, 2009). The result of melting (as well as other processes accompanying slip) is to lubricate the fault zone and to reduce sharply the shear stress on the fault plane (Di Toro et al., 2011, 2004). After melting, heat production still persists and is the result of viscous shear-heating concomitant with slip.

Our model aims at assessing the effect of frictional melting on the carbonization of fault rocks. A quantitative modelling would require the precise knowledge of the heat production in space and time, incorporating the effect of frictional slip, melting (and associated shear stress decrease) and viscous shear. These processes and their coupling are not quantitatively constrained. Consequently, our model is based on a simplified scenario of melting, aiming at orders of magnitudes rather than accurate estimates of the variables at stake. We have decomposed the fault zone evolution into two stages: (1) The slip and heat production until the onset of melting in the fault core and (2) the slip and heat production after melting, when a layer of melt with a thickness equal to the thickness of the Black Fault Rock, is sheared between two solid blocks of rock. In this second stage, we consider independently the effects of heat diffusion from a molten layer and the viscous heat production, as the molten layer is being sheared.

In addition, the heat production could be control by additional phenomena like the latent heat that occurs during the crystallization of the molten layer could control the temperature evolution by releasing heat. Based on the work of (Bohrson and Spera, 2003), we can estimate that the enthalpy production (H) ranges from 3.5 to 3.9e10^5 J/kg. For a 1mm thick layer on 1 square meter, the maximum heat diffusion corresponds 3.76e10^6 Joules. Based on these data, we obtain an estimated enthalpy production of 9.31e10^5 to 1.04e10^6 Joules. Hence, the enthalpy production is four times lower than the heat possible diffusion. Based on these results, we neglect the effect of latent heat release in the thermal modelling.

Evolution of the system until melting (Case 1)

We consider here the effects of the frictional heat production that occurs until melting. The heat production is restricted to the layer that eventually melts (i.e. with the same thickness as the Black Fault Rock). The amount of volumetric energy generated by the frictional slip is estimated as:

$$\dot{E} = \tau . \dot{\varepsilon} \quad (1)$$

Where, τ is the shear and $\dot{\varepsilon}$ the slip rate divided by the size of the sheared layer. The shear stress is estimated from few MPa (Lin et al., 2013; Yoshida et al., 2012) to a maximum of 10MPa (Hardebeck, 2012; Hasegawa et al., 2012). Considering this value, for a 1 mm thick layer sheared with a slip rate at 10 m/s (see in the next section) the volumetric energy generated is $1.0e10^{11}$ J/m^3/s.

Results have been presented in the Figure VI.6a and 6b. The melting point, estimated around 1100°C thanks to the literature (Mukoyoshi et al., 2006; Ujiie et al., 2007) is reached very quickly after only $3.0e10^{-2}$ s and the maximize melting temperature used in this study (i.e. 1400°C) is reached after $3.8.10^{-2}$ s. The critical distance, that consists in the distance of displacement before melting and slip weakening is about 30 cm and is totally comparable with the calculated critical distance for natural earthquake (Ide and Takeo, 1997). As a consequence of the very rapid temperature increase, the effect on carbonaceous material is not significant.

Evolution of the system after melting

Without viscous shear-heating (Case 2)

After reaching the melting point thanks to the frictional melting, the next step is to consider the heat diffusion of a 1400°C molten layer. Figure VI.6c and 6d presents the results obtained for the heat diffusion only: the temperature drops down very quickly and as a consequence there is a small evolution of the intensity ratio (0.56 in the core) inside the molten layer, still much lower than the values measured for the natural Black Fault Rocks (0.7 in median).

With viscous shear heating, considering displacement at 1m/s (Case 3.1)

Next step consisted to model the temperature field when a molten layer of the same thickness (h) as the Black Fault Rocks (i.e. 1mm in the model) is being sheared. We assume that the field of velocity in the molten layer is given by the Couette Flow equation (Turcotte and Schubert, 1982) and that the melt viscosity is uniform and constant in time.

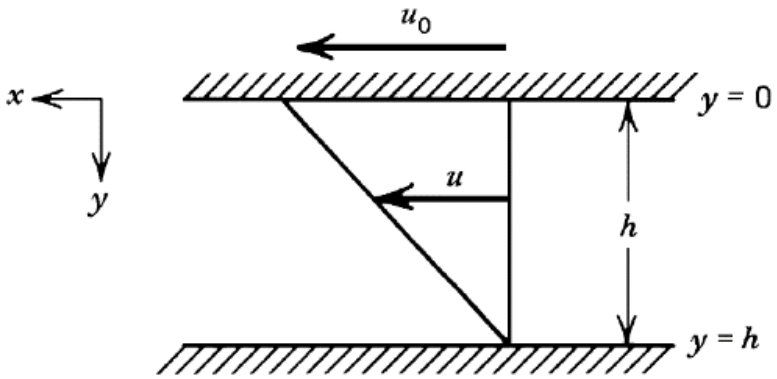

From Turcotte and Schubert, 1982

The shear stress within the molten layer writes as:

$$\tau = \mu \frac{du_x}{dy} \tag{2.1}$$

Where μ is the viscosity and u_x the velocity in the x direction. Based on the Couette Flow equation, for constant viscosity, the heat production yields:

$$\dot{E} = \tau . \dot{\varepsilon} = \tau \frac{d(u_x)}{dy} = \mu \left(\frac{u}{h}\right)^2 \tag{2.2}$$

Viscosity of melt for rocks similar to the Black Fault Rocks range between 10^0 and 10^2 Pa.s (Ujiie et al., 2007). The main factor that controls the amount of heat production is the slip velocity. Estimates for important earthquake (Di Toro et al., 2011, 2004; Scholz, 1990) (M>5) gave slip rate between 1 and 3 m/s. For example, during the mega-earthquake of Tohoku Oki, the maximum estimated slip rate was about 2.5 m/s (Wei et al., 2012). There is a correlation between the slip rate and the size of the fault (Kanamori and Heaton, 2000). Fault zones where Black Fault Rocks are described in the accretionary prisms are structures internal to tectonic units, without major gap either in the stratigraphic ages or in

paleotemperatures. For the Nobeoka Black Fault Rock, the sample comes from a second-order slip plane below the main slip plane of the Nobeoka Tectonic Line. As a consequence, these faults are second-order structures, with much lower slip rate than earthquakes on major, plate-boundary faults, such as 2011 Tohoku-Oki earthquakes.

In addition, melt is occurring from 0.1m/s based on natural example (Sibson, 1975) and from 0.4m/s on experimental examples (Tsutsumi and Shimamoto, 1997). According to these results, and in order to be consistent with studies focused on Black Fault Rocks in accretionary complexes, we consider here slip rate range from 0.1m/s to 1m/s.

Another way to obtain the average slip rate is to use the modelling function proposed by (Madariaga and Olsen, 2012).

$$Slip\ rate = u = \frac{\Delta\sigma}{G}\,\beta \tag{3}$$

The stress drop ($\Delta\sigma$), the modulus of rigidity (G) and the shear wave speed (β) are estimated at 1 to 10MPa, $3.0.10^4$MPa and 3500 m/s (Kanamori and Brodsky, 2004), respectively. Values obtained for the equation (3) are the same as previously found in the literature, as the slip rate calculated ranges between 0.2 and 1.2m/s. In order to consider the maximum heat production, we consider an upper bound on slip rate as 1m/s. The last parameter is the thickness of the molten layer, which is of the order of 1mm on the Black Fault Rocks studied. Based on these parameters we can estimate the maximum shear heating energy around $1.0e10^8$ J/m^3/s.

The last parameter to specify is the duration of viscous shear-heating of the molten layer. Considering an upper bound on slip rate as 1m/s, as explained above, then shear heating duration can be estimated from the total displacement during the earthquake. For pseudotachylytes bearing faults, the total displacement of slip is estimated from 0.1 to 4 meters for earthquakes from M_5 to M_8 (Sibson, 1989). According to (Hasegawa et al., 2019), and based on the thickness of the fault core similar to the one measured on the Gole Larghe fault in Italy, we can estimated the total displacement from 0.2 to 1.2 meters for a single tectonic event (Di Toro and Pennacchioni, 2005). Some earthquakes can generate bigger slip displacement, like 8.3 meters for the Chi-Chi earthquake (Ma et al., 2006) or in extreme case,

displacements as large as 50 meters for the M_9 Tohuko Oki earthquake in 2011 (Wei et al., 2012). However, as discussed above, these earthquakes occurred on major tectonic faults, at the scale of tectonic plates, which do not compare to the much smaller faults hosting the Black Fault Rocks considered here. We consider therefore that ~ 5 meters for a single event is a more appropriate upper bound for the Black Fault Rocks (Hasegawa et al., 2019; Ujiie et al., 2007; Ujiie and Kimura, 2014). Consequently, for a maximum fault displacement of 5 meters with a slip rate at 1m/s we obtain a slip duration of 5 second. We also consider that the viscous shear is effective during 5 second and drops to 0 after this duration. Figure VI.6e and 6f reports the results obtained for the modelling considering the viscous shear heating with a slip rate at 1m/s. However, no significant difference can be observed in comparison with the model without viscous shear heating.

Budget of energy: cooling down vs. shear heating

The case study (case 2), where no viscous shear heating occurs, leads to variation in intensity ratio that are small with respect to measurements in natural Black Fault Rocks (Figure VI.6c and 6d). Considering viscous shear heating for 5s at 1m/s (case 3.1) does not result in significant difference, because the production of heat is not sufficient. One can therefore wonder what conditions of slip might induce enough shear heating as to influence the intensity ratio of the carbonaceous matter.

A first approach to this issue can simply consider the budget of heat associated with the cooling of the molten layer of 1mm of thickness, initially at T_{melt} and cooling down to the host-rock temperature T_{host}:

$$E_n = Cp \,.\, \rho \,.\, h \,.\, Surf \,.\, (Tmelt - Thost) \quad (4)$$

For a square meter surface, we obtain a total energy budget of $3.76e10^6$ Joules.

This budget can be compared with the amount of energy that can be produced by viscous shear heating. Based on the equation (2.2), the heat production scales with the square of slip velocity. An upper bound on heat production can be obtained using extreme slip velocity, of the order of 10 m/s (Wei et al., 2012). Using equation (2.2), we can calculate the amount of energy produced by shear heating for slip duration in the range 0.1s to 1s and for slip rates in the range 1 m/s to 10 m/s, on a volume of V = h . Surf=1mm.$1m^2$ (in Joules):

	1 m/s	**10 m/s**
0.1 s	$1.0e10^4$	$1.0e10^6$
1 s	$1.0e10^5$	$1.0e10^7$

Comparing these values with the heat diffusion (E_n), it appears that shear heating produces a significant amount of energy only for very high slip rates (10m/s) and for duration of at least 0.1s.

With viscous shear heating, considering displacement at 10m/s (Case 3.2)

On the basis of the calculations above, only high slip rate of 10m/s can possibly produce enough energy as to influence the intensity ratio of the carbonaceous material in the molten layer. In order to compare these modelling results with natural data we have to set the shear parameters to find the same value (eg. 0.7 for the intensity ratio) in the center of the molten vein. The appropriate slip rate and the slip duration are at 10 m/s and 0.15 second respectively. The total displacement for these parameters is 1.5 meters and is consistent with naturel estimated slip displacement. Results obtained have been presented in the Figure VI.7a and 7b in the following.

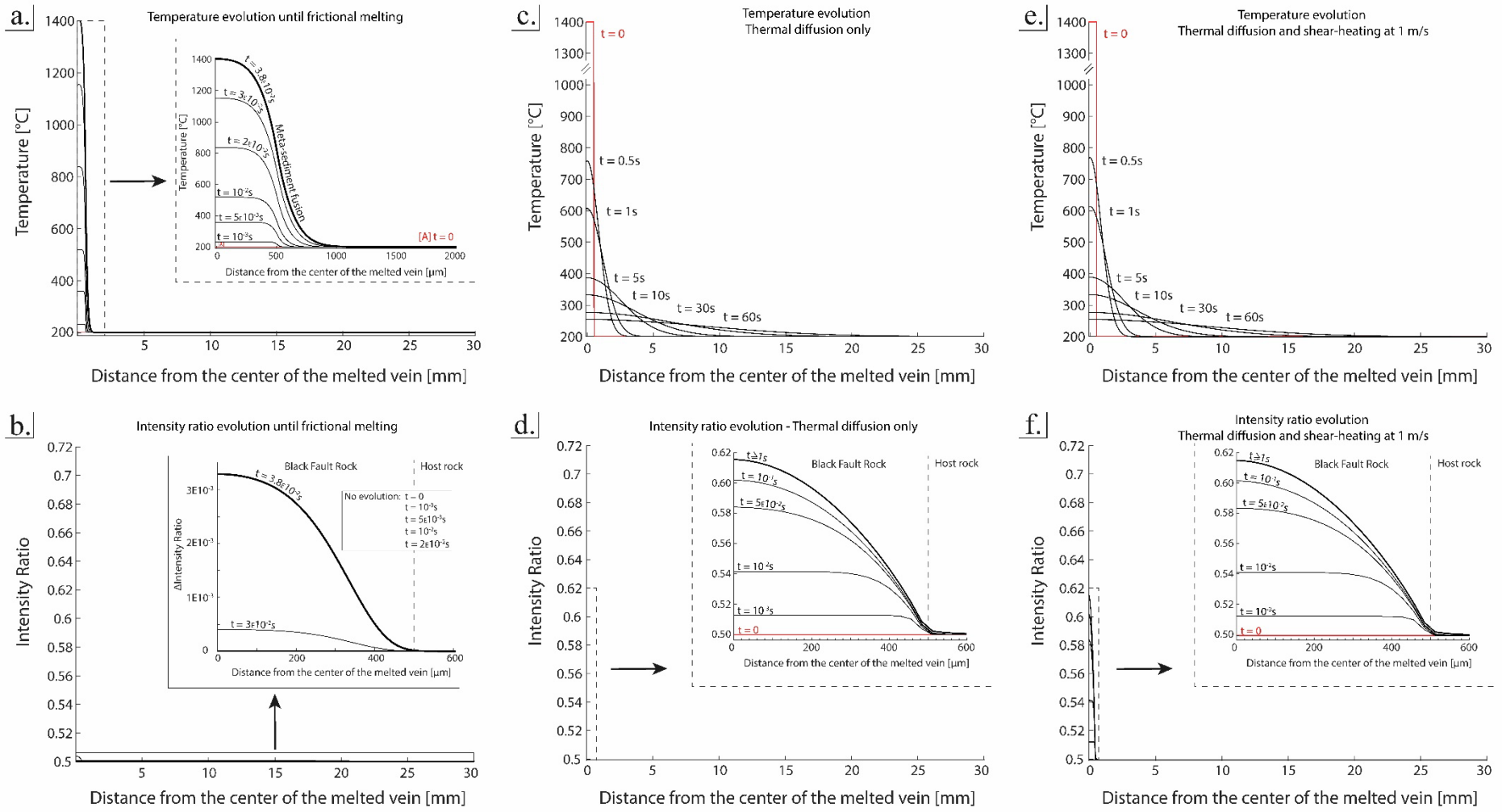

*Figure VI.6 : Thermal and Kinetics modellings for different phases and scenarios during frictional melting . **a. c. e.** Temperature and corresponding Raman Spectroscopy of Carbonaceous Material. **b. d. f**. Intensity ratio profiles across the molten layer and the host rock, for various times. **A. b.** Initial stage, with frictional melting until melting at 1400°C **c. d.** Following stage, with diffusional cooling of a 1400°C molten layer, without heat production **e, f,** same as c and d with heat production viscous shear. In **b. d. f.** for any time t and position x, the intensity ratio is calculated based on our kinetics model of organic matter maturation and the thermal history T(t)*

VI.3.5.3 Modelling results

The temperature evolution before melting (Case 1) is extremely short, as the frictional melting is reached after only few hundredths of second. For this short heating time, the evolution of the intensity ratio of Raman spectra, around 0.003, appear not significant (Figure VI.6b).

After melting at 1400°C, if viscous shear heating is negligible (Case 2), inside the molten layer the temperature drops down quickly (in few milliseconds) so that at the center of the layer, the temperature is reduced to 800°C after less than 1 second. In the host-rock, heat diffusion leads to an increase of temperature, locally up to 800°C, but for a very short time. In this scenario, the intensity ratio reaches 0.615 in the center of the molten layer and decreases rapidly laterally, down to unchanged values of 0.50 at the boundary with the host-rock.

The significant intensity ratio increase in the molten layer requires therefore incorporating the production of heat by viscous shear as the fault is slipping (Case 3). We adjusted the slip velocity to 10m/s and the duration to 0.15s so that the modelled intensity ratios in the center of the molten layer are equal to the natural ones measured in Nobeoka Black Fault Rock (ca. 0.68; Figure VI.7). In spite of significant heat production by viscous shear, the diffusion of heat away from the molten layer into the cold host-rock is extremely efficient, so that sharp temperature and intensity gradients develop exclusively within the molten layer (Figure VI.7a). Therefore, in the outer domains of the molten layer, the intensity ratio remains the same as host-rock values throughout slip (Figure VI.7b).

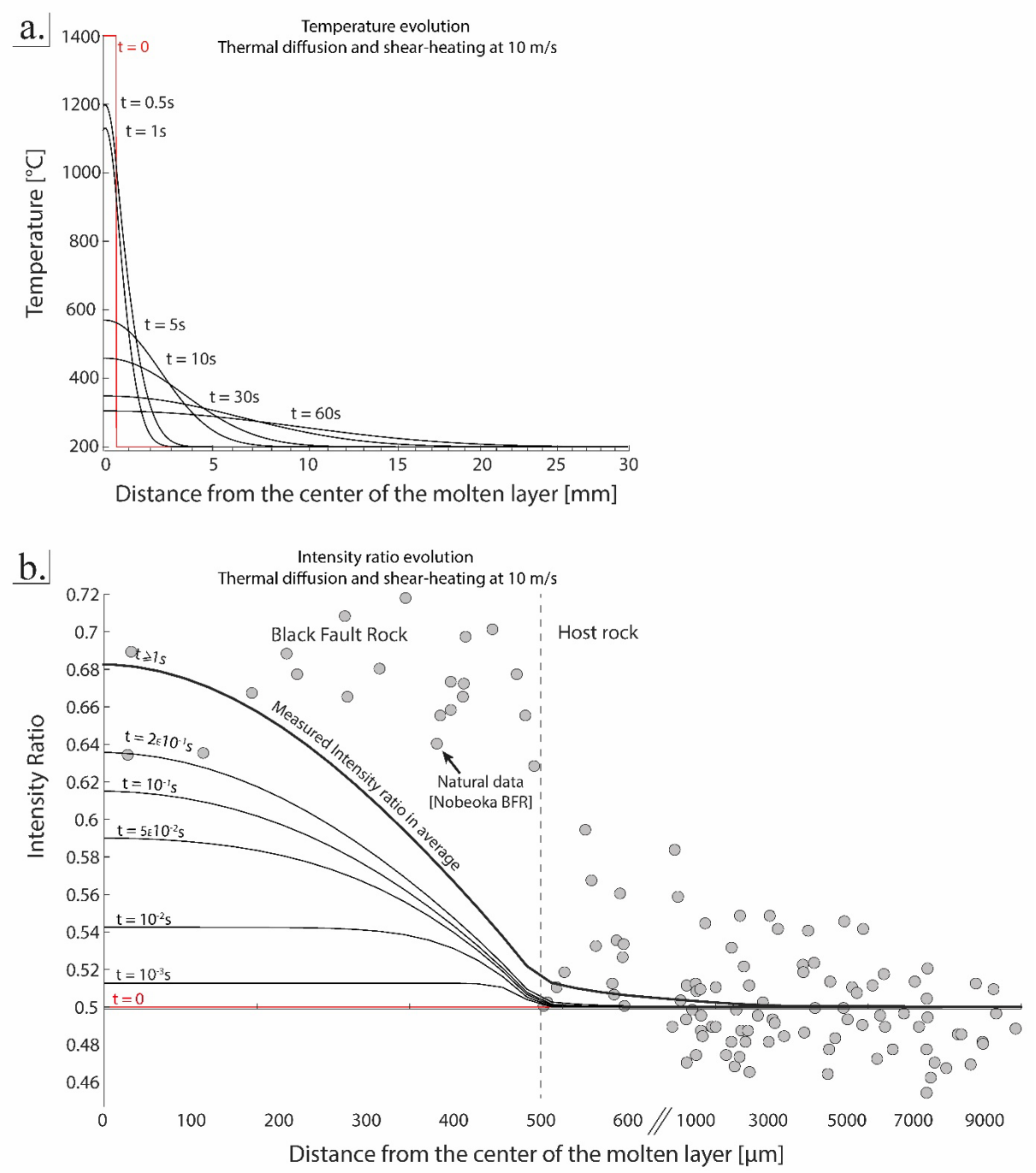

Figure VI.7 : Thermal and kinetic modellings obtained for a 1mm-thick molten layer where heat is transferred by diffusion to the host rock and is produced in the molten layer by viscous shear heating. ***a.*** *Temperature and* ***b.*** *Intensity ratio evolution at different times (curves). Also presented, intensity ratio of the Nobeoka Black Fault Rock. Slip parameters (slip rate and total slip) were adjusted so that the modelled intensity ratio reaches the natural values at the center of the molten layer.*

VI.4 Discussion/Conclusions

VI.4.1 Shape of modelled vs. natural RSCM ratio profile

Parametric models presented here show that frictional melting and viscous shear produce Gaussian shape profiles where symmetric gradients in intensity ratio are located within the molten layer, while natural profiles follow rectangular function shapes with major discontinuities (i.e. steps) coinciding with Black Fault rocks/host-rock physical boundaries. Furthermore, towards the outer boundary of Black Fault Rocks, the modelled peak values are much lower than those in natural cases, even considering extreme conditions of slip and heat production (Figure VI.6 and Figure VI.7b). Therefore, Raman spectra properties of carbonaceous material in the Black Fault Rocks are in contradiction with scenarios where melting occurred.

This conclusion is further supported in polystaged deformation faults such as the Black Fault Rock of Kodiak (Figure VI.5), where the presence of multiple steps in Raman Intensity ratio is difficult to reconcile with thermal models of multiple melting stages.

Other features of Raman Spectroscopy of Carbonaceous Material profiles are at variance with the hypothesis of melting. First, intensity ratios retrieved from injection structures are much lower than those in the fault core, again in contradiction with a common origin as a quenched melt (Figure VI.3 to VI.5). Second, the highest intensity ratio values are mostly measured on the rim of the fault core layer, which is colder than the fault core in thermal models because of heat diffusion. Third, the microstructures do not show evolution from the center of the vein to the rim whereas the temperature profile shows a Gaussian shape evolution.

VI.4.2 Interpretation of microstructural observations in terms of formation process

The three Black Fault Rocks described in this study show features very close to the ones described for the melt-origin pseudotachylytes. These samples are composed of an ultrafinegrained matrix with micro-scale sub-rounded clasts of quartz and plagioclase. Some of these clasts show fractures and corroded shapes interpreted as resulting from interactions with a melt (Hasegawa et al., 2019; Ujiie et al., 2007). However, the same corroded shape of the plagioclase has been observed in cataclastic rocks from the Kodiak Accretionary Complex (Figure VI.8). Moreover, the amorphous material that composes the

matrix of the Black Fault Rock cannot be considered as an undisputable evidence for the former presence of a melt. Indeed, microfault zones filled with amorphous material have also been described in slow creep experiments where frictional temperature increase is not significant (Pec et al., 2012b, 2012c). In addition, Ti-rich and Fe-rich particles, interpreted as droplets, have been described in the three samples (Hasegawa et al., 2019; Ikesawa et al., 2003; Meneghini et al., 2010; Rowe et al., 2005). Our observations confirm the presence of Ti-rich particles in the Black Fault Rock but their shape is systematically euhedral. We observed also in the Black Fault Rock the absence of Fe-rich particles, which are abundant in the host-rock. Incipient replacement of iron sulfides by Ti-rich oxides is already operative in the host-rocks, in the form of corona of Ti-oxides around iron-sulfide particles (Figure VI.2d). The difference in the proportion of the Fe-rich and Ti-rich particles between host-rock and Black Fault Rock can therefore be interpreted as a result of fluid-rock interactions under variable redox-conditions, associated with fluid circulation in fault zones (Yamaguchi et al., 2011). Black Fault Rocks have also an increase porosity with respect to host-rock (Figure VI.2). Increase in porosity might as well be the result of solid-state deformation, even at large depths, as demonstrated in viscously creeping crustal shear zones (Fusseis et al., 2009; Menegon et al., 2015). To finish, the presence of microlites, i.e. microcrystals crystallized from a melt, is not attested in the three Black Fault Rocks considered here. The very fined grained phyllosilicates wrapping the clasts in the Black Fault Rocks have the same nature as the metamorphic mineral present in the host-rock (Raimbourg et al., 2019) . In the Kodiak Black Fault Rock, micrometer-scale, euhedral and zoned plagioclase has been described (Meneghini et al., 2010). This plagioclase recrystallization could be the result of intense fluid-rock reaction (Yamaguchi et al., 2014).

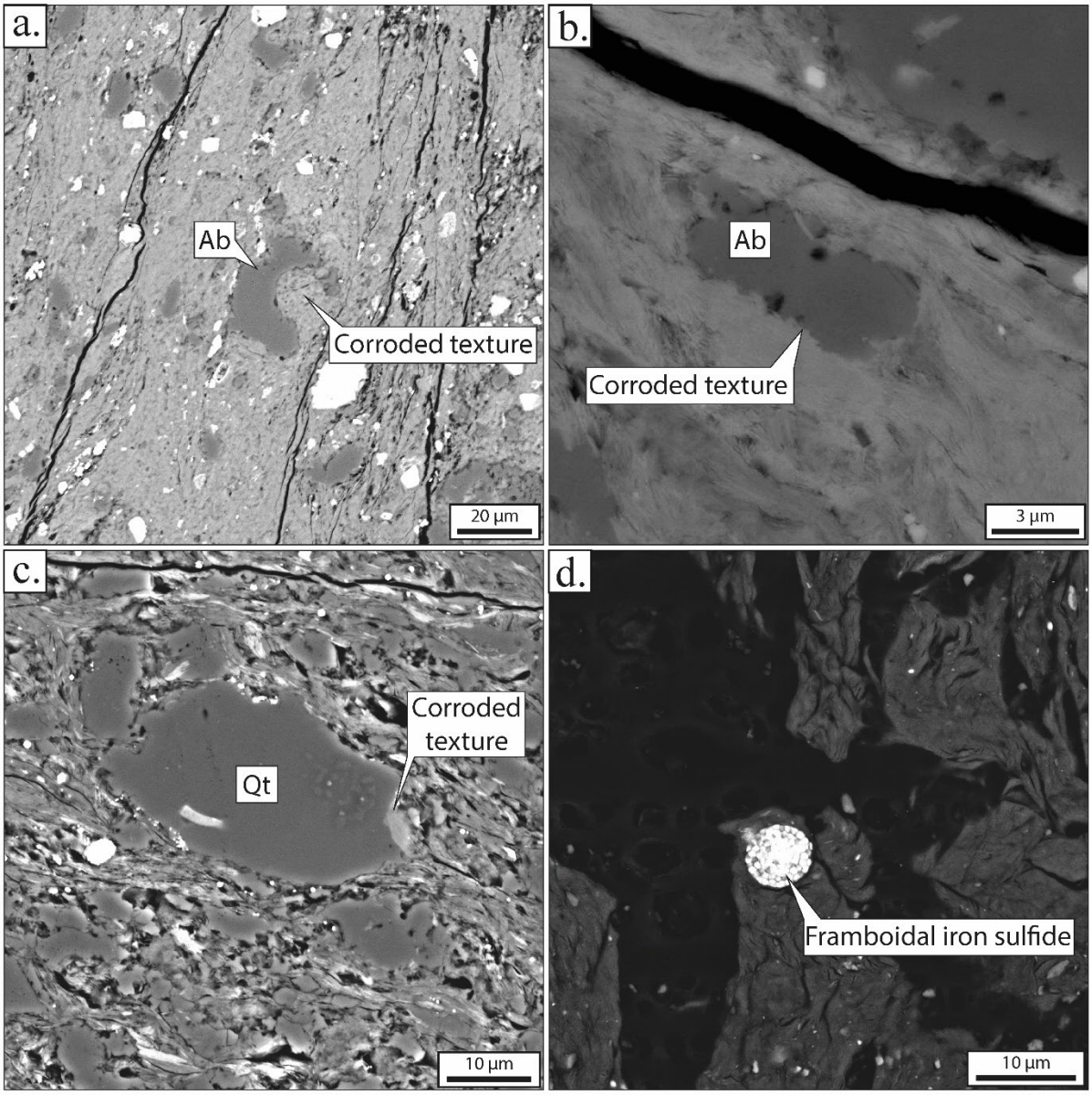

Figure VI.8 : Examples of corroded texture on albite in a cataclasite from the Kodiak Accretionary Complex and Shimanto Belt. ***a,*** *Gulf of corrosion on an albite grain observed in the cataclasite.* ***b,*** *Eroded and corroded texture of an albite grain wrapped in a shaly matrix.* ***c,*** *Corroded shape of quartz grain in the host-rock.* ***d,*** *Framboildal shape grain of iron sulfide in the Nobeoka BFR layer.* ***a, b,*** *Kodiak Accretionary Complex* ***c, d,*** *Shimanto Belt*

As a conclusion, in the three Black Fault Rock described here, none of the microstructures can be considered as irrefutable evidence to discriminate between melting (Sibson, 1975) and strain-related ultra-comminution (Marti et al., 2017; Pec et al., 2012b, 2012c; Wenk, 1978) as a formation process.

VI.4.3 An alternative model to melting: Raman Spectroscopy of Carbonaceous Material (RSCM) ratio profiles record the distribution of strain

While microstructures are rather ambiguous as to the origin of the Black Fault Rocks, the RSCM signal, both in terms of values and spatial distribution, is not consistent with any scenario of frictional heating and melting (Furuichi et al., 2015; Ito et al., 2017; Kouketsu et al., 2017; Kuo et al., 2018). Therefore, temperature is not the parameter that controlled the sharp spatial variations in the distribution of crystallinity of carbonaceous material observed in all the natural samples.

Alternately to temperature, strain might be the factor underlying the RSCM signal variations. The RSCM intensity ratio used in this work has been shown in natural and experimental examples to be sensitive to deformation (Kedar et al., 2021, 2020; Kouketsu et al., 2017; Kuo et al., 2017; Nakamura et al., 2015).

The interpretation of the intensity ratio in terms of strain is nevertheless not straightforward for several reasons. (1) The parameters of deformation (total amount of strain, strain-rate), as well as the conditions of deformation (pressure, temperature, fluid abundance), are only partially known, especially in natural samples, but also in experimental samples where macroscopic variables might be prescribed but local variables are only inferred. (2) The evolution from disordered carbonaceous material to graphite is not a monotonic and simple process, but rather a combination of many elementary processes. This is reflected in the complex evolution of RSCM spectra with increasing metamorphic temperature (Beyssac et al., 2002; Kouketsu et al., 2014; Lahfid et al., 2010): in disordered carbonaceous material, from catagenesis to low-grade metamorphic conditions, increase in temperature results in the increase in Raman Spectroscopy of Carbonaceous Material intensity ratio. Subsequently, at higher-grade conditions, increase in temperature results in the decrease in intensity ratio, up to the graphite where defect bands, i.e., D bands are absent. Therefore, comparison should be preferentially be carried out on carbonaceous matter in the same range of crystallinity. Most existing studies deal with relatively well-ordered carbonaceous particles pertaining to the higher-grade metamorphic conditions (Bustin et al., 1995; Kedar et al., 2020; Kuo et al., 2017; Nakamura et al., 2015; Suchy et al., 1997). In contrast, our

work focuses on relatively disordered carbonaceous typically present in external domains of orogenic belts (Lahfid et al., 2010; Raimbourg et al., 2019).

In natural samples, relationships between strain and crystallinity of carbonaceous particles point rather to an increase in carbonaceous material ordering in viscous mylonites (Kedar et al., 2020; Nakamura et al., 2015; Suchy et al., 1997). In these examples, the low strain-rate attested by the microstructures precludes any significant increase in temperature by shear heating. Beyond the total amount of strain, other parameters of deformation, such as strain-rate, are also likely to play a role: in high grades rocks from the Hidaka Belt, two opposite trends of evolution, i.e. towards higher and lower carbonaceous material ordering, were observed in two types of high strain zones (Nakamura et al., 2015).

In addition, experiments can also shed some lights on the relationship between strain and carbonaceous material ordering. Low strain-rate experiments have correlated without ambiguity zones of high strain with higher carbonaceous material ordering (Bustin et al., 1995). High strain-rate deformation experiments, aimed at reproducing fault zone deformation, have also shown that zones of localized deformation have higher carbonaceous material ordering (Ito et al., 2017; Kouketsu et al., 2017; Kuo et al., 2017), but without a clear quantitative connection between the parameters of slip and the RSCM signal evolution. The interpretation of these high velocity experiments in terms of strain- carbonaceous material ordering relationship is nevertheless difficult, as not only strain, but also temperature is increased in the domains where deformation localizes, so that the respective effect of strain and temperature are impossible to disentangle. In addition, the temperature increase estimation is difficult. In fact, for similar starting material, deformation apparatus and experimental conditions, the calculated temperature increases ranges from <300°C (Kuo et al., 2017) to more than 1000°C (Ito et al., 2017).

The processes behind this increase in crystallinity as a result of shear are active at the nano-structural scale. Shear is responsible for the coalescence of pores and the parallelization of the basic structural units that conducts to a more regular organization of the aromatic carbon layers and to widen carbon sheets (Bonijoly et al., 1982b; Bustin et al., 1995). Therefore, shear will directly catalyze the carbonization reactions and generate higher crystallinity.

In the studied samples, the shape of RSCM profile provides another argument in favor of the effect of strain on carbonaceous material ordering. The stepwise RSCM intensity ratio profiles across the natural Black Fault Rocks coincide well with the microstructure profiles, without evolution from the rim to the center of the vein, which reflect strain or strain-rate distribution (Figure VI.9). Contrarily to temperature profiles, strain or strain-rate profiles can be discontinuous, as a result of dynamic weakening processes.

As a summary, from existing natural and experimental evidences, and from the characteristics of RSCM intensity ratio distribution, we tentatively conclude that carbonaceous material crystallinity therefore reflects at the first order mechanical processes instead of frictional temperature increase. The Black Fault Rocks are composed of extremely fine-grained material, which may be in some cases down to amorphous state, as a result of comminution, i.e., a drastic mechanical work during fault slip. The increase of temperature during such deformation is not sufficient to influence the Raman Spectroscopy ratios within/outside the Black Fault Rocks. As shown by thermal modelling of Case (2), even without considering further heat production by shear heating (Case 3), the temperature increase required to melt the fault core and the subsequent cooling is sufficient to significantly increase (by 0.06) the intensity ratio in the center of the molten layer, but leaves its outer rim unaffected. The absence of such an anomaly in the natural Black Fault Rocks suggests a weak temperature increase, much below temperatures required melting occurs.

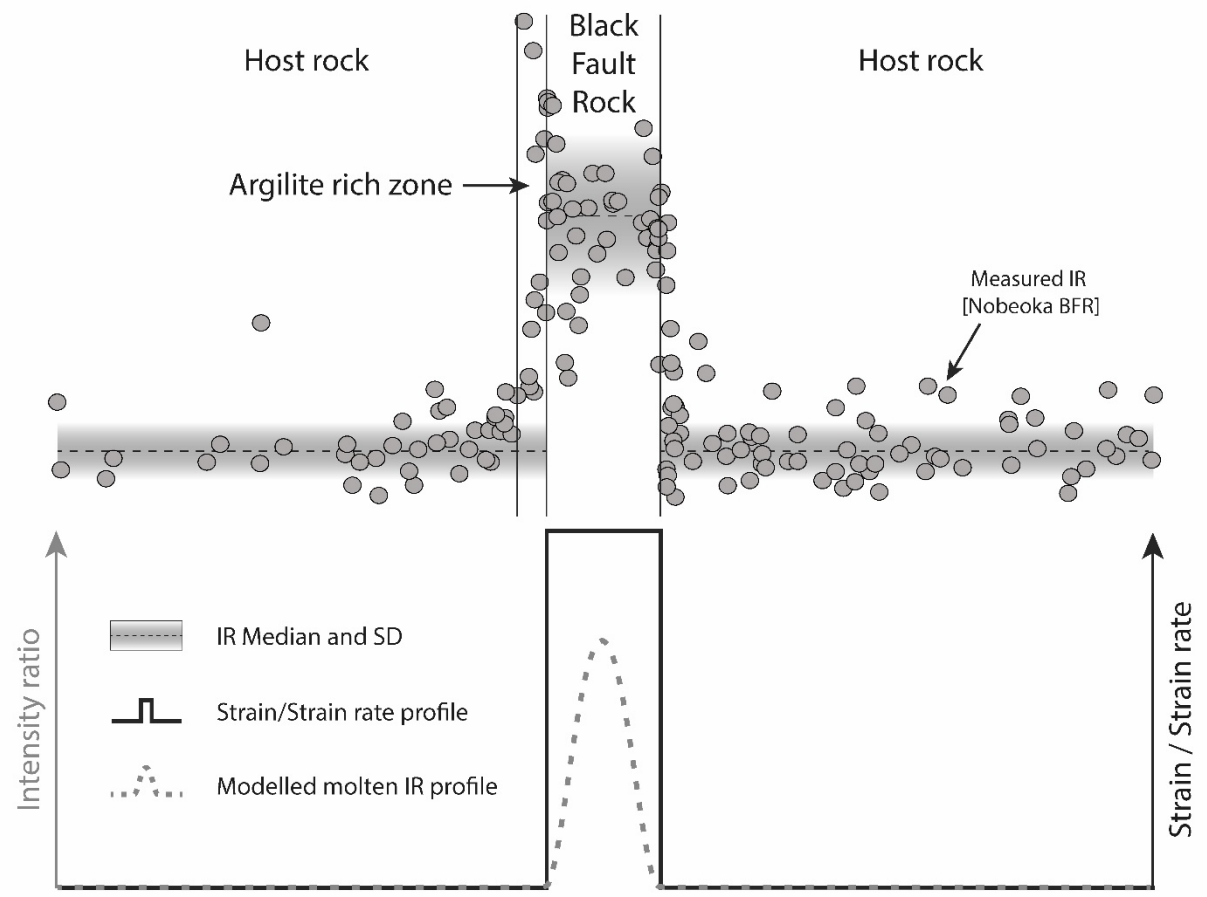

Figure VI.9: Intensity ratio profile and the amount of strain or strain rate across the host-rock and the Black Fault Rock for the Nobeoka case (with median and standard deviation shown as black dotted lines). Intensity ratio derived from thermal models of a viscously sheared molten layer (case (3)) is superimposed as a red dotted line. A hypothetical strain/strain rate profile is shown as a black bold line. The stepwise shape of natural profile matches strain/strain rate profile, while it stands at variance with thermal models.

VI.4.4 Implications

The nature of processes operating within fault zones, either melting or mechanical comminution, might ultimately rely on the proportion of available water, contained principally as H_2O mineral-bounds. Natural Black Fault Rocks considered here are hosted in rocks mostly composed of clays and phyllosilicates (Ujiie et al., 2007) and contain from 5 to 10 wt.% H_2O (Bebout, 2007). During the frictional slip, clays and phyllosilicates liberate free water when temperature increases, resulting in thermal pressurization, shear stress reduction and inhibition of further temperature increase up to melting (Brantut et al., 2010, 2008). Conversely, the low proportion of water-bearing minerals in crustal rocks is probably not sufficient to prevent large temperature increase and melting during frictional slip (Di Toro et al., 2011, 2006; Di Toro and Pennacchioni, 2009; Scholz, 1990; Sibson, 1975). A close

examination of natural Black Fault Rocks is therefore necessary, as similar microstructures may arise from completely different processes of formation.

The origin of the material forming the principal slipping zone of fault bears great consequences on fault dynamics. Our observations suggest that the amorphous or extremely fine-grained materials within the Black Fault Rocks result from mechanical comminution. Comminuted materials may behave mechanically in a fashion similar to a fluid (Lin, 1996; Pec et al., 2012b, 2012c), so that fluid-like microstructures, such as injection veins, can be observed. From a mechanical point of view, mechanical comminution results, similarly to melting, in an extreme weakening of the fault zone strength during slip. Nonetheless, as their nature is fundamentally different, the weakness of comminuted and molten material may have significantly contrasted characteristics with respect to fault slip. To model adequately fault zone properties and dynamics, the rheology of comminuted material appears therefore as a central aspect, yet it is essentially unknown at present time.

In addition, even if RSCM appears as a promising tool to decipher deformation processes in natural rocks, the quantitative influence of strain on the carbonaceous material crystallinity and the underlying microphysical processes remains to be elucidated. In particular, the combination of high strain-rate experiments where fault-like processes are reproduced (Ito et al., 2017; Kouketsu et al., 2017; Kuo et al., 2017), and low strain-rate experiments, where strain and temperature can be clearly discriminated, seems to be necessary.

Preface

In this chapter, the detection of intense short-life heating event (i.e. flahs-heating) is explored thanks to the RSCM method. Atypical shape of the Raman spectra have been detected in the literature for high velocity friction experiments. Additional review of experiments that have induced flash-heating leads to the same conclusion. Based on these results, the new Raman parameter $D_3/G_{sl.}$ ratio has been establishment and applied to two new BFR observed in the Mugi and Kure mélanges in addition to microstructural observations. This new parameter, is sensitive to the flash-heating, and allows us to decipher the melt or comminution only origin of the BFR observed in accretionary complexes. In addition, flash-heating experiments have been carried out and compared with previous results. This study has shown (1) the powerful usefulness of the new $D_3/G_{sl.}$ ratio for the flash-heating detection and (2) paired with the microstructural observations, the melt-origin of the two examples of the Mugi and Kure BFR.

Chapter VII – Flash-heating natural events and experiments as detected by Raman Spectroscopy of Carbonaceous Material

VII.1 Introduction

In crustal rocks, the frictional melting is one of the main slip weakening processes reducing friction on the slipping zone within a fault zone (Di Toro et al., 2011, 2006) (Figure VII.1). The clue of this frictional melting is the formation of pseudotachylyte veins whether they are concordant or discordant to the plane on which the movement is concentrated. These melt-origin veins are well-described in literature and present typical features such as the fill-in material made of a vitreous black thin material of the fault vein associated with orthogonal injection veins at the outcrop scale (Sibson, 1975). Initially described in crustal lithology including felsic rocks (Di Toro et al., 2006; Di Toro and Pennacchioni, 2009; Fabbri et al., 2000; Sibson, 1975), mafic rocks (Fabbri et al., 2018; Techmer et al., 1992), for different Pressure-Temperature conditions (Austrheim and Boundy, 1994; Fabbri et al., 2000). The common point of these examples is the "strong" behavior of the rock that is deformed in the brittle regime at velocities that are necessarily high. Recently, the occurrence of fault veins with a melt-origin have been described in accretionary complexes (Ikesawa et al., 2005, 2003; Meneghini et al., 2010; Mukoyoshi et al., 2006; Rowe et al., 2005; Ujiie et al., 2021, 2007; Ujiie and Kimura, 2014). However, the occurrence of molten veins is still debated in accretionary complexes, due to the link between these fault zones and the implication in geodynamic behaviors in accretionary complexes. Other slip weakening processes are envisioned to explain the friction drop during seismic events in accretionary complexes such as the thermal pressurization, the flash-heating of the nanopowder lubrication (Brantut et al., 2010, 2008; Di Toro et al., 2011; Rice, 2006). In the following, avoiding interpretation on the melt-origin or not, this fault veins are called Black Fault Rocks (BFR) and the associated injection veins are replaced by fluidization structure.

In addition, in accretionary complexes, the crystallinity of carbonaceous material (CM) has been used in order to detect evidences of the thermal release of frictional heating induced by the seismic events, like the CM crystallinity, and is considered as a sensitive indicator of the metamorphic peak temperature (Beyssac et al., 2002; Lahfid et al., 2010). Natural and experimental seismic objects, BFR, interpreted as pseudotachylytes (Ito et al., 2017; Ujiie et al., 2021), or fault gouges (Furuichi et al., 2015; Kouketsu et al., 2014; Kuo et al., 2018, 2017) have been analyzed using the Raman Spectroscopy of Carbonaceous

Material (RSCM) or the vitrinite reflectance and show an enhance of the crystallinity in the core of fault zones. However, thermal and mechanical effects are indistinguishable one from another and the potential effect of strain (Bonijoly et al., 1982; Bustin et al., 1995; Kedar et al., 2021; Suchy et al., 1997, Chapter IV of this study) is not considered.

In the previous Chapter VI, three BFR have been presented and analyzed in order to evaluate the contribution of both thermal and mechanical effects. Using a new innovative approach pairing RSCM high resolution mapping along profiles combined to thermal and CM kinetics modellings, the mechanical wear has been shown as the main controlling factor of the CM crystallinity increase in the BFR and the poor or absent role of the increasing temperature.

In this Chapter, the detection by RSCM of intense short-life thermal events from literature examples is highlighted by the atypical spectrum shape and the establishment of $D_3/G_{sl.}$ ratio. In a second time, we focused on two BFR different from the ones presented earlier in this manuscript (Chapter VI). Samples were selected on the Shikoku island (Southwest Japan) from the Mugi mélange (Ikesawa et al., 2005; Ujiie et al., 2007; Ujiie and Kimura, 2014) and the Kure mélange (Mukoyoshi et al., 2006) in the northern Shimanto Belt. They have been interpreted as genuine pseudotachylyte veins presenting more persuasive features associated with melt-origin and different host-rocks. To decipher the melt-origin or at least the frictional heat effects on the CM crystallinity in accretionary complexes, the high-resolution mapping approach using the RSCM has been used and compared with flash-heating experiments on pre-mature shale (HN78) close to the one observed in the BFR surroundings.

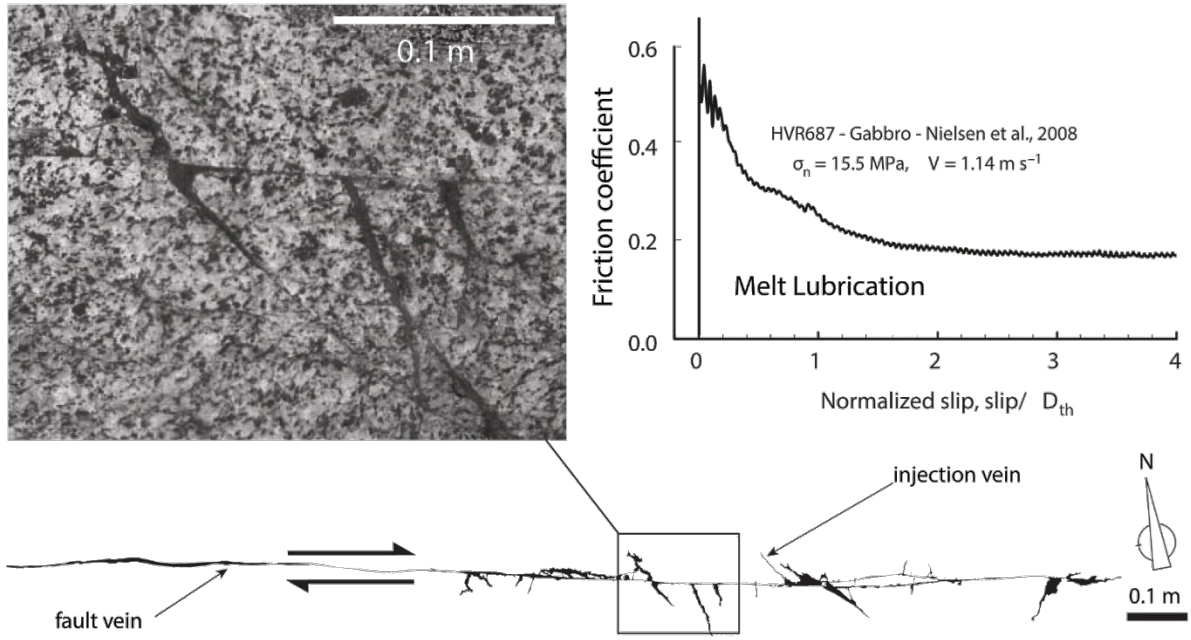

Figure VII.1 : Example of pseudotachylyte in crystalline rock with fault vein and injection structures associated with the slip weakening induced by melt lubrication (Modified from Di Toro et al., (2011, 2006))

VII.2 Geological settings and fault zones

The Shimanto belt stretches from Tokyo to Okinawa passing through the Shikoku and Kyushu islands. It is limited by the coast or by discordant Neogene unmetamorphosed sediments from the Miyasaki group on the east (Charvet and Fabbri, 1987; Murata, 1997; Taira et al., 1988), and on the west, separated to the Jurassic Chichibu Belt by the Butsuzo Tectonic Line (Figure VII.2a). The ancient accretionary complex is characterized by an accumulation of NW dipping coherent sedimentary units and tectonic mélanges of the Cretaceous age on the NW to Tertiary one on the SE. The Shimanto complex is divided into Cretaceous subbelt and Tertiary subbelt by a low dipping out-of-sequence fault, called Nobeoka Tectonic Line in Kyushu (Kondo et al., 2005; Mukoyoshi et al., 2007) and Aki Tectonic Line in Shikoku (Murata, 1997; Sakaguchi, 1996). Their thrust displacement explains a paleotemperature gap of 60°C on the Kyushu Island.

Samples selected for this study are from the Shikoku Island. Therefore, their description will be focused on this segment of the Shimanto Belt. In western Shikoku, the Cretaceous subbelt is traditionally split into two groups: the Shinjyogawa and Taisho Groups (Taira et al., 1988). The latter is mostly composed of coherent turbidites especially in the Nonokawa Formation. In addition, the Kure tectonic mélanges unit, i.e. the EW-thrust-bounded with coherent unit, is observed and composed of sandstones, silts and basalts boudins into a shaly matrix, which is characterized as mélange facies (Sakaguchi, 1996). Mukoyoshi et al. (2006) measured a vitrinite reflectance temperature from 220 to 240°C ± 30°C based on the thermometer of Barker (1988) for the Kure mélange. In eastern Shikoku, the southernmost part of the Cretaceous subbelt is composed of the Hisawa Formation and the Mugi mélange separated by the Minami-Awa fault (Figure VII.2b). The Hisawa Formation is characterized by a coherent turbidite unit. The Mugi mélange is composed red shales, cherts, tuffs and basalt blocks wrapped in a black shaly matrix attributed to the Campanian-Maastrichtian period (Kitamura et al., 2005). The Mugi unit can be split into two sub-units, separated by the Out of Sequence Thrust (OST) Mizzochi fault (Kitamura and Kimura, 2012), lower and upper Mugi based on geothermometric data, respectively at 130-150°C and 215 ± 10°C, derived from vitrinite reflectance (Ikesawa et al., 2005) and RSCM thermometers (Raimbourg et al., 2017a). In the following, we will be interested only in the upper part of Mugi where tectonic mélange sediments are described.

In the east of Mugi city along the coast, the contact between Hisawa Formation and the upper part of the Mugi mélange unit is marked by the E-W Minimi-Awa Fault separating meters thick sandstone layered coherent unit and mélange unit (Figure VII.2c). The top-to-the-south deformation of the fault zone, consistent with the kinematics of the penetrative deformation of the mélange and underplating thrust kinematics (Ujiie et al., 2007), lead to interpret it as a major décollement fault (Kitamura et al., 2005). A one meter-thick foliated cataclasite layer composed of shale and large sandstone clasts accompanied of fault veins parallel to the foliation and crack-

fill veins characterized this fault zone (Ikesawa et al., 2005; Kitamura et al., 2005). The black thin veins appear grossly parallel to the fault zone, sharply truncate the foliated cataclasite, and are associated with perpendicular fluidization structures (Figure VII.2d).

In the southeast of the Kure city, at the Cape Otsuzaki, the Kure mélange and Nonokawa Formation are crosscut by a set of NW-SE en échelon faults (Figure VII.2a). Mukoyoshi et al. (2006) reported 11 faults that show accentuating dipping toward the north, along 3km strike and interpreted it as a late out of sequence thrust (OST). The fault zone appears very limited, in comparison with subduction thrust, to a decimeter-thick. This fault zone is a 500mm fracture zone with breccia, cataclasite or fault gouge composed of angular to sub-rounded host rock fragments with mineralised veins (Figure VII.2f). In the core of the fault zone, a 0.5 to 1mm highly deformed ultra-cataclasite has been identified (Figure VII.2e). In the Nonokawa Formation, between a massive sandstone layer and a greenshale layer, a thin black vein has been described (Mukoyoshi et al., 2006) where the seismic deformation is localized (Figure VII.2e). Late brittle occurrence has been described in the fault zone and affects the BFR samples.

Both samples, called “Mugi BFR” and “Kure BFR” in the following, have been selected in the core of these fault zones.

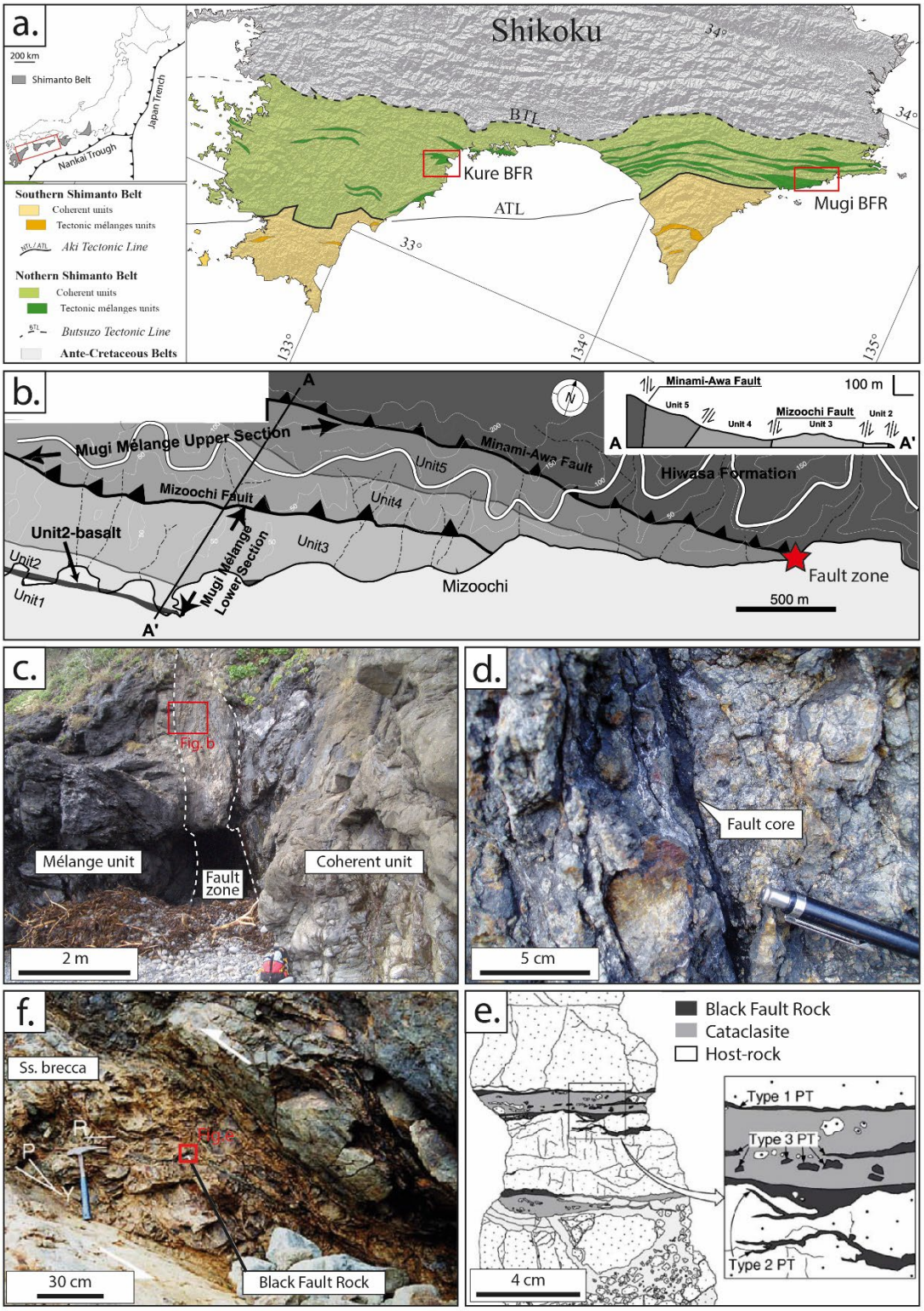

Figure VII.2 : Geological environment of the Mugi and Kure BFR. ***a.*** *Shimanto belt occurrence in Shikoku island and locations of the two BFR studied in this chapter* ***b.*** *Mugi mélange and Hiwasa Formation structural map indicating the fault zone where the Mugi BFR is observed along a coastal outcrop (red star) (Modified from (Kitamura and Kimura, 2012))* ***c.*** *Fault zone including the fault zone between a coherent unit and a mélange unit* ***d.*** *Close up view on the black fault core. (Modified from (Ujiie et al., 2007; Ujiie and Kimura, 2014)).* ***d.*** *Fault zone around the Kure BFR showing the breccia where the BFR vein is embedded* ***e.*** *Close up view on BFR Kure sample showing the alternation of BFR and cataclasite and late brittle deformation.*

VII.3 Results

In Ito et al. (2017), BFR and high velocity friction experiments have been described in order to characterize the record of short and intense heating events induced by seismic slip on the CM crystallinity. In this article, authors proposed to explore this flash-heating effect of the CM using a classic approach of the RSCM. Due to an atypical shape of the spectrum the use of RSCM thermometers was not possible. Indeed, the presence of a large D_3 band (i.e. on deconvoluted spectra) has been observed on natural and experimental CM spectra (Figure VII.3). However, the atypical shape of the CM spectra was not discussed in the literature and could be an important point for the detection of flash-heating. Therefore, in the following, the assumption of flash-heating detection is explored based on the establishment of a new RSCM parameter, the $D_3/G_{sl.}$ ratio on the raw spectra that corresponds to the intensity at the D_3 band center and the intensity of the $G_{sl.}$ band.

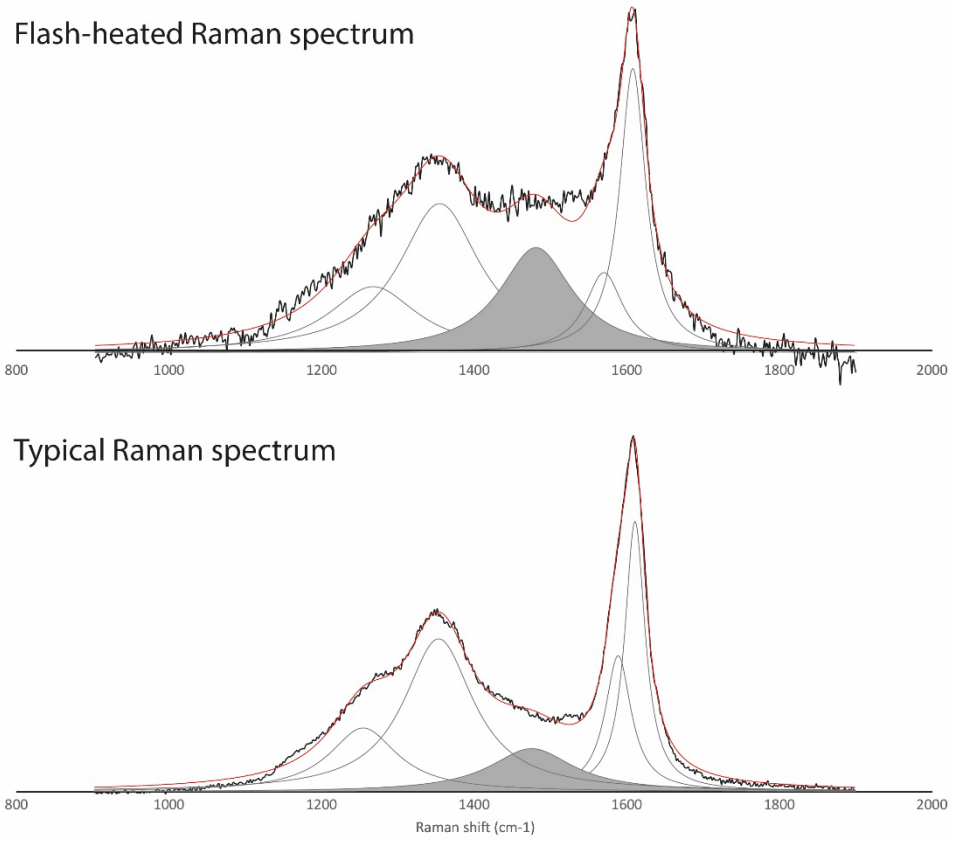

Figure VII.3 : Atypical spectrum shape from a flash-heated sample showing the presence of the large D3-band in comparison with the typical raman spectrum from a geological maturation.

VII.3.1 Review of experimental flash-heating and comparison with natural examples.

In this part, we review in a first section the experimental results of flash-heating reported in the literature through stick-slip, pyrolysis and high velocity friction experiments (Aubry et al., 2018; Ito et al., 2017; Muirhead, 2012). All of them show the same atypical shape of RSCM spectra. In a second section, the effect of natural flash-heating on CM is explored thanks to the study of immature sediments that were in contact with basalt flow or intrusion. The full Chapter VIII is dedicated to the detection of the flash-heating on CM contained in basalt in contact with sediment and the implication in the formation of tectonic mélange units. Both of these comparison and application of the $D_3/G_{sl.}$ ratio are realized to confirm our working hypothesis.

VII.3.1.1 Review of experimentally flash-heated CM

Three types of experiments producing intense short life heating and 1 natural example of flash heating have been analyzed in order to compare the RSCM results from the flash heating experiments. All the results of the $D_3/G_{sl.}$ ratio are shown in Figure VII.4

Stick slip experiments

Aubry et al. (2018) carried out series of stick-slip experiments on a carbon layer placed between two irregular pistons cut at 30° from the parallel of the forcing blocs. The IR of the starting material is ca. 0.45 and reach up to 0.90 after the stick-slip events. Felsic minerals presented on the forcing blocks have been melted locally indicating a minimum frictional temperature of 1650°C. The $D_3/G_{sl.}$ ratio measured on the spectrum obtained from one experiment shows a value at 0.62 (Figure VII.4). In addition, based on the calibration between the IR evolution and the heated samples in an atmospheric oven, no observation of the CM crystallinity evolution has been made under 700°C.

High Velocity Friction experiments

In Ito et al. (2017), High-Velocity Friction experiments (HVF) have been carried out to reproduce the BFR, interpreted as melt-origin object, at an equivalent slip rate of $1.1 m.s^{-1}$ at ambient pressure and temperature. Melt occurred during experiments and IR shows an evolution from 0.50, on shale cylinder from the Mugi mélange unit, up to 1.10 with an average value of 0.70 (Ujiie et al., 2009). $D_3/G_{sl.}$ ratio

measured on the Raman spectra from three HVF experiments shows values ranging from 0.31 to higher than 0.60 and a correlation between the frictional work and the increasing $D_3/G_{sl.}$ ratio.

Pyrolysis experiments

Two pyrolysis experiments have been carried out in order to calibrate kinetics laws of the CM crystallinity evolution using the RSCM. The first one was performed by Aubry et al. (2018) in which carbonaceous material was heated during 5 seconds from 900 to 1400°C using atmospheric oven. The other pyrolysis experiments run by Muirhead, (2012) is a set of experiments in which poorly mature CM, contained in the Murchison meteorite, have been heated from 5 to 80 seconds at temperature ranging from 250°C to 1000°C thanks to a pyrolysis apparatus. Both pyrolysis experiments show similar evolution of the Raman spectra, where an increase of the IR, from 0.25 to 0.50 at 100°C in (Muirhead, 2012) and from 0.60 to 0.85 in (Aubry et al., 2018) is observed and is associated with an increase of the $D_3/G_{sl.}$ ratio. In addition, a correlation between the increasing pyrolysis temperature and the $D_3/G_{sl.}$ ratio is noticed from 0.49 to 0.70 and from 0.52 to 0.73, respectively in Muirhead (2012) and Aubry et al. (2018).

VII.3.1.2 Natural examples of flash-heating: Basalt flows and intrusions in immature sediments

The review of experimental flash-heating effect on the CM is unanimous, the $D_3/G_{sl.}$ ratio increased for all examples of the literature. In this section, we present results obtained from basalt intrusion in the contact with shales from IODP drillings.

Two shale samples from the Ninetyeast Ridge hole (Leg 121 – site 758A) have been analyzed using the RSCM method at increasing distance with the basalt flow, one on the contact and another at 5cm from the contact with the basalt. Additional samples from this hole have been analyzed and CM spectra obtained from the RSCM analyzes show a typical immature shape up to reach the last five centimeters where poorly organized CM is observed. $D_3/G_{sl.}$ ratios range from 0.34 to 0.60 and the $D_3/G_{sl.}$ ratio increases when the distance with the basalt decreases. Chapter VIII is dedicated in detail to the detection of basalt flow flash heating and the implications in the tectonic mélange formation.

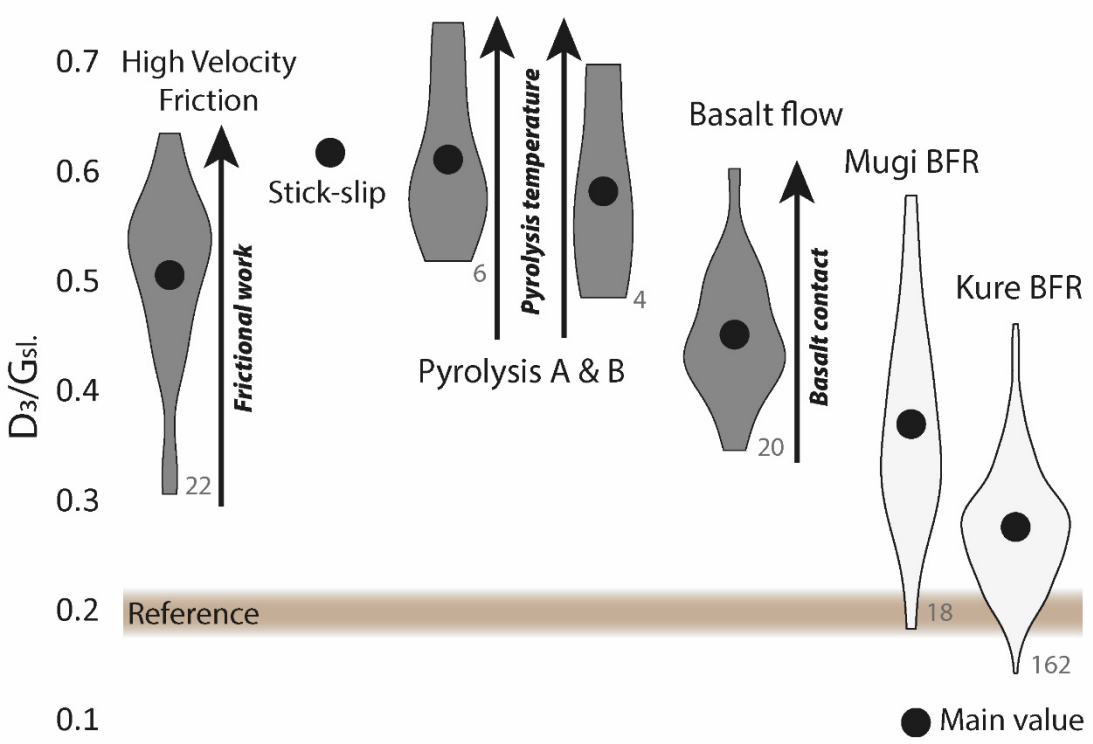

Figure VII.4: Others examples of D3/Gsl ratio increase for intense short-life heating in comparison with Mugi and Kure BFR. HVF: High-Velocity Frictional experiments from (Ito et al., 2017); Stick-slip experiments from (Aubry et al., 2018); Pyrolysis A : 5 seconds heating from 900 to 1400°C in (Aubry et al., 2018) ; Pyrolysis B : 20 seconds from 400 to 1000°C in (Muirhead, 2012) and basalt flow from Ninetyeast Ridge (IODP).

To summarize, Figure VII.4 shows high values of the $D_3/G_{sl.}$ ratio for different examples of intense and short-life heating from ca. 0.30 to 0.70. In comparison, samples that have undergone a regional metamorphism heating present traditional spectrum shape and $D_3/G_{sl.}$ ratio values from 0.15 to 0.20. In addition, a positive correlation can be observed between the quantity of heat released and the increase of $D_3/G_{sl.}$ ratio. Finally, the $D_3/G_{sl.}$ ratio has shown increasing values for both natural and experimental flash-heated samples.

VII.3.2 Mugi and Kure BFR examples

The $D_3/G_{sl.}$ ratio has shown its application to the detection of flash-heating. The application of this new RSCM parameter could help to decipher the origin of BFR and especially to debate about the fractional melting in accretionary complexes. Before interpreting the RSCM results, microstructure description, reported from the literature (Mukoyoshi et al., 2006; Ujiie et al., 2007), have been provided in order to link the RSCM results and to localize eventual molten zones.

VII.3.2.1 Microstructures

Both Black Fault Rocks are characterized by sharp black thin veins of 1 to 3mm fill-in with an aphanatic material crosscutting the host-rock mostly composed of sandstones (Figures VII.2e and VII.5a). Fluidization structures are observed along the black veins that show the coexistence of ultra-fine material and ultra-cataclasite (Figure VII.7c). These features are partially erased by local alteration of the aphanitic material, particularly for the Mugi BFR (Figure VII.6a). The ultra-fine material is composed of an amorphous matrix where are scattered iron-rich and titanium-rich particles with irregular shapes and of rounded clasts of quartz with sizes ranging from 5 to 50µm and 5 to 10µm, respectively in the Mugi BFR and in Kure BFR (Figure VII.5b). In addition, potassic feldspars present eroded shape (Figure VII.5d). The amorphous matrix mainly composed of shale and rounded pores are observed with recrystallized fine grains of mullite (20 to 200nm) and acicular muscovite (2µm), respectively, in the Mugi BFR and Kure BFR (Figure VII.5c). All these microstructures are summed up in Table VII.1.

Table VII.1 : Microstructures information about Mugi and Kure BFR

				Textures						
Sample	**Location**	**Latitude**	**Longitude**	**Geological unit**	**Fault core width**	**Single/Multi tectonic event**	**Fluidization structure**	**Glassy matrix**		
Mugi	Japan	33.685691	134.479710	Mugi mélange	1 mm	Single	Yes	Yes		
Kure	Japan	33.307346	133.250186	Kure mélange	1 - 3mm	Single	Yes	Yes		
	Micro- to nano-textures									
Sample	**Rounded clasts**	**Clasts grain size**	**Corrosion / Embayment structure**	**Flow texture**	**Matrix grain size**	**Fine-grains within matrix**	**Nature of fine-grains**	**Fine-grains size**	**Pores in the matrix**	**References**
Mugi	Yes	5 - 50 µm	Yes	No	-	Yes	Accicular mullites, Fe-rich, Ti-rich particles	20 - 200 nm and 1 - 10 µm	Yes	Ujiie et al., 2007
Kure	Yes	5 - 10 µm	Yes	No	-	Yes	Acicular muscovites	2 µm	Yes	Mukoyoshi et al., 2006

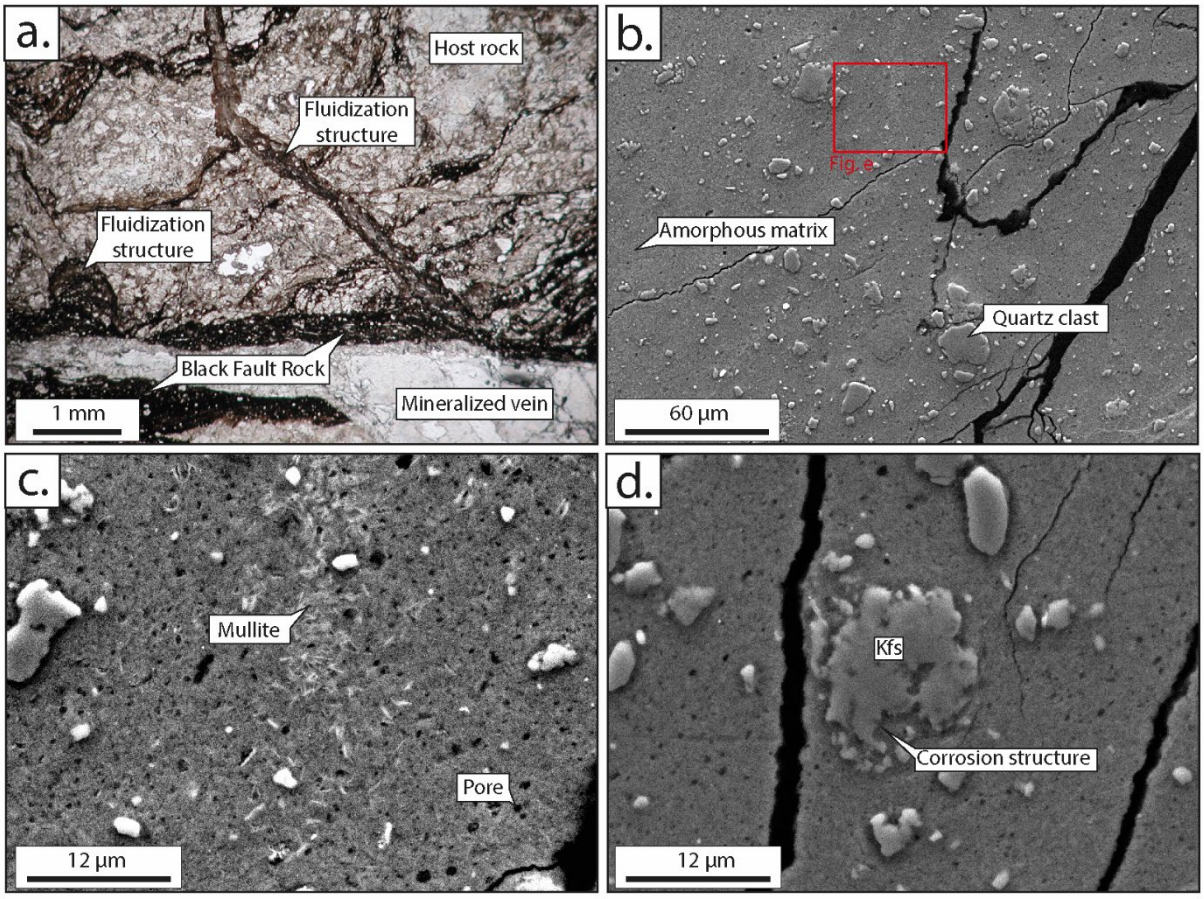

Figure VII.5 : Structure and microstructures of the Mugi BFR (modified from (Ujiie et al., 2007; Ujiie and Kimura, 2014)). ***a.*** *BFR and fluidization structure in the sandstone host-rock* ***b.*** *SEM image illustrating the amorphous matrix and scattering clasts* ***c.*** *Microlites of mullite and round vesicles in an amorphous matrix* ***d.*** *Corrosion structure on potassic feldspar (Kfs).*

VII.3.2.2 RSCM

The RSCM has been used to characterize the CM crystallinity along high-resolution profiles through the both BFR and the host-rock. Due to the high content of secondary quartz within the host-rock it is difficult to have the same continuity as the one observed in the previous Chapter VI.

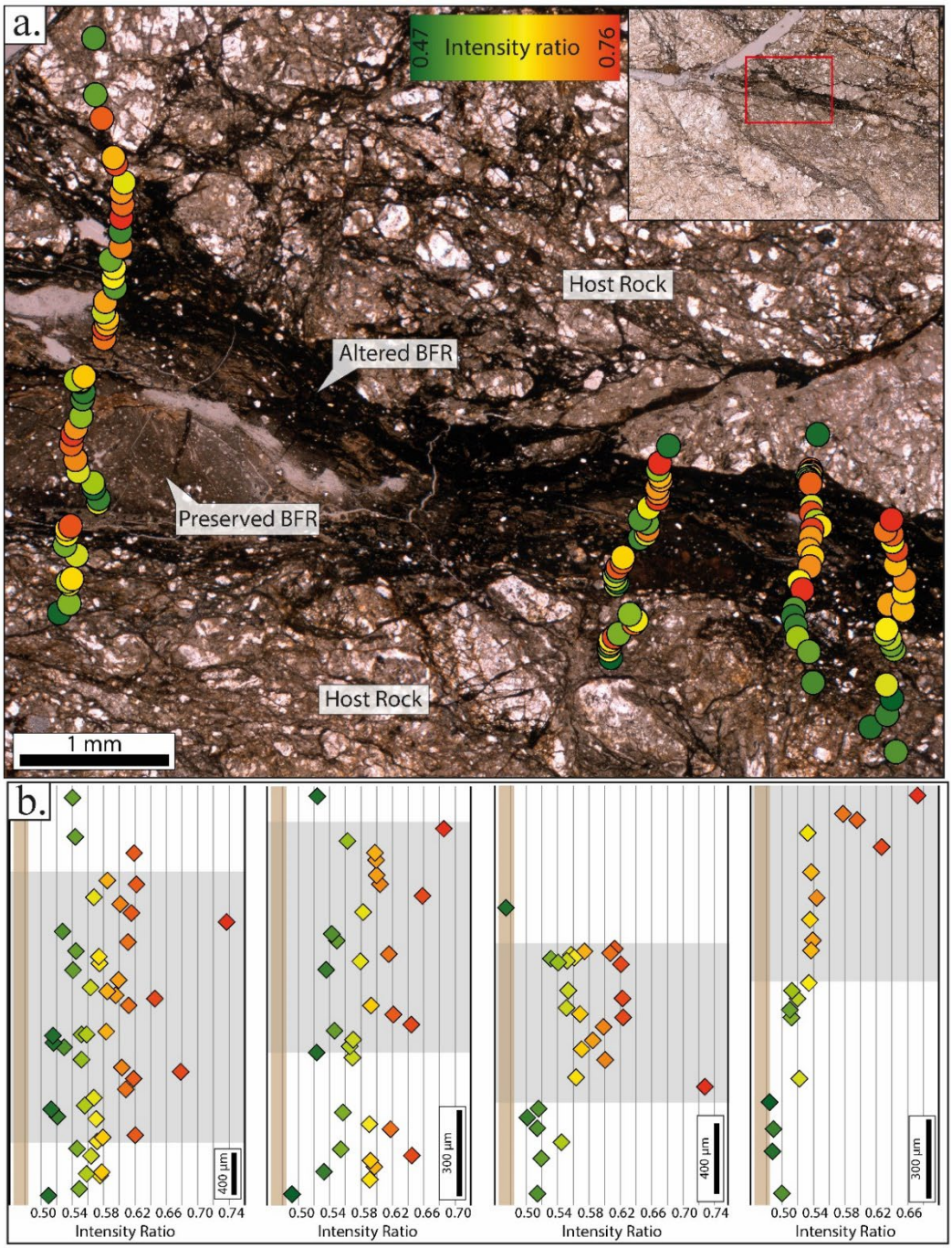

Figure VII.6 : Raman spectroscopy results obtained for the Mugi Black Fault Rock and its host-rock. ***a.*** *Intensity ratio mapping along high-resolution cross-sections across the Black Fault Rock* ***b.*** *Intensity ratio evolution diagram along profiles.*

The intensity ratio (IR), sensitive to the deformation and characteristic of the CM crystallinity, has been used (Figures VII.5 and 6). All profiles show an increase of the IR in the BFR with respect to their host-rock, respectively for the Mugi BFR and Kure BFR, from 0.549 ± 0.059 to 0.577 ± 0.047 and 0.589 ± 0.059 to 0.658 ± 0.073, so +5% (Figure VII.6) and +12% (Figure VII.7). However, a large dispersion of values is observed in the BFR with respect to host-rocks and leads to difficult to decipher the evolution.

In the Kure BFR, the IR is increasing in the black zone composed of amorphous material and in the cataclasite in the same proportion.

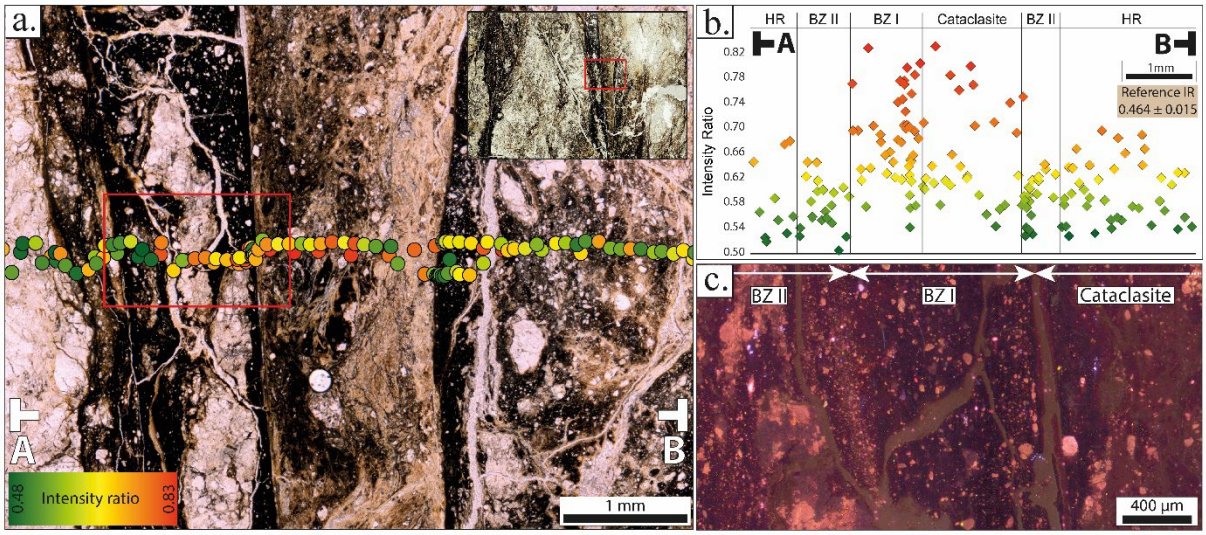

Figure VII.7: Raman spectroscopy results obtained for the Kure Black Fault Rock and its relative host-rock. ***a.*** *Intensity ratio evolution along high-resolution cross-sections of the Black Fault Rock* ***b****. Intensity ratio evolution diagram along profiles and accros the different zones. c. Cathodoluminescence image showing the distinction of the fault veins in two black zones and cataclasite. HR = Host-rock; BZ = Black zone*

In addition to the unclear evolution of IR in the BFR, an atypical shape has been observed on the spectra measured in the strained zone. Indeed, an anomalous intensity of the D_3 band is observed, similarly to the spectrum shapes presented above (Figure VII.8a). Values measured for both sides of the BFR within the host-rock are included between 0.15 to 0.20. However, a clear and large increase is observed in the BFR analyses with a large dispersion of the results from 0.25 to 0.60 for the Mugi BFR and from 0.20 to 0.45 for the Kure BFR (Figure VII.8b). These values in the BFR veins are closed to the ones measured in the literature experiments and in the contact with basalts (Figure VII.4).

Conversely, $D_3/G_{sl.}$ ratio values from the three previous studied BFR from Nobeoka, Okitsu and Kodiak (Chapter IV) show very different results. Despite a large variation of this ratio, it appears almost similar for the BFR comparing to the ones that characterize the host-rocks. For the two Shimanto Belt BFR (Nobeoka and Okitsu) the values are dispersed but are similar and do not overshoot 0.35 (Figure VII.8b). Similar observation is made for the Kodiak BFR, where equivalent values are measured from 0.15 to 0.20 for the BFR and the host-rock (Figure VII.8b).

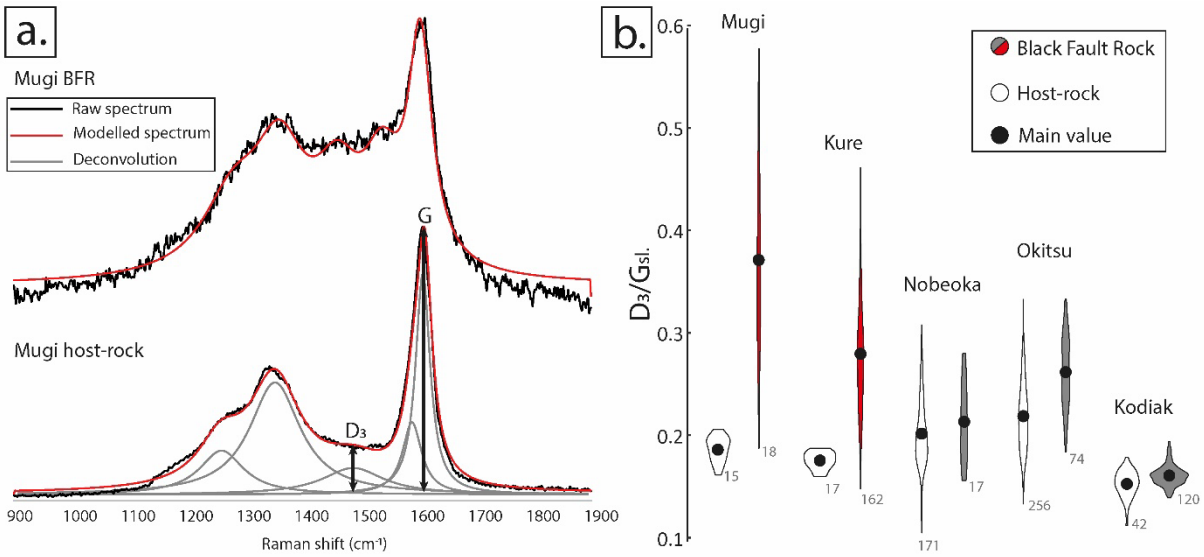

Figure VII.8 : D_3/G_{sl} ratio in Black Fault Rocks and respective host-rocks. ***a.*** *Spectrum evolution in the BFR of Mugi and the host-rock indicating the intensity selected for the calculation of the D_3/G_{sl} ratio* ***b.*** *D_3/G_{sl} ratio diagram of 5 BFR and respective host-rocks from the Shimanto Belt and Kodiak Accretionary Complex.*

VII.3.3 Flash-heating experiments

RSCM results obtained on the natural BFR from Mugi and Kure both show a peculiar feature that we ascribe to the effect of a short yet very intense heating. This working hypothesis has been tested using Laser-aided flash-heating experiments. Estimated temperature from the literature based on the mineral fusion or crystallization of the frictional heating is superior to 1100°C in Mugi (Ito et al., 2017; Ujiie et al., 2007) and from 650°C up to 1100°C in Kure (Mukoyoshi et al., 2006). In addition, the calibration of the fusion temperature has been carried out using an atmospheric oven. Results and estimation from the literature, leads to set the flash-heating temperature at 1400°C.

Based on this interpretation and test of fusion using an atmospheric oven, the selected flash heating temperature was set at 1400°C when total fusion was observed. Flash-heating experiments using couple of CO_2 lasers have been carried out from 0.5 to 60 seconds, under argon atmosphere, on pre-mature shale in the same CM-organization as the two BFR studied. All the experimental procedures are described in Chapter III.

The starting material (HN78) shows values of 0.484 ± 0.029 for IR and 0.205 ± 0.036 for D_3/G_{sl} ratio. IR and D_3/G_{sl} ratio were measured on experimental products after 0.5, 1, 2, 3, 4, 5, 7.5, 10, 30 and 60 seconds. The first results of these experiments show similar atypical CM spectra as the ones observed in natural BFR and flash-heated examples (Figure VII.9c and 9d).

After few microseconds, the first effect of flash heating is perceptible. Indeed, from 0.5 to 1 second of heating, the first signs of fusion are observed on the surface with a whitening and slight vitreous plane on surface. In response to the heating of one second, RSCM results show a sharp increase of heterogeneity of the values of 0.875 ± 0.116 and 0.287 ± 0.078 for the IR and the $D_3/G_{sl.}$ Ratio, respectively (Figure VII.9a and 9b). From 1 to 4 seconds of heating, when a weak fusion is observed on the surface of the sample with the formation of degassing pores, the IR and the $D_3/G_{sl.}$ ratio become constant around 0.90 and 0.50, respectively and keep the large dispersion of the values as observed above. From 4 to 10 seconds, a penetrative fusion is observed, illustrated by the developed of gas extraction pores in all the samples and the sample looks like a pumice stone. In addition, the fusion induced a weak reshaping of the sample. During this step, the IR remains constant (Figure VII.9a) and a slight decrease of the $D_3/G_{sl.}$ ratio is observed (Figure VII.9b). After 10 seconds of heating, a total fusion of the sample is observed and the sample is sub-rounded to rounded shape. The IR value overpasses 0.90 and reaches 1.1 after 60 seconds and the $D_3/G_{sl.}$ ratio decreases from 0.50 to 0.30 (Figure VII.9b).

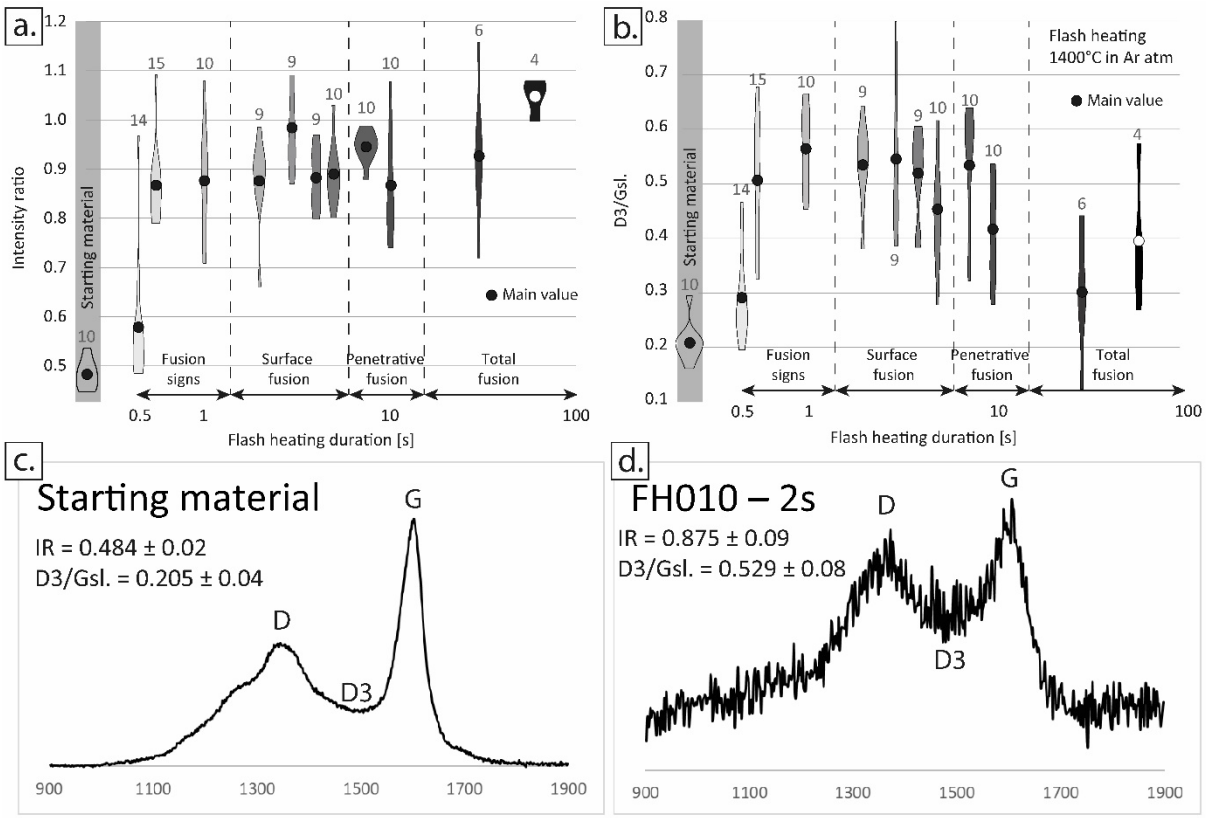

Figure VII.9 : Intensity ratio and D_3/G_{sl} ratio evolution during the flash heating maturation experiments and textural evolution. a. Intensity ratio diagram evolution from the starting material (HN78) up to 60 seconds of flash heating b. D_3/G_{sl} ratio diagram evolution from the starting material (HN78) up to 60 seconds of flash heating c. Typical spectrum of the starting material d. Spectrum after an exposition at 1400°C during 2 seconds.

VII.4 Discussion

VII.4.1 Evolution of the RSCM parameters during flash-heating (natural and experimental)

The RSCM reflects the organization of the CM lattice that progressively evolves in diagenesis and metamorphic heating during geological time-scales through the carbonization and the graphitization processes. During this progressive evolution of the CM crystallinity by complex simultaneous processes, the RSCM spectrum shape changes, and by consequence, RSCM parameters, such as the IR, vary too. This kinetics has been described as a slow evolution and would need a long heating process. However, it seems that short-life yet intense heating, i.e. much shorter duration than geological time-scales, records in the CM with considerable differences.

The IR enhance reflects an increase of the CM crystallinity on poorly organized CM during the carbonization stage identically as the one observed for long geological time heating. In addition, a

correlation with the temperature-duration of the flash heating is observed. However, in difference with the heating in the geological scale, a quick increase of this ratio occurs and the evolution is not monotonous as shown by our flash heating experiments in which a “plateau” of values at ca. 0.80 to 1.00 is observed from 1 to 10 seconds of heating at equivalent temperature of 1400°C. Now comparing IR with corresponding temperature, the plateau observed in the flash heating experiments correlates with the transition between the carbonization and the graphitization maturation stages (Tissot and Welte, 1984). Therefore, this plateau could correspond to the upper bound of the carbonization zone from which an additional energy, brought by extra annealing time, is needed to overpass this stage and pass in the graphitization stage.

Moreover, the shape of the natural and experimental samples that experienced short heating is different and shows a large D_3 band intense than that of natural samples that experienced geological (i.e. “long”) heating (Aubry et al., 2018; Ito et al., 2017; Muirhead, 2012; Nakamura et al., 2017). The D_3 band is associated with the vibrational mode of the residual amorphous carbonaceous material when the CM crystallinity increases (Cuesta et al., 1994; Jawhari et al., 1995; Sadezky et al., 2005). Based on this result, we have developed the $D_3/G_{sl.}$ ratio in order to characterize the evolution of the D_3 band between flash-heated samples and the respective host-rocks. Geological heating shows similar values, from 0.15 to 0.20, for several samples experienced the carbonization and early graphitization stage (i.e. from 200 to 360°C) independently to the CM crystallinity. However, in flash heated samples, irrespectively from the source of heat, a clear increase of $D_3/G_{sl.}$ ratio is recorded with values ranging from 0.30 up to 0.70. Furthermore, a correlation between the intensity of the D_3 band, that influences the $D_3/G_{sl.}$ ratio, and the intensity of the flash heating (time or temperature) has been observed for several examples such as the HVF, pyrolysis experiments and in the natural examples related to the heat dissipated from basalt flows (Figure VII.4). In addition, the $D_3/G_{sl.}$ ratio seems to be limited to a value of 0.70 during the carbonization stage without regarding the temperature-time pairs.

Finally, flash heating experiments suggest that after a certain time of exposition of the sample, which should be the limit between the carbonization and the inception of the graphitization, identically to the IR, the $D_3/G_{sl.}$ ratio decreases slightly and the sample would be less affected by the flash heating during

the graphitization. In order to confirm this working hypothesis, it would be benefit to carry out similar flash-heating experiments on well-organized CM contained in graphitized samples.

VII.4.2 The $D_3/G_{sl.}$ RSCM ratio as detector of flash-heating: description and limitations

The $D_3/G_{sl.}$ ratio presented in this study has shown a strong reliability with short yet intense heating. In the future, this RSCM parameter could be used as a powerful tool to detect the possible flash heating effect on the CM crystallinity. Furthermore, its application to the BFR presents also a strong advance in order to decipher if BFR has been generated by ultra-comminution or by melting.

However, as other RSCM parameters, the use of $D_3/G_{sl.}$ ratio has some limitations and caution has to be taken. Indeed, the intense D_3 band generated during the flash heating experiments is also observed in the different contexts where free hydrocarbons exist (Cuesta et al., 1994; Jawhari et al., 1995). Indeed, the characterization of hydrocarbons using the RSCM method show identical spectrum shape as the immature CM contained in these samples. Therefore, the use of the RSCM detection of flash-heating should be limited to the CM already organized like the one observed during the carbonization and early graphitization stages.

In flash heating experiments performed in this study, the CM included in the starting material was already poorly organized and in a similar degree of crystallinity of the ones on the Mugi and Kure BFR. In addition, all the experiments carried out in this study and from the literature have been performed under ambient pressure. However, the pressure seems to have an important effect on the kinetics of the CM evolution during the carbonization (see Chapter V) and the graphitization (Nakamura et al., 2020). Therefore, some changes could occur for flash heating effects on the CM under pressure.

VII.4.3 RSCM thermometers use

RSCM geothermometers are useful tools, widely accepted and used by petrologist in metamorphic environment in order to estimate the metamorphic peak-temperatures (Beaudoin et al., 2015; Clerc et al., 2015; Lanari et al., 2012). Their calibrations are based on the evolution of the RSCM parameters such as the area ratio (Beyssac et al., 2002; Lahfid et al., 2010) or the Full Width at Half Maximum (FWHM) (Kouketsu et al., 2014); an extensive review of all these parameters are available in Chapter

II and in Henry et al. (2019). The RSCM has also been applied to BFR and presumably pseudotachylytes but retrieving the maximum temperature far below temperatures indeed generated during seismic events and sometimes responsible to the melt generation (Ito et al., 2017). However, in the cases of flash heating, an intense D_3 band is observed and influences others RSCM parameters measured. Indeed, the occurrence of the intense D_3 band overtakes others bands during deconvolution, especially the G band. In Beyssac et al.'s (2002) calibration, the D_3 band is not explicitly considered in the calculation of the temperature and therefore the G band area is reduced, whereas in Lahfid et al. (2010) the additional area generated by D_3 band reduces the RA1 area ratio. Therefore, this evolution of the area induced by the intense D_3 band conducts to an underestimation of the RSCM temperatures. In addition, the intense D_3 band reduce the D2 band and D1 band FWHM that conducts to an overestimation of the RSCM temperature using Kouketsu et al.'s (2014) calibration. The error provoked by the presence of a prominent D_3 band on the temperature estimates is correlated to the intensity of the flash heating and more the effect of flash heating is predominant more the under- or overestimation is important.

VII.4.4 Application to the Mugi and the Kure BFR

The Mugi BFR and Kure BFR present similar structural and microstructural features, typical of the molten origin rocks as the one described in the literature (Sibson, 1975). Indeed, quartz clasts are rounded and potassic feldspars show corroded shape, typical of the golf of corrosion generated during frictional melting. In addition, the matrix that embeds theses survivor clasts is amorphous without distinction of structure even in MET images. Moreover, pores scattered in the shaly matrix are round and Ti-rich and Fe-rich particles are rounded or with irregular shapes like droplets. Most importantly, locally recrystallized mullite sticks in Mugi and acicular muscovites in Kure are described and interpreted as microlites that have been recrystallized during the quenching (Mukoyoshi et al., 2006; Ujiie et al., 2007). Based on the microstructural observations, all evidences of melt-origin rock are gathered; such is not always the case for other examples studied in this PhD (Chapter VI).

RSCM data show an increase of IR in the BFR with respect to its host-rocks but are limited with evolution of IR from 5 to 12%. Profiles show a shallow evolution between the BFR and corresponding host-rock with a gradually increase of the CM crystallinity and a large dispersion of the values is

observed in the core of the BFR and in the host-rock. However, the large amount of sandstones, mostly composed of quartz, prevent for keeping the same high-resolution profile and sometimes measurements of the CM crystallinity are absent in the quartz-rich zone due to the large noise generated by this mineral due to the fluorescence detected by the RSCM. The large heterogeneity of values measured in the BFR host-rocks could be interpreted as the redistribution of CM grains during late brittle events that occur after the formation of the BFR.

Comparing now the Mugi and Kure BFR with previous three BFR studied in Chapter VI, some major differences are observed on microstructural and RSCM analyses. On these five BFR, an amorphous matrix with embedded clasts and Fe-rich and Ti-rich particles is observed. However, clasts in Mugi and Kure are rounded whereas the clasts in the Nobeoka, Okitsu and Kodiak BFR are sub-rounded to angular. Fe-rich and Ti-rich particles are rounded or irregular in these two BFR investigated in this study whereas the particles are euhedral in other three BFR similarly to the respective particles observed in host-rocks. Finally, microlites are described in the Mugi and Kure BFR when the absence of these recrystallized minerals is noteworthy for other BFR. In terms of CM crystallinity profiles acquired with the RSCM method, the shape of the profile is continuous with a large dispersion of the values in Mugi and Kure whereas the evolution of IR is sharp between the BFR and the host-rock in the Nobeoka, Okitsu and Kodiak BFR. In addition, the evolution of IR is limited in the Shikoku BFR (i.e. 5 and 12%) when in the other thre BFR the evolution is measured at 36%, 20% and 10% respectively for the Nobeoka, Okitsu and Kodiak BFR.

The $D_3/G_{sl.}$ ratio measured in the Mugi and Kure BFR shows high values and the spectrum shapes are similar to the ones recorded for the flash heating experiments and flash heating examples presented above. We interpret this result, supported by the microstructural observation, as the clue of the record of the frictional heating induced by the seismic slip. In addition, the $D_3/G_{sl.}$ ratio in the BFR are high with a range of values comparable to those of the host-rock flash heating samples without logic with microstructures. This result could be interpreted as an heterogeneous heating linking with the nature of phases as observed by Aubry et al. (2018) in stick-slips experiments. This hypothesis is also supported by the local occurrence of microlites, the coexistence in the BFR of ultra-cataclasite and melt-origin

zones or the occurrence of layering in the blackened zones of Kure, all of that show a heterogeneous repartition of microstructures.

The Mugi and Kure BFR have shown typical microstructures of the melt-origin rocks which are different from the non-molten BFR described in Nobeoka, Okitsu and Kodiak. The IR evolution that reflects the CM crystallinity is also different among these five BFR and the $D_3/G_{sl.}$ ratio highlights evidence of flash-heating induced by the frictional heating during the seismic slip. Therefore, based on the microstructural and RSCM analyses, the Mugi and Kure BFR are interpreted as melt-origin fault veins and can be considered as genuine pseudotachylytes. The difference of the Mugi and Kure BFR with the Nobeoka, Okitsu and Kodiak BFR may be found in the nature of their host-rocks. Even if both sets of BFR are contained in tectonic mélange the Kure and Mugi mélanges are mostly composed of large sandstone blocks whereas the others are in a tectonic mélange mainly composed of shale. The shaly host-rocks may play an important role on the slip weakening because the abundance of phyllosilicates that could inhibit the frictional melting during thermal pressurization (Brantut et al., 2010, 2008). However, the host-rock of the Mugi and Kure BFR is mainly composed of quartz which influences the weakening processes by the lower amount of water and fluids and, consequently, modifies the petro-physical conditions.

VII.5 Conclusions

In this chapter, we tried to identify, using the RSCM approach, robust markers of short-lived heating that are falling completely out of the RSCM geothermometer due to its assumption of exposition to temperature in geological time-scales. Atypical shape of RSCM spectra has been observed in molten origin samples showing an intense D_3 band. In addition, examples reported from the literature of flash-heating experiments and natural flash-heating samples have shown the same spectrum shapes and lead us to establish a new RSCM parameter: the $D_3/G_{sl.}$ Ratio, a sensitive one to the flash-heating.

Furthermore, we studied two extra Black Fault Rocks (BFR) sampled in the Shimanto Belt on the Shikoku island, the Mugi and the Kure BFR present remarkable differences with the BFR studied in Chapter VI. Microstructural observations paired with RSCM, using the IR similarly to the previous

Chapter VI parameter, have been used. In addition to the RSCM, the $D_3/G_{sl.}$ ratio has been used as well to highlight the flash heating effect on the CM crystallinity. This application is based on flash-heating detection during experiments, examples of flash-heating published in the literature and the analyses of natural flash-heating with CM contained in shale in the contact with basalt flows or intrusions.

Microstructural observations of these two BFR show similarities with the Nobeoka, Okitsu and Kodiak BFR studied in the previous Chapter VI, however, important differences have been highlighted and cannot be associated with other producing process than melting (i.e. microlites and droplets). In addition, the IR shows an increase of the CM crystallinity in the BFR core comparing with the host-rocks even if a large dispersion of the IR values is observed. However, the intensity of evolution between the BFR and the host-rock, the shape of the high-resolution profiles and the distribution of the values are different in the Mugi and Kure BFR comparing to the BFR described in Chapter VI. In addition, the shape of the CM spectra in the BFR presents an intense D_3 band that is not detected in the host-rock neither in other BFR. Therefore, the application of the $D_3/G_{sl.}$ ratio in these two BFR revealed similar values as the ones observed in the literature and different from the three BFR studied in Chapter VI.

The distinction between the heating and the deformation effects on the CM crystallinity in the BFR is still problematic in this chapter (see Chapter VI). Therefore, flash-heating experiments have been carried out in order to explore the effect of intense and short-life heating on the CM crystallinity using the $D_3/G_{sl.}$ ratio and IR. $D_3/G_{sl.}$ ratio and IR show a constant increase from the starting material to flash heated material from 0.5 to 60 seconds at an equivalent temperature of 1400°C. Similar CM spectra and $D_3/G_{sl.}$ ratio have been observed in results from the literature and a correlation between the intensity of the flash-heating and the increase of the $D_3/G_{sl.}$ ratio has been described. In addition, flash-heating experiments have shown that the $D_3/G_{sl.}$ ratio reaches a maximum of 0.70 in the carbonization stage of maturation and decreases when reaching the inception of the graphitization stage. This suggests the effect of the flash-heating is less important when the CM presents a higher degree of crystallinity. Finally, the effect of the flash-heating could be detected thanks to the anomalous shape of the CM spectra caused by the intense D_3 band. The RSCM method and especially $D_3/G_{sl.}$ ratio parameter, taking some

cautions on the CM included in the starting material discussed earlier, present a robust tool to highlight the occurrence of a flash-heating event in the geological history of a natural sample.

Microstructures are typical from a melt-origin rocks. The CM crystallinity shows an increase in the BFR and the $D_3/G_{sl.}$ ratio is very similar to the ones observed for examples of rocks that experienced natural or experimental flash-heating event. These points suggest that the BFR of Mugi and Kure have been subjected to an important heating for a short duration. Combining the RSCM parameters and the microstructural observations, the Mugi and the Kure BFR are interpreted as the result of a frictional melting induced by a seismic event followed by a quick quench. The $D_3/G_{sl.}$ ratio is, therefore, a useful tool to decipher the genesis of the BFR in the accretionary complexes associated with microstructural observations, which are not sufficient alone to insure the melt-origin of these BFR.

Preface

This chapter present the application of the $D_3/G_{sl.}$ ratio, establishment in the chapter VII, and the IR on on-contact basalt and shale. This work aims to determine if the basalt intrusions or extrusions can be detected and conserved on shale in accretionary complexes in order to decipher the basalt lenses origin in these zones. The $D_3/G_{sl.}$ ratio parameter and the Raman spectra shape evolution has been used on immature sediment, from Ninetyeast Ridge, Shatsky Rise and Hawaii Emperor Volcanic Lineament IODP sites, on-contact with basalt layers. These results have been compared with the ones obtained on mature shale from the Hyuga tectonic mélange unit and the Makimine mélange from the Shimanto Belt. The results suggest that the detection of the flash-heating induced by molten basalts on shale is detectable using RSCM method showing a $D_3/G_{sl.}$ ratio and IR increases. During the carbonization stage of maturation, the $D_3/G_{sl.}$ ratio is overprinted by the regional metamorphism but the IR increase induced by flash-heating is still observed. However, during the graphitization stage, no more observation of this flash-heating effect is visible and both $D_3/G_{sl.}$ ratio and IR are overprinted by regional metamorphism.

Chapter VIII – Flash heating detection on on-contact basalt and shale in accretionary complexes: the application of RSCM new $D_3/G_{sl.}$ ratio parameter.

VIII.1 Introduction

The understanding of the convergent zones and especially subduction zones is a major issue for geoscientists because of the seismogenic aspect of these tectonic zones. Two approaches can be combined: the study of active margins, mostly through geophysics, and the analysis of fossil structures, such as accretionary complexes, through tectonic and geochemical studies.

Accretionary complexes are composed of tectonically accreted sediments mostly constituted of thick sequence of "coherent" turbidites (i.e. preserving their original sedimentary layering), alternating with tectonic mélanges of sediments in which strain has disrupted the original stratification. In addition, green rocks, such as basalt, are volumetrically minor, but widespread in many of these tectonic mélanges. Basalt occurrence is often composed of an alternation of basalt, cherts and shale, typical of the original ocean floor plate stratigraphy. Other geological examples are far less clear, and the origin of the imbrication of basalt and sediment lense in tectonic mélanges is debated (Festa et al., 2012; Kitamura and Kimura, 2012; Wakita, 2015). Indeed, some basalt lenses can originated from tectonic processes, such as the plucking of oceanic crust slices and imbrication with sediments, or from magmatic/volcanic processes, such as repeated basalt flows on or within seafloor sediments, possible when a ridge approaches the trench (Kiminami and Miyashita, 1992; Osozawa, 1992).

The Raman Spectroscopy of Carbonaceous Material (RSCM) reflects the carbonaceous material (CM) crystallinity, sensitive to the temperature, and its evolution through carbonization and graphitization processes during regional metamorphism (Beyssac et al., 2002; Lahfid et al., 2010). RSCM has been adapted more recently for short-duration heat pulses such as sill intrusion, so that it can be used in the case of contact metamorphism (Aoya et al., 2010). CM crystallinity, through the intensity ratio (IR) and another RSCM parameter of $D_3/G_{sl.}$ ratio, has shown its sensitivity to the short-duration and intense heating, called flash heating in the following (see Chapter VII).

Here, the RSCM has been used in order to characterize the occurrence of basalt bodies in accretionary complexes. In the case of basalt intrusion within sediments or basalt flow onto sediments, we make the assumption that the short-lived heating of the sediments results in an anomaly of RSCM signal. We

propose in this chapter to assess whether this hypothesis is valid or not, first in ocean floor sediments, where basalt intrusion into sediments are documented and material is available through IODP drilling. Second, we apply a similar analysis in sediments in contact with basalt lenses, in tectonic mélanges where the basalt-sediment relationship is unclear (Hyuga tectonic mélange Makimine formation in Japan).

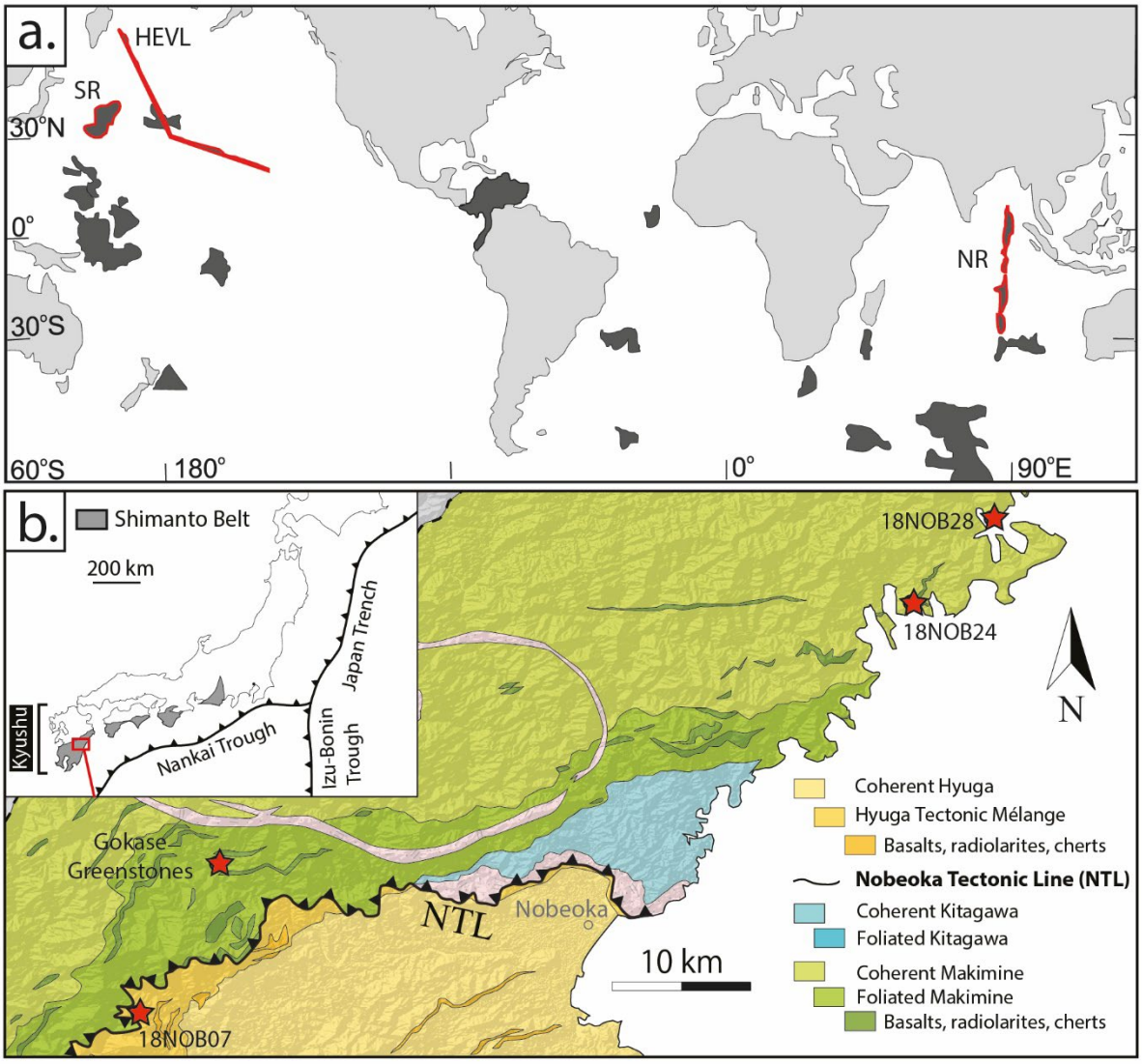

Figure VIII.1 : Sample location maps. ***a****. Basalt occurrence maps on seafloor sediments, NR: Ninetyeast Ridge, SR: Shatsky Rise, HEVL: Hawaii Emperor Volcanic Lineament (Modified from (Ernst, 2014))* ***b.*** *Locations of basalt lenses and greenstones sampled in the Shimanto Belt (Japan).*

VIII.2 Results

VIII.2.1 Outcrop and sample descriptions

VIII.2.1.1 Immature sediments

Immature sea-floor sediments in contact with basalt flows have been selected in three IODP drilling sites. Basalt layers show size ranging from tens of centimeters up to few meters with an intrusive or extrusive origin. Samples from the Ninetyeast Ridge, the Shatsky Rise and the Hawaii Emperor Volcanic Lineament have been selected (Figure VIII.1a) based on the occurrence of this type of contact. Distances with basalt layers are indicated in Table VIII.1.

Ninetyeast Ridge

Samples have been selected from the drilling site 758A leg 121, at depth of ca. 530m below seafloor. This series is composed of clay tuff in alternation with two basalt flows (Figure VIII.2). The upper part of the section is composed of a 11 meters thick extrusive basalt lava flow on greenish clayey to calcareous micritic tuff. The second occurrence of basalt is characterized by an intrusion of a 20 meters thick sill in dark clayey tuff. Samples of sediments have been selected on each rim of the basalt bodies and then at 10cm and 20cm to the sill contact. Samples far from the contact have been selected as reference.

Shatsky rise

Shatsky rise samples correspond to the site U1346A leg 324 from the core 4R to 5R at ca. 120m below seafloor. This sampling profile is composed of black calcareous sediments containing in different proportion volcanic angular clasts, crosscut by an intrusive 50 centimeter-thick aphyric basalt (Figure VIII.2). Samples have been selected on each rim of the intrusive basalt up to 9 meters below the contact.

Hawaii Emperor Volcanic Lineament

The last sampling profile comes from the IODP site 1204A leg 197, from core 17R at 950m below seafloor. The mainly calcareous clastic series shows a lobate to sub-planar contact with a 3 meters-thick overlying basalt. The contact is characterized by a 5 mm-thick glassy material and an alteration aureole (Figure VIII.3a). Sample on this contact has been selected in addition to other samples selected at 0.25, 1 and 1.5 meters away from the contact.

Table VIII.1 : Samples selected from three IODP drilling sites and respective distances with basalts. When two distances are indicated the first one is the top basalt contact.

IODP	Sample	Type	Thermal source	Distance contact (m)
Ninetyeast Ridge	A	Reference	-	70
	B	Contact	Basalt flow	0.0 / 5.2
	C	Reference	-	0.2 / 5.0
	D	Reference	-	4.0 / 1.2
	E	Reference	-	5.0 / 0.2
	F	Reference	-	5.1 / 0.1
	G	Contact	Basalt intrusion	5.2 / 0.0
Shatsky Rise	A	Reference	-	0.1
	B	Contact	Basalt intrusion	0.0
	C	Reference	-	1.0
	D	Reference	-	8.0
	E	Reference	-	9.0
Hawai	A	Contact	Basalt flow	0.0
	B	Reference	-	0.25
	C	Reference	-	1.0
	D	Reference	-	1.5

VIII.2.1.2 Shimanto Belt

In the Shimanto Belt accretionary complex, basalt bodies have been observed, especially in tectonic mélange units. In this study, two units at different degree of metamorphism and carbonaceous material crystallinity, the Hyuga tectonic mélange unit and the Makimine unit, respectively at 270 ± 18°C and 335 ± 5°C, have been used (Figure VIII.1b). Samples have been selected in poorly deformed zones in order to avoid the strain effect in addition to the eventual thermal effect.

Hyuga tectonic mélange unit

The Hyuga tectonic mélange is composed of blocks of sandstones, silts and basalts scattered in a shaly matrix that shows a consistent foliation. Contacts between the basalt and the sediment are irregular (Figure VIII.4a and 4b). The studied sample (18NOB07D) is composed of clasts of quartz in a phyllosilicate matrix. The shale in contact with the basalt is darker than the reference in the host-rock (Figure VIII.4c and 4d).

Makimine unit

Two types of contacts between the basalt and shale are observed in the Makimine unit. On one hand, xenoliths of shale are observed in large pluri-metric basalt lenses (Figure VIII.5a). On the other hand, basalt lenses are included in the shale series (Figure VIII.5b). The contact is irregular and locally lobate

in both occurrences at sample and outcrop scales (Figure VIII.5). Three samples have been selected (Figure VIII.5c), one in contact with a lenses of basalt included in the shale series (18NOB24A) and two xenoliths (18NOB28A and 18NOB28B).

VIII.2.2 Raman Spectroscopy of Carbonaceous Material (RSCM) analyses

The RSCM has been used to detect the possible thermal effect of the basalt bodies on the CM crystallinity. RSCM spectra, intensity ratio (IR) and $D_3/G_{sl.}$ ratio have been used to explore the evolution of the CM crystallinity.

VIII.2.2.1 Effect of basalt contact metamorphism on immature deep-sea sediments

In immature samples, the CM crystallinity is in general too low to be deconvoluted into defined peaks after the RSCM acquisition. Therefore, only the shape of the spectra is described and when the CM crystallinity is sufficient the IR and $D_3/G_{sl.}$ ratio have been used.

Ninetyeast Ridge

In the Ninetyeast Ridge, one sample has been selected at 70 meters from every basalt body in order to characterize the immature CM crystallinity. The typical spectrum of immature CM is composed of three main zones from 1100 to 1300 cm^{-1}, a band from 1400 to 1500 cm^{-1} and another centered at 1600 cm^{-1} (Figure VIII.2 – spectrum A). In addition, an important noise has been observed. All the samples from the upper part of the sampling profile, including the sample in contact with the upper basalt body, present the same spectrum shape. However, the evolution is observed on three samples in contact with the 20 meters-thick sill, detectable up to 20 cm with a slightly increase of the IR from 0.606 to 0.63 toward the contact. At 20cm from the contact, the most of the CM measurements show immature CM but few spectra show a higher crystallinity. In comparison, at 10cm and on the contact all the CM spectra show the same shape with a poorly organized lattice of the CM. In addition, the $D_3/G_{sl.}$ ratio is ranging from 0.389 to 0.466 from the sample at 20cm to the contact with a monotonous increase when the distance with the contact decreases.

Shatsky rise

In the Shatsky rise, an intrusive basalt flow crosscut the immature sediments of 50 centimeters. In this case, only one spectrum on the sample selected at 10 centimeters above the sill shows a poorly organization and a large value of $D_3/G_{sl.}$ ratio at 0.612. All the others CM spectra of samples show immature shape of the CM spectra close to the one observed in the Ninetyeast Ridge but with a large noise (Figure VIII.2).

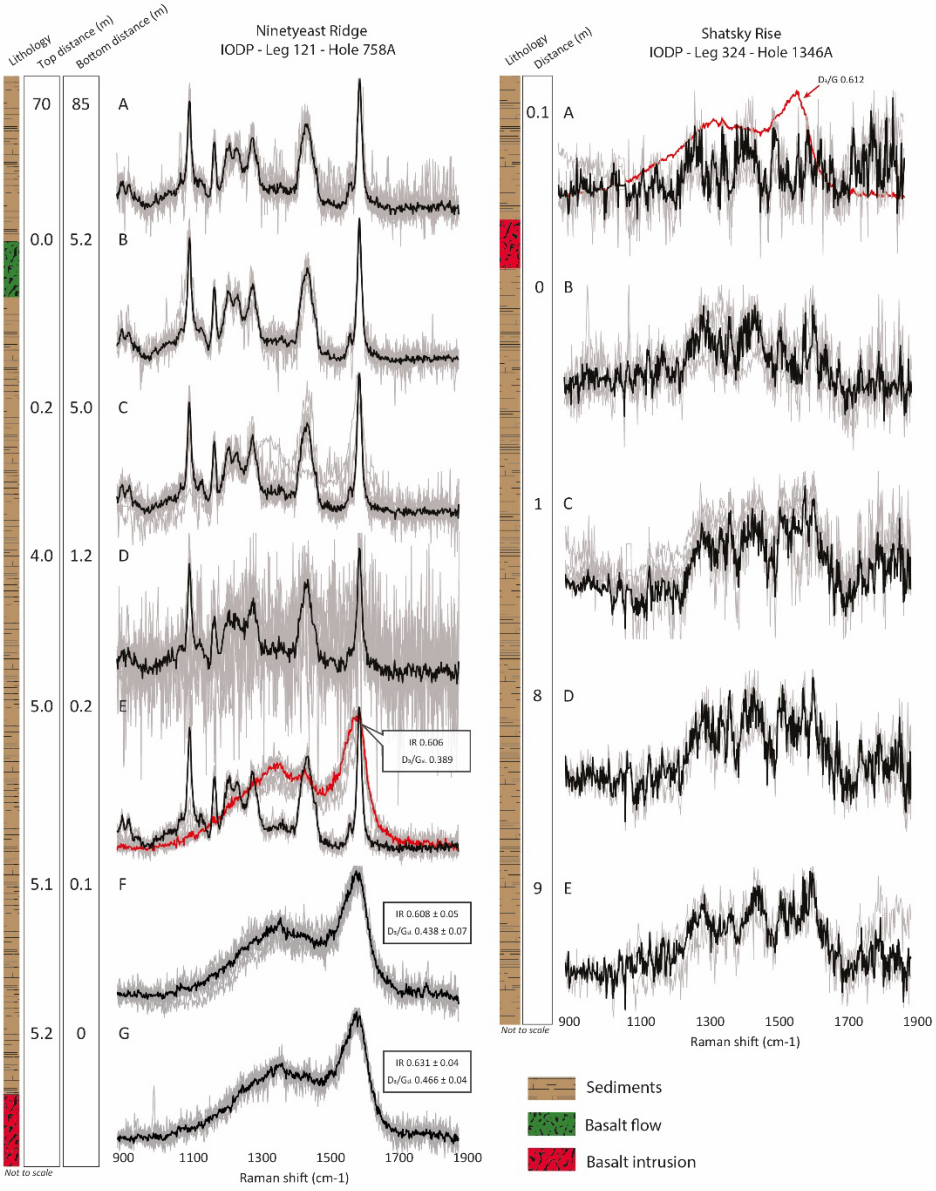

Figure VIII.2 : RSCM spectra evolution of the Ninetyeast Ridge and Shatsky Rise samples along sampling gradients with basalt layers showing the increasing organization of the CM approaching the basalt bodies. Top and bottom distances correspond to the distance between the basalt bodies on the top and on the bottom and the selected samples, respectively. Black spectra correspond to the mean spectra of the sample, red spectrum is an atypical one measured in one sample.

Hawaii Emperor Volcanic Lineament

Samples selected at 0.25, 1 and 1.5 meters below the basalt contact show only immature CM spectra (not show here). However, on contact with the basalt in the last hundredth of microns, a duality of the CM spectra is observed. Indeed, immature CM spectra are observed in association with well-organized closed to the perfect organization (i.e. graphite) (Figure VIII.3b).

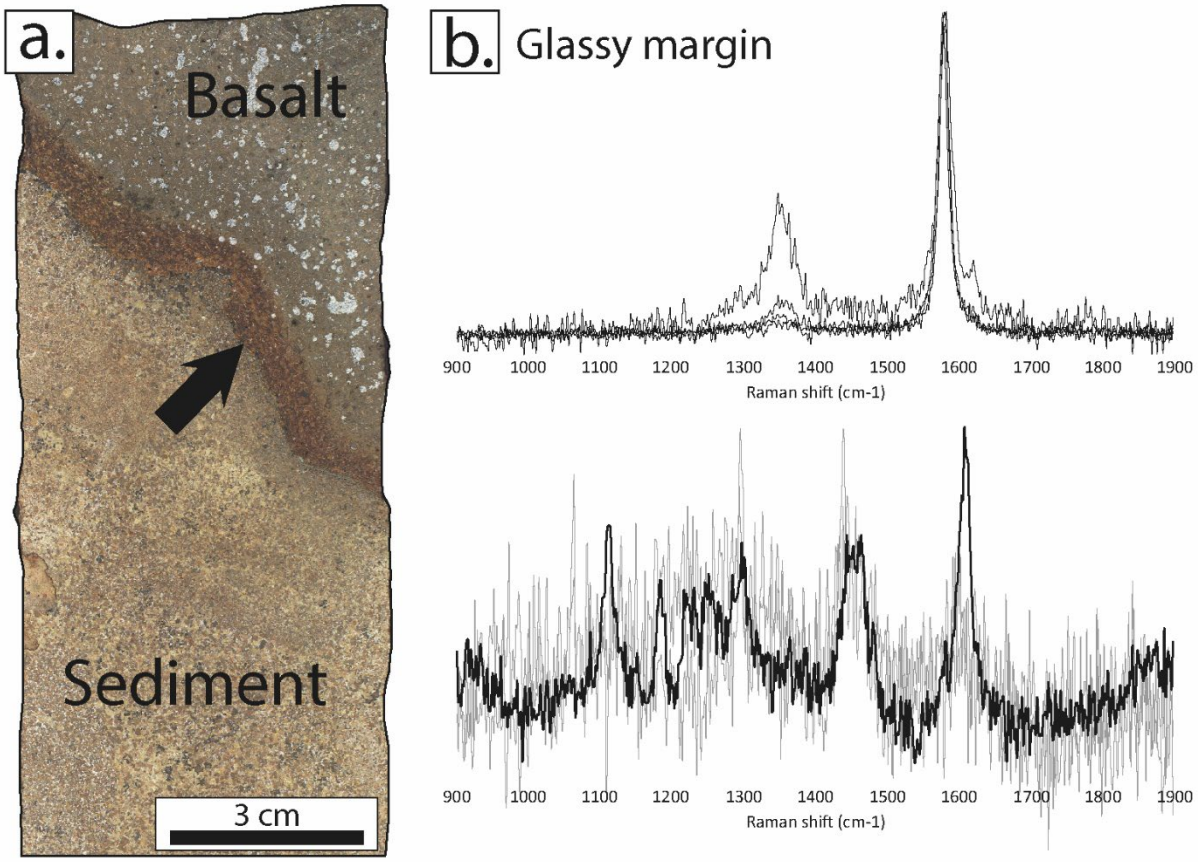

Figure VIII.3 : Structure and RSCM results from the IODP sample from the Hawaii Emperor Volcanic Lineament. ***a.*** *Contact between immature sediment and basalt flow showing a millimetric glassy and reactional margin* ***b.*** *RSCM spectra measured on the contact between the clastic sediment and the basalt showing duality of CM crystallinity. Black spectrum corresponds to the mean spectrum of the sample.*

VIII.2.2.2 On-contact basalt influence on metamorphic shales

In Shimanto Belt samples, the nearest zone with the basalt contacts has been analyzed and compared with the host-rock in the very close proximity (i.e. few centimeters or less). The two RSCM parameters IR and $D_3/G_{sl.}$ ratio have been used in this section.

Hyuga tectonic mélange unit

On the sample 18NOB07D that represents the Hyuga tectonic mélange unit RSCM maps of the IR and the $D_3/G_{sl.}$ ratio have been produced using GIS software. In the host-rock values of IR have been measured at 0.514 ± 0.03, whereas, on the last millimeter in contact with the basalt the IR evolve from to 0.579 ± 0.04, so +13% (Figure VIII.4c and 4e). In comparison, the $D_3/G_{sl.}$ ratio does not show the same evolution with scatter values varying from 0.12 to 0.23 without any correlation with the distance to basalt-sediment contact (Figure VIII.4d and 4e).

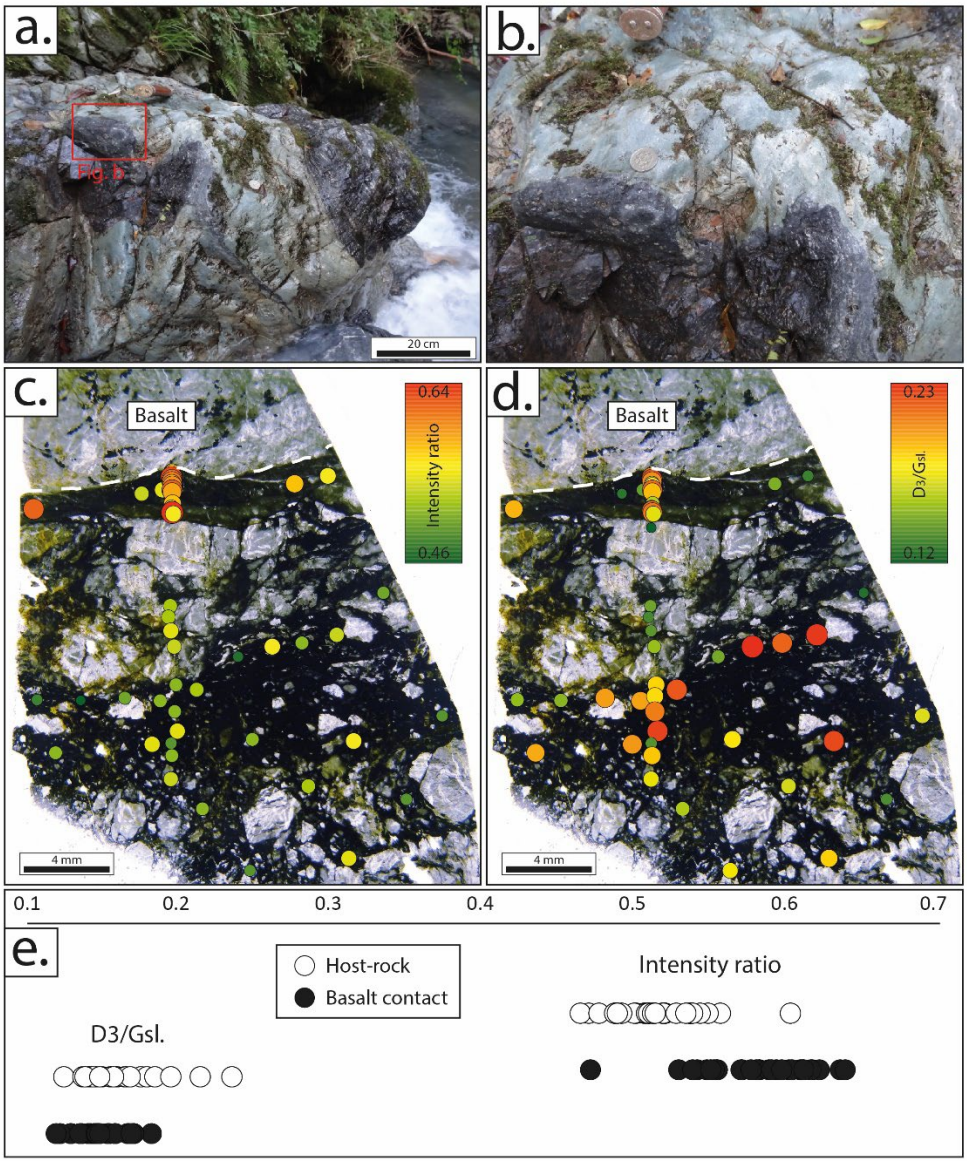

Figure VIII.4 Structure and RSCM results in the Hyuga tectonic mélange unit. ***a.*** *Basalt and tectonic mélange contact in the Hyuga tectonic mélange unit.* ***b.*** *Close up on the irregular contact between the basalt and the tectonic mélange* ***c. and d.*** *Intensity ratio and $D_3/G_{sl.}$ ratio along the contact with the basalt and in the host-rock.* ***e.*** *IR and $D_3/G_{sl.}$ ratio evolution diagram.*

Makimine

Samples selected in the Makimine unit present a higher degree of CM crystallinity of the starting material based on the IR ranging from 0.8 to 1.4 (Figure VIII.5d). RSCM results from the contact and the host-rock do not show evolution of the IR and the $D_3/G_{sl.}$ ratio for each sample. $D_3/G_{sl.}$ ratio measured shows values from 0.10 to 0.20 except for two measurements in 18NOB24A and 18NOB28A on contacts that reach ca. 0.25 (Figure VIII.5d).

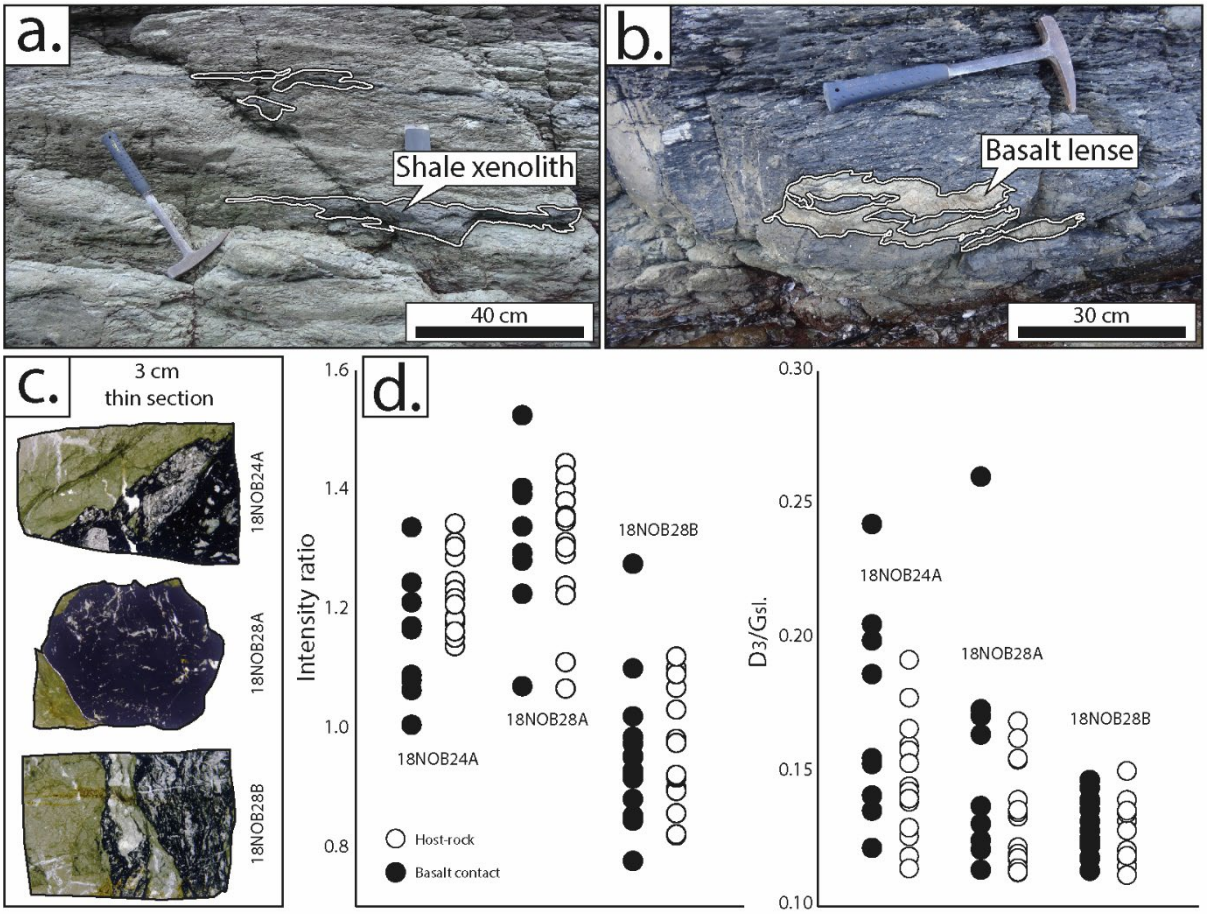

Figure VIII.5 : Structure and RSCM results in the Makimine unit. ***a.*** *Xenolith of shale in metric body of basalt* ***b.*** *Basalt lens in a shale intercalation* ***c.*** *Thin sections of three samples selected from two basalt-shale contact occurrences* ***d.*** *Intensity ratio and $D_3/G_{sl.}$ ratio evolution between the contact and reference material away from the contact ("host-rocks"). No systematic trend is visible.*

VIII.3 Discussion

In this study, the RSCM associated with a structural observation have been made in order to decipher the origin of basalt lenses in accretionary complexes. Two hypotheses can be considered to account for

the multiple basalt lenses embedded in sediments in tectonic mélanges: the tectonic imbrication of oceanic crust lenses in sediments related to deformation within the accretionary prism, or an original, ocean-floor repetitive sequence of basalt intrusions/flows and sediment layers. The second hypothesis implies a short-lived heating of sediments. As the CM is sensitive to the temperature and tends to increase its crystallinity under thermal stress, the IR, the $D_3/G_{sl.}$ ratio and the shape of spectrum have been used to detect a possible inheritance of such short-lived heating stage in sediments at the contact with basalts.

VIII.3.1 RSCM parameters evolution in immature sediments

Three IODP drilling have been analyzed based on the occurrence of basalt flows or intrusions on or in sea-floor sediment at shallow depth where immature CM is observed. Sampling profiles selected from IODP drilling from the Ninetyeast Ridge, Shatsky rise and Hawaii Emperor Volcanic Lineament have been analyzed using the RSCM.

As most of the CM grains analyzed were immature, the determination of the IR was impossible. Therefore, the comparison is mainly based on the spectrum shape along sampling profiles and rarely on the IR and $D_3/G_{sl.}$ ratio (Figures VIII.2 and VIII.3). In Ninetyeast Ridge and Hawaii samples, the detection of flash heating is clear and visible on the contact with the basalt: CM grains spectra show higher crystallinity compared with immature CM observed elsewhere. In addition, the $D_3/G_{sl.}$ ratio increases in the heated zone closed to the basalt contacts and shows a weak but evident correlation between the increasing values and the decreasing distance with the contact (Figure VIII.2). This correlation has also been made for the IR in the case of the Ninetyeast Ridge. Moreover, intrusive (Ninetyeast ridge) and extrusive (Hawaii Emperor Volcanic Lineament) samples show the same increasing CM crystallinity on the contact with basalt. However, the intensity of the flash heating effect is high in the Hawaii sediments where CM crystallinity quasi-perfectly organized is observed but limited in terms of spatial diffusion, whereas the sill of the Ninetyeast Ridge is more limited in terms of intensity but the spatial distribution is larger (up to 20cm). Therefore, for both types of basalt flow, a flash heating is detectable on the CM crystallinity but the intrusive mode seems to be more spatially penetrative.

VIII.3.2 RSCM parameters evolution in metamorphosed shales

In the Shimanto Belt, in southwest Japan, metric basalt lenses occurred in tectonic mélange (Hyuga tectonic mélange unit) and in coherent turbiditic units (Makimine unit). These occurrences are characterized by irregular or lobate contacts, in poorly foliated zones, with host-rock and difficult to link with the tectonic imbrication. Consequently, the RSCM has been used on 4 samples, one in the Hyuga tectonic mélange and three in Makimine, in order to detect potential evidence of residual flash heating on CM induced by the contact of basalt with sediments after regional metamorphism. The general metamorphic grade of the Hyuga tectonic mélange is lower than that of the Makimine formation. Accordingly, the CM crystallinity of the Hyuga tectonic mélange is less organized (i.e. carbonization stage) than the one observed in the Makimine (i.e. early graphitization stage).

RSCM results show in the Hyuga tectonic mélange an increase of the crystallinity in the first millimeter of the contact with the basalt lens, of the order of +13% in average based on the IR evolution. After this millimeter, all the IR values are almost constant and no high crystallinity is observed. Therefore, the influence of the basalt flash heating is very limited in space. For higher CM crystallinity samples, in the Makimine unit, the IR measured in the three Makimine on-contact sediment do not show evolution between the host-rock and the direct contact with the heating bodies. In the Gokase river, in the Makimine unit, alternation of shale and greenstones show granular aspect more or less foliated (Figure VIII.6). Thereby, the occurrence of these greenstones is associated with an intrusive history and must induce heat on sediments but no evidence of flash-heating is detected on the shales. Therefore, for this range of CM crystallinity in the Makimine samples, after 300°C, the effect of the flash-heating is no more visible due to the overprinting of the regional metamorphism.

The $D_3/G_{sl.}$ ratio does not show evolution in these two units, independently to the degree of crystallinity of the CM. Indeed, all the values are ranging from 0.10 to 0.25 irrespective of the unit considered or the distance to the basalt-sediment contact. In addition, these values are similar to the ones measured in references in the Shimanto Belt on the Black Fault Rocks and far from the values (i.e. ca. 0.5) reached by-flash heating experiments (Aubry et al., 2018; Ito et al., 2017; Muirhead, 2012) (see Chapter VII). A large residual D_3 band has been observed in immature sediments after flash heating (Cuesta et al., 1994;

Jawhari et al., 1995). However, the metamorphic samples considered here have all experienced a stage of long-term metamorphic heating. Therefore, the metamorphic maturation of the CM tends to erase the original, ocean-floor, short-lived heating signal in $D_3/G_{sl.}$ ratio.

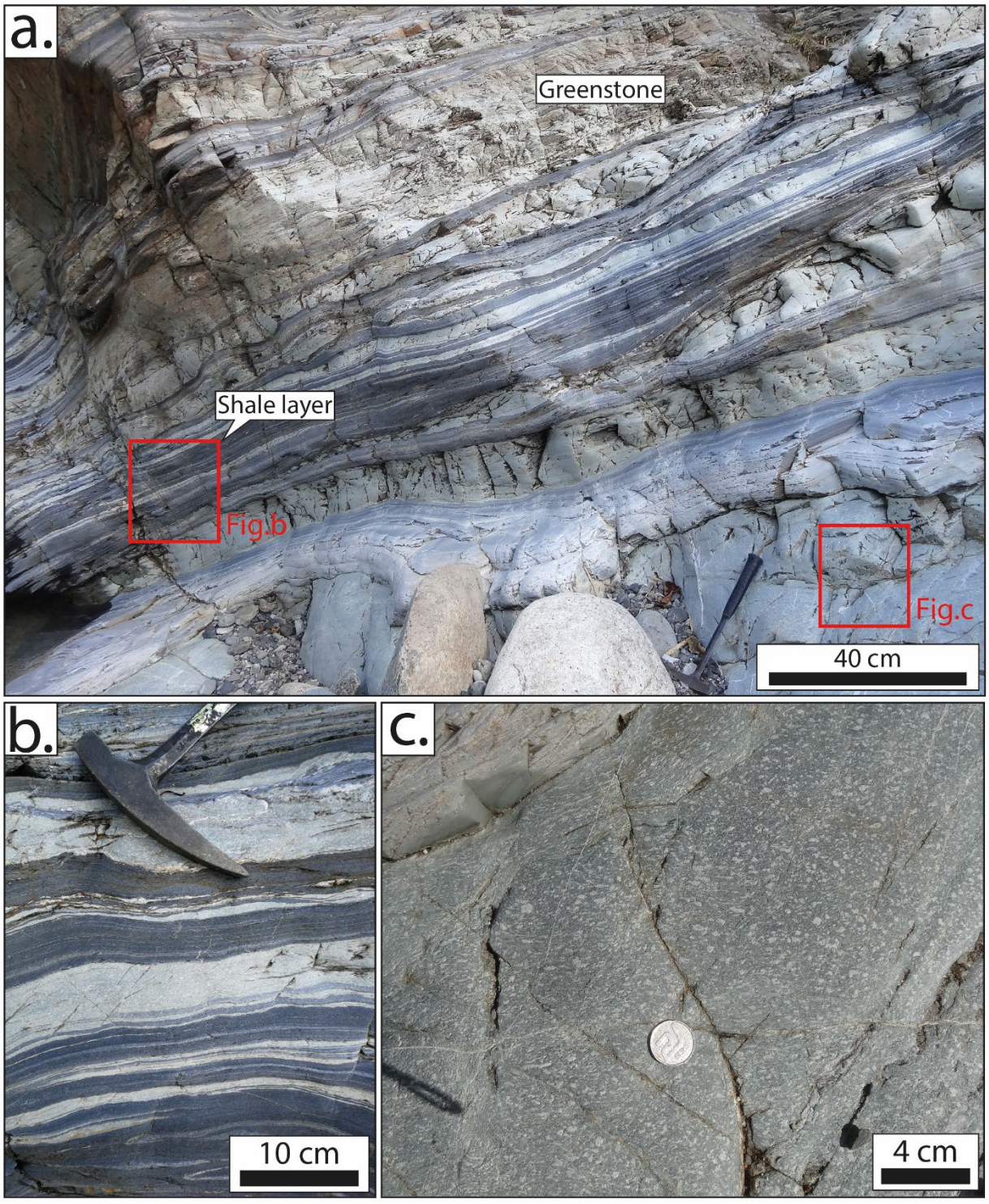

Figure VIII.6:Greenstones layers in contact with metamorphosed shales in the Gokase river. ***a.*** *Alternation of greenstones and shales showing strain gradients* ***b.*** *Close up on strongly foliated shale and greenstone* ***c.*** *Close up on igneous greenstone in poorly deformed zone showing sub-euhedral replaced plagioclase.*

Finally, the messages given by the IR and the $D_3/G_{sl.}$ ratio are quite different and respond to two distinctive reactions. Both show the flash heating effect on the CM, however, the IR gives an indication on the maximum crystallinity reached during the flash heating and is conserved up to 300°C. In contrast, the $D_3/G_{sl.}$ ratio indicates the occurrence of immature CM in the grains despite the crystallinity enhance induced by flash heating and is easily removable when the regional metamorphism occurs even at low temperature (i.e. 250°C).

VIII.3.3 Limits of detection

The RSCM has shown that it is possible to detect evidence of flash heating on CM contained in accreted and immature sediments (Figure VIII.7). Despite this availability, some limits have been observed during the study. The most important limit is the spatial resolution of this study. Indeed, the effect of flash heating has been detecting in a short diced of few millimeters or few centimeters to the contact with the basalt body. In addition, it seems that a correlation between the size of the basalt body and the increasing intensity exists and in the case of very thin basalt flow the detection is impossible (i.e. Shatsky rise). These points could be explained by a quick quench of the basalt in contact with sea-floor sediments and the quantity of heat available that depends on the thickness of the melted body.

The second issue of the detection concerns the large heterogeneity measured on the CM grains, which do not react homogeneously. Indeed, even for large amount of heat transfer, such in Hawaii with the occurrence of quasi-perfectly organized CM, the majority of CM grains remains non-organized and immature. In contrast, in the Ninetyeast Ridge, all CM grains show the same crystallinity on the contact. The clastic aspect of the samples from Hawaii is different from the clayey aspect of the Ninetyeast Ridge samples, the latter are more homogeneous. The evolution of the CM more or less heterogeneously could be interpreted as the effect of the matrix on the CM crystallinity as already proposed (Beyssac et al., 2002; Lahfid et al., 2010; Pasteris and Wopenka, 1991; Wada et al., 1994).

The last limit is the overprint of the RSCM parameters by the metamorphism induced during the accretion. Indeed, the $D_3/G_{sl.}$ ratio increase, caused by the immature residual CM in the grains, is quickly equilibrated and tends to disappear despite the crystallinity enhance during the carbonization phase (Figure VIII.7). In addition, the IR on contact with basalt in the Shimanto Belt is overprinted after 300°C

by the regional metamorphism (i.e. in graphitization phase) and does not show any evolution between the contact and the host-rock in terms of crystallinity (Figure VIII.7).

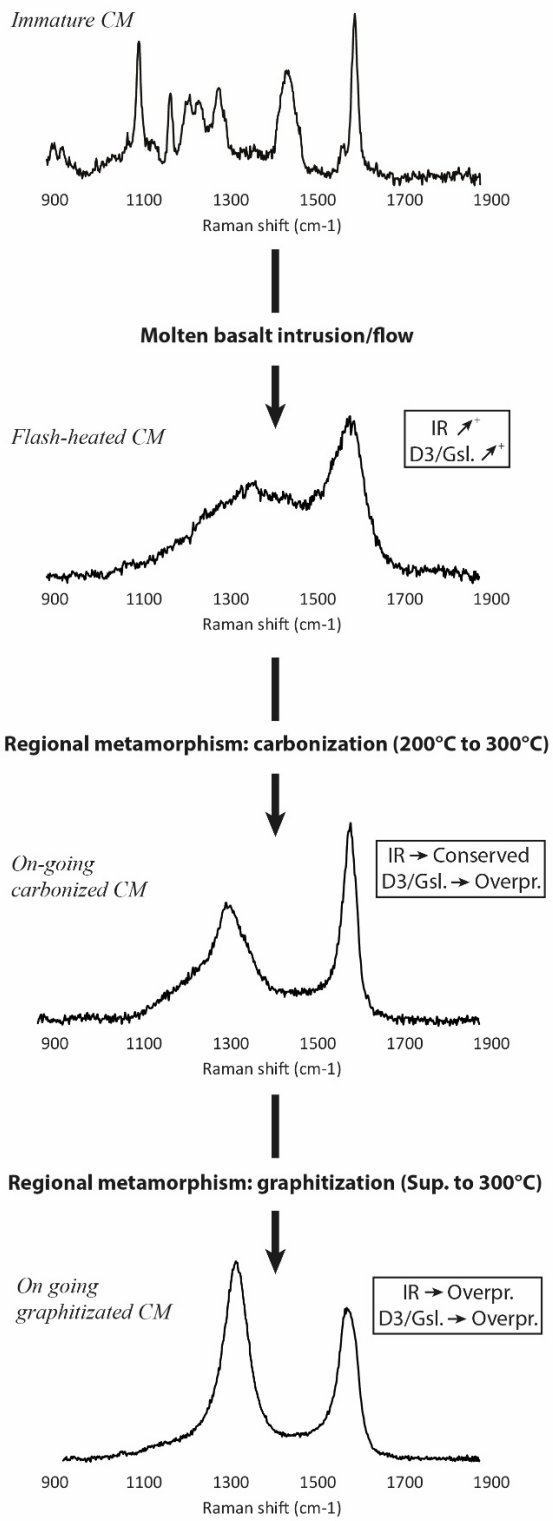

Figure VIII.7: Evolution of the CM spectrum shape from immature CM in seafloor sediments to the early graphitization stage in sediments in contact with basalt layers showing the evolution of the IR and D3/Gsl. ratio and the overprinting by the regional metamorphism.

VIII.3.4 Implications

In the previous sections of the discussion, the RSCM analyses, especially IR and $D_3/G_{sl.}$ ratio, have shown that is possible to detect the flash heating generated by basalt flow. Combining these results with the structural and micro-structural observations of the imbrication of basalt in the accreted sediments, it appears to be an efficient method to decipher the genesis of the basalt lenses observed in accretionary complexes and to discriminate tectonic imbrication processes from seafloor and magmatic processes. Nevertheless, such discrimination is limited to low grade metamorphism (~250°C), as above these temperatures all CM grains converge towards the same spectra and the potential record of the seafloor history is lost.

Results obtained in the Hyuga tectonic mélange suggest that not all the basalt lenses observed in accretionary complexes occurred through a tectonic imbrication of a oceanic crust slate during the accretion but could be generated by successive lava flows from the ridge directly to the trench (Kiminami and Miyashita, 1992). Basalt geochemistry have also been used in order to discriminate the basalt origin (Nakamura et al., 2000). Indeed, based on major and minor elements analyses it seems that a part of the basalt layers indicate an island-arc signature and can be only tectonically accreted. However, using the geochemistry to decipher the tectonic or flow/intrusive basalt genesis is not sufficient.

VIII.4 Conclusions

The occurrence of basalt in accretionary complexes series generates controversies about their origin, either as a result of tectonic imbrication or near-trench magmatism and resulting in multilayering of basalt and sediments. The RSCM has been proposed to discriminate the origin of basalt based on the flash heating effect on the CM crystallinity of grains included in accreted rocks. In addition, immature sea floor sediments in contact with basalt lava flows have been analyzed in order to understand the power of flash heating on the CM crystallinity. The IR and the $D_3/G_{sl.}$ ratio have been used to explore the thermal effect in complement to the spectrum shape of CM in immature sediments. IR and $D_3/G_{sl.}$ ratio suggest an increase of the CM crystallinity by the flash heating on contact with basalt for both sets of samples but the spatial resolution of the effect is limited to the first millimeters up to few centimeters. Immature sediments show an evolution of the crystallinity that is conserved in the accreted sediment up

to 300°C where the IR increase is overprinted by the regional metamorphism. Nevertheless, the $D_3/G_{sl.}$ ratio, that reflects the immature CM remained during the flash heating, tends to disappear during the metamorphic maturation. Three issues have been highlighted for this method in the discrimination of the genesis of basalt lenses in accretionary complexes: (1) the small spatial resolution, (2) the heterogeneity of the flash heating and (3) the overprinting after 300°C. However, paired with structural and micro-structural observations of the contact with sediments, the RSCM analyses could be a quick and non-destructive alternative method to the geochemistry analysis on basalt, the latter is not sufficiently discriminant for the same source of basalt. In the Hyuga tectonic mélange unit, the IR on the contact up to 1mm was 13% higher than the IR of the host-rock. It suggests the flash heating effect of the CM contained in the sediment is preserved throughout the metamorphic history. This anomaly in IR at the sediment-basalt contact also suggests an origin of the basalt lens as basalt lava flow or intrusion in the near–trench turbidite sediments. It brings therefore information about the origin of basalts in mélange, but also about the possible occurrence of ridge subduction.

General discussion

In this study, we aim to explore the effect of strain on the carbonaceous material (CM) crystallinity through natural examples and experimentally produced samples. The effects of strain on the CM crystallinity have been explored by many researchers, however most of their studies are based on well-organized to perfectly organized CM during the graphitization stage of maturation (Bonijoly et al., 1982a; Bustin et al., 1995; Kedar et al., 2021, 2020; Kuo et al., 2018, 2017; Nakamura et al., 2015; Suchy et al., 1997). Indeed, the effects of deformation on poorly organized CM (i.e. during the carbonization and early graphitization stage) remains unexplored except for the seismic deformation; the problem is that in the latter case, it is impossible to decipher the thermal effects from the deformation ones (Ito et al., 2017; Ujiie et al., 2021). Therefore, in this study, we focused on the effects of deformation on the poorly organized to organized crystallinity of CM (i.e. from 200 to 360°C) that contained along seismic and non-seismic strain gradients in natural zones and experimentally deformed samples.

The effect of deformation on the CM crystallinity

In order to explore the evolution of the CM along strain gradient, the intensity ratio (IR ; R1 in Beyssac et al. (2002)) has been used based on its natural increase from 0.5 to 1.6 during the carbonization and the early graphitization stage (i.e. on the temperature range from 200 to 360°C). IR is directly related to the crystallinity of the CM (Beny-Bassez and Rouzaud, 1985; Pasteris and Wopenka, 1991) and sensitive to the deformation, especially for high degree of crystallinity of the CM (Bustin et al., 1995). During this study, we explored the seismic and non-seismic deformation effects. The main finding of our work is that irrespective of deformation type and domains of strain localization show positive correlations with IR values.

The same observations, increase of CM crystallinity correlated with strain, had been made for higher degree of crystallinity during the graphitization stage (Bonijoly et al., 1982a; Bustin et al., 1995; Kedar et al., 2020; Kuo et al., 2018; Nakamura et al., 2015; Suchy et al., 1997). Though the nanoscale processes governing the links between strain and IR, in the relatively immature CM considered here, have not been explored in our work, we can nevertheless tentatively suggest that they bear some similarity with the processes active during the graphitization, i.e. for more crystalline CM. In nano-scale, shear

structurally leads to the coalescence of pores and the parallelization of basic structural units, which conduct to the a more regular organization of the aromatic carbon layers and to the widening of the carbon sheets during deformation (Bonijoly et al., 1982a; Bustin et al., 1995).

In the following, we will make the comparison of, in one hand, the seismic vs. the non-seismic deformation and, on the other hand, the natural vs. experimental samples.

Seismic deformation vs. non-seismic deformation: CM crystallinity evolution and microstructures

Microstructural evolution, texture and mineralogy changes vary according to the seismic and non-seismic deformation. Natural and experimental samples deformed in the non-seismic regime are described respectively in Chapter IV and V and the microstructures description of the seismically generated BFR is provided in Chapter VI (Figure VI.2). Indeed, in natural and experimental samples of non-seismic deformation, a general recrystallization of phyllosilicates such as white mica or chlorite is observed in shear-zones accompanied with a reduction of the grain size of quartz clasts and the destabilization of albite clasts (Figures V.13 and V.16). This evolution leads to a rheological weakening of the rock in the layer and the concentration of the strain that could be applied to CM grains. In opposition, the mineralogy remains very similar between the host-rock and the BFR and the difference is observable on phases amount and on the very important grain size reduction resulting from the ultra-comminution (Figure VI.2). In addition, the deformation is mostly brittle based on the observation of angular clasts embedded in a shaly matrix mostly composed of clays in which interstitial recrystallized chlorite is sometimes observed. Therefore, in the seismically deformed samples, the deformation makes mostly mechanical grain size reduction in the fault core, whereas shear-zones show rather a combination of chemical (preferential dissolution and precipitation of phases) and mechanical (grain size reduction) processes.

Even if seismic and non-seismic crystallinity show enhancement in the organization of CM along strain gradients, their distinction can be made on the CM crystallinity evolution by the link between intensity ratio and microstructures in high-resolution profiles. Indeed, the quantity of strain seems to be the main

controlling factor of the intensity of increase of IR. For non-seismic deformation, the IR increase ranges from ca. 5% up to 50% depending on the strain quantity and its localization. In the seismic deformation, microstructures show a large amount of strain in the BFR associated with a very strong IR increase. However, comparing profiles, their spectrum shapes are different (Figure IV.15). In fact, the non-seismic profiles are smoother and show a large disparity of the values whereas in the BFR the IR profiles increase sharply on the rims of the fault core vein and contain constant values. These IR profile evolutions could be linked with microstructures. Indeed, in the BFR, the deformation controlled by ultra-comminution is strongly localized in the fault core vein and the entire strained layer is affected. In opposition, in non-seismic deformed zones, the deformation is gradual up to the core of the shear-zone and controlled by the mineralogy.

To finish, additional factors could control the CM crystallinity evolution in the deformed zones such as the fluid circulation or the heat induced by the frictional work during faulting. The first factor is important in deformed zones because they act as preferential pathways for fluid circulation. However, during thermal maturation using autoclaves, presented in the Chapter V, this factor has been explored by adding 10 wt% of distilled water in sample capsules (Figure V.27), which did not produced any significant effect (i.e. below 1%). The second factor that could control the difference of IR and make higher increase of the CM crystallinity in seismic deformed zones is the heat generated during frictional work. Based on the results of Chapter VI, the observed faults are minor and the heat needed to produce the observed IR values would represent an unreasonably high slip rate. Therefore, according to the RSCM profiles (Figures VI.3 to VI.5),these results suggest that IR increase is controlled by mechanical wear and the heat produced during fault slip was not large enough to affect CM crystallinity.

Finally, based on the CM crystallinity evolution along profiles (i.e. continuous or sharp) presented above it is possible to decipher the seismic deformation and the non-seismic ductile deformation (see Chapter IV) and to determine if the seismic objects are induced by frictional melting or not (see Chapter VI and VII) for poorly organized CM during the carbonization and the early graphitization stage.

Natural vs. experimental samples

Natural strain gradients have shown a significant increase in CM crystallinity in shear-zones at different scales (Chapter IV). Nevertheless, the largest variations were observed in a temperature range from 260°C to 300°C (Figures IV.6 to IV.10). The experiments carried out in this study aim to reproduce deformation structures in this range of temperature when the CM is still poorly organized, and the pairs of time-temperature have been adapted to reach this range of crystallinity, based on our experiments of CM maturation (Chapter V). In addition, the analyses of natural samples do not allow us to determine strain parameters such as strain rate, strain quantity or the fluids quantity and nature, or to recognize the variation of a single parameter. Experimental approach enables to control the effect of a single parameter, such as strain or pressure.

The effect of pressure can be explored through the comparison between the Griggs apparatus and the Paterson rig experiments (Chapter V). Indeed, two experiments (T609BM and PP641) have been carried out at the same time-temperature pair with different pressures of 1000MPa and 150MPa, respectively, for the Griggs and the Paterson experiment. The results suggest that the pressure has a major catalyzing role in the maturation kinetics of the CM, similar to the results shown by Nakamura et al. (2020) during the graphitization stage. It is worthy to notice that a special attention should be paid to the results on the CM crystallinity evolution in experimental studies because the pressure ranges from room pressure up to 1GPa, preventing experiments to be directly compared (Bonijoly et al., 1982a; Bustin et al., 1995; Ross et al., 1991a).

For comparing now results from the natural (Chapter IV) and experimental (Chapter V) samples some parameters need to be taken into consideration. Indeed, during experiments, the deformation is essentially prograde whereas natural strained samples recorded several deformation episodes, and are sometimes overprinted by later brittle deformation. Nevertheless, the CM crystallinity, reflecting by the IR using the RSCM method, reveals the higher crystallinity recorded during the event without overprinting by retrograde reactions such as the ones observed in mineralogical evolution for example. This point explains why the IR evolutions measured in the natural and experimental samples show similar points. Moreover, the IR increases are correlated to the strain quantity and the IR profiles show

the same shape. It can be explained by microstructural observations that show similar strain localization mechanisms than in the natural sample, such as the recrystallization of white micas and chlorite in shear-zone and the grain size reduction of quartz clasts and the absence of albite. Moreover, the surrounding of strain zones, including the neighbor of the main shear-zone, show a slightly higher IR than the host-rock or undeformed rock in both natural and experimental samples. To sum up, very similar observation on CM crystallinity evolution have been observed in the natural and experimental shear-zones explained by similar microstructural and mineralogical evolution during the carbonization and early graphitization stage.

Finally, similar to the ductile deformation during the graphitization stage (Bustin et al., 1995), comparing PP641 and PP649 experiments using the Paterson Rig apparatus, the shear deformation seems to be more efficient than the coaxial deformation for similar displacement. Indeed, the IR values in the shear-zones are higher than those homogeneously deformed cylinder samples for the same displacement associated to the ductile deformation (i.e. ca. 2mm). In addition, IR values from the undeformed zone in shear deformation (PP641) are similar with coaxial PP649, however the time of experiments is almost twice shorter (Figure V.25).

RSCM thermometry issues

Strain applied on samples shown in this work has an effect on CM crystallinity and RSCM spectra. On the other hand, RSCM is used as the basis of thermometer calibration (Aoya et al., 2010; Beyssac et al., 2002; Kouketsu et al., 2014; Lahfid et al., 2010; Rahl et al., 2005). Strain could therefore modify the temperatures estimated through RSCM calibrations.

These calibrations are based either on area ratio between the D and the G-bands or on the FWHM width. The increasing IR indicates a more important D1 band in the strained-zones and the creation of artificial area under the D-band raw spectrum. Therefore, after the deconvolution, the D1 band has its area and FWHM increased by the deformation. Consequently, RSCM thermometers could be influenced by the effect of deformation and overestimate calculated temperature. In the following, we will discuss the effect of strain on the thermometers in non-seismic and seismic deformed zones.

High strain in non-seismic deformed zones

Most of the increases of IR are included between 10 and 20% for ductile deformation in average and 5% in maximum for the brittle deformation observed in non-seismic deformed zones. The errors based on the RSCM method are comprised between 25 to 50°C and the maximum 20% of strain-induced increase in IR is smaller than the error range of the method itself. In addition, a higher standard deviation is observed in strained zones and could interfere with interpretation.

In contrast, in high strained zones, such those observed in the Glarus Thrust area or in Kodiak Accretionary Complex, the IR measured could reach up to 60% of increase and is mostly included between 40 to 50% in average. In these cases, the calculated temperature is widely affected and could correspond to an increasing temperature of more than 50°C in average and locally of 90°C for a regional temperature of 280°C. Therefore, for a such quantity of deformation the error of the RSCM method is no more covering the deviation induced by the deformation and the temperature is largely overestimated.

Consequently, in low strain domains, the RSCM thermometry application will indicate reasonable temperatures but providing a largest standard deviation that could disturb the interpretation. In high strained domains, the use of the RSCM method should be paired with additional thermometers, instead based on the CM crystallinity (RSCM, vitrinite reflectance) such as fluid inclusion or illite crystallinity. At the end, if the RSCM is used in high strain zones, the results should be carefully used.

Seismic deformation

In the seismically deformed zones, the RSCM method has been first used to demonstrate the recording of the frictional heating/melting by CM crystallinity (see Chapter VI). Moreover, Ito et al. (2017) showed that the peak of temperature occurred during the seismic slip cannot be recorded by the RSCM. However, the results obtained in Chapter VI on the Black Fault Rocks studies, when no melt occurred and no flash-heating is detected, suggest that the mechanical wear is more responsible of this CM crystallinity whereas the frictional heat induced by the faulting is negligible. In addition, the IR increass measured in the BFR ranges, in average, from +40 to +60%. Therefore, the same conclusions from the high strain zones could be made for the use of the seismic deformation with a widely overestimated temperature induced by the seismic strain.

In Chapter VII, the RSCM has been applied to flash heated samples generated during a seismic event, such as stick slip experiments or melt-origin BFR. The atypical shape of the RSCM spectrum shows the increase in the D3-band after the deconvolution. In this case, the RSCM thermometers become impossible to apply due to the over-covering of this band on the D1-band and the G-band with underestimating the temperature for area ratio's calibrations (Beyssac et al., 2002; Lahfid et al., 2010) for FWHM width calibration (Kouketsu et al., 2014). In conclusion, the use of the D3/Gsl. ratio is a new tool using the RSCM that decipher quickly the heating or strain effect that conducts to the CM crystallinity enhance.

General conclusions

The carbonaceous material (CM), corresponding to the residual organic matter in the sediment derived from the diagenesis and the metamorphism, is an ubiquitous material that is composed of meta-sediments involved in convergent zones. Through the carbonization and the graphitization processes induced by temperature, the CM crystallinity increases up to its final stage, i.e. the perfectly-organized graphite. However, external factor such as the pressure, the rock-fluid interaction or the strain could catalyze the CM crystallinity enhance. In the past, for well-crystallized CM the effect of strain has been described as a catalyzer and revealed the sensitivity of the CM to the deformation. However, no study has been carried out to constrain the influence of strain on the CM crystallinity of poorly organized CM during the carbonization and the early graphitization stage, at low temperature from 200 to 360°C, despite of the various microstructures observed in this range of temperature. This study of the strain effects on the CM crystallinity attains three main objectives: (1) assess the validity of RSCM thermometer in strained zones; (2) estimate the finite strain quantity; and (3) determine the conditions of fault slip (melting or not of the fault core).

In this study, we have documented the effect of strain during seismic and non-seismic deformation on the CM crystallinity through natural examples with different strain gradients exhumed from ancient accretionary complexes and experimental ones. The CM crystallinity has been examined thanks to the RSCM method and especially the intensity ratio (IR) that is the main sensitive parameter to the strain and evolves monotonously along the carbonization and early graphitization processes. The results suggest that even on poorly organized CM the strain has an effect on the CM crystallinity and conducts to an increase in IR independently of the regime of deformation. Nevertheless, the distinction between the seismic and non-seismic deformation on the CM crystallinity evolution is visible through the intensity of increase and the shape of CM crystallinity evolution across strain structures. Indeed, the seismic deformation indicates a higher intensity and a sharper evolution of the CM crystallinity whereas the non-seismic deformation the intensity is weaker and the evolution smoother, except for high strain zones where high intensity of increase is observed and with a different profile IR shape. External catalyzing factors have been tested during this study such the fluid interaction and the pressure. Results

reveals that, similarly to the strain, the pressure plays a major role in the CM kinetics, in opposition, the fluid added during maturation did not show any visible effect.

To summarize, the strain has shown the influence on CM crystallinity increase during the carbonization and the early graphitization stages for both seismic and non-seismic deformations. The intensity of the CM crystallinity increase is variable from few percent for brittle non-seismic deformation up to 60% in the seismic deformed and ductile high strain zones. Therefore, the application of the thermometers is possible in most of the cases during the non-seismic deformation but should be used with cautions in high strain zones, because of a large overestimation up to 30%. In addition, the RSCM with respective parameters has proved its efficiency to decipher the melted origin of fault core veins and allows the detection of flash-heating events.

Following research works

During this work, many questions have been unveiled and remain totally or partially unexplored on the carbonaceous material crystallinity evolution when strain is applied. Three mains issues have been noticed and would need to be explored in future work.

The first one (1), and the more important, is the morphological characterization of the carbonaceous grains in the strained zone and the surrounding. It aims to demonstrate what nanostructural processes control the relationship between RSCM signal and strain. Based on measurements of the CM grains, using the Transmission Electron Microscopy, it would possible to link the RSCM signal evolution of the intensity ratio with the CM grain parameters such as the organization of the layers and the interlayer spaces.

The second point (2) deals with the quantification of the RSCM signal evolution, especially the intensity ratio, with a known quantity of strain using experimental apparatus (i.e. medium-solid Griggs and Paterson rig apparatuses) with systematic procedures. It aims to propose a calibration to use RSCM as a strain gauge.

The last issue (3) is the exploration of the strain effect at high degree is crystallinity during the graphitization stage. Indeed, based on the literature and the results from experimentally and naturally deformed samples at high temperature, the CM crystallinity and the intensity ratio have been shown as sensitive to the deformation. However, these studies are mainly concentrated during the 80 and the 90's and do not make use of RSCM. RSCM enables a very spatial resolution, necessary to correlate small-scale microstructures with CM properties. The Filabrès decollement, in the Betics Belt (Spain), represents an ideal imbricated strain gradients containing rocks that conserve the bedding up to highly strained rock with the development of millimetric S-C structures. This area would permit us to explore the effect of the deformation during the graphitization stage at different scales from the kilometric to the millimetric sampling scales. In addition, due to the high degree of metamorphism, classic petrological approach using mineralogical changes and P-T estimation could be used in order to compare the results obtained on the RSCM and petrological thermometries along the kilometric strain gradient.

References

Akker, I.V., Kaufmann, J., Desbois, G., Klaver, J., Urai, J.L., Berger, A., Herwegh, M., 2018. Multiscale porosity changes along the pro- and retrograde deformation path: an example from Alpine slates. Solid Earth 9, 1141–1156. https://doi.org/10.5194/se-9-1141-2018

Ammar, M.R., Rouzaud, J.-N., 2012. How to obtain a reliable structural characterization of polished graphitized carbons by Raman microspectroscopy. Journal of Raman Spectroscopy 43, 207–211. https://doi.org/10.1002/jrs.3014

Aoya, M., Kouketsu, Y., Endo, S., Shimizu, H., Mizukami, T., Nakamura, D., Wallis, S., 2010. Extending the applicability of the Raman carbonaceous-material geothermometer using data from contact metamorphic rocks. Journal of Metamorphic Geology 28, 895–914. https://doi.org/10.1111/j.1525-1314.2010.00896.x

Aubry, J., Passelègue, F.X., Deldicque, D., Girault, F., Marty, S., Lahfid, A., Bhat, H.S., Escartin, J., Schubnel, A., 2018. Frictional Heating Processes and Energy Budget During Laboratory Earthquakes. Geophysical Research Letters 45, 12,274-12,282. https://doi.org/10.1029/2018GL079263

Austrheim, H., Boundy, T.M., 1994. Pseudotachylytes Generated During Seismic Faulting and Eclogitization of the Deep Crust. Science 265, 82–83. https://doi.org/10.1126/science.265.5168.82

Badertscher, N.P., Burkhard, M., 2000. Brittle-ductile deformation in the Glarus thrust Lochseiten (LK) calc-mylonite. Terra Nova 12, 281–288. https://doi.org/10.1046/j.1365-3121.2000.00310.x

Barker, Charles.E., 1988. Geothermics of Petroleum Systems: Implications of the stabilization of Kerogen Thermal Maturation after a Geologically Brief Heating Duration at Peak Temperature, in: Petroleum Systems of the United States. U.S. Geological Survey bulletin, pp. 26–29.

Barzoi, S.C., 2015. Shear stress in the graphitization of carbonaceous matter during the low-grade metamorphism from the northern Parang Mountains (South Carpathians) — Implications to graphite geothermometry. International Journal of Coal Geology 146, 179–187. https://doi.org/10.1016/j.coal.2015.05.008

Barzoi, S.-C., Guy, B., 2002. Rôle de la déformation métamorphique dans la cristallinité du graphite : l'exemple des schistes graphiteux de la vallée de la Lotru (Carpathes, Roumanie). Comptes Rendus Geoscience 334, 89–95. https://doi.org/10.1016/s1631-0713(02)01706-6

Beaudoin, A., Augier, R., Laurent, V., Jolivet, L., Lahfid, A., Bosse, V., Arbaret, L., Rabillard, A., Menant, A., 2015. The Ikaria high-temperature Metamorphic Core Complex (Cyclades, Greece): Geometry, kinematics and thermal structure. Journal of Geodynamics 92, 18–41. https://doi.org/10.1016/j.jog.2015.09.004

Bebout, G.E., 2007. Trace Element and Isotopic Fluxes/Subducted Slab, in: Treatise on Geochemistry. Elsevier, pp. 1–50. https://doi.org/10.1016/B978-008043751-4/00231-5

Beny-Bassez, C., Rouzaud, J.N., 1985. Characterization of Carbonaceous Materials by Correlated Electron and Optical Microscopy and Raman Microspectroscopy. Scanning Electron Microscopy 119–132.

Bertrand, P., Bordenave, M.L., Brosse, E., Espitalié, J., Houzay, J.P., Pradier, B., Vandenbroucke, M., Walgenwitz, F., 1993. Other methods and tools for source rock appraisal., in: Applied Petroleum Geochemistry. pp. 279–371.

Beyssac, O., Goffé, B., Chopin, C., Rouzaud, J.N., 2002. Raman spectra of carbonaceous material in metasediments: a new geothermometer. Journal of Metamorphic Geology 20, 859–871. https://doi.org/10.1046/j.1525-1314.2002.00408.x

Beyssac, O., Pattison, D.R.M., Bourdelle, F., 2019. Contrasting degrees of recrystallization of carbonaceous material in the Nelson aureole, British Columbia and Ballachulish aureole, Scotland, with implications for thermometry based on Raman spectroscopy of carbonaceous material. Journal of Metamorphic Geology 37, 71–95. https://doi.org/10.1111/jmg.12449

Bohrson, W.A., Spera, F.J., 2003. Energy-constrained open-system magmatic processes IV: Geochemical, thermal and mass consequences of energy-constrained recharge, assimilation and fractional crystallization (EC-RAFC): OPEN-SYSTEM MAGMATIC PROCESSES. Geochemistry, Geophysics, Geosystems 4. https://doi.org/10.1029/2002GC000316

Bonijoly, M., Oberlin, M., Oberlin, A., 1982a. A possible mechanism for natural graphite formation. International Journal of Coal Geology 1, 283–312. https://doi.org/10.1016/0166-5162(82)90018-0

Bonijoly, M., Oberlin, M., Oberlin, A., 1982b. A possible mechanism for natural graphite formation. International Journal of Coal Geology 1, 283–312. https://doi.org/10.1016/0166-5162(82)90018-0

Bourdelle, F., Cathelineau, M., 2015. Low-temperature chlorite geothermometry: a graphical representation based on a T–R2+ –Si diagram. ejm 27, 617–626. https://doi.org/10.1127/ejm/2015/0027-2467

Bourdelle, F., Parra, T., Chopin, C., Beyssac, O., 2013. A new chlorite geothermometer for diagenetic to low-grade metamorphic conditions. Contrib Mineral Petrol 165, 723–735. https://doi.org/10.1007/s00410-012-0832-7

Boyer, M., 2016. Synthèse de nouvelles céramiques polycristallines transparentes par cristallisation complète du verre. Université d'Orléans.

Brantut, N., Schubnel, A., Corvisier, J., Sarout, J., 2010. Thermochemical pressurization of faults during coseismic slip. Journal of Geophysical Research 115. https://doi.org/10.1029/2009JB006533

Brantut, N., Schubnel, A., Rouzaud, J.-N., Brunet, F., Shimamoto, T., 2008. High-velocity frictional properties of a clay-bearing fault gouge and implications for earthquake mechanics. Journal of Geophysical Research 113. https://doi.org/10.1029/2007JB005551

Bunge, H.J., 1982. Texture Analysis in Materials Science: Mathematical Models, 1st edition. ed. Butterworth-Heinemann, London.

Burkhard, M., Kerrich, R., Maas, R., Fyfe, W.S., 1992. Stable and Sr-isotope evidence for fluid advection during thrusting of the glarus nappe (swiss alps). Contributions to Mineralogy and Petrology 112, 293–311. https://doi.org/10.1007/BF00310462

Burnham, A.K., Sweeney, J.J., 1989. A chemical kinetic model of vitrinite maturation and reflectance. Geochimica et Cosmochimica Acta 53, 2649–2657. https://doi.org/10.1016/0016-7037(89)90136-1

Bustin, R.M., 1995. Mechanisms of graphite formation from kerogen: experimental evidence 36.

Bustin, R.M., 1983a. Heating during thrust faulting in the rocky mountains: friction or fiction? Tectonophysics 95, 309–328. https://doi.org/10.1016/0040-1951(83)90075-6

Bustin, R.M., 1983b. Heating during thrust faulting in the rocky mountains: friction or fiction? Tectonophysics 95, 309–328. https://doi.org/10.1016/0040-1951(83)90075-6

Bustin, R.M., Ross, J.V., Rouzaud, J.N., 1995. Mechanisms of graphite formation from kerogen: experimental evidence. International Journal of Coal Geology 28, 1–36.

Byrne, T., 1982. Structural evolution of coherent terranes in the Ghost Rocks Formation, Kodiak Island, Alaska. Geological Society, London, Special Publications 10, 229–242. https://doi.org/10.1144/GSL.SP.1982.010.01.15

Carslaw, H.S., Jaeger, J.C., 1959. Conduction of Heat in Solids, 2nd edition. ed. Oxford University Press.

Cavelan, A., 2019. Role of the chemical properties and the chemical transformations of organic matter with increasing thermal maturity on the development of the porosity of organic-rich shales. Université d'Orléans.

Cermak, V., Rybach, L., 1982. Thermal properties: Thermal conductivity and specific heat of minerals and rocks. G. Angeneister.

Charvet, J., Fabbri, O., 1987. Vue générale sur l'orogenèse Shimanto et l'évolution tertiaire du Japon sud-ouest. Bulletin de la Société Géologique de France III (8), 1171–1188.

Clerc, C., Lahfid, A., Monié, P., Lagabrielle, Y., Chopin, C., Poujol, M., Boulvais, P., Ringenbach, J.-C., Masini, E., de St Blanquat, M., 2015. High-temperature metamorphism during extreme thinning of the continental crust: a reappraisal of the North Pyrenean passive paleomargin. Solid Earth 6, 643–668. https://doi.org/10.5194/se-6-643-2015

Connelly, W., 1978. Uyak Complex, Kodiak Islands, Alaska: A Cretaceous subduction complex. Geological Society of America Bulletin 89, 755. https://doi.org/10.1130/0016-7606(1978)89<755:UCKIAA>2.0.CO;2

Cuesta, A., Dhamelincourt, P., Laureyns, J., Martínez-Alonso, A., Tascón, J.M.D., 1994. Raman microprobe studies on carbon materials. Carbon 32, 1523–1532. https://doi.org/10.1016/0008-6223(94)90148-1

Delchini, S., 2018. Etude tectono-thermique d'un segment orogénique varisque à histoire géologique complexe: analyse structurale, géochronologique et thermique du massif des Jebilet, de l'extension à la compression. Université d'Orléans.

Di Toro, G., Goldsby, D.L., Tullis, T.E., 2004. Friction falls towards zero in quartz rock as slip velocity approaches seismic rates. Nature 427, 436–439. https://doi.org/10.1038/nature02249

Di Toro, G., Han, R., Hirose, T., De Paola, N., Nielsen, S., Mizoguchi, K., Ferri, F., Cocco, M., Shimamoto, T., 2011. Fault lubrication during earthquakes. Nature 471, 494–498. https://doi.org/10.1038/nature09838

Di Toro, G., Hirose, T., Nielsen, S., Pennacchioni, G., Shimamoto, T., 2006. Natural and Experimental Evidence of Melt Lubrication of Faults During Earthquakes. Science 311, 647–649. https://doi.org/10.1126/science.1121012

Di Toro, G., Pennacchioni, G., 2009. Pseudotachylytes and Earthquake Source Mechanics, in: Fault-Zone Properties and Earthquake Rupture Dynamics. Fukuyama, E., pp. 88–133.

Di Toro, G., Pennacchioni, G., 2005. Fault plane processes and mesoscopic structure of a strong-type seismogenic fault in tonalites (Adamello batholith, Southern Alps). Tectonophysics 402, 55–80. https://doi.org/10.1016/j.tecto.2004.12.036

Dielforder, A., Berger, A., Herwegh, M., 2016. The accretion of foreland basin sediments during early stages of continental collision in the European Alps and similarities to accretionary wedge tectonics: FORELAND BASIN ACCRETION. Tectonics 35, 2216–2238. https://doi.org/10.1002/2015TC004101

Ebert, A., Herwegh, M., Pfiffner, A., 2007. Cooling induced strain localization in carbonate mylonites within a large-scale shear zone (Glarus thrust, Switzerland). Journal of Structural Geology 29, 1164–1184. https://doi.org/10.1016/j.jsg.2007.03.007

Ernst, R.E., 2014. Oceanic LIPs: oceanic plateaus and ocean-basin flood basalts and their remnants through time, in: Large Igneous Provinces. Cambridge University Press, pp. 90–110. https://doi.org/10.1017/CBO9781139025300

Espitalié, J., Deroo, G., Marquis, F., 1985a. Rock-Eval Pyrolysis and Its Applications (Part One). Rev. Inst. Franç. Pétrole 40, 563–579. https://doi.org/10.2516/ogst:1985035

Espitalié, J., Deroo, G., Marquis, F., 1985b. Rock-Eval Pyrolysis and Its Applications (Part Two). Rev. Inst. Franç. Pétrole 40, 755–784.

Fabbri, O., Faure, M., Charvet, J., 1990. Back-thrusting in accretionary prisms: microtectonic evidence from the Cretaceous-Lower Tertiary Shimanto belt of southwest Japan. Journal of Southeast Asian Earth Sciences 4, 195–201. https://doi.org/10.1016/S0743-9547(05)80013-3

Fabbri, O., Lin, A., Tokushige, H., 2000. Coeval formation of cataclasite and pseudotachylyte in a Miocene forearc granodiorite, southern Kyushu, Japan. Journal of Structural Geology 22, 1015–1025. https://doi.org/10.1016/S0191-8141(00)00021-3

Fabbri, O., Magott, R., Fournier, M., Etienne, L., 2018. Pseudotachylyte in the Monte Maggiore ophiolitic unit (Alpine Corsica): a possible lateral extension of the Cima di Gratera intermediate-depth Wadati-Benioff paleo-seismic zone. BSGF - Earth Sciences Bulletin 189, 18. https://doi.org/10.1051/bsgf/2018020

Ferraina, C., 2018. Partage des métaux entre liquide sulfuré et liquide silicaté : Expérimentation, modélisation et applications aux gisements de sulfures magmatiques. Université d'Orléans.

Ferralis, N., Matys, E.D., Knoll, A.H., Hallmann, C., Summons, R.E., 2016. Rapid, direct and non-destructive assessment of fossil organic matter via microRaman spectroscopy. Carbon 108, 440–449. https://doi.org/10.1016/j.carbon.2016.07.039

Festa, A., Dilek, Y., Pini, G.A., Codegone, G., Ogata, K., 2012. Mechanisms and processes of stratal disruption and mixing in the development of mélanges and broken formations: Redefining and classifying mélanges. Tectonophysics 568–569, 7–24. https://doi.org/10.1016/j.tecto.2012.05.021

Fisher, D., Byrne, T., 1987. Structural evolution of underthrusted sediments, Kodiak Islands, Alaska. Tectonics 6, 775–793. https://doi.org/10.1029/TC006i006p00775

Fisher, D.M., Byrne, T., 1992. Strain variations in an ancient accretionary complex: Implications for forearc evolution. Tectonics 11, 330–347. https://doi.org/10.1029/91TC01490

Früh-Green, G.L., 1994. Interdependence of deformation, fluid infiltration and reaction progress recorded in eclogitic metagranitoids (Sesia Zone, Western Alps). J Metamorph Geol 12, 327–343. https://doi.org/10.1111/j.1525-1314.1994.tb00026.x

Fukuchi, R., Fujimoto, K., Kameda, J., Hamahashi, M., Yamaguchi, A., Kimura, G., Hamada, Y., Hashimoto, Y., Kitamura, Y., Saito, S., 2014. Changes in illite crystallinity within an ancient tectonic boundary thrust caused by thermal, mechanical, and hydrothermal effects: an example from the Nobeoka Thrust, southwest Japan. Earth, Planets and Space 66, 116. https://doi.org/10.1186/1880-5981-66-116

Furuichi, H., Ujiie, K., Kouketsu, Y., Saito, T., Tsutsumi, A., Wallis, S., 2015. Vitrinite reflectance and Raman spectra of carbonaceous material as indicators of frictional heating on faults: Constraints from friction experiments. Earth and Planetary Science Letters 424, 191–200. https://doi.org/10.1016/j.epsl.2015.05.037

Fusseis, F., Regenauer-Lieb, K., Liu, J., Hough, R.M., De Carlo, F., 2009. Creep cavitation can establish a dynamic granular fluid pump in ductile shear zones. Nature 459, 974–977. https://doi.org/10.1038/nature08051

Green, H.W., Borch, R.S., 1989. A new molten salt cell for precision stress measurement at high pressure. ejm 1, 213–220. https://doi.org/10.1127/ejm/1/2/0213

Grunewald, U., Sparks, R.S.J., Kearns, S., Komorowski, J.C., 2000. Friction marks on blocks from pyroclastic flows at the Soufriere Hills volcano, Montserrat: Implications for flow mechanisms. Geology 28, 827–830. https://doi.org/10.1130/0091-7613(2002)030%3C0190:FMOBFP%3E2.0.CO;2

Guedes, A., Noronha, F., Prieto, A.C., 2005. Characterisation of dispersed organic matter from lower Palaeozoic metasedimentary rocks by organic petrography, X-ray diffraction and micro-Raman spectroscopy analyses. International Journal of Coal Geology 62, 237–249. https://doi.org/10.1016/j.coal.2005.03.016

Guedes, A., Valentim, B., Prieto, A.C., Rodrigues, S., Noronha, F., 2010. Micro-Raman spectroscopy of collotelinite, fusinite and macrinite. International Journal of Coal Geology 83, 415–422. https://doi.org/10.1016/j.coal.2010.06.002

Hara, H., Kimura, K., 2008. Metamorphic and cooling history of the Shimanto accretionary complex, Kyushu, Southwest Japan: Implications for the timing of out-of-sequence thrusting. Island Arc 17, 546–559. https://doi.org/10.1111/j.1440-1738.2008.00636.x

Hardebeck, J.L., 2012. Coseismic and postseismic stress rotations due to great subduction zone earthquakes: STRESS ROTATIONS IN SUBDUCTION ZONES. Geophysical Research Letters 39. https://doi.org/10.1029/2012GL053438

Hasegawa, A., Yoshida, K., Asano, Y., Okada, T., Iinuma, T., Ito, Y., 2012. Change in stress field after the 2011 great Tohoku-Oki earthquake. Earth and Planetary Science Letters 355–356, 231–243. https://doi.org/10.1016/j.epsl.2012.08.042

Hasegawa, R., Yamaguchi, A., Fukuchi, R., Hamada, Y., Ogawa, N., Kitamura, Y., Kimura, G., Ashi, J., Ishikawa, T., 2019. Postseismic fluid discharge chemically recorded in altered pseudotachylyte discovered from an ancient megasplay fault: an example from the Nobeoka Thrust in the Shimanto accretionary complex, SW Japan. Progress in Earth and Planetary Science 6. https://doi.org/10.1186/s40645-019-0281-2

Henry, D.G., Jarvis, I., Gillmore, G., Stephenson, M., 2019. Raman spectroscopy as a tool to determine the thermal maturity of organic matter: Application to sedimentary, metamorphic and structural geology. Earth-Science Reviews 198, 102936. https://doi.org/10.1016/j.earscirev.2019.102936

Henry, D.G., Jarvis, I., Gillmore, G., Stephenson, M., Emmings, J.F., 2018. Assessing low-maturity organic matter in shales using Raman spectroscopy: Effects of sample preparation and operating procedure. International Journal of Coal Geology 191, 135–151. https://doi.org/10.1016/j.coal.2018.03.005

Herwegh, M., Hürzeler, J.-P., Pfiffner, O.A., Schmid, S.M., Abart, R., Ebert, A., 2008. The Glarus thrust: excursion guide and report of a field trip of the Swiss Tectonic Studies Group (Swiss Geological Society, 14.–16. 09. 2006). Swiss Journal of Geosciences 101, 323–340. https://doi.org/10.1007/s00015-008-1259-z

Huang, W.-L., 1996. Experimental study of vitrinite maturation: effects of temperature, time, pressure, water, and hydrogen index. Organic Geochemistry 24, 233–241. https://doi.org/10.1016/0146-6380(96)00032-0

Hunziker, J.C., Frey, M., Clauer, N., Dallmeyer, R.D., Friedrichsen, H., Flehmig, W., Hochstrasser, K., Roggwiler, P., Schwander, H., 1986. The evolution of illite to muscovite: mineralogical and isotopic data from the Glarus Alps, Switzerland. Contributions to Mineralogy and Petrology 92, 157–180. https://doi.org/10.1007/BF00375291

Ide, S., Takeo, M., 1997. Determination of constitutive relations of fault slip based on seismic wave analysis. Journal of Geophysical Research: Solid Earth 102, 27379–27391. https://doi.org/10.1029/97JB02675

Ikesawa, E., Kimura, G., Sato, K., Ikehara-Ohmori, K., Kitamura, Y., Yamaguchi, A., Ujiie, K., Hashimoto, Y., 2005. Tectonic incorporation of the upper part of oceanic crust to overriding plate of a convergent margin: An example from the Cretaceous–early Tertiary Mugi Mélange, the Shimanto Belt, Japan. Tectonophysics 401, 217–230. https://doi.org/10.1016/j.tecto.2005.01.005

Ikesawa, E., Sakaguchi, A., Kimura, G., 2003. Pseudotachylyte from an ancient accretionary complex: Evidence for melt generation during seismic slip along a master décollement? Geology 31, 637. https://doi.org/10.1130/0091-7613(2003)031<0637:PFAAAC>2.0.CO;2

Ito, K., Ujiie, K., Kagi, H., 2017. Detection of increased heating and estimation of coseismic shear stress from Raman spectra of carbonaceous material in pseudotachylytes: Raman Spectra in Pseudotachylytes. Geophysical Research Letters. https://doi.org/10.1002/2016GL072457

Jawhari, T., Roid, A., Casado, J., 1995. Raman spectroscopic characterization of some commercially available carbon black materials. Carbon 33, 1561–1565. https://doi.org/10.1016/0008-6223(95)00117-V

Kanamori, H., Brodsky, E.E., 2004. The physics of earthquakes. Reports on Progress in Physics 67, 1429–1496. https://doi.org/10.1088/0034-4885/67/8/R03

Kanamori, H., Heaton, T.H., 2000. Microscopic and macroscopic physics of earthquakes, in: Rundle, J.B., Turcotte, D.L., Klein, W. (Eds.), Geophysical Monograph Series. American Geophysical Union, Washington, D. C., pp. 147–163. https://doi.org/10.1029/GM120p0147

Kaneki, S., Hirono, T., 2019. Diagenetic and shear-induced transitions of frictional strength of carbon-bearing faults and their implications for earthquake rupture dynamics in subduction zones. Sci Rep 9, 7884. https://doi.org/10.1038/s41598-019-44307-y

Kaneki, S., Hirono, T., 2018. Kinetic effect of heating rate on the thermal maturity of carbonaceous material as an indicator of frictional heat during earthquakes. Earth, Planets and Space 70. https://doi.org/10.1186/s40623-018-0868-7

Kaneki, S., Hirono, T., Mukoyoshi, H., Sampei, Y., Ikehara, M., 2016. Organochemical characteristics of carbonaceous materials as indicators of heat recorded on an ancient plate-subduction fault:

ANOMALY IN CM FROM MEGASPLAY FAULT. Geochem. Geophys. Geosyst. 17, 2855–2868. https://doi.org/10.1002/2016GC006368

Katagiri, G., Ishida, H., Ishitani, A., 1988. Raman spectra of graphite edge planes. Carbon 26, 565–571. https://doi.org/10.1016/0008-6223(88)90157-1

Kedar, L., Bond, C.E., Muirhead, D., 2021. Raman spectroscopy in thrust-stacked carbonates: an investigation of spectral parameters with implications for temperature calculations in strained samples (preprint). Tectonic plate interactions, magma genesis, and lithosphere deformation at all scales/Structural geology and tectonics, rock physics, experimental deformation/Mineral and rock physics. https://doi.org/10.5194/se-2021-70

Kedar, L., Bond, C.E., Muirhead, D., 2020. Carbon ordering in an aseismic shear zone: Implications for Raman geothermometry and strain tracking. Earth and Planetary Science Letters 549, 116536. https://doi.org/10.1016/j.epsl.2020.116536

Kelemen, S.R., Fang, H.L., 2001. Maturity Trends in Raman Spectra from Kerogen and Coal. Energy & Fuels 15, 653–658. https://doi.org/10.1021/ef0002039

Kiminami, K., Miyashita, S., 1992. Occurrence and geochemistry of greenstones from the Makimine Formation in the Upper Cretaceous Shimanto Supergroup in Kyushu, Japan. The Journal of the Geological Society of Japan 98, 391–400. https://doi.org/10.5575/geosoc.98.391

Kirilova, M., Toy, V., Rooney, J.S., Giorgetti, C., Gordon, K.C., Collettini, C., Takeshita, T., 2018. Structural disorder of graphite and implications for graphite thermometry. Solid Earth 9, 223–231. https://doi.org/10.5194/se-9-223-2018

Kitamura, Y., Kimura, G., 2012. Dynamic role of tectonic mélange during interseismic process of plate boundary mega earthquakes. Tectonophysics 568–569, 39–52. https://doi.org/10.1016/j.tecto.2011.07.008

Kitamura, Y., Sato, K., Ikesawa, E., Ikehara-Ohmori, K., Kimura, G., Kondo, H., Ujiie, K., Onishi, C.T., Kawabata, K., Hashimoto, Y., Mukoyoshi, H., Masago, H., 2005. Mélange and its seismogenic roof décollement: A plate boundary fault rock in the subduction zone - An example from the Shimanto Belt, Japan. Tectonics 24. https://doi.org/10.1029/2004TC001635

Koizumi, Y., Otsuki, K., Takeuchi, A., Nagahama, H., 2004. Frictional melting can terminate seismic slips: Experimental results of stick-slips: FRICTIONAL MELTING STOPS STICK-SLIPS. Geophysical Research Letters 31, n/a-n/a. https://doi.org/10.1029/2004GL020642

Kondo, H., Kimura, G., Masago, H., Ohmori-Ikehara, K., Kitamura, Y., Ikesawa, E., Sakaguchi, A., Yamaguchi, A., Okamoto, S., 2005. Deformation and fluid flow of a major out-of-sequence thrust located at seismogenic depth in an accretionary complex: Nobeoka Thrust in the Shimanto Belt, Kyushu. Tectonics 24, n/a-n/a. https://doi.org/10.1029/2004TC001655

Kouketsu, Y., Mizukami, T., Mori, H., Endo, S., Aoya, M., Hara, H., Nakamura, D., Wallis, S., 2014. A new approach to develop the Raman carbonaceous material geothermometer for low-grade metamorphism using peak width: Raman CM geothermometer using FWHM. Island Arc 23, 33–50. https://doi.org/10.1111/iar.12057

Kouketsu, Y., Shimizu, I., Wang, Y., Yao, L., Ma, S., Shimamoto, T., 2017. Raman spectra of carbonaceous materials in a fault zone in the Longmenshan thrust belt, China; comparisons with those of sedimentary and metamorphic rocks. Tectonophysics 699, 129–145. https://doi.org/10.1016/j.tecto.2017.01.015

Kuo, L.-W., Di Felice, F., Spagnuolo, E., Di Toro, G., Song, S.-R., Aretusini, S., Li, H., Suppe, J., Si, J., Wen, C.-Y., 2017. Fault gouge graphitization as evidence of past seismic slip. Geology 45, 979–982. https://doi.org/10.1130/G39295.1

Kuo, L.-W., Huang, J.-R., Fang, J.-N., Si, J., Song, S.-R., Li, H., Yeh, E.-C., 2018. Carbonaceous Materials in the Fault Zone of the Longmenshan Fault Belt: 2. Characterization of Fault Gouge from Deep Drilling and Implications for Fault Maturity. Minerals 8, 393. https://doi.org/10.3390/min8090393

Lafargue, E., Marquis, F., Pillot, D., 1998. Rock-Eval 6 Applications in Hydrocarbon Exploration, Production, and Soil Contamination Studies. Revue de l'Institut Français du Pétrole 53, 421–437. https://doi.org/10.2516/ogst:1998036

Lahfid, A., Beyssac, O., Deville, E., Negro, F., Chopin, C., Goffé, B., 2010. Evolution of the Raman spectrum of carbonaceous material in low-grade metasediments of the Glarus Alps (Switzerland): RSCM in low-grade metasediments. Terra Nova 22, 354–360. https://doi.org/10.1111/j.1365-3121.2010.00956.x

Lanari, P., Guillot, S., Schwartz, S., Vidal, O., Tricart, P., Riel, N., Beyssac, O., 2012. Diachronous evolution of the alpine continental subduction wedge: Evidence from P–T estimates in the Briançonnais Zone houillère (France – Western Alps). Journal of Geodynamics 56–57, 39–54. https://doi.org/10.1016/j.jog.2011.09.006

Lanari, P., Vidal, O., De Andrade, V., Dubacq, B., Lewin, E., Grosch, E.G., Schwartz, S., 2014. XMapTools: A MATLAB©-based program for electron microprobe X-ray image processing and geothermobarometry. Computers & Geosciences 62, 227–240. https://doi.org/10.1016/j.cageo.2013.08.010

Landais, P., Michels, R., Elie, M., 1994. Are time and temperature the only constraints to the simulation of organic matter maturation? Organic Geochemistry 22, 617–630. https://doi.org/10.1016/0146-6380(94)90128-7

Lihou, J.C., 1996. Structure and deformational history of the Infrahelvetic flysch units, Glarus Alps, eastern Switzerland. Eclogae Geologicae Helvetiae 89, 439–460. https://doi.org/10.5169/SEALS-167909

Lin, A., 1996. Injection veins of crushing-originated pseudotachylyte and fault gouge formed during seismic faulting. Engineering Geology 43, 213–224. https://doi.org/10.1016/0013-7952(96)00062-2

Lin, W., Conin, M., Moore, J.C., Chester, F.M., Nakamura, Y., Mori, J.J., Anderson, L., Brodsky, E.E., Eguchi, N., Expedition 343 Scientists, Cook, B., Jeppson, T., Wolfson-Schwehr, M., Sanada, Y., Saito, S., Kido, Y., Hirose, T., Behrmann, J.H., Ikari, M., Ujiie, K., Rowe, C., Kirkpatrick, J., Bose, S., Regalla, C., Remitti, F., Toy, V., Fulton, P., Mishima, T., Yang, T., Sun, T., Ishikawa, T., Sample, J., Takai, K., Kameda, J., Toczko, S., Maeda, L., Kodaira, S., Hino, R.,

Saffer, D., 2013. Stress State in the Largest Displacement Area of the 2011 Tohoku-Oki Earthquake. Science 339, 687–690. https://doi.org/10.1126/science.1229379

Lünsdorf, N.K., Dunkl, I., Schmidt, B.C., Rantitsch, G., von Eynatten, H., 2014. Towards a Higher Comparability of Geothermometric Data obtained by Raman Spectroscopy of Carbonaceous Material. Part I: Evaluation of Biasing Factors. Geostandards and Geoanalytical Research 38, 73–94. https://doi.org/10.1111/j.1751-908X.2013.12011.x

Ma, K.-F., Tanaka, H., Song, S.-R., Wang, C.-Y., Hung, J.-H., Tsai, Y.-B., Mori, J., Song, Y.-F., Yeh, E.-C., Soh, W., Sone, H., Kuo, L.-W., Wu, H.-Y., 2006. Slip zone and energetics of a large earthquake from the Taiwan Chelungpu-fault Drilling Project. Nature 444, 473–476. https://doi.org/10.1038/nature05253

Madariaga, R., Olsen, K.B., 2012. Earthquake dynamics, International handbook of earthquake and engineering seismology. Elsevier.

Mansard, N., 2019. The role of metamorphic reactions for strain localization in the middle and lower crust: Insights from field observations and deformation experiments. Université d'Orléans.

Marti, S., Stünitz, H., Heilbronner, R., Plümper, O., Drury, M., 2017. Experimental investigation of the brittle-viscous transition in mafic rocks – Interplay between fracturing, reaction, and viscous deformation. Journal of Structural Geology 105, 62–79. https://doi.org/10.1016/j.jsg.2017.10.011

Masch, L., Wenk, H.R., Preuss, E., 1985. Electron microscopy study of hyalomylonites—evidence for frictional melting in landslides. Tectonophysics 115, 131–160. https://doi.org/10.1016/0040-1951(85)90103-9

Meneghini, F., Di Toro, G., Rowe, C.D., Moore, J.C., Tsutsumi, A., Yamaguchi, A., 2010. Record of mega-earthquakes in subduction thrusts: The black fault rocks of Pasagshak Point (Kodiak Island, Alaska). Geological Society of America Bulletin 122, 1280–1297. https://doi.org/10.1130/B30049.1

Menegon, L., Fusseis, F., Stünitz, H., Xiao, X., 2015. Creep cavitation bands control porosity and fluid flow in lower crustal shear zones. Geology 43, 227–230. https://doi.org/10.1130/G36307.1

Milnes, A.G., Pfiffner, O.A., 1977. Structural development of the infrahelvetic complex, eastern Switzerland. Eclogae Geologicae Helvetiae 70, 83–95.

Muirhead, D.K., 2012. A kinetic model for the thermal evolution of sedimentary and meteoritic organic carbon using Raman spectroscopy. Journal of Analytical and Applied Pyrolysis 9.

Mukoyoshi, H., Hara, H., Ohmori-Ikehara, K., 2007. Quantitative estimation of temperature conditions for illite crystallinity: comparison to vitrinite reflectance from the Chichibu and Shimanto accretionary complexes, eastern Kyushu, Southwest Japan. Bull. Geol. Surv. Japan 58, 23–31.

Mukoyoshi, H., Hirono, T., Hara, H., Sekine, K., Tsuchiya, N., Sakaguchi, A., Soh, W., 2009. Style of fluid flow and deformation in and around an ancient out-of-sequence thrust: An example from the Nobeoka Tectonic Line in the Shimanto accretionary complex, Southwest Japan: Fluid flow

and deformation in and around OST. Island Arc 18, 333–351. https://doi.org/10.1111/j.1440-1738.2009.00670.x

Mukoyoshi, H., Sakaguchi, A., Otsuki, K., Hirono, T., Soh, W., 2006. Co-seismic frictional melting along an out-of-sequence thrust in the Shimanto accretionary complex. Implications on the tsunamigenic potential of splay faults in modern subduction zones. Earth and Planetary Science Letters 245, 330–343. https://doi.org/10.1016/j.epsl.2006.02.039

Murata, A., 1997. Geological map of Miyazaki prefecture.

Nakamura K., Fujinaga K., Kato Y., 2000. Rare earth element geochemistry of in-situ basalts from the Upper Cretaceous Shimanto Belt and its implication for their origin. Japanese Magazine of Mineralogical and Petrological Sciences 29, 175–190. https://doi.org/10.2465/gkk.29.175

Nakamura, Y., Oohashi, K., Toyoshima, T., Satish-Kumar, M., Akai, J., 2015. Strain-induced amorphization of graphite in fault zones of the Hidaka metamorphic belt, Hokkaido, Japan. Journal of Structural Geology 72, 142–161. https://doi.org/10.1016/j.jsg.2014.10.012

Nakamura, Y., Yoshino, T., Satish-Kumar, M., 2020. Pressure dependence of graphitization: implications for rapid recrystallization of carbonaceous material in a subduction zone. Contributions to Mineralogy and Petrology 175. https://doi.org/10.1007/s00410-020-1667-2

Nakamura, Y., Yoshino, T., Satish-Kumar, M., 2017. An experimental kinetic study on the structural evolution of natural carbonaceous material to graphite. American Mineralogist 102, 135–148. https://doi.org/10.2138/am-2017-5733

Oberlin, A., 1989. High-resolution TEM studies of carbonization and graphitization., Chemistry and Physics of Carbon.

Osozawa, S., 1992. Double ridge subduction recorded in the Shimanto accretionary complex, Japan, and plate reconstruction. Geology 20, 939. https://doi.org/10.1130/0091-7613(1992)020<0939:DRSRIT>2.3.CO;2

Palazzin, G., Raimbourg, H., Famin, V., Jolivet, L., Kusaba, Y., Yamaguchi, A., 2016. Deformation processes at the down-dip limit of the seismogenic zone: The example of Shimanto accretionary complex. Tectonophysics 687, 28–43. https://doi.org/10.1016/j.tecto.2016.08.013

Passelègue, François.X., Schubnel, A., Nielsen, S., Bhat, H.S., Deldicque, D., Madariaga, R., 2016. Dynamic rupture processes inferred from laboratory microearthquakes: DYNAMIC PROCESSES OF STICK-SLIP. Journal of Geophysical Research: Solid Earth 121, 4343–4365. https://doi.org/10.1002/2015JB012694

Pasteris, J.D., 1989. In Situ Analysis in Geological Thin-Sections by Laser Raman Microprobe Spectroscopy: A Cautionary Note. Applied Spectroscopy 43, 567–570. https://doi.org/10.1366/0003702894202878

Pasteris, J.D., Wopenka, B., 1991. Raman Spectra of Graphite as Indicators of Degree of Metamorphism. Canadian Mineralogist 29, 1–9.

Pec, M., Stünitz, H., Heilbronner, R., 2012a. Semi-brittle deformation of granitoid gouges in shear experiments at elevated pressures and temperatures. Journal of Structural Geology 38, 200–221. https://doi.org/10.1016/j.jsg.2011.09.001

Pec, M., Stünitz, H., Heilbronner, R., 2012b. Semi-brittle deformation of granitoid gouges in shear experiments at elevated pressures and temperatures. Journal of Structural Geology 38, 200–221. https://doi.org/10.1016/j.jsg.2011.09.001

Pec, M., Stünitz, H., Heilbronner, R., Drury, M., de Capitani, C., 2012c. Origin of pseudotachylites in slow creep experiments. Earth and Planetary Science Letters 355–356, 299–310. https://doi.org/10.1016/j.epsl.2012.09.004

Pfiffner, O.A., 1993. The structure of the Helvetic nappes and its relation to the mechanical stratigraphy. Journal of Structural Geology 15, 511–521. https://doi.org/10.1016/0191-8141(93)90145-Z

Pfiffner, O.A., 1985. Displacements along thrust faults. Eclogae Geologicae Helvetiae 78, 313–333.

Pfiffner, O.A., 1981. Fold-and-thrust tectonics in the Helvetic Nappes (E Switzerland). Geological Society, London, Special Publications 9, 319–327. https://doi.org/10.1144/GSL.SP.1981.009.01.28

Pfiffner, O.A., 1977. Tektonische Untersuchungen im Infrahelvetikum der Ostschweiz. Translated title: Tectonic studies of the Infrahelvetic Complex, eastern Switzerland. Institut ETH und Universität Zürich.

Précigout, J., Stünitz, H., Pinquier, Y., Champallier, R., Schubnel, A., 2018. High-pressure, High-temperature Deformation Experiment Using the New Generation Griggs-type Apparatus. Journal of Visualized Experiments. https://doi.org/10.3791/56841

Rahl, J., Anderson, K., Brandon, M., Fassoulas, C., 2005. Raman spectroscopic carbonaceous material thermometry of low-grade metamorphic rocks: Calibration and application to tectonic exhumation in Crete, Greece. Earth and Planetary Science Letters 240, 339–354. https://doi.org/10.1016/j.epsl.2005.09.055

Rahn, M., Mullis, J., Erdelbrock, K., Frey, M., 1995. Alpine metamorphism in the North Helvetic Flysch of the Glarus Alps, Switzerland. Eclogae Geologicae Helvetiae 88, 157–178. https://doi.org/10.5169/SEALS-167669

Raimbourg, H., Augier, R., Famin, V., Gadenne, L., Palazzin, G., Yamaguchi, A., Kimura, G., 2014. Long-term evolution of an accretionary prism: The case study of the Shimanto Belt, Kyushu, Japan: Long-term evolution of the Shimanto Belt. Tectonics 33, 936–959. https://doi.org/10.1002/2013TC003412

Raimbourg, H., Famin, V., Palazzin, G., Yamaguchi, A., Augier, R., 2017a. Tertiary evolution of the Shimanto belt (Japan): A large-scale collision in Early Miocene: Early Miocene Collision in Shimanto Belt. Tectonics 36, 1317–1337. https://doi.org/10.1002/2017TC004529

Raimbourg, H., Famin, V., Palazzin, G., Yamaguchi, A., Augier, R., Kitamura, Y., Sakaguchi, A., 2019. Distributed deformation along the subduction plate interface: The role of tectonic mélanges. Lithos 334–335, 69–87. https://doi.org/10.1016/j.lithos.2019.01.033

Raimbourg, H., Thiéry, R., Vacelet, M., Famin, V., Ramboz, C., Boussafir, M., Disnar, J.-R., Yamaguchi, A., 2017b. Organic matter cracking: A source of fluid overpressure in subducting sediments. Tectonophysics 721, 254–274. https://doi.org/10.1016/j.tecto.2017.08.005

Reimold, W.U., 1995. Pseudotachylite in impact structures — generation by friction melting and shock brecciation?: A review and discussion. Earth-Science Reviews 39, 247–265. https://doi.org/10.1016/0012-8252(95)00033-X

Rice, J.R., 2006. Heating and weakening of faults during earthquake slip: HEATING AND WEAKENING OF FAULTS. Journal of Geophysical Research: Solid Earth 111, n/a-n/a. https://doi.org/10.1029/2005JB004006

Robert, P., 1971. Etude pétrographique des matières organiques insolubles par la mesure de leur pouvoir réflecteur: contribution à l'exploration pétrolière et à la connaissance des bassins sédimentaires. Rev. Inst. Franç. Pétrole 26, 105–135.

Romero-Sarmiento, M.-F., Rouzaud, J.-N., Bernard, S., Deldicque, D., Thomas, M., Littke, R., 2014. Evolution of Barnett Shale organic carbon structure and nanostructure with increasing maturation. Organic Geochemistry 71, 7–16. https://doi.org/10.1016/j.orggeochem.2014.03.008

Ross, J.V., Bustin, R.M., 1990. The role of strain energy in creep graphitization of anthracite. Nature 343, 58–60. https://doi.org/10.1038/343058a0

Ross, J.V., Bustin, R.M., Rouzaud, J.N., 1991a. Graphitization of high rank coals—the role of shear strain: experimental considerations. Organic Geochemistry 17, 585–596. https://doi.org/10.1016/0146-6380(91)90002-2

Ross, J.V., Bustin, R.M., Rouzaud, J.N., 1991b. Graphitization of high rank coals—the role of shear strain: experimental considerations. Organic Geochemistry 17, 585–596. https://doi.org/10.1016/0146-6380(91)90002-2

Rowe, C.D., Moore, J.C., Meneghini, F., McKeirnan, A.W., 2005. Large-scale pseudotachylytes and fluidized cataclasites from an ancient subduction thrust fault. Geology 33, 937. https://doi.org/10.1130/G21856.1

Rubie, D.C., 1986. The catalysis of mineral reactions by water and restrictions on the presence of aqueous fluid during metamorphism. Mineralogical Magazine 50, 399–415. https://doi.org/10.1180/minmag.1986.050.357.05

Sadezky, A., Muckenhuber, H., Grothe, H., Niessner, R., Pöschl, U., 2005. Raman microspectroscopy of soot and related carbonaceous materials: Spectral analysis and structural information. Carbon 43, 1731–1742. https://doi.org/10.1016/j.carbon.2005.02.018

Saito, M., Kimura, K., Naito, K., Sakai, A., 1996. Geological Map of Japan - Shiibamura.

Sakaguchi, A., 1999. Thermal maturity in the Shimanto accretionary prism, southwest Japan, with the thermal change of the subducting slab: fluid inclusion and vitrinite reflectance study. Earth and Planetary Science Letters 173, 61–74. https://doi.org/10.1016/S0012-821X(99)00219-8

Sakaguchi, A., 1996. High paleogeothermal gradient with ridge subduction beneath the Cretaceous Shimanto accretionary prism, southwest Japan. Geology 24, 795. https://doi.org/10.1130/0091-7613(1996)024<0795:HPGWRS>2.3.CO;2

Sample, J.C., Fisher, D.M., 1986. Duplex accretion and underplating in an ancient accretionary complex, Kodiak Islands, Alaska. Geology 14, 160. https://doi.org/10.1130/0091-7613(1986)14<160:DAAUIA>2.0.CO;2

Sample, J.C., Moore, J.C., 1987. Structural style and kinematics of an underplated slate belt, Kodiak and adjacent islands, Alaska. Geological Society of America Bulletin 99, 7. https://doi.org/10.1130/0016-7606(1987)99<7:SSAKOA>2.0.CO;2

Scharf, A., Handy, M.R., Ziemann, M.A., Schmid, S.M., 2013. Peak-temperature patterns of polyphase metamorphism resulting from accretion, subduction and collision (eastern Tauern Window, European Alps) - a study with Raman microspectroscopy on carbonaceous material (RSCM). Journal of Metamorphic Geology 31, 863–880. https://doi.org/10.1111/jmg.12048

Schmid, S.M., 1975. The Glarus overthrust : field evidence and mechanical model. Eclogae Geologicae Helvetiae 68, 247–280. https://doi.org/10.5169/SEALS-164386

Scholz, C., 1990. The Mechanics of Earthquakes and Faulting, 1st edition. ed. Cambridge University Press.

Schön, J., 1996. Physical Properties of Rocks Fundamentals and Principles of Petrophysics, Second edition. ed, Developments in Petroleum Science. Elsevier B.V.

Shand, S.J., 1916. The Pseudotachylyte of Parijs (Orange Free State), and its Relation to “Trap-Shotten Gneiss” and “Flinty Crush-Rock.” Quarterly Journal of the Geological Society 72, 198–221. https://doi.org/10.1144/GSL.JGS.1916.072.01-04.12

Shuto, T., 1961. Palaeontological Study of the Miyazaki Group : A General Account of Faunas. Memoirs of the Faculty of Science, Kyūsyū University. Series D, Geology 10, 73–206. https://doi.org/10.5109/1526109

Sibson, R.H., 1989. Earthquake faulting as a structural process. Journal of Structural Geology 11, 1–14. https://doi.org/10.1016/0191-8141(89)90032-1

Sibson, R.H., 1975. Generation of Pseudotachylyte by Ancient Seismic Faulting. Geophysical Journal International 43, 775–794. https://doi.org/10.1111/j.1365-246X.1975.tb06195.x

Silva, M.B., Kalkreuth, W., 2005. Petrological and geochemical characterization of Candiota coal seams, Brazil — Implication for coal facies interpretations and coal rank. International Journal of Coal Geology 64, 217–238. https://doi.org/10.1016/j.coal.2005.04.003

Spray, J.G., 1995. Pseudotachylyte controversy: Fact or friction? Geology 23, 1119. https://doi.org/10.1130/0091-7613(1995)023<1119:PCFOF>2.3.CO;2

Suchy, V., Frey, M., Wolf, M., 1997. Vitrinite reflectance and shear-induced graphitization in orogenic belts: A case study from the Kandersteg area, Helvetic Alps, Switzerland. International Journal of Coal Geology 34, 1–20. https://doi.org/10.1016/S0166-5162(97)00018-9

Sweeney, J.J., Burnham, A.K., 1990. Evaluation of a Simple Model of Vitrinite Reflectance Based on Chemical Kinetics. AAPG Bulletin 74, 1559–1570. https://doi.org/10.1306/0C9B251F-1710-11D7-8645000102C1865D

Tagiri, M., Tsuboi, S., 1979. Mixed carbonaceous material in Mesozoic shales and sandstones from the Yamizo Mountain-system, Japan. The Journal of the Japanese Association of Mineralogists, Petrologists and Economic Geologists 74, 47–56. https://doi.org/10.2465/ganko1941.74.47

Taira, A., Katto, J., Tashiro, M., Okamura, M., Kodama, K., 1988. The Shimanto Belt in Shikoku, Japan-Evolution of Cretaceous to Miocene accretionary prism. Modern Geology 12, 5–46.

Techmer, K.S., Ahrendt, H., Weber, K., 1992. The development of pseudotachylyte in the Ivrea—Verbano Zone of the Italian Alps. Tectonophysics 204, 307–322. https://doi.org/10.1016/0040-1951(92)90314-V

Teraoka, Y., Okumura, K., 1992. Tectonic division and Cretaceous sandstone compositions of the Northern Belt of the Shimanto Terrane, Southwest Japan. Memoirs of the Geological Society of Japan 38, 261–270.

Tissot, B.P., Welte, D.H., 1984. Petroleum Formation and Occurrence, 2nd ed. Springer-Verlag Berlin Heidelberg.

Tsutsumi, A., Shimamoto, T., 1997. High-velocity frictional properties of gabbro. Geophysical Research Letters 24, 699–702. https://doi.org/10.1029/97GL00503

Tuinstra, F., Koenig, J.L., 1970. Raman Spectrum of Graphite. The Journal of Chemical Physics 53, 1126–1130. https://doi.org/10.1063/1.1674108

Tullis, T.E., Tullis, J., 1986. Experimental rock deformation techniques, in: Hobbs, B.E., Heard, H.C. (Eds.), Geophysical Monograph Series. American Geophysical Union, Washington, D. C., pp. 297–324. https://doi.org/10.1029/GM036p0297

Turcotte, Donald.L., Schubert, G., 1982. Geodynamics, 2nd edition. ed. Cambridge.

Ujiie, K., Ito, K., Nagate, A., Tabata, H., 2021. Frictional melting and thermal fracturing recorded in pelagic sedimentary rocks of the Jurassic accretionary complex, central Japan. Earth and Planetary Science Letters 554, 116638. https://doi.org/10.1016/j.epsl.2020.116638

Ujiie, K., Kimura, G., 2014. Earthquake faulting in subduction zones: insights from fault rocks in accretionary prisms. Progress in Earth and Planetary Science 1, 7. https://doi.org/10.1186/2197-4284-1-7

Ujiie, K., Tsutsumi, A., Fialko, Y., Yamaguchi, H., 2009. Experimental investigation of frictional melting of argillite at high slip rates: Implications for seismic slip in subduction-accretion complexes. Journal of Geophysical Research 114. https://doi.org/10.1029/2008JB006165

Ujiie, K., Yamaguchi, H., Sakaguchi, A., Toh, S., 2007. Pseudotachylytes in an ancient accretionary complex and implications for melt lubrication during subduction zone earthquakes. Journal of Structural Geology 29, 599–613. https://doi.org/10.1016/j.jsg.2006.10.012

Vidal, O., De Andrade, V., Lewin, E., Munoz, M., Parra, T., Pascarelli, S., 2006. P-T-deformation-Fe3+/Fe2+ mapping at the thin section scale and comparison with XANES mapping: application to a garnet-bearing metapelite from the Sambagawa metamorphic belt (Japan): P-T-DEFORMATION-FE3+/FE2+ MAPPING. Journal of Metamorphic Geology 24, 669–683. https://doi.org/10.1111/j.1525-1314.2006.00661.x

Vrolijk, P., Myers, G., Moore, J.C., 1988. Warm fluid migration along tectonic melanges in the Kodiak Accretionary Complex, Alaska. Journal of Geophysical Research: Solid Earth 93, 10313–10324. https://doi.org/10.1029/JB093iB09p10313

Wada, H., Tomita, T., Matsuura, K., Tuchi, K., Ito, M., Morikiyo, T., 1994. Graphitization of carbonaceous matter during metamorphism with references to carbonate and pelitic rocks of contact and regional metamorphisms, Japan. Contributions to Mineralogy and Petrology 118, 217–228. https://doi.org/10.1007/BF00306643

Wakita, K., 2015. OPS mélange: a new term for mélanges of convergent margins of the world. International Geology Review 57, 529–539. https://doi.org/10.1080/00206814.2014.949312

Wang, A., Dhamenincourt, P., Dubessy, J., Guerard, D., Landais, P., Lelaurain, M., 1989. Characterization of graphite alteration in an uranium deposit by micro-Raman spectroscopy, X-ray diffraction, transmission electron microscopy and scanning electron microscopy. Carbon 27, 209–218. https://doi.org/10.1016/0008-6223(89)90125-5

Wei, S., Graves, R., Helmberger, D., Avouac, J.-P., Jiang, J., 2012. Sources of shaking and flooding during the Tohoku-Oki earthquake: A mixture of rupture styles. Earth and Planetary Science Letters 333–334, 91–100. https://doi.org/10.1016/j.epsl.2012.04.006

Wenk, H.R., 1978. Are pseudotachylites products of fracture or fusion? Geology 6, 507. https://doi.org/10.1130/0091-7613(1978)6<507:APPOFO>2.0.CO;2

Wilks, K.R., Mastalerz, M., Ross, J.V., Bustin, R.M., 1993. The effect of experimental deformation on the graphitization of Pennsylvania anthracite. International Journal of Coal Geology 24, 347–369. https://doi.org/10.1016/0166-5162(93)90019-7

Wopenka, B., Pasteris, J.D., 1993. Structural characterization of kerogens to granulite-facies graphite: Applicability of Raman microprobe spectroscopy. American Mineralogist 78, 533–557.

Wu, W., Kuo, L., Ku, C., Chiang, C., Sheu, H., Aprilniadi, T.D., Dong, J., 2020. Mixed-Mode Formation of Amorphous Materials in the Creeping Zone of the Chihshang Fault, Taiwan, and Implications for Deformation Style. Journal of Geophysical Research: Solid Earth 125. https://doi.org/10.1029/2020JB019862

Yamaguchi, A., Cox, S.F., Kimura, G., Okamoto, S., 2011. Dynamic changes in fluid redox state associated with episodic fault rupture along a megasplay fault in a subduction zone. Earth and Planetary Science Letters 302, 369–377. https://doi.org/10.1016/j.epsl.2010.12.029

Yamaguchi, A., Ishikawa, T., Kato, Y., Nozaki, T., Meneghini, F., Rowe, C.D., Moore, J.C., Tsutsumi, A., Kimura, G., 2014. Fluid-rock interaction recorded in black fault rocks in the Kodiak accretionary complex, Alaska. Earth, Planets and Space 66. https://doi.org/10.1186/1880-5981-66-58

Yoshida, K., Hasegawa, A., Okada, T., Iinuma, T., Ito, Y., Asano, Y., 2012. Stress before and after the 2011 great Tohoku-oki earthquake and induced earthquakes in inland areas of eastern Japan: STRESS CHANGE BY 2011 TOHOKU EARTHQUAKE. Geophysical Research Letters 39. https://doi.org/10.1029/2011GL049729

Benjamin MORIS-MUTTONI

Réorganisation structurale des matériaux carbonés lors de l'enfouissement et de la déformation : Expériences de déformation et exemples naturels

Les particules de matériaux carbonés (CM), présentes dans la majorité des sédiments, enregistrent une évolution progressive lors de l'enfouissement, passant d'une structure amorphe à une structure parfaitement ordonnée (i.e. graphite). Cette évolution s'effectue via de deux phases successives, la carbonisation et la graphitisation, qui peuvent être quantitativement suivies grâce à la spectroscopie Raman (RSCM). Cependant, le contrôle unique supposé de la température, ignorant d'autres potentiels facteurs, est encore débattu. Dans cette étude, l'effet de la déformation sur la cristallinité de la CM a été exploré à travers l'analyse d'échantillons naturels, provenant de prismes d'accrétions (Shimanto Belt, Kodiak Accretionary Complex, Alpes), et d'expériences de déformation reproduisant des déformations à vitesses faibles (non-sismique) et rapides (sismique). L'analyse a été focalisée sur des températures allant de 200 à 350°C, couvrant les processus de carbonisation et de graphitisation précoce. L'utilisation de profils de haute-résolution ont permis de corréler les microstructures et le signal RSCM. Le ratio d'intensité (IR) s'est montré comme un paramètre RSCM approprié à l'étude de l'effet de la déformation. Indépendamment du mécanisme de déformation (i.e. sismique ou non-sismique), l'IR augmente lorsque la déformation est localisée, montrant l'effet de la déformation sur le signal Raman. De plus, basé sur des échantillons ayant connu un métamorphisme de contact, couplés à des expériences de flash-heating, le Raman a montré son efficacité (D3/Gsl Ratio) dans la détection des chauffages courts et intenses. Cette méthode a été appliquée à des Black Fault Rocks considérées comme le résultat d'une trempe d'une veine fondue formée lors de glissement sismique. Les profils d'IR et le D3/Gsl Ratio ont permis de discriminer les mécanismes de formations (i.e. fusion ou comminution seul) de ces objets.

Mots clés : Matière carbonée ; RSCM ; Gradient de déformation ; Microstructures ; Expérimental ; Réorganisation cristalline

Reorganization of carbonaceous materials during geological burial and deformation: Experiments and natural examples

Particles of carbonaceous material (CM), present in most sediments, experience a progressive evolution during their burial from immature and amorphous structure to fully mature and crystalline graphite. This transformation, decomposed in two successive stages (carbonization then graphitization), can be quantitatively followed with Raman spectroscopy (RSCM), and is assumed to be controlled at the first order by temperature, while the potential role of other parameters is still controversial. In this work we explore the effect of strain on CM crystallinity with natural examples from accretionary complexes (Shimanto belt, Kodiak Accretionary Complex, Alps) and experiments encompassing both high strain rate (seismic) and low strain-rate (non-seismic) deformation. We focused on the low temperature range from 200 to 350°C, spanning the carbonization and the early graphitization stages. We used high-resolution profiles to correlate RSCM signal to microstructures. Intensity ratio (IR) appears to be the most relevant RSCM parameter to record deformation. Irrespective of the deformation mechanism (i.e. in low and high strain-rate examples), IR is increased in the zone where strain is localized, demonstrating the large influence of strain on Raman signal. In addition, using geological examples of contact metamorphism, combined with flash heating experiments, we demonstrated the potential of a RSCM feature (D3/Gsl Ratio) to detect short-lived and intense heating events. When applied to Black Fault Rocks considered as the result of quenching of a melt formed during fast seismic slip, these new tools (profiles of IR and D3/Gsl Ratio) can discriminate fault cores that melted from those where only mechanical comminution was active.

Keywords: Carbonaceous material; RSCM; Strain gradients; Microstructures; Experiments; Crystalline reorganization

Institut des Sciences de la Terre d'Orléans

Institut des Sciences de la Terre d'Orléans
1A rue due la Férollerie
45100 ORLEANS

UNIVERSITE D'ORLEANS